Studies on characterization and application of ultrashort higher harmonic radiation

By

MUKUND KUMAR

PHYS 03 2014 04 004

Raja Ramanna Centre for Advanced Technology, Indore

A thesis submitted to the

Board of Studies in Physical Sciences

In partial fulfilment of requirements

for the Degree of

DOCTOR OF PHILOSOPHY

of

HOMI BHABHA NATIONAL INSTITUTE

July 2019

Homi Bhabha National Institute[1]

Recommendations of the Viva Voce Committee

As members of the Viva Voce Committee, we certify that we have read the dissertation prepared by **Mukund Kumar** entitled **"Studies on characterization and application of ultrashort higher harmonic radiation"** and recommend that it may be accepted as fulfilling the thesis requirement for the award of Degree of Doctor of Philosophy.

Chairman – Prof. S. K. Dixit, RRCAT, Indore	S.K. Dixit
Guide / Convener – Prof. J. A. Chakera, RRCAT, Indore	16/6/2020
Examiner - Prof. D. N. Rao, University of Hyderabad	D Nagesha
Member 1- Prof. S. R. Mishra, RRCAT, Indore	SRMishra 16.6.2020
Member 2- Prof. S. K. Majumder, RRCAT, Indore	Sramajumder 16/6/2020
Member 3- Prof. Y. Choyal, DAVV, Indore	16/6/2020

Final approval and acceptance of this thesis is contingent upon the candidate's submission of the final copies of the thesis to HBNI.

I/~~We~~ hereby certify that I/~~we~~ have read this thesis prepared under my/our direction and recommend that it may be accepted as fulfilling the thesis requirement.

Date: 16/06/2020.

Place: Indore.

16/6/2020.

Signature

Guide

डॉ. ज. अ. चकेरा / Dr. J. A. Chakera
प्रमुख, लेज़र प्लाज़्मा प्रभाग
Head, Laser Plasma Division

[1] This page is to be included only for final submission after successful completion of viva voce.

STATEMENT BY AUTHOR

This dissertation has been submitted in partial fulfilment of requirements for an advanced degree at Homi Bhabha National Institute (HBNI) and is deposited in the Library to be made available to borrowers under rules of the HBNI.

Brief quotations from this dissertation are allowable without special permission, provided that accurate acknowledgement of source is made. Requests for permission for extended quotation from or reproduction of this manuscript in whole or in part may be granted by the Competent Authority of HBNI when in his or her judgment the proposed use of the material is in the interests of scholarship. In all other instances, however, permission must be obtained from the author.

Mukund Kumar

DECLARATION

I, hereby declare that the investigation presented in the thesis has been carried out by me. The work is original and has not been submitted earlier as a whole or in part for a degree / diploma at this or any other Institution / University.

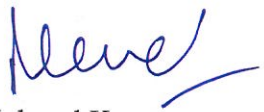

Mukund Kumar

List of Publications arising from the thesis

Journal

1. High order harmonic radiation source for multicolour extreme ultraviolet radiography of carbon plumes, **M. Kumar**, H. Singhal and J. A. Chakera, *J. Appl. Phys,* **2019**, *125*,155902
2. Study of Higher Diffraction Order Contribution in a Flat Field Grating Spectrograph Using a High-Order Harmonic Source, **M. Kumar**, H. Singhal, J. A. Chakera, and P. A. Naik, *Applied Spectroscopy*, **2018**,*72(9),* 1416-1424.
3. Enhancement of conversion efficiency and spatial coherence of high order harmonics generated from pre-formed plasma plumes using an apertured laser beam, **M. Kumar**, U. Chakravarty, R. Rathore, J. A. Chakera, P. A. Naik and P. D. Gupta, *J. Phys. B: At. Mol. Opt. Phys.*, **2016**, *49*, 075601.
4. Study of the spatial coherence of high order harmonic radiation generated from pre-formed plasma plumes, **M. Kumar**, H. Singhal, J. A. Chakera, P. A. Naik, R. A. Khan and P. D. Gupta, *J. Appl. Phys*, ***2013, 114***, 033112
5. Restoration of absolute diffraction efficiency and blaze angle of carbon contaminated gratings by ultraviolet cleaning, **M. Kumar**, H. Singhal, J. A. Chakera, P. A. Naik, R. A. Khan and P. D. Gupta, Appl. Opt, **2013**, *52*, 1725-1730.
6. Spatial coherence of spectrally resolved higher harmonics from argon gas cell using single and two color laser fields, **M. Kumar**, H. Singhal, A. Ansari, J. A. Chakera, (Manuscript under Review)

Conferences

1. High Resolution Electron Time of Flight Spectrograph for Temporal Characterization of Ultrashort High Order Harmonic Pulses, **M. Kumar**, H. Singhal, A. Ansari, and J. A. Chakera, *DAE-BRNS Theme Meeting on Ultrafast Science 2018, RRCAT, Indore, Oct.22-24, 2018*

   This was presented as a poster in the theme meeting and received Best Poster Award

2. High Order Harmonic Generation of Ti: Sapphire Laser from Neon Filled Gas Cells, H. Singhal, **M. Kumar**, A. Ansari, and J. A. Chakera, *DAE-BRNS Theme Meeting on Ultrafast Science 2018, RRCAT, Indore, Oct.22-24, 2018*

3. Study on generation and optimization of high order harmonic radiation from gas cell using 1 kHz laser system, **M. Kumar**, H. Singhal, J. A. Chakera, and P. A. Naik, *32nd National Symposium on Plasma Science & Technology, Gandhinagar, Nov 7-10, 2017*

4. Study on the role of electron trajectories in high order harmonic generation using single and two color laser fields, **M. Kumar**, H. Singhal, J. A. Chakera, and P. A. Naik, 32nd *National Symposium on Plasma Science & Technology, Gandhinagar, Nov. 7-10, 2017*

5. Initial Results of Magnetic Bottle Time of Flight Electron Spectrograph for the Measurement of Attosecond pulses, H. Singhal, **M. Kumar**, J. A. Chakera, P. Mohania, P. Shrivastava and P. A. Naik, 32nd *National Symposium on Plasma Science & Technology, Gandhinagar, Nov 7-10, 2017*

6. Ultra-fast Shadowgraphy of Plasma Plumes Using High Order Harmonics of Ti: sapphire Laser, H. Singhal, **M. Kumar**, J. A. Chakera and P A Naik, *DAE-BRNS Theme Meeting on Ultrafast Science 2017, Hyderabad, Nov 2-4, 2017*

This was presented as a poster in the theme meeting and received best poster Award

7. Shadowgraphy of Plasma Plumes using EUV Radiation Generated through High Order Harmonic Generation of Ti: Sapphire Laser pulse, **M. Kumar**, H. Singhal, J. A. Chakera, P. A. Naik and P D Gupta, 30th *National Symposium on Plasma Science & Technology, SINP, Kolkata, Dec. 1-4, 2015*

This was presented as a poster in the symposium and received best poster award

8. Spatio-spectral study of high order harmonic radiation generated from pre-formed carbon plume, **M. Kumar**, H. Singhal, J. A. Chakera, P. A. Naik and P. D. Gupta, 30th *National Symposium on Plasma Science & Technology, SINP, Kolkata, Dec. 1-4, 2015*

9. Intensity enhancement of harmonic generation from plasma plume using apertured Laser Beam, **M. Kumar**, U. Chakravarty, R. Rathore, J. A. Chakera, P. A. Naik, and P. D. Gupta, 29th *National Symposium on Plasma Science & Technology, Kottayam, Dec. 8-11, 2014*

MUKUND KUMAR

DEDICATIONS

I dedicate this thesis to my parents, whose sacrifice has taken me to this level, provided opportunity and made me capable to fulfil my dreams

ACKNOWLEDGEMENTS

I would like to express my thanks to all those who have helped me directly or indirectly during course of this thesis work. First and foremost, I would express my sincere gratitude to my thesis supervisor *Prof. J. A. Chakera* for his constant motivation, encouragement and guidance. I am highly grateful to him for providing ideas in the results on daily basis during the experiment. I am extremely thankful to him for sparing time despite his busy schedule as the Head, Laser Plasma Division to ensure the smooth progress and timely completion of the research work and the valuable comments during the finalization of thesis. I am greatly thankful to ex-director *Prof. P. A. Naik* for his support and his easy approachable nature for scientific discussions. I am sincerely thankful to *Dr. H. Singhal* for his suggestions and active support in planning and executing the experiment. I am profoundly thankful to the Doctoral committee (DC-3) on Basic Sciences for their valuable suggestions during the yearly review. I am also thankful to laser operation and maintenance team member viz. *Mr. R. A. Khan, Mr. R. K. Bhat* and *Mr. R. A. Joshi* for their full support to run the laser system and to *Mr. P. K. Tripathi, Mr. R. P. Kushwaha, Mr. S. Sebastin, Mr. K. C. Paramar and Mr Kisku* for providing the mechanical support for the experimental set up. I would like to thank my colleagues *Dr. V. Arora, Dr. B. S. Rao, Mr M. Tayyab, Dr. S. Bagchi, and Mr T. Mandal* for the discussions on several topics relevant to the present work in cordial atmosphere. I would also like to thank all my colleagues at Laser Plasma Division, RRCAT who have supported directly and indirectly during course of my research work. Finally, I am wordlessly thankful to my parents, my wife, my small kid for their continuous support and encouragement. It would certainly not be possible to complete this work without their selfless contribution.

CONTENTS

LIST OF FIGURES

LIST OF TABLES

Chapter 7:

Summary and Future Outlook

In this research work, an experimental investigation on coherent ultrashort higher harmonic generation from intense laser atom interaction is carried out. The study shows that, precise control over the laser and non-linear medium parameter is essential for efficient generation of higher harmonics. In this direction, we explored pre-formed plasma plumes as well as gas cells and optimized various relevant parameters viz. laser intensity, laser pulse shape, non-linear medium length, medium density and its position relative to laser focus etc. These parameters are found to be crucial for HHG and therefore, are carefully optimized to achieve higher yield alongwith good coherence property of the generated harmonics. The study is further extended to temporally characterize the high harmonic pulse, which is a challenging task due to its sub-femtosecond time structure and extreme ultraviolet wavelength. The characterization is performed using an in-house developed high resolution magnetic bottle electron time of flight spectrograph. The thesis also presents an application of the harmonic source in multicolor radiography of plasma plume for the first time. The technique is capable of characterizing density profile of multiple species of the plume simultaneously. The present research work highlights an effort towards efficient generation of higher harmonics with good spatial coherence. This will help in better understanding of the complex process of harmonic generation and also in future endeavour, in the field of extreme nonlinear optics.

7.1 Summary of the research work

The study on higher harmonics has been performed in pre-formed plasma plume to generate a coherent and intense source at short wavelength. The carbon

plume has been extensively explored for this purpose, which is an established non-linear medium for generation of intense mid-order harmonics (11^{th} to 21^{st} order). In this work, we focus on the spatial coherence property of the harmonic source, which is investigated using a double slit experiment. Double slit of width ~30μm and separation ~100μm to ~170μm) was used for this and spatial coherence property of 21^{st} to 11^{th} (λ ~ 35nm to 60nm) harmonic order was investigated. High contrast interference fringes were observed (fringe contrast > 0.7), which shows high spatial coherence property of harmonics. It is further observed that the spatial coherence decreases with increase in harmonic order. The experimental observation is supported by a theoretical model, which reveals the dominant role of time dependent electron density fluctuation inside the plume, in deteriorating spatial coherence property. Even small electron density fluctuation (~5%), is found to be enough to deteriorate the spatial coherence of higher harmonics significantly. The theoretical calculation of fringe visibility for ~5% density fluctuation, matches well with the experimentally observed values for all harmonic orders.

The generation of efficient harmonics is one of the major goals of the present research work. I have worked in this direction and selected graphite plume for the study. Different laser and plasma plume parameters are optimized viz. laser intensity, position of plasma plume relative to focus etc. The possibility of using spatially shaped laser beam for HHG is explored and it is found that harmonic generation efficiency is crucially affected by the spatial shaping of the driving laser beam. The spatial shaping is performed by using a variable opening hard aperture in the path of the laser beam. The study shows that, with decrease in the aperture opening diameter, the harmonic intensity first increases, achieves maximum value at half the laser beam diameter and then decreases. At an optimum aperture size, conversion efficiency of

15^{th} harmonics is observed to be ~10^{-6}, which gives a harmonic yield of ~ 20nJ per laser pulse. The experimental observation of optimum aperture diameter for maximum harmonic efficiency is understood from theoretical analysis based on phase matching between the laser pulse and harmonics. In the analysis, the dominant contribution of the off-axis phase matching is revealed, which gets improved at small aperture size and leads to improvement in CE. Although, contribution of off-axis phase matching is often ignored, due to its small magnitude as compared to the on-axis phase matching. However, after minimizing the on-axis phase mismatch, the off-axis phase matching do play dominant role. In this study, we concluded that it is the coherent volume ($\approx \pi R_c^2 \times Lc$) that leads to generation of efficient harmonics. The L_c (longitudinal coherence length) is maximized by optimizing the longitudinal (on-axis) phase matching and R_c (coherence radius) is maximized by optimizing the transverse (off-axis) phase matching. The improvement in off-axis phase matching is evident from the measured spatial coherence with aperture size, which shows an increase in coherent volume, with decrease in aperture size and improves harmonic yield.

The study was extended to generate higher harmonics from inert gas filled cells of different lengths. Different inert gases are used to explore different spectral range. A maximum harmonic cutoff order of 43^{rd} (λ ~19nm) was observed in argon, 73^{rd} (λ ~11nm) in neon and 99^{th} (λ ~8nm) in helium gases. The optimization of gas cell length, gas pressure and gas cell position has been performed and a maximum harmonic yield of ≈ 250nJ (photon flux ~ 10^{13} ph/sec) at 31^{st} harmonic order in argon, ~25nJ (~10^{12} ph/sec) per harmonic order (from 31^{st} to 51^{st} order) in neon and ~10nJ (~10^{10} ph/sec) per harmonic order (35^{th} to 63^{rd} order) in helium is achieved. The study is also performed using two colour laser pulses, where both odd and even harmonics are observed in the spectrum.

The spectral characteristics of higher harmonics generated from argon gas, are investigated in detail and remarkable variation with change in gas pressure is observed. With increase in gas cell pressure, the harmonic spectrum first broadens and then splits at high gas pressure (≥ 40mbar). The analysis of the experimental observations reveals that the splitting in the spectrum is due to the contribution of different electron trajectories viz. short and long trajectory, responsible for harmonic generation. Different trajectories are identified from the difference in divergence and spectral width of harmonics, generated from these trajectories. Few theoretical reports have already shown that a particular trajectory can be selected by optimizing laser and gas parameter or by using two color laser pulses e.g. (λ ~ 800nm + 400nm). We experimentally observed that when harmonics are generated using two color laser pulses, the contribution of short trajectory is dominant. The effect of the electron trajectories in the spatial coherence of these harmonics has also been investigated. It is found that the spatial coherence of harmonics generated by short electron trajectory is higher compared to the long trajectory. A theoretical model is developed, which showed that the role of intensity dependent dipole phase is crucial and the harmonics generated by these two trajectories have different spatial coherence.

An investigation on the temporal characteristics of higher harmonics has also been performed. A group of phase locked odd harmonic orders generates attosecond pulse trains separated by half laser cycle. The characterization is performed using magnetic bottle electron time of flight spectrograph using RABITT technique. High resolution MBETOF is in-house developed and characterized. The energy resolution ($\Delta E/E$) of MBETOF spectrograph is measured to be better than ~150 at 17eV, ~200 at 5eV. The spatial and temporal overlapping of higher harmonics and laser pulse is achieved on gas sheath, which generates the cross-correlation photoelectron signal

(sidebands). The sideband peak corresponds to the even harmonic order. By changing the delay between the harmonics and IR laser pulse, the oscillation in the intensity of these sidebands is recorded and the relative phase between the odd harmonics is calculated. The amplitude of harmonics is measured from the observed photoelectron count and the photo-ionization cross section at given photoelectron energy. From the measured amplitude and relative phase between the harmonics, the attosecond pulse train is reconstructed. The pulse width of individual attosecond pulses in pulse train generated from 17^{th} to 25^{th} harmonic order is measured to be ~290 attosecond.

Finally, application of higher harmonic source in multicolour radiography of plasma plume is presented. This technique provides multispecies characterization of carbon plasma plume density using multiple harmonic orders. The high order harmonics from 11^{th} to 21^{st} order are simultaneously used to record radiogram of the carbon plume. From the radiogram recorded at multiple wavelengths, the density profile of multiple species (CI, CII and C_2 molecule) are determined. It is found that at laser intensity of ~10^{11} W/cm^2 and at a delay of ~ 50 ns (after formation of plasma plume), the peak density of the CI, CII and C_2 is measured to be ~ 8×10^{18} cm^{-3}, ~ 4×10^{18} cm^{-3} and ~ 3.5×10^{17} cm^{-3} at a distance of ~150μm, ~170μm and ~ 120 μm away from the target surface. Carbon plume expansion speed of ~ 2×10^6 cm/s for singly charged carbon ions and ~ 4×10^5 cm/s for C_2 molecule is determined respectively.

7.2 Future perspective

Although, extensive study on generation and optimization of higher harmonics is presented in this thesis, still there is scope to improve the harmonic yield further, by using long focal length optics and long length of non-linear medium.

The present study addressed the spatial, spectral and temporal aspects of higher harmonics; however the polarization characteristics of higher harmonics remain untouched. Characterization and control of higher harmonic polarization is an important area of research. Few recent studies have shown the circularly polarized [221] higher harmonic generation, which finds potential application in wide are of research including in material science to explore the element selective ultrafast demagnetization dynamics of magnetic materials.

The design of MBETOF can be modified, so that both electron and ion signal can be detected simultaneously, which provides a better insight in the photoelectron spectroscopy of any gas atoms/molecules and also precise characterization of the generated attosecond pulses. In the present work, only attosecond pulse trains from lower harmonic orders (17^{th} 25^{th} order) are studied; there is wide spectral range of harmonics generated from neon and helium gases which can be explored for generation of shorter duration attosecond pulse trains. In the calculation of attosecond pulse duration, the role of atomic phase is ignored, which may be crucial when the shorter duration attosecond pulses are to be characterized and will pursued in future work. The study of ultrafast phenomena needs single attosecond pulses, which requires a few cycle laser pulses for HHG. This will also be explored in future studies.

SUMMARY

The present thesis work is mainly focused on the experimental investigation on efficient generation, characterization and application of higher harmonic radiation generated from ultrashort intense laser matter interaction. The study on spatial, spectral, temporal and photon flux characterization has been performed. Two different non-linear mediums viz. pre-formed plasma plumes and gas filled cells of different lengths, has been explored to improve the conversion efficiency of the generated harmonics in different spectral range. In case of higher harmonic from pre-formed plasma plumes, the study on the effect of spatial shaping (using a variable opening hard circular aperture) of laser pulse on yield and conversion efficiency of harmonics from plasma plume is carried out. Under optimum conditions, the conversion efficiency improved by more than an order of magnitude (from ~10^{-7} to ~10^{-6}). A theoretical formulation to explain the observed result is also carried out, which highlighted the dominant role of the off-axis phase matching in such enhancements. The study on spatial coherence property of the harmonics is studied using double slit experiment and high contrast fringes (contrast > 0.7) were observed, which shows high spatial coherence of the source. The study was further extended to improve the conversion efficiency and the harmonic yield and we explored the feasibility of long length gas cell (5mm, 15mm, 25mm and 35mm) for the harmonic generation. High conversion efficiency ~ 10^{-4} is achieved (~0.25μJ for 31^{st} harmonic order) for higher harmonics from argon gas under optimum parameter conditions (cell length ~15mm). The harmonic cutoff was extended to 99^{th} order (λ~8nm) in case of helium gas with photon flux of ~10^{10} ph/s at 77^{th} harmonic order. A study on trajectory resolved harmonic emission from argon gas and its spatial coherence is also carried out using single and two color laser pulses. We observed that the spatial coherence of harmonic

generated from short trajectory is higher compared to that from long trajectory and the spatial coherence of harmonics using two color laser fields is higher compared to that of single color, which infers control of electron trajectories in harmonic emission using two color laser pulses.

Further, the study on temporal characterization of higher harmonic pulses is carried out using RABITT (Reconstruction of Attosecond Beating by Interference of Two Photon Transition) technique. For this purpose, a high resolution (~5×10^{-3} at ~14eV) magnetic bottle electron time of flight spectrograph (MBETOF) is in-house developed and is precisely calibrated. The MBETOF spectrograph is used for characterization of attosecond pulse train generated through higher harmonics. The duration of each attosecond pulse in pulse train was measured to be ~ 290as, which repeat itself at half the laser cycle (~1.33fs). After the characterization, an application of higher harmonic source for multicolour ultrafast radiography of plasma plume is carried out for the first time. Due to ultrashort time structure, the effect of motion blurring in radiogram is negligible and presence of multiple discrete wavelengths in higher spectrum makes it possible to simultaneous measure the density profile of multiple species in plasma plume. The density profile of neutral atom (CI), ion (CII) and molecule (C_2) is simultaneously estimated.

Chapter 1:

Introduction

1.1 Higher Harmonic Generation: An overview

The first demonstration of laser system by Theodore Maiman in 1960, initiated the experimental research in the field of non-linear optics [1]. The first observation on non-linear optical phenomena was reported by Franken et al from university of Michigan in 1961. The second harmonics of Ruby laser (λ_0 ~694.3 nm) was generated in Quartz crystal, however the conversion efficiency was very low [2]. The generation of harmonics from any non-linear crystal is limited to ultraviolet regime (~ 165nm for Potassium-fluoroboratoberyllate crystal), due to strong absorption below this wavelength. To increase the harmonic order further, a medium with small absorption was required and low density gas medium was explored [3]. Due to low density, the absorption of harmonics was expected to be small in this medium. The first observation of third harmonic generation was reported in noble gases by New et al, where they observed strong third harmonics at few bar gas pressures [3].

All non-linear optical phenomena rely on the strength of the electric field applied to a medium. In conventional optics, (also called as linear optics) when a medium is placed in an oscillating electric field, it gets polarized. The induced polarization developed in the medium varies linearly with the strength of applied field. With increase in the strength of electric field, the induced polarization becomes nonlinear. The non-linear polarization of a medium can be expressed as the sum of all polarizibility terms [4]

$$P = P^{(1)}(t) + P^{(2)}(t) + P^{(3)}(t) + \ldots \qquad (1.1)$$

This non-linear polarization leads to generation of integral multiple frequency of applied field, known as higher harmonics of the fundamental laser frequency. The Eq 1.1 can be expressed in terms of susceptibility [4] as

$$P = \varepsilon_0 \left(\chi^{(1)} E(t) + \chi^{(2)} E^2(t) + \chi^{(3)} E^3(t) + ... \right) \quad (1.2)$$

Where $\chi^{(2)}$, $\chi^{(3)}$ are called as second and third order non-linear susceptibilities. The numerical value of higher order susceptibilities ($\chi^{(2)} \sim 1.94\times10^{-12}$ *m/V*, and $\chi^{(3)} \sim 3.78\times10^{-24}$ m^2/V^2) decreases with increase in order of non-linearity [4]. If the strength of applied electric field is very small, as compared to the atomic field (~5×10^9 *V/cm for Hydrogen atom*), the generation of lower order harmonics takes place e.g. second harmonic, third harmonic etc. This regime of harmonic generation is known as perturbative regime of harmonic generation. In this regime, the spectral intensity decreases fastly with increase in harmonic order [4]. With further increase in the strength of applied electric field, when it becomes comparable to the atomic field, the new regime of harmonic generation came to picture [5]. In this regime, the perturbative theories were no longer applicable. This new era in the field of nonlinear optics was called as "strong field physics", which deals with interaction of atom/molecules with intense electric field exceeding the perturbative regime [5].

The study of laser matter interaction using such high electric field has become possible due to advent of high peak power ultrashort laser pulses. By focusing such ultrashort laser pulses in low density gases, the laser electric field reaches close to atomic field and generation of higher harmonics beyond perturbative regime took place. The experiment by McPherson et al showed non-perturbative harmonic generation by focusing a laser pulse from KrF laser system (λ~248nm) to an intensity of ~10^{15} *W/cm*^{2}. The higher harmonics upto 17th order was observed, which falls in extreme ultraviolet (XUV) region of electromagnetic spectrum [6]. Similar spectral

intensity of a group of harmonics was also observed (which was named as plateau region). Following these observations, intense research had been carried out by different research groups to explore the higher harmonic generation further. The researches were performed by several groups with a motivation to extend the higher harmonic wavelength to x-ray regime with high photon flux, to make the source useful for applications in wide area of research [7, 8]. The coherence (both spatial and temporal coherence) properties of higher harmonic radiation were investigated and high spatial and temporal coherence [9, 10] was reported. The source has ultrashort time structure, which may vary from sub-fs to tens of attosecond [11]. These unique characteristics make higher harmonic source suitable for various applications viz. interferometry [12], lithography [13], time resolved imaging of ultrafast phenomena [14], study of ultrafast magnetization dynamics in magnetic materials [15] etc. Before proceeding further the basic concepts on intense laser interaction with matter will be discussed.

1.2 Parameter relevant to laser atom interaction

When an intense ultrashort laser pulse is focused on the target ($I \sim 10^{14\text{-}15}$ W/cm^2), the atoms of the medium instantly gets ionized. The mechanism of ionization depends on the incident laser intensity, laser wavelength, pulse duration [16] etc. Before discussing different ionization mechanisms, it is essential to discuss various parameters relevant to ultrahigh intensity laser atom interaction, viz. ponderomotive energy / potential, Keldysh parameter etc. This will be followed by discussion on different ionization mechanisms, which includes multiphoton ionization (MPI), tunnel ionization (TI) and barrier suppression ionization (BSI) [17].

1.2.1 Ponderomotive Energy (U_p)

Ponderomotive energy (U_p) is the average energy (quiver energy) of the electrons in the oscillating electric field [18]. Consider the electron motion in linearly polarized sinusoidal electric field i.e. the laser field $E = E_0 \cos\omega t$. The ponderomotive energy is written as

$$U_p = \tfrac{1}{2} m \langle v^2 \rangle$$

$$U_p = e^2 E_o^2 \langle \sin^2\omega t \rangle / 2 m \omega^2 = e^2 E_o^2 / 4 m \omega^2 \quad (1.3)$$

$$U_p (eV) = 9.33 \times 10^{-14} I (W/cm^2) \lambda^2 (\mu m) \quad (1.4)$$

For $\lambda = 0.8$ μm, $I \sim 10^{14}$, $U_p \sim 6$eV and for $I \sim 10^{18}$, Up ~ 0.1 MeV. In general, the laser field can be expressed as $\underline{E} = E_o (\cos\omega t \underline{X} + \alpha \sin\omega t \underline{Y})$, where $\alpha = 0$ for linear polarization, $\alpha = 1$ for circular polarization and $0 < \alpha < 1$ for elliptical polarization. The ponderomotive energy can be written as $U_p = e^2E_o^2 < (\sin^2\omega t + \alpha^2 \cos^2\omega t)> /2m\omega^2 = e^2E_o^2 (1+ \alpha^2) / 4m\omega^2$. In either case, maximum ponderomotive energy = $e^2 E_o^2 / 2m\omega^2$

1.2.2 Keldysh Parameter (Γ)

The Keldysh parameter is a function of ponderomotive energy and the ionization energy [19]. Square of the Keldysh parameter equals the ratio of the ionization potential of the atoms to the maximum ponderomotive energy i.e. Γ^2 = I.P. / Upmax. For Hydrogen-like ions, I.P. = 13.6 Z^2 eV, $U_{pmax} = e^2E_o^2/2m\omega^2$

$$\Gamma^2 = 13.6 Z^2 / 2 \times 9.33 I_{14} \lambda(\mu m)^2 \approx 0.73 Z^2 / I_{14} \lambda(\mu m)^2 \quad (1.5)$$

For $\Gamma > 1$, i.e. ionization potential of atom is greater than the maximum ponderomotive energy, the multiphoton ionization dominates. In case of $\Gamma << 1$, the maximum ponderomotive energy gained by the electron is very high as compared to

ionization potential of atom, the barrier suppression ionization dominates and in between (0<Γ<1) the tunnel ionization dominates.

1.3 Ultra-short laser Matter interaction: Ionization processes

The ultrashort intense laser pulse (I ~ $10^{14\text{-}15}$ W/cm^2) focused to solid / gaseous targets, it instantly ionization of medium. The laser intensity and pulse duration are crucial parameters that decide various ionization regimes. Depending on laser intensity and pulse duration, three different ionization regimes are identified viz. multi-photon ionization (MPI), tunnel ionization (TI) and barrier suppression ionization (BSI).

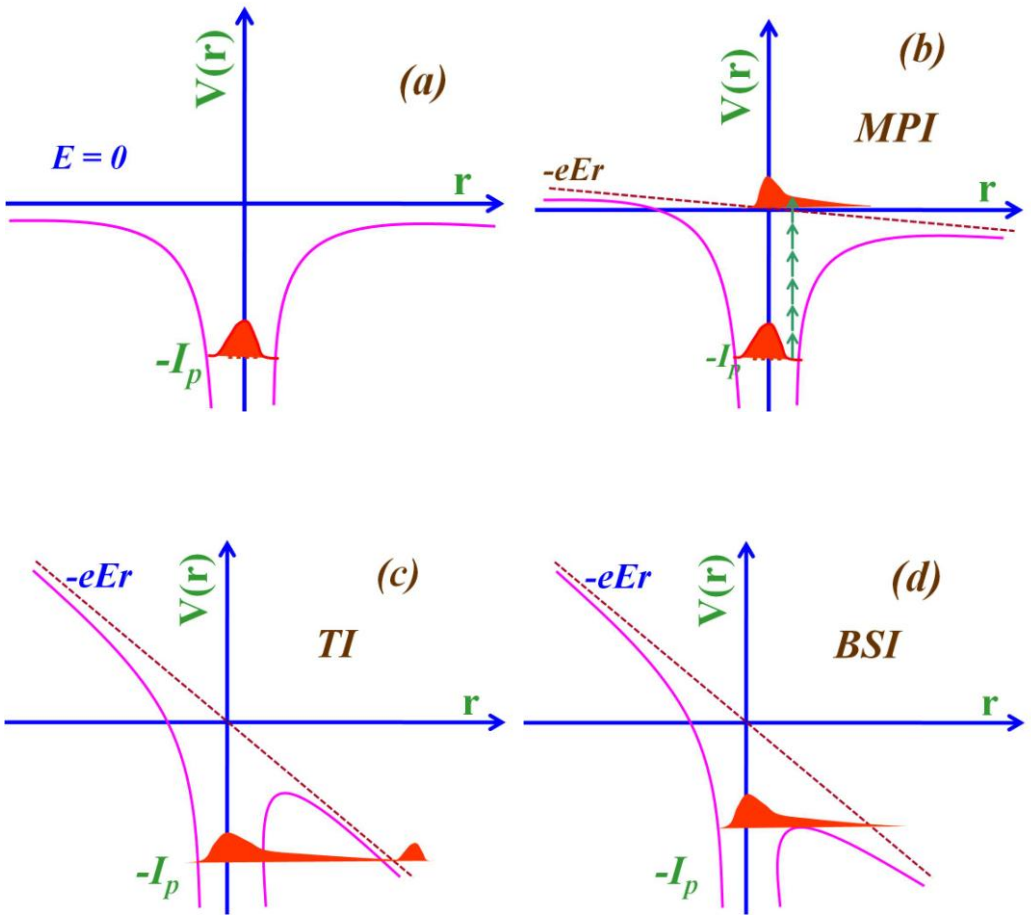

Figure 1.1: ***A)*** *atomic potential V(r), with no laser field.* ***B)*** *Multiphoton ionization (Γ>>1)* ***C)*** *tunnel ionization (0<Γ<1)* ***D)*** *barrier suppression ionization (Γ<<1)*

These three ionization regimes are also governed by the Keldysh parameters (Γ) as explained above. Figure 1.1 shows different ionization mechanisms depending on the value of Keldysh parameter. Figure 1.1a represents pure coulomb potential at zero external electric field. The presence of laser field distorts the coulomb potential, which is shown in fig 1.1b to fig 1.1d. The Keldysh parameter for Fig 1.1b to Fig 1.1d is shown in the caption of Fig 1.1. Different theoretical models were proposed to explain different ionization mechanisms and estimation of ionization rates [20-23]. The different ionization mechanisms are discussed in detail below.

1.3.1 Multi-photon Ionization ($\Gamma > 1$)

Multi-photon ionization is dominant at small laser intensity ($\approx 10^{11}$ W/cm^2 for femtosecond pulses), so that the electron field strength is much smaller than the atomic field ($E_{at} \sim 5\times10^9$ V/cm) [23]. The energy of single photon (~1.55eV for $\lambda \sim$ 800nm) is also much smaller compared to the ionization potential of atom (~13.6 eV for atomic hydrogen), hence atom cannot be photo-ionized by absorbing single photon. However, lasers induced optical breakdown of material, in which neutral matter is converted into plasma, has already been observed [24]. Thus the ionization may be due to simultaneous absorption of multiple photons. This is referred to as multi-photon ionization (MPI), which was theoretically predicted way back in 1931 by Goeppert-Mayer [25]. In order to ionize an atom of ionization potential I_p the total number of simultaneously absorbed photons should be such that $m\hbar\omega < I_p < (m+1)\hbar\omega$, where m is positive integer and $\hbar\omega$ is energy of single photon viz. photon energy ~1.55eV for λ~800nm. The mechanism of multi-photon ionization can be explained by considering the existence of short-lived virtual states, whose life time can be estimated using

Heisenberg's uncertainty relation $\Delta E \times \Delta t \geq \hbar$, where $\Delta E = \hbar\omega$ is energy separation of two virtual states and Δt is the life-time (typically femto-seconds).

When an atom is exposed to low intensity (~10^{11} W/cm^2) ultrashort laser pulses, the bound electron moves to higher virtual level, after absorption of each laser photon. For example electron which is present in i^{th} virtual excited states, should absorbed one photon within its lifetime, so that it can move to ($i+1^{th}$) virtual excited state. The process of laser photon absorption continues till ionization of atom takes place. After ionization, the electron is liberated with kinetic energy $\approx (n+1)\hbar\omega - Ip$. If σ is probability of one photon absorption, than probability of q photon absorption becomes σ^q, which shows that the probability of atom decreases with increase in ionization potential of atom as more number of photons are needed to be absorbed. Hence it is difficult to ionize the atom with higher ionization potential. Figure 1.1b shows that though presence of weak laser field has negligibly small effect on atomic potential, still electron can be lifted to continuum through MPI. When virtual states are energetically close to the real electronic states, it leads to resonance, which enhances the ionization probability. In case, more number of photons is absorbed than required for ionization, characteristic maxima separated by the energy $p\hbar\omega$ ($p > 0$) is observed in the electron spectra. The electron kinetic energy can be expressed as

$$E_k = (n+m)h\nu - I_p \qquad (1.6)$$

This process is known as Above Threshold Ionization (ATI). An ATI-electron spectrum shows characteristic maxima, with a separation of photon energy. Hence from the experimental study of electron energy and momentum distribution, the study on ionization process can be performed [16]**.** Several theories have been developed to explain ATI processes. The electron spectra for laser intensity ~ 10^{13} W/cm^2 can be theoretically calculated using high-order perturbation theory. The non-perturbative

approach to explain the ATI spectra at high laser intensities has also been developed, viz. Keldysh, Faisal and Reiss (KFR) theory [18]. The interest in above threshold ionization has been strengthened after the observation of higher harmonic radiation from intense laser atom interaction. The Higher harmonic radiation is emitted, when electrons present in a high energy continuum state, recombine to the parent atom after absorbing several photons (above ionization potential of atom) [26] and in this way laser photon energy is converted into extreme ultraviolet and even to keV x-ray regime [27].

1.3.2 Barrier Suppression Ionization ($\Gamma << 1$)

The increase in laser intensity distorts the atomic potential significantly. When the laser field is comparable to or exceeds the coulomb potential, the atom is ionized. This leads to an important question that, what is the intensity at which the laser field strength becomes comparable to the coulomb field that binds electron to an atom? The perturbation theories are no longer valid in this situation. In order estimate the strength of electron field, Bohr model of hydrogen atom can be used, in which an electron is considered to be moving on its orbit around a proton at a distance of Bohr radius (r_b). The strength of electric field (E_b) that keeps the electron in the orbit can be classically calculated to be

$$r_b = \frac{\hbar^2}{m_e e^2} = 5.3\times10^{-9}\,cm \;and\; E_b = \frac{e}{4\pi\varepsilon_0 r_b^2} = 5.1\times10^{9}\,V/cm \qquad (1.7)$$

Where m_e is the electron mass, ε_o is permittivity of vacuum and e is electron charge. The calculated field (E_b) is equivalent to an atomic unit of intensity, $I_{at} \sim 3.5\times10^{16}$ W/cm^2. This shows that placing a hydrogen atom in laser field of intensity (I_{at}) ~ 3.45×10^{16} W/cm^2, coulomb potential will be completely suppressed [20]. However,

experimentally the ionization is observed at much lower intensity. This experimental study shows that even at lower intensity (< I_a,), the laser field significantly affects atomic potential. The distortion of atomic coulomb potential due to laser field was proposed by Bethe and Salpeter [28], where a laser intensity was predicted at which atom gets ionized and was given a name "appearance intensity (I_{ap})". Here, the starting point is superposition of static external electric field and the nuclear potential, which can be expressed as (for 1D case)

$$V(\mathrm{x}) = -\frac{Ze^2}{x} - eEx \tag{1.8}$$

Where E is electric field strength Z is the charge state of ion produced. It can be seen from the Fig 1.1d that the coulomb barrier is completely suppressed, hence the electron can easily escape from the barrier. The position of the barrier x_{max} = Ze/E can be derived by using ∂V(x)/∂x = 0. The critical electric field E_c (taking $V(x_{max}) = I_p$) can be expressed as

$$E_{crit} = \frac{I_p^2}{4Ze^3} \tag{1.9}$$

The ionization energy of particular charge state is given by I_p. In this case, the laser field is so strong that the Coulomb barrier is completely suppressed and the bound electron can escape freely [29]. This ionization mechanism is termed as barrier suppression ionization (BSI). In BSI, the minimum required laser intensity is written as

$$I_{BSI} = \frac{\pi^2 c \varepsilon_0^3 I_p^4}{2Z^2 e^6} = 4\times10^9 \left(I_p\left(eV\right)\right)^4 Z^{-2}\ \ W/cm^2 \tag{1.10}$$

The relation expressed in Eq 1.10 is experimentally found to be valid in wide range of laser intensity (over several orders of magnitude) in noble gases [29]. In case of atomic hydrogen, (Z = 1, I_p ~ 13.6 eV), the laser intensity for barrier suppression

ionization is calculated to be ~ 1.4×10^{14} W/cm^2. This clearly shows that the ionization of atom takes place at lower intensity compared to the predicted value.

1.3.3 Tunnel Ionization ($0<\Gamma<1$)

The laser intensity required for ionization of atom, as predicted by BSI theory is in good agreement with experimental observations. Although, the BSI theory gives threshold, however one cannot estimate the rate of ionization. The ionization rate was evaluated by quantum mechanical calculations of the tunnelling probability of the electron wave packet through the coulomb barrier. The tunnel ionization is schematically represented in Fig 1.1c. It can be seen from Fig 1.1c, that the coulomb barrier is not suppressed by the laser field to such an extent that electrons can escape freely, however it can tunnel out of coulomb barrier. The calculations of electron tunnelling through coulomb barrier had been performed by Keldysh [19] and later extended by Perelomov [30], assuming a low frequency quasi-static electric field in quasi-static (adiabatic) approximation, viz. an electron has enough time to tunnel through the barrier. Keldysh et al had also separated two regimes (tunnel ionization and above threshold ionization) by introducing a dimensionless parameter known as Keldysh parameter (Γ), which is discussed in the earlier section. When $\Gamma < 1$, tunnel ionization is dominant, which can be achieved for strong fields and long wavelengths. For $\Gamma > 1$, the time required for tunnelling by the electron is larger than the laser period, thus the quasi-static approximation is no longer valid and the ATI is a dominant ionization process. For the outer electrons of noble gases (Argon, Neon, Helium etc.), this regime starts at laser intensities of $\sim 10^{14}$ W/cm^2 at 800nm wavelength. Following Keldysh, the ionization rates W is given for hydrogen-like configuration by

$$W = 4\omega_a \left(\frac{I_p}{I_h}\right)\frac{E_a}{E_t}\exp\left\{-\frac{2}{3}\left(\frac{I_p}{E_h}\right)^{3/2}\frac{E_a}{E(t)}\right\} \qquad (1.11)$$

In Eq 1.11, I_p/I_h is the fraction of the ionization potential with respect to that of hydrogen, E_a the atomic electric field and $\omega_a = m_e^4/\hbar^3 = 4.16 \times 10^{16}\ s^{-1}$ is the atomic frequency. The extended version of the theory was developed by Ammosov, Delone and Krainov (ADK), who obtained a general, analytical expression of the constant in Coulomb wave function in terms of effective quantum numbers by considering the semi-classical solutions to the radial wave equation [21]. The ionization rate (W) was derived for complex atoms and ions for arbitrary quantum numbers of the electronic configuration (ADK-theory**).** The ADK ionization rate is written as

$$W_{ADK} = C_{n^*l}^2 f(l,m)|E|\left(\frac{3F}{\pi\left(2|E|^{3/2}\right)}\right)^{1/2}\left(\frac{2\left(2|E|^{3/2}\right)}{F}\right)^{2n^*-|m|-1} e^{-\frac{2\left(2|E|^{3/2}\right)}{3F}} \qquad (1.12)$$

$$C_{n^*l} = \left(\frac{2e}{n^*}\right)^{n^*}(2\pi n^*)^{-1/2},\quad f(l,m) = \frac{(2l+1)(l+|m|)!}{2^{|m|}\,|m|!(l-|m|)!},\quad n^* = \frac{z}{k} = \frac{z}{\sqrt{2|E|}}$$

Where n* is called effective quantum number l and m is orbital and magnetic quantum number respectively, F is the electric field strength amplitude and |E| is the ionization potential.

The ionization rate predicted by ADK theory has been confirmed for many noble gases like helium, argon, neon and xenon in an intensity range from 10^{13} W/cm^2 up to 10^{18} W/cm^2 using 1 ps pulses (λ = 1.053 nm) [31,32] **.**

1.3.4 Pulse duration effect on ionization

Laser pulse duration is another important parameter (apart from laser intensity), which influence ionization process. For the laser pulse of duration few picoseconds

and below, the tunnel ionization is dominant, as compared to above threshold ionization [31]. In case of large laser pulse duration (100's of ps to sub ns) or the presence of prepulse ahead of the ultrashort laser pulse, the medium gets ionized by multi-photon ionization prior to entering the tunnelling regime. In this condition, there is high probability that the ionization of medium saturates at a laser intensity known as saturation intensity (I_{SAT}), which may be much lower than laser intensity needed for barrier suppression ionization (I_{BSI}) [33]. This situation arises when the life time of the electronic state is shorter than the rising edge of laser pulse. Hence, for ultrashort, intense laser pulse with high prepulse contrast, the tunnel ionization mechanism is dominant. The above discussion

It can be concluded from the above discussion that apart from ionization potentials of the atom, wavelength, pulse duration, intensity and pre-pulse contrast of the laser pulse, play important role in deciding the dominant mechanism of medium ionization. Depending on the duration and intensity of laser pulse, the atom can be ionized by all possible ionization paths viz. MPI, TI, BSI [21]. The number of electrons generated in medium ionization (up to time *t*), is given by the integration of the relevant ionization rate

$$N(t) = 1 - \exp\left(-\int_{-\infty}^{t} W(\tau)\, d\tau \right) \tag{1.13}$$

1.4 Theoretical description of higher harmonic generation

After the discussion on the basics of laser atom interaction, the different ways of higher harmonic generation is presented in the following sections. This includes the generation of higher harmonics from intense laser interaction with solid surface (overdense plasma) and the generation of harmonic from underdense plasma, which

includes the generation from atomic / molecular gases and low density pre-formed plasma plumes.

1.4.1 Higher harmonic generation from solid surface

Higher harmonic generation from solid surface has been observed in wide range of laser intensities, extending from moderate intensity (~10^{15} W/cm^2) to relativistic intensities (≥ 10^{18} W/cm^2). The first observation of HHG from solid surface was reported in 1977 by Burnett et al., by focusing a nanosecond laser pulse (from CO_2 laser) on solid surface and harmonics upto 11^{th} order was observed [34]. In 1981, Carman et al used similar laser, focused to higher intensity (~ 10^{15} W/cm^2) and observed higher harmonics upto 46^{th} orders [35]. With the availability of high power femtosecond lasers, the peak intensity exceeding ~10^{18} W/cm^2 can be easily achieved. By using high peak power (~petawatt) Ti:Sapphire ($\lambda \approx 800$nm) laser pulse, focused to intensity ~ 10^{21}W/cm^2 on the solid surface, the harmonic order exceeding 3000 has been reported [36].

The generation of higher harmonics from solid surface can be categorized into two different regimes depending on the laser intensity viz. in moderate intensity regime (~10^{15} W//cm^2) and in relativistic intensity regime (≥ 10^{18} W/cm^2). In relativistic intensity regime, the harmonic generation can be explained using relativistic oscillating mirror model [37], whereas in non-relativistic regime [38], it can be explained using coherence wake emission. The relativistically oscillating mirror (ROM) model was proposed by Lichters et al. in 1996 [37]. When an intense ultrashort laser pulse (of high pre-pulse contrast) is focused onto a solid target surface, it forms sharp density gradient plasma (electron density) on the surface at the foot (leading edge) of the laser pulse. Rest of the laser pulse can penetrate upto critical

density (n_c) for normal incidence of laser light and upto $n_c cos^2\theta$ at an oblique incidence, (where θ is the angle of incidence of laser light on the target surface). In case of ultrashort (femtosecond) laser pulse, the critical density lies close to the solid surface (10's nm). The electric field oscillation of the laser pulse, leads to oscillation of the critical density surface. At high laser intensity (≈10^{18} W/cm^2), the velocity of critical density oscillation may reach close to the speed of light. This leads to relativistic Doppler shift of the laser pulse and its frequency (ω) is up-shifted to $4\gamma^2\omega$, where γ is the relativistic Lorentz factor of oscillating electron density surface. The pulse duration of the reflected light will reduce to ~$\tau/4\gamma^2$, (where τ is the laser pulse duration), which may go upto few attosecond for higher orders. Although, this theory (ROM) explained most of the experimental observation of harmonics from solid surface, it was unable to explain the experimentally observed cutoff scaling.

Later the theory was modified by Baeva et al, popularly known as "theory of γ-spikes" [39]. This model assumes that the efficient higher harmonics is generated from an apparent reflection point; viz. the maximum up shift of laser frequency takes place when the electron velocity reaches the speed of light. The value of γ forms a γ-spike, which leads to maximum Doppler upshifted of laser frequency. The temporal width of γ-spike is found to be scaled as ~$1/\gamma$, and the emitted up-shifted frequency also scaled up accordingly. Due to this confinement, the temporal duration of the pulse should scale as ~$1/\gamma^3$, and hence the frequency component scale as ~ γ^3, as compared to the earlier scaling of ~ $4\gamma^2$. The simulation by Baeva et al [39] has shown that the exact scaling of the cutoff frequency using the γ-spike model is ~2.83 γ^3.

The "ROM" and "*γ spike model"* were successfully explained harmonic generation from solid surface at high laser intensity (≥ 10^{18} W/cm^2). These theories failed to explain the harmonic generation process at small laser intensity (~10^{15}

W/cm^2), as the Doppler shift becomes insignificant in this case. Another theoretical model was proposed by Quere el al in 2006 [38], known as "coherent wake emission (CWE)", to explain the harmonic generation in low intensity regime (~10^{15} W/cm^2). The CWE model is based on the oscillation of electrons inside and outside the plasma boundary similar to vacuum heating of plasma by laser pulse viz. the electrons are pulled in and out of plasma by the laser pulse. The electron which goes inside the plasma in the earlier part of the laser pulse experiences less electric field and thus moves slowly inside high density plasma. However the electron moves inside the plasma near the peak of the laser pulse and experience high electric field. These electrons move with higher velocity but are trailing behind the slow moving elections. This leads to formation of electron bunch, which moves inside the dense plasma. During travelling, the electron bunch excites plasma wave oscillation. The linear mode conversion takes place inside dense plasma at positions, where plasma wave oscillation frequency (ω_p) matches with integral multiple of laser frequency ($m \times \omega_L$, where m is an integer >1 and ω_L is the laser frequency). This leads to generation of higher harmonics inside the dense plasma. Maximum harmonic order (also called harmonic cutoff) depends on the density of overdense plasma, upto which the plasma wave oscillation propagates and it is found to be close to density of target material. The cutoff frequency can be given as $(hv)_c \sim \sqrt{(n_s/n_c)}$, where $(hv)_c$ is the harmonic cutoff frequency, n_c is the critical density for the incident laser light and n_s is the density upto which the plasma wave. One of the major differences between the harmonic generated at relativistic and non-relativistic intensity is that at non-relativistic intensity the harmonic cutoff order depends on density of target material, whereas at relativistic intensity, the harmonic cutoff is independent of target material.

1.4.2 High order harmonic generation from gaseous medium

When an intense ultra-short (sub-ps to few-fs) laser pulse is focused in a gaseous medium to an intensity of ~10^{14}-10^{15} W/cm^2, higher harmonics of the laser frequency are emitted [40]. These harmonics are emitted in the direction of the laser pulse propagation. The harmonic spectrum has only odd harmonic orders and the cutoff wavelength may extend below water window ($\lambda \sim 2.3$ nm to 4.4 nm) region [41]. The harmonic spectrum can be divided into different regimes. The first regime is known as "perturbative regime", in which the harmonic intensity decreases rapidly over first few orders. This region is followed by "plateau region", in which the intensity of harmonics remains almost constant. The plateau region ends up with a sharp cut-off, where the intensity of harmonics drops to zero within few harmonic orders. The process of HHG from the gaseous medium can be understood using semi-classical model popularly known as "three step model" proposed by Krause in 1992 [42] and Corkum in 1993 [43].

Three Step Model: The three steps involved in higher harmonic generation are:

a) The presence of intense laser field distorts the atomic coulomb potential of outermost bound electron, which may tunnel out of atomic field and become free with zero velocity.

b) This free electron is accelerated away from the parent atom in intense laser field in classical electron trajectories. The average energy gained by the electrons, is known as ponderomotive energy.

c) With the reversal of the laser cycle, the electron returns back to the parent atom and may undergo collision. This recollision may lead to several processes viz. above threshold ionization originates from elastic scattering of electron with an atom or non-

sequential double ionization of atom originates from inelastic scattering of electron from atom or recombination to ground state with emission of high energy photons.

The schematic of the three step processes involved in emission of higher harmonics is presented in Fig 1.2b) to Fig 1.2d). Figure 1.2a shows the undisturbed coulomb potential of atom for outermost bound electron. Under the influence of external laser electric field, the potential is distorted and the electron gets tunneled out (see Fig 1.2b) and gets accelerated in the laser field. With the reversal of laser cycle, it recollides back to parent atom, as shown in Fig 1.2c. The recombination of this electron to ground state leads to emission of high energy photons, which is shown in Fig 1.2d.

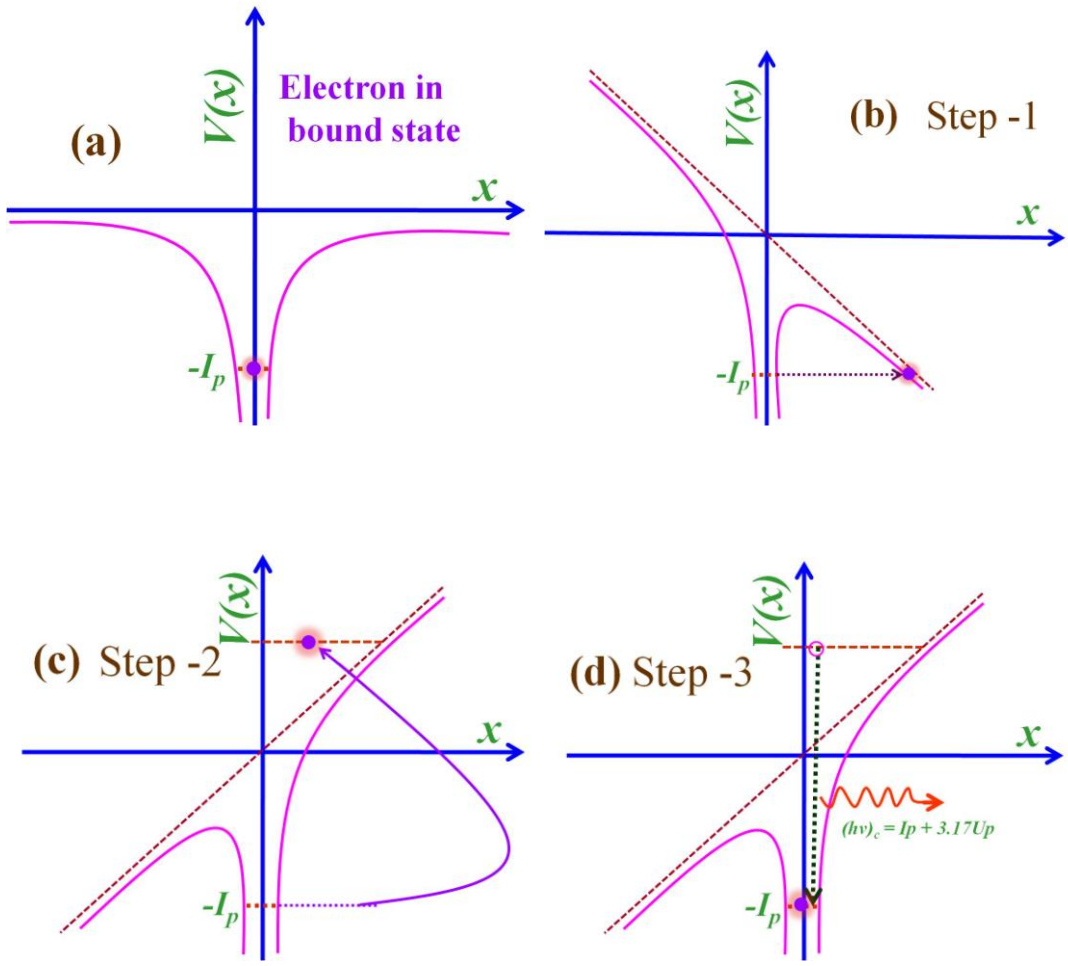

Figure 1.2: *The three stages of the Corkum "three step model"*

The energy of the emitted photon depends on the total energy gained by the electron, which is equal to sum of ionization potential and the net kinetic energy gained by electron. The gain in kinetic energy depends on the laser phase at which the electron is tunnelled out from the atom. The maximum photon energy, (also called as cutoff energy) is calculated using classical as well as quantum models [43, 44].

$$Cutoff\ energy\ (h\upsilon_{max}) = Ip + 3.17\ U_p \qquad (1.14)$$

Where U_p is the ponderomotive energy, which is average kinetic energy, gained by electron in laser field. The ponderomotive energy can be expressed as

$$U_p = 9.33\times10^{-14}\ I\ (W/Cm^2)\ \times\lambda^2\ (\mu m) \qquad (1.15)$$

From Eq 1.14 and Eq 1.15, it can be seen that the harmonic cutoff energy can be increased either by using long wavelength or by using higher laser intensity. The harmonic generation efficiency is higher for shorter-wavelength driver laser pulse due to small electron wave packet spread during its excursion time. This will increase recombination amplitude, which increases the probability of harmonic emission. The other way to increase the harmonic cutoff is to use higher laser intensity, however increase in laser intensity will lead to significant plasma formation, which will destroy the optimum condition of phase matching required for efficient harmonic generation.

The three steps involved in higher harmonic generation as mentioned above is discussed below in detail. When the laser electric field becomes comparable to the atomic field (~ 10^9 V/cm), it start distorting the coulomb potential of the atom. When the laser intensity increases beyond ~10^{14} W/cm^2, the potential well gets distorted to such an extent that the bounded electron of an atom can tunnel out from the atomic potential barrier and becomes nearly free (effect of coulomb potential becomes negligibly small). In this intensity regime (~10^{14}-10^{15} W/cm^2) tunnel ionization is the dominant mechanism of ionization. The ionization rate in case of hydrogen atom was

well explained by Keldysh theory of ionization [19] and for more complex molecules of multi electron atoms, the ionization rate is well explained by ADK theory of ionization [21]. This is the first step of the three step model and is a purely quantum mechanical phenomena. After tunnelling out from atom, the electron experiences an oscillating laser electric field, starts accelerating and gains energy. This is the second step of the three step model. Let us assume the laser field to be

$$E(t) = E_0 \cos(\omega t) \tag{1.16}$$

The electron can be treated classically in this case. Thus the equation of motion of the electron in one dimension can be written as

$$m\frac{d^2x}{dt^2} = -eE(\mathrm{t}) = -\mathrm{eE}_0\cos(\omega \mathrm{t}) \tag{1.17}$$

If an electron is gets free from atomic (coulomb) potential barrier at time $t = t_0$, the time dependent velocity and position of electron can be written as

$$v(t) = \frac{-eE_L}{m\omega}\left(\sin(\omega t) - \sin(\omega t_0)\right) \tag{1.18}$$

$$x(t) = \frac{-eE_L}{m\omega^2}\left(\left(\cos(\omega t) - \cos(\omega t_0)\right) + \omega_0 \sin(\omega t_0)(t - t_0)\right) \tag{1.19}$$

Where the $x(t)$ is time dependent displacement of electron from parent atom. Assuming the electron freed at $t=0$, the maximum displacement can be written as $x_0 = 2eE_L/m\omega^2$. For a laser intensity of ~ 5×10^{14} W/cm^2, the displacement (x_0) will be ~ 2 nm. The normalized time dependent electron trajectory with initial phase (ωt_0) of linearly polarized laser field is plotted in Fig 1.3a.

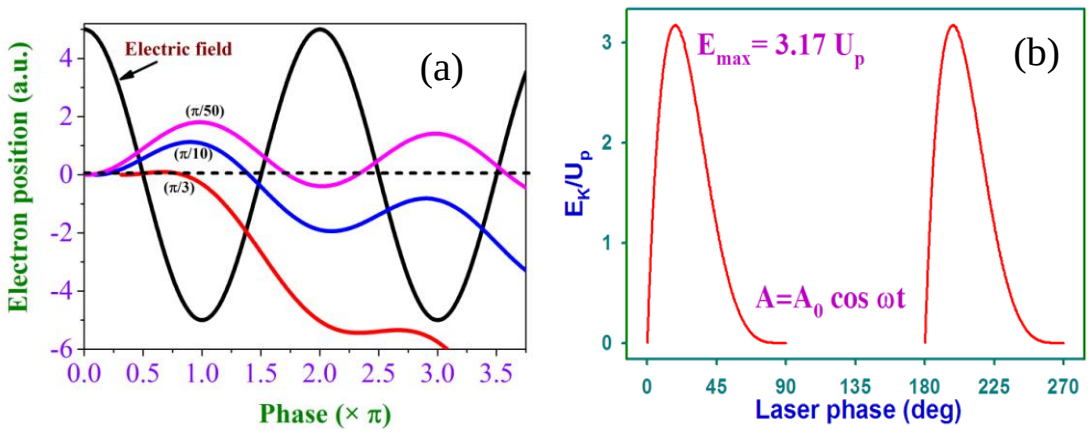

Figure 1.3: *a) Different electron trajectory responsible for harmonic emission b) the energy of photons emitted when electron is tunnelled from atom at different phase.*

The atomic motion can be neglected in this ultrashort time scale (femtosecond), and hence its position can be taken to be fixed (x=0). Figure 1.3a show the electron trajectory for three different laser phases, at which electron is tunneled out and is recombined to atom. For recolliding back to parent atom/ion, the electron must tunnel out from atom in proper laser phase. After recolliding, the electron gets recombined with the parent atom and emits high energy photons. Due to symmetry involved in the generation process, the emitted frequencies consist of only odd-order harmonics of the incident laser light [5].

The tunneled electron gets accelerated in the laser electric field and gains energy. Figure 1.3b shows the ratio of return kinetic energy and ponderomotive energy (U_p) of electrons, tunneled at different phases of the laser cycle. It can be seen from Fig 1.3a that the electron tunneled in the phase region [0, π/2] and [π, 3π/2] will return to the parent atom (Fig. 1.3b), whereas the electron tunneled at any other phase, will not return back. It can also be seen from Fig 1.3b, that the electron tunneled at laser phase ~ π/10, gains maximum kinetic energy of ~*3.2Up*. Also, there are two possible electron trajectories associated with any kinetic energy below ~*3.2Up*. They are termed as long trajectory and short trajectory. The electron tunnelled out from atom at

laser phase from 0 to π/10 radian, follow long trajectory and it spends more time in the continuum. The electron tunnelled out from atom at laser phase from π/10 radian to π/2 radian, follow short trajectory and it spends less time in the continuum. The total energy (kinetic + potential energy) gained by the electrons following any classical trajectory can be expressed as

$$\varepsilon(t) = I_p + \frac{1}{2}mv^2 = I_p + 2U_p\left\{\left(\sin(\omega t) - \sin(\omega t_0)\right)\right\}^2 \qquad (1.20)$$

Where I_p is the ionization potential of atom and U_p is the ponderomotive energy of electron. The maximum energy gained by the electron can be calculated using Eq 1.20, which comes out to be I_p*+3.17* U_p, which is cutoff photon energy predicted by three step model (Eq 1.14). The cutoff harmonic energy depends on the ionization potential of atom. Therefore, to maximize the harmonic cutoff, the gas atom with highest ionization potential should be used. The three step model discussed above was able to explain the harmonic cutoff, which agrees well with the experimental results of HHG from noble gases.

The polarization of laser field used for higher harmonic generation also play crucial role in harmonic generation. The higher harmonic from gases takes place for linearly polarized laser pulse. Change in the laser polarization from linear to circular (changing the ellipticitiy from 0 to 1), the probability of electron recollision with parent atom/ion decreases, which leads to reduction in harmonic intensity. For perfectly circularly polarized light, the electron trajectory never returns to the vicinity of the ion, hence no harmonic emission takes place.

A typical spectrum of higher harmonics is shown in time and frequency domain in Fig. 1.4. The emission spectrum in time domain is separated by half laser cycle (see Fig 1.4a). Fig 1.4b shows the three different regions (as discussed

previously) in the harmonic spectrum. The perturbative region, plateau region and cutoff region are marked clearly in Fig 1.4b.

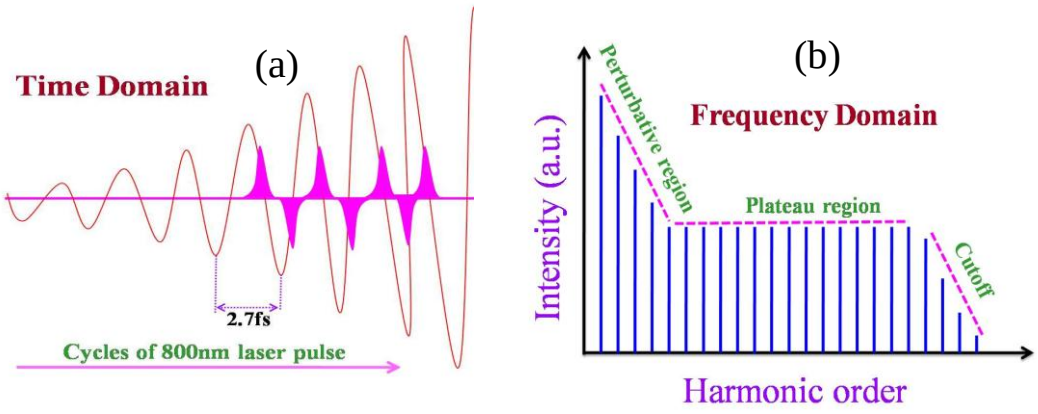

Figure 1.4: *Typical spectrum of HHG in a) time domain and b) frequency domain*

The three step model has been successfully in explaining the harmonic cutoff order (maximum harmonic order). Further, the motion of electron in different trajectories was found to play crucial role in controlling spectral features of harmonic emission viz. spectral broadening and splitting, harmonic divergence, coherence [10] etc.

After generation of higher harmonics from single atom, it propagates in the medium, where there is large number of atoms emitting harmonics. Depending on their phase, the constructive / destructive interference of these harmonics may take place in the medium, which leads to increase / decrease in harmonic intensity. Therefore, the propagation of harmonics in a non-linear medium, affects the harmonic characteristics crucially viz. the intensity, spatial and spectral characteristics and its coherence. It is therefore important to consider the effect of laser beam propagation in non-linear medium. The important issue which is to be considered during propagation

of harmonics is its absorption and the phase matching between the harmonics and the driving laser pulse.

Experimental Studies: High order harmonics are generated by focusing an ultra-short laser pulse at intensity ~ $10^{13\text{-}15}$ W/cm^2 to a gas jet. These generated harmonics are then dispersed by a grazing incidence grating and recorded by XUV detector (like micro channel plate (MCP) with optical CCD camera, or a back illuminated x-ray CCD camera) [45]. Due to high sensitivity and spatial resolution of MCP, it is the most widely used detector for detection of harmonic radiation [46]. The experimental study of higher harmonic radiation has been initiated by McPherson et al in 1987, which attracted the attention of various research groups, to explore this field. In 1993, Macklin et al used 125 femtosecond Ti: sapphire laser ($\lambda \sim 800$nm) pulse focused to intensity 10^{15} W/cm^2 in Neon gas and observed higher harmonics upto of 109th order [47]. Further research in this field was initiated by several groups to improve the harmonic intensity [48], extend the maximum harmonic cutoff order [41], generate high repetition rate harmonic source [49] etc. Few research groups were able to extend the harmonic cutoff to water windows region [50]. The longer wavelength laser pulses ($\lambda \approx 3.9\mu$m) were found to be useful, in extending the harmonic cutoff to x-ray region beyond 1keV photon energy [41]. The investigation were also performed to improve harmonic yield by optimization of phase matching condition [48], use of two color laser field [51], use to long length medium [52] etc.

Although, the gas jets were simple to use but there were few limitations viz. difficult to achieve uniform density in gas jets, small repetition rate operation (limited by opening and closing time of solenoid valve), limited number of available inert gases, load on vacuum pumping systems in high gas pressure operation etc. Few

research groups explored the possibility of using plasma plume as an alternative nonlinear medium for harmonic generation. Several interesting and exciting results were observed [53-56]. The use of plasma plume also provided a vast scope to explore large number of material plumes. In the forthcoming section, the higher harmonic generation from plasma plume is discussed.

1.4.3 HHG from Plasma Plumes

To generate higher harmonic radiation, a low excited plume is created by focusing a long duration (100's of ps to few ns) laser pulse on solid target surface and it is allowed to expand so that the plasma is cooled down. The expansion time is to be optimized so that it should have sufficiently high atomic density for harmonic generation and low free electron plasma density to achieve better phase matching. In this condition, the plasma plume preferably consists of neutral atoms, thus it behaves very much like a low density gas medium [53]. The first experiment on higher harmonic generation from laser ablated plasma plumes was performed by Wahlström et al. in year 1995 [53]. The harmonics order upto 27^{th} was observed in Na^+/K^+ plume, however unlike gases no plateau region was observed in their study. Later, Ganeev et al. reported plateau-like harmonic emission from the plasma plumes generated from the surface of various solid targets [54-56]. Maximum harmonic cutoff up-to 101^{st} was observed in manganese plume [57]. In addition to the plateau-like structure, several interesting and unique features were observed in plasma plume medium. It is found that in some material plume (viz. Indium plume), the intensity of a particular harmonic order (viz. 13^{th} order in Indium plume) was one or two order higher compared to the neighbouring harmonics [58]. This is known as resonance enhancement and it takes place when a particular harmonic order falls close in frequency with one of the atomic

resonance lines in that medium [58]. Plasma plumes have certain advantages over the gas jets, such as, experimentally easy to generate harmonics, minimum target depletion, higher harmonic generation at high repetition rate and availability of large number of target materials. Due to this, one can explore the nonlinear properties of different materials, to efficiently generate higher harmonics for practical applications [12-14]. The resonance enhancement of a harmonic order [58] due to overlapping of atomic/ionic transitions with harmonic wavelengths is an added advantage, which can be useful for high resolution imaging [59]. In of our earlier study, ~200 times enhancement of the 13th order harmonic is observed in case of Indium plume [58].

1.4.4 Propagation Effects and Phase matching

After the generation of higher harmonics, it propagates in the nonlinear medium viz. gaseous medium and plasma plumes (discussed above), which plays crucial role in the higher harmonic characteristics. During propagation, harmonic intensity is critically affected by absorption and the phase matching between harmonics and laser pulse. The number of harmonic photons emitted after propagation in a non-linear medium of length L [60] is written as

$$N_{out} \propto \frac{\omega_q}{4c\varepsilon_0 h}\left|\int_0^{L_{med}} \rho A_q(z)\exp\{i\varphi_q(z)\}\exp\left(-\frac{(L_{med}-z)}{2L_{abs}}\right)dz\right|^2 \qquad (1.21)$$

Here N_{out} is on-axis harmonic photons per unit time per unit area, A_q is amplitude of the atomic response for qth harmonics, c is speed of light, h is planks constant, ρ is medium density, ω_q is frequency of qth harmonics, $\varphi_q(z)$ is integrated harmonic phase for q^{th} order and L_{med} is the length of non-linear medium. Taking total number of photon generated along laser axis [60] can be expressed as

$$N_{out} \propto \rho^2 A_q^2 \frac{4L_{abs}^2}{1+4\pi^2\left(L_{abs}^2 / L_{coh}^2\right)}\left\{1+\exp\left(-\frac{L_{med}}{L_{abs}}\right)-2\cos\left(\frac{\pi L_{med}}{L_{coh}}\right)\exp\left(-\frac{L_{med}}{2L_{abs}}\right)\right\} \quad (1.22)$$

Here $L_{coh}=\pi/\Delta k$ and Δk is the wavevector mismatch between the laser and generated harmonics and can be written as $\Delta k = k_q - qk_{0,}$ k_q is wavevector for qth harmonics, k_0 is wavevector of the fundamental laser pulse. In Eq 1.22, N_{out} depends on various factors viz. density of the medium, medium length, absorption length, coherence length and the oscillator strength (A_q). The oscillator strength depends on the laser intensity used for higher harmonic generation etc. The absorption length (L_{abs}) of q^{th} harmonics in a medium [60] is given by

$$L_{abs} = \frac{1}{2\alpha_q} = \frac{1}{N\sigma_q} \quad (1.23)$$

Here α_q is absorption coefficient for the qth harmonics, N is medium density and σ_q is absorption cross section. The absorption cross section varies with harmonic photon energy. It was shown by Constant et al. that when coherence length is equal to absorption length, the photon flux oscillates with medium length. When the coherence length is much higher than absorption length, the photon flux firstly increases with medium length and then it saturates. An optimum condition for achieving maximum photon flux as calculated by constant et al is $L_{med} > 3L_{abs}$ and $L_{coh}>5L_{abs}$. Typically the absorption length ~2 mm for 21st harmonics and ~2.5 mm for 41st harmonics in low density silver plume (~2×10^{17} cm^{-3}), hence the coherence length should be more than ~10 mm for 21st harmonic order and ~12.5 mm for 41st harmonic order. The wavevector mismatch (Δk) should be 0.3 rad/mm for 21st harmonics and 0.25 rad/mm for 41st harmonics [61], where $\Delta k=\pi/ L_{coh}$. Such small values of wavevector mismatch can be achieved by precisely optimizing the phase matching conditions. In order to have large coherence length the wavevector mismatch (Δk) should be as small as possible, ideally Δk should be zero for best phase matching.

Phase matching: When harmonics are generated in gases / low density plasma plumes, the phase mismatch (Δk) should be small in order to get intense harmonics. There are several factors that cause the wavevector mismatch between the harmonics and the laser [5]. These include:

(a) Neutral atom dispersion

(b) Free electron dispersion

(c) Gouy phase

(d) Intensity dependent dipole phase

We will discuss the effect of all the above factors in creating the wavevector mismatch.

(a) Neutral atom dispersion: The dispersion arises due to presence of neutral atoms in the medium. When a laser source with wavelength close to some atomic transition lines is passed though the medium, its refractive index changes, which varies with change in wavelength. The mismatch in wavevector ($k=2\pi/\lambda$) between the laser and q^{th} harmonics is expressed as $\Delta k = k_q - qk_0$. In terms of refractive index of the medium the phase mismatch between laser and harmonics [61], when travelling in a medium is expressed as

$$\Delta k_q = \frac{q\omega}{c}\left(n_q - n_0\right) \tag{1.24}$$

Here n_q is refractive index of medium for q^{th} harmonics and n_0 is refractive index of medium for the laser light. The refractive index of a gas medium for bound electron can be expressed as:

$$n = 1 + 2\pi\chi_b(\omega), \text{where } \chi_b(\omega) \approx \frac{n_b e^2}{m}\sum_{i,j} f_{i,j}(\omega) \tag{1.25}$$

In Eq 1.27 $f_{i,j}$ is the real part of atomic scattering factor, where subscript i and j represents the ground state and any lowest energetic excited states respectively and n_b

is the density of bound electrons in the medium (considering only the outermost electron in the atom). The bound electron density can be calculated by knowing the ionization fraction of medium. It is written as $n_b = (1- \eta)\, n_a$, where η is the ionization fraction of a medium at a given laser intensity and n_a is atomic density of a medium. The ionization fraction can be calculated by using ADK theory which gives ionization fraction calculated for optical field ionization [21]. The phase mismatch between harmonics and the laser beam can be rewritten using Eq 1.24 and 1.25 as

$$\Delta k_a = -(1-\eta)\frac{n_a e^2}{\pi m c^2 \lambda_q}\sum_{i,j}\left\{\frac{\left(\lambda_0^2-\lambda_q^2\right)\lambda_{i,j}^4 f_{i,j}}{\left(\lambda_{i,j}^2-\lambda_q^2\right)\left(\lambda_0^2-\lambda_{i,j}^2\right)}\right\} \qquad (1.26)$$

It can be seen from Eq 1.26 that Δk_a is always negative, since for high order harmonics $\lambda_q<\lambda_{12}<\lambda_0$, where λ_q is wavelength of qth harmonics, $\lambda_{i,j}$ is wavelength of j^{th} state to i^{th} state (ground state) transition. Thus, the phase mismatch due to bound electrons in an atom (called as neutral atom dispersion) is always negative. In order to calculate a typical value a transition from *1s-2p* of hydrogen atom is considered for which λ_{12} = 121.5nm and f_{12} ~0.1388, atomic density to be ~10^{18} cm^{-3} (typical value used in harmonic generation experiment), the value of Δk_a for 27^{th} harmonic order (λ~29.6nm) is calculated to be -0.2rad/mm. The phase mismatch due to atomic dispersion is small and it increases with increase in the density of medium.

(b) Free electron dispersion: An intense ultrashort laser pulse is needed to be focused in non-linear medium for higher harmonic generation, thus the ionization of the medium can't be avoided. Owing to different wavelength of laser pulse and the higher harmonics, the refractive index due to presence of free electron is different for the two. The refractive index for a light in plasma containing free electrons can be written as

$$n_0 = \left(1 - \frac{\omega_p^2}{\omega_0^2}\right)^{1/2} \; and \; n_q = \left(1 - \frac{\omega_p^2}{\omega_q^2}\right)^{1/2} \tag{1.27}$$

In Eq. 1.27, ω_p is known as plasma frequency, ω_0 is laser frequency and ω_q is harmonic frequency. The phase mismatch due to free electrons present in the non-linear medium [61] can be expressed as (using Eq 1.27)

$$\Delta k_{pl} = \frac{\eta n_a e^2 q}{c\omega_0 m_e \varepsilon_0} \; for \; q \gg 1 \tag{1.28}$$

Where q is harmonic order and ε_0 is permittivity of free space. In order to calculate typical value of the phase mismatch due to free electron dispersion, taking the atomic density to be ~10^{18} cm^{-3} and the fraction of ionization to be ~10%, the value of Δk_{pl} *for* 27^{th} harmonics of laser (central wavelength ~ 800nm) will be ~ 12 rad/mm. Thus, the phase mismatch due to free electron dispersion is higher than neutral atom dispersion. For very low medium ionization (~ few percent), the dispersion due to free electron and bound electron may cancel each other. However for higher ionization, the dispersion due to free electron dominates. It can also be seen from Eq 1.28, that the phase mismatch increases with increase of harmonic orders and therefore it is important phase mismatch parameter for higher harmonic orders.

(c) Gouy Phase: Gouy phase or Geometrical phase mismatches arises primarily due to phase shift introduced in the Gaussian laser beam, when it passes through the focus position. There is phase change of π between both sides of the focused Gaussian laser beam. The Gouy phase of focused Gaussian laser beam [62] is expressed as

$$\phi_0 = \tan^{-1}\left(\frac{z}{z_R}\right) \tag{1.29}$$

In Eq. 1.29, z is any point in the path of propagating Gaussian beam and z_R is the Rayleigh range of focused Gaussian laser beam. For a q^{th} order harmonics generated by a Gaussian laser beam, the Gouy phase is written as

$$\phi_q = q\tan^{-1}\left(\frac{z}{z_R}\right) \tag{1.30}$$

The phase shift between the harmonics and laser pulse [63] can be written using Eq 1.29 and 1.30, which can be expressed as

$$\Delta\phi = (q-1)\tan^{-1}\left(\frac{z}{z_R}\right) \tag{1.31}$$

The on-axis wave vector mismatch can be calculated using Eq. 1.31. The intensity variation of a Gaussian laser beam can be written to be

$$I(\mathrm{r},z) = \frac{I_0}{1+\left(\frac{z}{z_R}\right)^2}\exp\left(-\frac{r^2}{2\omega^2(z)}\right) \tag{1.32}$$

Where $\omega(z)$ is the radius of Gaussian beam at any spatial position z, in the direction of propagation. The on-axis (r=0) wave-vector mismatch between the harmonics and the laser beam [63] is calculated to be

$$\Delta k_G = \frac{\partial(\Delta\varphi_G)}{\partial z} = (q-1)\frac{z_R}{\left(z^2+z_R^2\right)} \tag{1.33}$$

The Gouy phase variation is high near the focus of Gaussian laser beam, thus the effect can be reduced by placing the non-linear medium away from the laser focus viz. for $z>>z_R$ the wave vector mismatch $\Delta k_G \rightarrow 0$. It can be seen from Eq 1.33 that the other way to reduce the value of Δk_G is to reduce Rayleigh range. However, in order to reduce the Rayleigh range (z_R), the Gaussian beam has to be focused tightly, which leads to increase in ionization of medium and increases the phase mismatch due to free electron dispersion. Thus, it is better to keep the non-linear medium away from laser

focus to reduce the effect of Δk_G. It is also evident from Eq 1.33 that the sign of Δk_G doesn't change with change in sign of *z*.

(d) The intensity dependent dipole phase: As discussed earlier, that there are different electron trajectories that contributes in the process of harmonic emission. Electrons tunneled from the atom at different laser phase, spend different amount of time in the laser field before recombination. The phase gained in different electron paths are different and leads to the different phase mismatch between laser and harmonics. This phase is known as "dipole phase". Due to its dependence on laser intensity, this phase is also known as "intensity dependent dipole phase". This extra phase introduced by intensity dependent dipole was theoretically and experimentally studied by Peatross et al. [64, 65]. The dipole phase depends on the intensity of laser pulse and can be written as

$$\Delta\varphi_{IDP} = \alpha_q I \tag{1.34}$$

Where, I is the laser intensity and α_q is coefficient of the dipole phase. The coefficient α_q depends on the trajectories responsible of harmonic generation. For short trajectory the value of α_q varies from ~1 to 5×10^{-14} cm^2/W and for long trajectory the value varies from ~20 to 25×10^{-14} cm^2/W. The phase mismatch will be higher, if harmonics are generated by the long trajectory compared to that of short trajectory. Taking the intensity profile of the laser pulse to be Gaussian (as written in Eq 1.32), the on-axis ($r = 0$) wavevector mismatch due to intensity dependent dipole phase [64] is written as

$$\Delta k_{IDP} = \frac{\partial\left(\Delta\varphi_{IDP}\right)}{\partial z} = \alpha_q \frac{\partial I}{\partial z} = -2\alpha_q I_0 \frac{z\, z_R^2}{\left(z^2 + z_R^2\right)^2} \tag{1.35}$$

It can be seen from Eq. 1.35 that the term Δk_{IDP}, increases with increase in laser intensity. Although, at low intensity, the mismatch between the laser and harmonics (Δk_{IDP}) is small, however the harmonic intensity itself reduces at small laser intensity. Also, with change the position of non-linear medium relative to laser focus (sign of z), the sign of Δk_{IDP} changes.

Due to several unique property of higher harmonic source, it finds application in several areas of research, which motivated me to pursue the present research work.

1.5 Applications of High Harmonic Radiation

The higher harmonic radiation possess unique properties viz. high spatial and temporal coherence, ultrashort time structure (which may extends from sub-fs to tens of attosecond), shorter wavelength (which extends from XUV to hard x-ray region), and the frequency comb of odd harmonic order of laser frequency. These unique characteristics make the source suitable for variety of applications. One of the important applications of higher harmonic source is in interferometry to probe high density plasmas [12]. The visible / IR laser pulse can be used for this purpose; however the IR laser pulse can penetrate into the plasma only upto their critical densities. For example in case of Ti:Saphhire laser at central wavelength ~800nm, the critical density ~ 1.7×10^{21} cm^{-3}, which is much smaller than the solid density (~ 10^{23} cm^{-3}) [66]. To probe the overdense region of plasma (density > 10^{21} cm^{-3}), one needs shorter wavelength source and the higher harmonic source is most suitable candidate for this purpose [66]. The XUV interferometry using higher harmonics was reported by Descamps et al., where the plasma is formed by focusing a 300ps laser pulse on foil target to an intensity of ~10^{13} W/cm^2. The electron density at ~ 1.2 ns after plasma formation was estimated to be ~ 2×10^{20} cm^{-3} at ~ 20μm from the target [12].

Due to short wavelength (XUV to x-ray) and high coherence property, the higher harmonics source is a potential candidate for high resolution imaging. In the imaging applications, the ultimate resolution is limited by the wavelength of the light source, thus the use of higher harmonic source at XUV wavelength alongwith its ultrashort pulse duration (sub fs), can provide very high resolution. Recently, coherent diffractive imaging or lensless imaging using higher harmonic radiation source [67] is reported. In this technique, the far field diffraction pattern from a sample is recorded on a CCD camera. The diffraction pattern has information of the object, which can be retrieved using the phase retrieval algorithms. As there is no imaging optics used in this imaging technique, the resolution is not limited by the optics. The resolution in this case is limited by the type of algorithms used for the phase retrieval. There are several phase retrieval algorithms available, which can be used to reconstruct the image with an unprecedented resolution of 10's of nanometre resolution. Different research groups have demonstrated high resolution coherent diffractive imaging using higher harmonic source [59, 68]. A resolution of ≈22 nm is demonstrated using higher harmonic source at $\lambda \sim 13$ nm by Sandberg et al. [67]. Apart from all the above applications, the higher harmonic source is also a potential candidate for attosecond pulse generation [5, 69]. As discussed in the previous section, that the higher harmonic spectrum consists of odd harmonic frequencies, when they are generated in gases using multicycle laser pulses. Using few cycle laser pulses, a broadband harmonic supercontinumm is generated in place of odd harmonic frequency comb [69, 70]. This broadband spectrum is used to generate attosecond pulse, after compensating the harmonic chirp (also known as attochirp) [71, 72]. The attosecond pulses are essential tool for the study of ultrafast dynamics of electron motion in atom and molecules [73].

The imaging of molecular orbital is also performed using sub-fs XUV sources generated through high order harmonics [74].

1.6 Summary and Scope of the present thesis work

High order harmonic generation by an interaction of ultrashort intense laser pulse with matter is a highly nonlinear process. The study of higher harmonic generation is an established route to generate attosecond pulses, which can provide unprecedented time resolution (~ attosecond) to the researchers. This time resolution can uncover several unexplored phenomena viz. ultrafast electron dynamics in material, tunnelling dynamics, ultrafast demagnetization dynamics of magnetic material etc. However, the conversion efficiency of harmonic source is low (~10^{-7} to ~10^{-9} per harmonic order), which further deteriorates at smaller wavelengths. This results in poor yield of the harmonic source. Further, being a highly non-linear process, the laser intensity and nonlinear medium property, crucially affect the harmonic generation condition. Being a short wavelength source (spectrum may reach to x-ray regime), it is a most suitable candidate for probing high density plasma using XUV interferometry, which is highly desirable for the fusion studies. However, the generation of such coherent and efficient harmonic generation is still a challenging task. The researchers are still in search of new techniques, to generate coherent and intense harmonics at shorter wavelength.

In the present thesis, we took up the problem of estimating and enhancing the conversion efficiency of higher harmonics, to improve its overall yield. We explored two different nonlinear medium viz. plasma plumes and inert gas filled gas cell. In the plasma plume, the conversion efficiency and yield is enhanced by using spatially shaped laser beam, and the spatial coherence characteristics of harmonic source is also

studied. These study results in generation of efficient and coherent mid-order harmonics (11^{th} to 21^{st} order) from carbon plume. The other nonlinear medium (inert gas filled cell) is also explored and gas cell length, gas type and gas cell position relative to laser focus is optimized, which results in harmonic yield of ~ 0.25μJ energy at λ~26nm wavelength in Argon and ~10nJ at λ~10nm and the harmonic cutoff extended to beyond 99^{th} order (λ~8nm) in Helium. As the higher harmonics can generate attosecond pulses, it is important to study the spectral property of harmonics. Due to complex process involved in harmonic generation, the spectral behaviour of the harmonics is not straight forward to understand. We tried to understand the spectral property of higher harmonic generated from argon gas filled cell using single and two color laser fields. Complicated spectral structural viz. broadening and splitting is observed when gas pressure is varied from 20mbar to 100mar. To unravel the mechanism, the harmonic divergence, harmonic spectrum and spatial coherence is also studied. It is found that the electron trajectories which are responsible for the harmonic generation, is also responsible for this spectral structure. I was able to identify that the spatial coherence of the short trajectory harmonics is higher than the long trajectory harmonics. The study using two color laser pulse, provided tool to select one of these trajectories, hence smooth harmonic spectrum. The study will be useful in optimizing the duration of attosecond pulses generated from such nonlinear medium.

The wavelength of higher harmonic source extends from extreme-ultraviolet to soft x-ray regime and its pulse duration may extend from sub-femtosecond to attosecond. Therefore, the conventional ultrashort pulse characterization techniques viz. streak camera and autocorrelation technique can’t be used for the characterization of higher harmonic pulse. Specialized techniques “Reconstruction of Attosecond

Beating by Interference of Two Photon Transition" (RABITT) with high end diagnostics (high resolution electron spectrograph) alongwith ultrafast electronics are required to diagnose such ultrashort XUV pulses. Although, few studies have been reported, still this is an inception and many research groups are struggling for techniques to precisely characterize such pulses.

I have investigated the temporal characteristics of higher harmonics. The magnetic bottle electron time of flight spectrograph is developed in-house and characterized. The attosecond pulse characterization technique (RABITT) is adopted, which reconstruct the attosecond pulse train from the experimentally measured amplitude and relative phase between the harmonics. In the present study, the measurement of individual attosecond pulses in pulse train generated from 17^{th} to 25^{th} harmonic order is investigated. The FWHM width of reconstructed individual attosecond pulses is measured to be ~300as and pulse to pulse separation is 1.33fs.

The practical application of the higher harmonic source is demonstrated to only few research areas, due to its low photon flux. However, an optimization of photon flux in the present study has motivated us to explore for some unique application of the source. In the present study, we found that the harmonic spectrum has multiple discrete wavelengths and its time structure extends to attosecond regime, we explored the feasibility of ultrafast multicolour radiography, for the measurement of the density profile of multiple species of plasma plume, which can't be performed by monochromatic x-ray source. The ultrashort time structure reduces the effect of motion blurring and presence of multiple discrete wavelengths makes it possible to simultaneous measure the density profile of multiple species in plasma plume. The technique is demonstrated for the first time and is used to measure the density profile

of neutral carbon atom (CI), singly charged carbon ion (CII) and carbon dimer molecule (C_2) present in carbon plume.

The chapter wise summary of the thesis is presented below.

Chapter 1: The basic concept of laser plasma interaction including brief discussion on “Ponderomotive energy” and “Keldysh parameter” is presented. Various ionization mechanisms involved in laser plasma interaction are described. Theoretical description of harmonic generation processes, a brief discussion on literature survey as well as its application to higher harmonic source to different areas of research is discussed.

Chapter 2: The laser systems used in the present research work and the diagnostics used for the measurement of focal spot, laser spectrum, and laser pulse duration is discussed. The chapter also includes discussion on focusing optics and the diagnostics used for spatial, spectral and temporal characterization of high order harmonic pulses viz. AXUV diodes, flat field grating spectrograph, toroidal mirror etc.

Chapter 3: The work on generation of coherent higher harmonics from pre-formed plasma plume is discussed. The experimental results on the spatial coherence characteristics of higher harmonics and the role of spatially shaped laser pulse on the efficiency / yield of higher harmonics generated from plasma plume is presented. Theoretical formulation to explain the experimentally observed results on the spatial coherence as well as effect of spatial shaping on harmonic generation is also discussed.

C**hapter 4**: Experimental study on harmonic generation and optimization of gas cell length, gas cell pressure and gas cell position to improve harmonic yield and cutoff is

discussed. The estimation of photon flux of harmonics using AXUV diode from different gases is presented. A study on spatial coherence of the trajectory resolved higher harmonics using single and two color laser fields is also presented.

Chapter 5: This chapter deals with an experimental study on the temporal characteristics of higher harmonics using RABITT technique. The temporal characterization of higher harmonics needs a high resolution electron time of flight spectrograph (Magnetic Bottle Electron Time of Flight spectrograph), which is in-house developed and characterized. The design and characterization of the spectrograph is presented in detail. This chapter also presents the experimental results of the cross-correlation between the xuv and IR laser pulse and generation of RABITT trace by varying the delay between the two pulses. The reconstruction of attosecond pulse trains from the RABITT trace is also presented.

Chapter 6: The application of higher harmonic source for multispecies characterization of carbon plasma plume using multicolor radiography is discussed in this chapter. The experimental results on estimation of density profiles of CI, CII and C_2 molecule from the recorded radiogram of plasma plume using higher harmonics from 11^{th} to 21^{st} order is presented.

Chapter 7 presents a brief summary and conclusions drawn from the present work. A brief discussion on the future work to be carried out is also discussed.

Chapter 2:

Laser Systems and Diagnostics

In the present chapter, we describe the laser systems and important diagnostics used in the experimental studies on higher harmonic generation, characterization and its application.

2.1 Ti:Sapphire Lasers used in the study

The experimental studies presented in this thesis have been carried out using two different laser systems available at laser plasma division, RRCAT, India. Both the laser facilities are chirp pulse amplification (CPA) [75] based Ti: Saphhire laser systems operating at wavelength ($\lambda_{central} \approx$ 800nm), delivering 45fs duration (FWHM) laser pulses. One of these laser systems can operate at a maximum peak power of ~10TW at 10Hz repetition rate and the second laser system can operate at a maximum peak power of ~0.2 TW at 1 kHz repetition rate. In this chapter, description of both the laser systems and a brief discussion on the measurements of various laser pulse parameters viz. pulse duration, laser spectrum and focal spot, is presented. The diagnostics used for characterization of various parameters of higher harmonic radiation viz. photon flux, spatial and spectral features, harmonic focusing etc. is discussed. The photon flux measurement via AXUV diode (Make : IRD, Model: AXUV20HS1), focusing of harmonic radiation using toroidal mirror, measurement of spatial and spectral characteristics using Flat field grating spectrograph is presented in detail.

2.1.1 10 TW, Ti: Sapphire laser system

This laser system is used for the study of higher harmonic generation from pre-formed plasma plumes. The schematic of the laser system is shown in Fig 2.1.

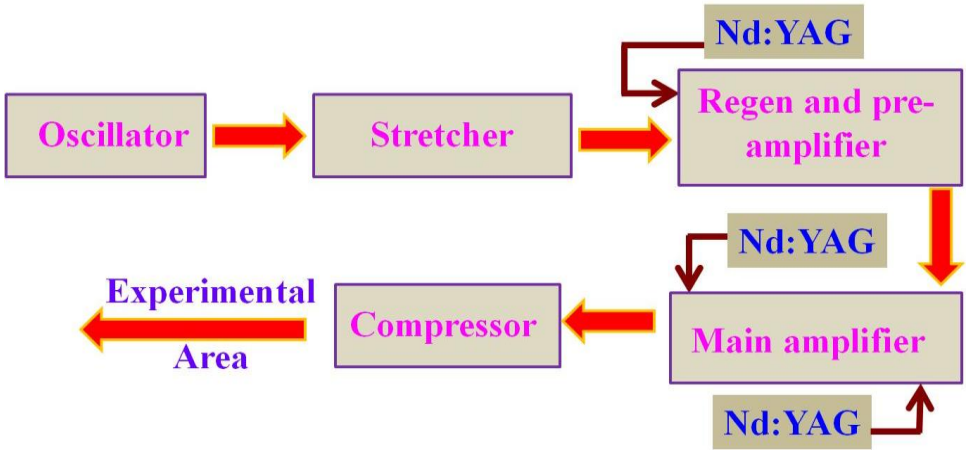

Figure 2.1: *The schematic layout of the Ti: sapphire laser system.*

The laser system (M/s Thales, France, Model: Alpha xx) comprises of an oscillator, pulse stretcher, regenerative Amplifier, pre-amplifier, main amplifier and pulse compressor. The laser oscillator (pumped by second harmonic of Nd:YVO_4 laser) deliver laser pulses of ~15 fs duration at 76 MHz repetition rate (separation between successive pulses ≈ 13ns) with nanojoule energy per pulse. The ultrashort laser pulses in the oscillator are generated by passive mode-locking technique known as "Kerr-lens mode-locking" [76]. The pulses generated from oscillator are sent to Öffner type stretcher [77], which introduces a positive chirp in laser pulse viz. the longer wavelengths (red) travel ahead of shorter wavelengths (blue). This leads to temporal stretching of the pulse and the pulse duration increases to ~200ps. Further, the pulse repetition rate is reduced to 10Hz, (i.e. the pulse at every 100ms is selected) using a combination of polarizer and Pockel cell and it is injected into a regenerative amplifier. The regenerative amplifier is a high gain seeded amplifier (gain ≥ 10^5), which amplifies the laser pulse energy from nanojoule to millijoule [78]. The regenerative amplifier is pumped by second harmonic of Nd:YAG laser (Make: Thales, Model: COMPACT). The amplified laser pulse is ejected out of the regenerative amplifier by a combination of polarizer and Pockel cell. As the gain of regenerative

amplifier is very high (~10^5 to ~10^6), it will also amplify the spontaneous emission from amplifier crystal (known as "Amplified Spontaneous Emission" or "ASE"). This unwanted pre-pulse is removed from the main laser pulse, using a pulse cleaner, which is based on fast polarization switching of Pockel cell (rise time ≈ 3 ns). After pulse cleaner, the laser pulse is passed to pre-amplifier, which is pumped by the second harmonic of the same Nd:YAG laser system (COMPACT) used for pumping regenerative amplifier. After preamplifier, the laser pulse energy is increased to ~ 40 millijoule. This amplified pulse is injected to a multi-pass amplifier, which is pumped by two second harmonic of Nd.YAG lasers (Thales, Model: SAGA1 and SAGA2). After the main amplifier, the laser energy of 200ps laser pulse is increased to ~ 700 millijoule. This amplified uncompressed laser pulse is finally sent to the pulse compressor, to compensate the chirp introduced by the pulse stretcher, laser crystals at various amplifying stages and other optics in the laser beam path.

The laser compressor comprises of two parallel grating separated by an optimum distance which compensates positive chirp and compress the laser pulse to ~ 45 fs [79]. The finally achieved pulse duration (~ 45fs) is higher than that of oscillator pulse (~15 fs). The reason behind the increased pulse duration is gain narrowing, taking place at different amplifiers, which reduces the laser bandwidth from ~ 60nm at oscillator, to ~ 20nm at pulse compressor. As the maximum gain is taking place in regenerative amplifier (~10^6), the gain narrowing is also highest at this stage. A photograph of 10TW Ti: sapphire laser system is shown in Fig 2.2.

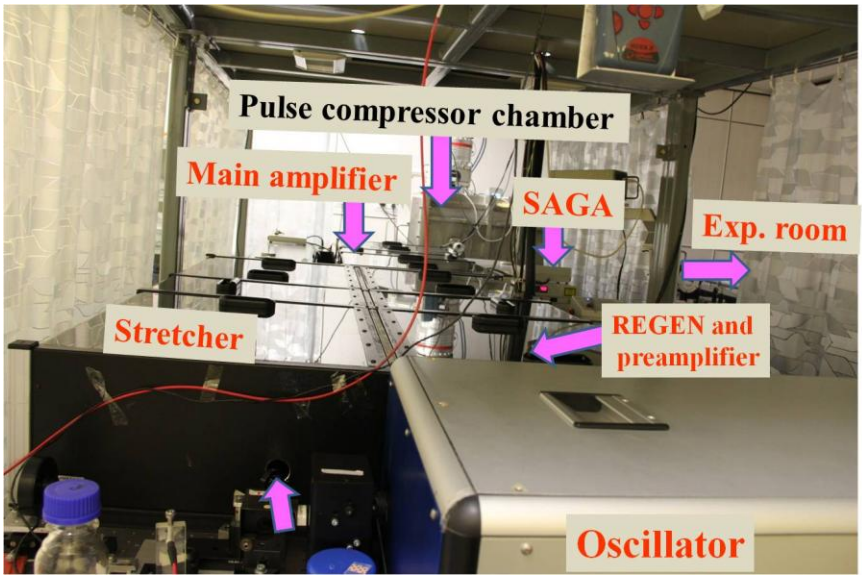

Figure 2.2: *Photograph of the 10 TW Ti: sapphire laser system operating at 10Hz.*

In Fig 2.2, the laser pulse oscillator (Femtosource Scientific), pulse stretcher, regenerative amplifier (REGEN), preamplifier and main amplifier, SAGA (amplifier used for pumping of main amplifier) and pulse compressor are seen and tagged. The laser parameters at the final output stage after pulse compressor are given in table 2.1.

Laser Parameters	**Value**
Maximum Pulse energy	~450 mJ
Pulse duration	~45 fs (FWHM)
Central wavelength (λ)	~800 nm
Spectral width, $\Delta\lambda$	~ 20 nm
Laser pulse peak power	10 TW
Maximum Repetition rate	10 Hz
Nanosecond pre-pulse contrast (ns level)	Better than 10^6

Table 2.1: *The parameters of 10TW Ti: sapphire laser system at laser plasma division, RRCAT*

2.1.2 1 kHz Ti: Sapphire laser system

This laser system is used for the study of higher harmonic generation from inert gas filled cell. The schematic of this laser system is shown below in Fig 2.3.

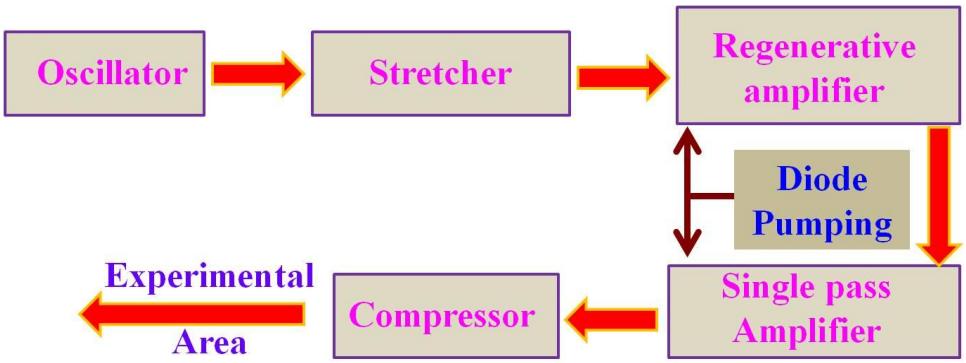

Figure 2.3: *Schematic layout of the 1 kHz Ti: sapphire laser system.*

The laser system (M/s Coherent Inc.) comprises of an oscillator, pulse stretcher, regenerative amplifier, single pass amplifier and pulse compressor. This laser system shares the same oscillator (Femtosource Scientific) used in 10TW laser system discussed in section 2.1.1. The pulse from oscillator is sent to stretcher, which introduces a positive chirp in the pulse and it is temporally stretched to ~ 200ps. Further, the laser pulse repetition rate is reduced to 1 kHz, (i.e. the pulse at every 1ms is selected) using a combination of polarizer and Pockel cell and is send to regenerative amplifier. The regenerative amplifier amplifies the laser pulse energy from nanojoule to ~ 5.5 millijoule. In this laser system, the regenerative amplifier is pumped by second harmonics of Nd: YLF laser (pumped by diode array) with maximum power of 50W (Model: “EVOLUTION-HE”). The amplified laser pulse is ejected out from the regenerative amplifier using a combination of polarizer and Pockel cell. The laser pulse is injected to single pass amplifier, which is also pumped by the same laser (Model: “EVOLUTION-HE”) system used for pumping regenerative amplifier. After single pass amplifier, the laser pulse energy is increased

to ~ 9 millijoule. Due to high gain of the single pass amplifier, the spontaneous emission also gets amplified along with laser (stimulated) emission, which leads to increase in ASE prepulse. The pre-pulse is removed by a pulse cleaner, which is based on fast polarization switching of Pockel cell with rise time ≈ 3 ns. This suppresses the ASE level at ~ 1ns ahead of main pulse. The amplified pulses after pulse cleaner are finally sent to the pulse compressor, to compensate for the positive chirp introduces by the stretcher and various optics in the beam path including various amplifier Ti:Sapphire crystals. The laser compressor structure is similar to the 10TW laser system discussed in section 2.1. The final laser pulse duration after the compressor is again increased to ≈ 50 fs due to the gain narrowing taking place in regenerative amplifier. A photograph of ~0.2 TW kHz Ti:Sapphire laser system is shown in Fig 2.4.

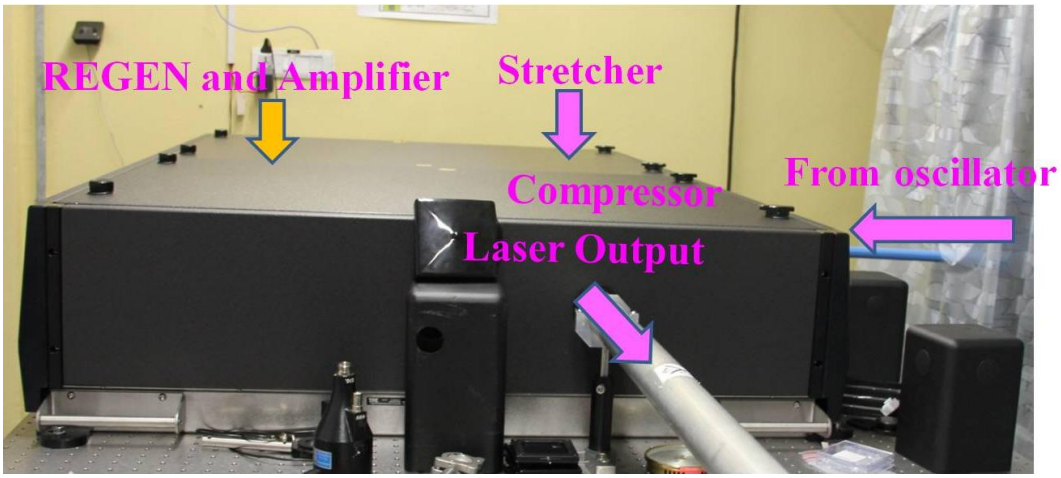

Figure 2.4: *Photograph of the 0.2 TW, 1 kHz Ti: sapphire laser system.*

The final kHz laser parameters at the output of pulse compressor are given in table 2.2.

Laser Parameters	Value
Maximum Pulse energy	~7.5 mJ
Pulse duration	~ 45 fs (FWHM)
Central wavelength (λ)	~ 800 nm
Spectral width, Δλ	~ 20 nm
Laser pulse peak power	~ 0.2 TW
Maximum Repetition rate	1 kHz

Table 2.2: *Parameters of 1 kHz Ti:Sapphire laser system, laser plasma division, RRCAT*

2.2 Characterization of laser parameters

It is essential to measure various laser parameters for the present research work. These parameters crucially affect the laser matter interaction studies presented in this thesis. In the following section, the measurement techniques of different laser parameters are discussed in detail and the value of various laser parameters are presented.

2.2.1 Laser Focal Spot Measurement

The measurement of spot size and energy content in laser focal spot is important in order to calculate the peak laser intensity. The peak laser intensity [80] can be expresses as

$$I_{peak} = \frac{\alpha \times E}{\tau \times \left(\pi \omega_0^2 / 2\right)} \quad \left(for\ Gaussian\ beam \right) \qquad (2.1)$$

Where α is the energy content inside the focal spot, E is laser pulse energy, ω_0 is $1/e^2$ focal spot radius, and τ is laser pulse duration. The peak intensity of the laser pulse is an important parameter, which significantly affects the laser plasma interaction

process [81]. As the laser intensity is inversely proportional to the square of the focal spot size, any change in spot size will affects laser intensity critically. As discussed in chapter 1, laser intensity in the range of ~ $10^{14\text{-}15}$ W/cm^2 is required in the present research work, which can be easily achieved by focusing a laser pulse of few millijoule laser energy and 45fs duration to a spot size of ~10's of μm. In order to achieve such intensity, one can use refractive optics (like lenses) or reflective optics (like Off Axis Parabolic (OAP) mirror). In the present research, both refractive (lens) and reflective (OAP mirrors) optics are used to focus the laser pulses. In some of the studies (discussed in chapter 3), we have focused the laser pulse using OAP mirror, whereas in rest of the studies the laser pulse is focused using plano-convex lens. The alignment of refractive optics (lenses) is relatively easier. However, focusing of high power lasers using lens may lead to non-linear effect, which may modify the laser spectrum as well as laser spatial profile [82]. This makes focusing of laser pulse to small spot size with good spatial quality difficult. In case of reflective optics (OAP), due to absence of non-linear effect, the laser pulse can be focused to smaller spot size. However, the alignment of the OAP mirror is crucial to achieve good quality focal spot (smooth profile, high energy content in the focal spot etc.). Slight misalignment may lead to aberration, which increases the focal spot size and lowers the maximum achievable laser intensity. In most of the cases, the estimation of focal spot size is not straight forward, due to deviation of the laser beam profile from a Gaussian. It is also equally important to estimate the energy content inside focal spot to calculate the actual peak laser intensity at the focus. In view of this, an experimental setup is installed to measure the focal spot size and the energy content inside the spot.

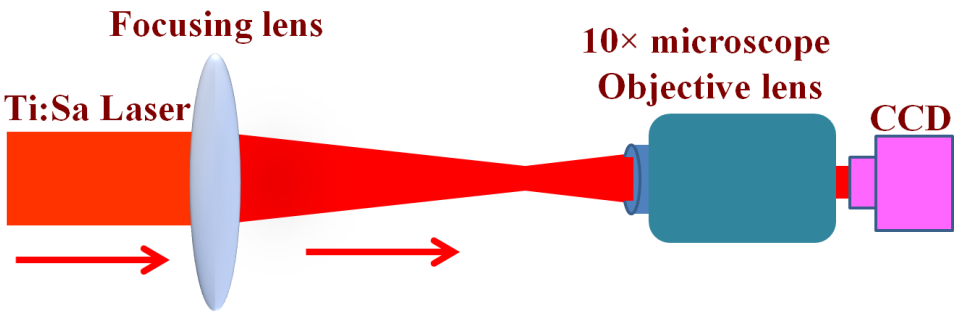

Figure 2.5: *Experimental setup used for focal spot measurement.*

Figure 2.5 shows the experimental setup used in measurement of spot size of laser beam, focused by a refractive / reflective optics. The selection of magnification of microscope objective, for the focal spot imaging should be taken carefully. The use of higher magnification of microscope objective should increase the image resolution, but at the same time it increases the aberration as well. Also, the alignment of high magnification objective is critical i.e. slight misalignment leads to large aberration and results in large error in the measured focal spot. The use of smaller magnification of microscope objective will reduce the resolution in focal spot imaging and leads to significant error in the measurement of focal spot size.

In the present work, a 10× magnification of microscope objective lens is used to image the focal region onto a 12 bit charge couple device (CCD) camera (Make: PCO pixelfly). The laser energy is attenuated significantly by placing suitable optical filters, to avoid any damage in CCD camera from high intensity laser exposure. The magnification of the experimental setup was determined using a calibrated graticule with 100 μm line spacing. This setup is also used for estimation of the Rayleigh range of the focusing optics by placing it on a linear translation stage and moving the whole setup laser beam propagation direction.

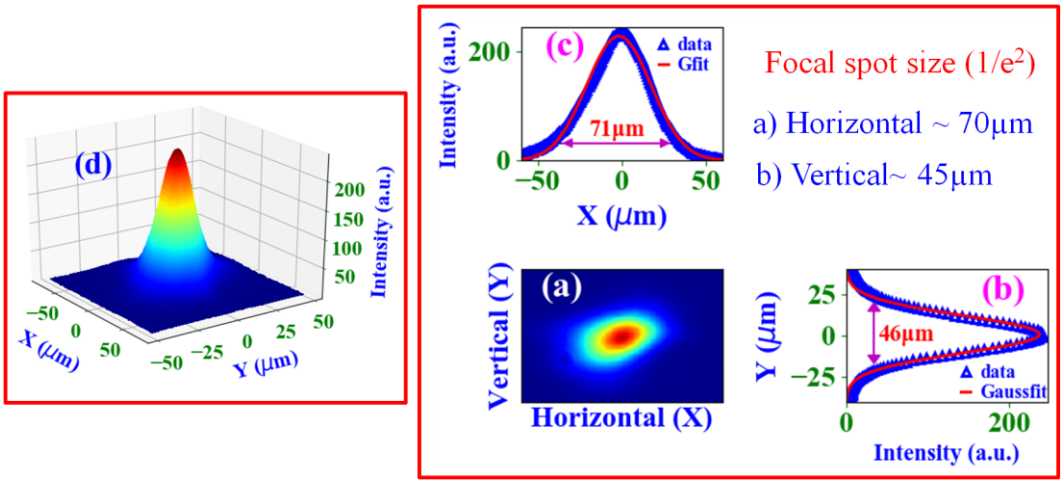

Figure 2.6: *a) shows laser focal spot image, b)and c) shows line intensity profile along Y=0 and along X=0 of raw and Gaussian beam fit , d) shows 3D plot of the focal spots shown in a).*

The experimental setup shown in Fig 2.5 is used to measure the focal spot size of the laser pulse focused using a 750mm focal length plano-convex lens (f#42) and is shown in Fig 2.6a. Fig. 2.6b and 2.6c shows a lineout of the focal spot at X= 0 and at Y= 0 respectively. A 3D plot of the focal spot shown in Fig 2.6a is plotted in Fig 2.6d, which shows a smooth elliptical profile. The ellipticity in the focal spot is due to combined effect of the ellipticity in the laser beam as well as spherical aberration of the focusing lens. The laser beam size is elliptical in vertical direction, which leads to ellipticity in horizontal direction after focusing using lens. The horizontal focal spot diameter is measured to be ~70μm ($1/e^2$ diameter) and vertical spot size to be ~45μm ($1/e^2$ diameter). The focal spot diameter for equivalent circular spot is calculated to be ~ 55μm ($1/e^2$ diameter) and the total energy content measured inside the $1/e^2$ focal spot diameter is calculated to be ≈ 50%. The same focal spot measurement setup (as shown in Fig 2.5) is used, when laser pulse is focused using OAP (f/7.5) mirrors in the experimental studies presented in chapter 3 of this thesis. The focal spot size ($1/e^2$ diameter) was estimated to be ~ 20μm with energy content inside the focal spot to be ≈ 55%.

2.2.2 Laser Spectrum and Pulse duration measurement

The shortest pulse duration achievable in a mode locked laser system depends on the spectral width of the laser pulses [83]. During the amplification of laser pulses in amplifiers, the gain narrowing takes place, which is detrimental in achieving the minimum attainable pulse duration. It is therefore important to measure the spectral width of laser pulse.

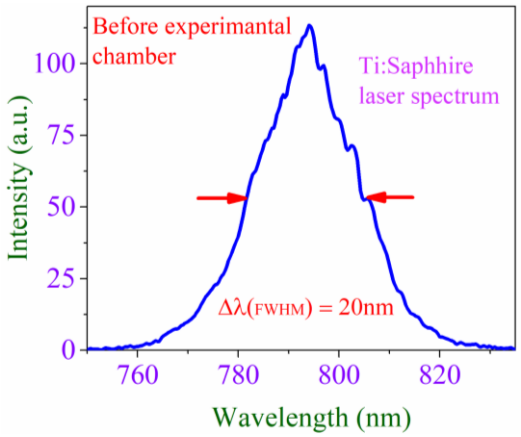

Figure 2.7: *Typical laser spectrum of both Ti: sapphire laser system (section 2.1.1 and 2.1.2).*

Spectral width of laser pulses from both the laser systems viz. ~10TW@ 10Hz and ~0.2TW@1kHz (as discussed in section 2.1.1 and 2.1.2) is measured using an optical spectrograph (Make: Avantes Inc.). A typical laser spectrum after the laser pulse compressor of a 10 TW laser system is shown in Fig. 2.7. The laser spectrum peaks at $\lambda \approx 800$ nm with a spectral bandwidth ($\Delta\lambda$) of 20nm. Although, laser pulses with 20 nm spectral bandwidth should give the transform limited pulse duration of ~ 35fs. However, the nonlinear dispersion in the laser pulse during amplification at different amplifier stages, may not be fully compensated by the pulse compressor. This results in increase in the minimum attainable pulse duration. It is therefore essential to

experimentally measure the laser pulse duration using autocorrelator before performing experiments.

The laser pulse duration is one of the most crucial and important parameter, which affects the ultrashort laser interaction with matter [84]. A single shot second order intensity autocorrelation technique is used for measurement of the laser pulse duration [85]. A schematic of the autocorrelator setup is shown in Fig. 2.8. First of all, the laser beam is splitted into two parts using a beam splitter and a delay line is installed in one of the beam path as shown in Fig. 2.8.

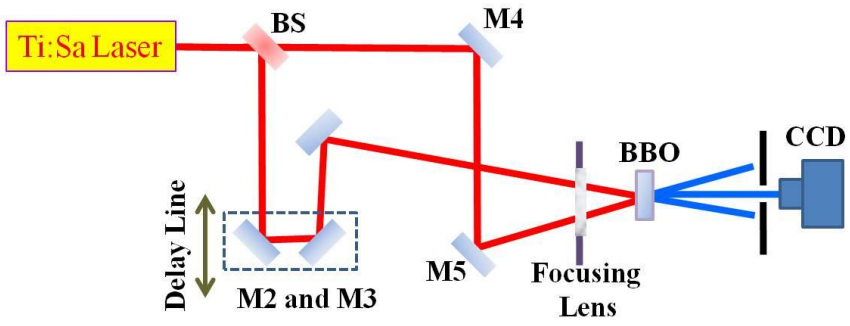

Figure 2.8: *A typical schematic of a single shot second order intensity autocorrelator.*

The two splitted laser beams are then focused in a thin second harmonic crystal (BBO KDP etc.) with a small angle between them. The second harmonic signal, generated by the autocorrelation and by the individual beams, is separated after the crystal (Fig. 2.8). Both the beams on the crystal are spatially and temporally (spatiotemporal) overlapped by adjusting the delay line and the mirrors (M1 and M5). In the overlapping condition, intense autocorrelation signal is visible. The region of the crystal where both the beams overlap is imaged on a CCD camera (Fig. 2.9(a)).

The second harmonic beam generated directly from the two individual splitted laser beams is blocked by a hard aperture so that only autocorrelation signal reaches to the CCD camera. A typical autocorrelation trace is shown in Fig. 2.9(b) [85]. The width of the autocorrelation trace is used to estimate the laser pulse duration for a known laser pulse temporal shape.

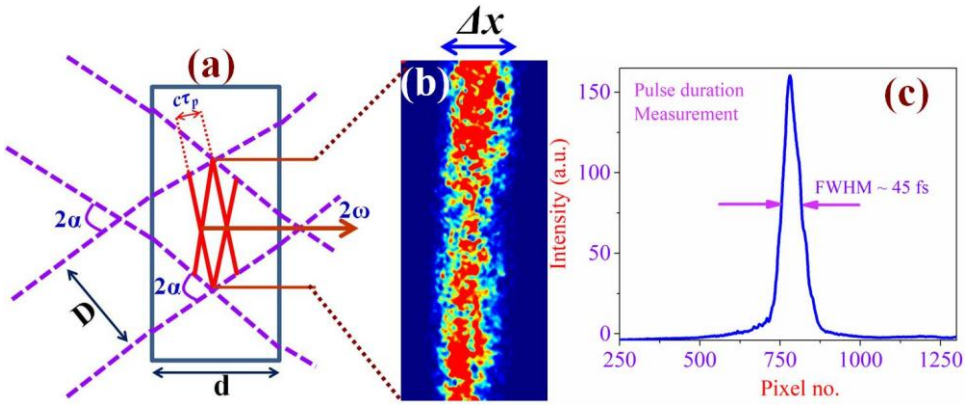

Figure 2.9: *a) conceptual design of second order autocorrelation b) autocorrelation trace and c) the pulse duration measured from the width of autocorrelation trace from b).*

It can be seen from Fig 2.9a that the two splitted beams are overlapping at half angle alpha (α) in space and time inside the crystal. Here "*D*" is the diameter of the laser beam and "*d*" is the thickness of the SHG crystal. For a laser pulse of duration "τ_p", it will occupy a width of $c\,\tau_p$ in space as shown in Fig. 2.9 (a). From Fig 2.9(b), the FWHM width of the autocorrelation trace (Δx) can be calculated, which is related to the laser pulse duration (τ_p) by the following relation [85]:

$$Pulse\ duration\ (\tau) = \frac{K\Delta x\ \sin(\alpha)}{c} \qquad (2.2)$$

In Eq 2.2, α is the half angle between the two beams, c is speed of light and K is a parameter dependent on the temporal shape of laser pulse (for Gaussian K ≈ 1.4, for $Sech^2$ K ≈ 1.3).

Using autocorrelator set up shown in Fig 2.8, I have measured the laser pulse duration and also optimized the grating laser pulse compressor for achieving shortest pulse duration. The minimum pulse duration is measured to be ~ 45 fs in both laser systems.

2.3 Higher harmonic diagnostics

As discussed in section 1.4 of chapter 1, the wavelength of higher harmonic radiation extends from extreme-ultraviolet to soft x-ray range [86]. This radiation requires vacuum for its propagation, which makes characterization of this radiation a challenging task. Some of the detectors that are used for the characterization of this radiation are XUV photodiode [87], X-ray CCD camera [88], micro channel plates (MCP) [89] etc. The photodiode mainly consists of reversed biased p-n junction. When the XUV photon is absorbed in the depletion region it results into generation of electrons-hole pair and generates photo-current, which can be recorded using an oscilloscope. The photon flux is calculated from the oscilloscope trace and the quantum efficiency of photodiode. In case of x-ray CCD camera, the incident XUV photons are absorbed in two dimensional CCD pixels array, which records two dimensional image of the XUV signal. The photon flux can be obtained by knowing the quantum efficiency of the x-ray CCD camera. In case of x-ray CCD camera, the noise is small, due to cooling of CCD chip to very low temperature (-30 to -50 ^{o}C).

The AXUV diode as well as X-ray CCD camera doesn't have any internal gain to amplify the weak signal. Hence detecting weak signal may using these detector is challenging. One needs a detector with an internal gain to detect such weak signals. Microchannel plate (MCP) detector has internal gain, which depends on the applied voltage. In MCP, there is bundle of lead glass capillary having many tiny holes with

diameter ~10 μm and length ~ 500μm. The inner surface of each hole is coated with resistive secondary electron emitter, connected to the input and output electrodes, to provide continuous amplification of secondary electrons. The inside surface of these holes is usually coated with layers of resistive layer coating (e.g. Al_2O_3), to provide high resistance and an emissive layer (e.g. Mo) coatings is used to provide secondary electron emission and multiplication, when high voltage is applied across these holes [89,90]. The XUV photons incident on this array of holes, generate photoelectrons, which are multiplied in the channels (called as internal gain) and strikes the phosphor kept at the proximity of the channels. The phosphor gives light emission which is recorded on a visible CCD. The MCP has a typical gain of > 10^3 at an accelerating voltage of ~ 1000V for single stage MCP. In order to increase the gain further, two / three stages MCP are stacked together, which can provide higher gain >10^6 [89]. Thus multi-stage MCP can detect very low level signal, however due to high gain, the noise level is also significantly higher.

In the present work, the generation, characterization and application of higher harmonic radiation source is carried out. The characterization of XUV radiation includes spatial, spectral, coherence and temporal characterization. The spatial and spectral characterization is performed using an XUV spectrograph known as flat field grating spectrograph (FFGS) coupled with a MCP-CCD detector and the photon flux is measured using AXUV diodes, which will be discussed in detailed. Further, detail of toroidal mirror used to focus the higher harmonic radiation, in the present research work will also be discussed.

2.3.1 Flat field grating spectrograph

The study of the spectral characteristics of the harmonic radiation has been carried out using an XUV spectrograph. The choice of the type of spectrograph is dependent on the spectral range, spectral resolution, and geometry of the dispersion required in the particular experiment. However, compact size, ease of installation and alignment, coupling with online detectors (which are flat detectors) viz. micro-channel plate, x-ray CCD camera etc. are equally important parameters that should be taken into consideration in the spectrograph design. The dispersive element and detector is a major component of a spectrograph. Both transmission and reflection grating can be used as a dispersive element in spectrograph. Transmission grating spectrograph has good spectral resolution covers large spectral range and also easy to align, however, due to small size of free standing transmission grating (few mm), the collection efficiency is very low [91]. The XUV spectrograph based on spherical reflective grating can be used as an alternative, which has good collection efficiency with high spectral resolution [92]. The spherical grating with constant line spacing has to be used in Rowland circle geometry; therefore the online detector (viz. MCP, x-ray CCD camera) which is 2-dimensional flat detector cannot be used in this case. Alternatively, a variable line spaced grating can be used, which focuses the spectrum in a flat plane (hence named as “Flat Field Grating Spectrograph (FFGS)”).

FFGS consists of a spectrograph slit, a variable line spaced (VLS) concave grating and a flat x-ray detector viz. microchannel plate (MCP) or x-ray CCD camera [93, 94]. The grazing incidence x-ray focusing optics viz. toroidal mirror, cylindrical mirror etc. may be used to enhance the intensity at the detector of the spectrograph. A typical schematic of FFGS is shown in Fig 2.10a. Figure 2.10b shows the spectrally

resolved image of higher harmonics generated from carbon plume and c) shows the line profile of harmonic spectrum shown in Fig 2.10b.

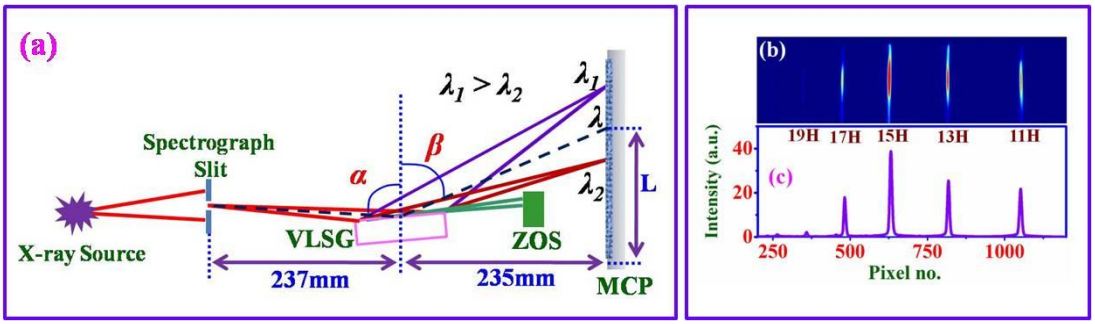

Figure 2.10: *a) A schematic of flat field grating spectrograph b) typical higher harmonic image generated from pre-formed carbon plume (11^{th} to 19^{th} order) c) line profile of image b).*

The key component of FFGS is variable line spaced concave grating, which disperses the x-ray spectrum in one direction and image the spectrograph slit in the other direction. This preserves the spatial information of x-ray source in one direction. The parameters of VLS grating used in our experiment are shown in table 2.3.

Parameters	Value
Radius of curvature (R)	~5469mm
Groove density (at centre) (σ_0)	1200 grooves/mm
Grating Dimensions (length × width × thickness)	50mm ×30mm×10mm
Blaze Angle	~3.2 deg
Incidence Angle	~87 deg
Blaze Wavelength (λ_B)	10nm
Source to grating centre distance	~237mm
Grating centre to detector distance	~235mm

Table 2.3: *The parameters of VLS grating used in FFGS*

In VLS grating, the groove spacing varies along the x-ray propagation direction (*x* direction), which can be approximated using a polynomial equation [45, 95].

$$\sigma(z) = \sigma_0\left(1+\frac{2b_2 z}{R}+\frac{3b_3 z^2}{R^2}+\frac{4b_4 z^3}{R^3}\right) \tag{2.3}$$

Where b_2, b_3 and b_4 are ruling parameter of grating and their values are -20, 455.8, and -11841 respectively, *z* is direction of propagation of x-ray beam, *R* is radius of curvature of grating and $\sigma(z)$ is the variation of groove spacing in x-ray beam propagation direction, σ_0 is central groove density (1200 lines/mm in our case). As groove spacing increases from one side to other, therefore it is important to place the grating correctly in the spectrograph. In case of the VLS grating, dispersion equation [95] is given by the relation

$$m\lambda = \sigma_0\left(\sin(\alpha)-\sin(\beta)\right) \tag{2.4}$$

Where α and β is the angle if incidence and angle of diffraction for a given wavelength λ and m (1, 2, 3…) is order of diffraction. The zero order diffraction ($m=0$), also called as specular reflection, should be blocked to record the dispersed wavelength in first or higher diffraction orders. The important parameters of the spectrograph are the dispersion and resolving power. The dispersion is defined as wavelength per unit length in detector plane. From Fig 2.10a, the diffraction angle (β) for wavelength λ and its spatial position L is related [45] as

$$L = 235\cot(\beta) \tag{2.5}$$

Using Eq 2.4 and Eq 2.5, the dispersion of the spectrograph [93] is calculated to

$$\frac{d\lambda}{dL} = \frac{\sigma_0}{235m}\left(\sin\alpha-\frac{m\lambda}{\sigma_0}\right)^2\left\{1-\left(\sin\alpha-\frac{m\lambda}{\sigma_0}\right)^2\right\}^{1/2} \tag{2.6}$$

At wavelength, λ = 60 nm, the dispersion is calculated to be 1.1nm/mm, whereas at λ = 5 it turn out to be 0.4nm/mm in first diffraction order. This shows the spectral dispersion is not linear with wavelength as well as with diffraction order. Further, it can be seen from the Eq 2.4 that the first diffraction order of a wavelength (λ) and the second diffraction order of a radiation at $\lambda/2$ will coincide. This will create ambiguity in the wavelength characterization. Therefore accurate calibration of FFGS is essential, especially when first and higher diffraction order is simultaneously present in the spectrum [96]. This is discussed in detail in chapter 4 of this thesis.

Another parameter of spectrograph is resolving power ($\lambda/\Delta\lambda$), which is calculated [93] using Eq 2.4 to be

$$\text{Resolving power}(R) = \frac{\lambda}{d\lambda} = \frac{\sin(\beta) - \sin(\alpha)}{\sigma_0 \cos(\beta) d\beta} \tag{2.7}$$

Using Eq 2.7, at wavelengths 5nm and 60nm, taking the values of β(5nm) = 830, $d\beta$ (5nm) = 1.72×10^{-4}, β(60nm) = 67.90, $d\beta$(60nm) =1.98×10^{-4}, the resolving power is calculated to be ~290 and ~800 respectively. The diffraction efficiency of grating plays an important role in deciding the number of photons diffracted in different diffraction orders. The diffraction efficiency of VLS grating, used in our experiment is measured for different orders, using reflectivity beamline of Indus-1 synchrotron radiation source at our centre [97]. The measured diffraction efficiency in first and second order is shown in Fig 2.11. It is to be noted from Fig 2.11, that the grating reflectivity is peaked at ~20 nm, which shows apparently a grating blaze wavelength at ~20nm. However, the grating should have a blaze wavelength of ~10 nm as per grating specification. This draws our attention towards the possibility of carbon deposition over the grating, which may have changed the blaze wavelength from ~10 nm to ~20 nm. Also, the absolute reflectivity was reduced to a very low value of 1% at

~10nm. To remove the carbon contamination from the grating surface, it was irradiated with UV radiation. It was observed that after irradiation of ~6 to 7 hours, the grating reflectivity was restored to its original value. The reflectivity peak was also shifted to ~10 nm, as per the design specification of the grating (Fig. 2.11) [97].

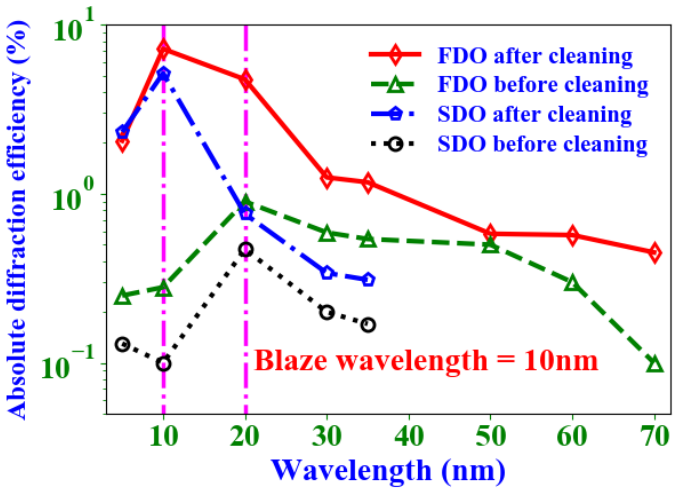

Figure 2.11: *Absolute diffraction efficiency of VLS grating before and after UV cleaning measured using reflectivity beamline of INDUS-1 synchrotron radiation source, RRCAT, India.*

In Fig 2.11, the term FDO and SDO refers to first diffraction order and second diffraction order respectively. It can be seen from Fig 2.11 that the blaze angle is restored to ~10nm and the diffraction efficiency improves by more than an order of magnitude.

FFGS can be used to measure the spatial and spectral profile as well as the photon flux of higher harmonics. Once the absolute diffraction efficiency of grating is known, the photon flux can be calculated. The photon flux can be estimated [98] by taking into account the parameters of each component of FFGS as

$$Photon\ flux = \frac{N_{CCD} \times S_{CCD}}{\Omega \times G_{MCP} \times \eta_{MCP} \times DE_G \times S_P \times \eta_{CCD} \times C_L} \qquad (2.8)$$

In Eq 2.8, the Ω is the fraction of x-ray radiation passing through the spectrograph slit, N_{CCD} is the intensity count recording on the CCD camera, G_{MCP} is the MCP gain at an operating MCP voltage, η_{MCP} is the quantum efficiency of the MCP, DE_G is the diffraction efficiency of the VLS grating measured using Indus-1 beam line, S_P is the sensitivity of the MCP phosphor screen, η_{CCD} and S_{CCD} are the quantum efficiency and sensitivity of the CCD camera imaging the phosphor screen of MCP respectively, C_L is the fraction of phosphor screen light collected by the imaging optics of the CCD.

2.3.2 XUV diode for absolute photon flux measurement

One of the primary goals of this thesis work is, to measure and improve the photon flux of higher harmonic radiation source. The AXUV diode (Make: IRD, Model: AXUV20HS1), which is a semiconductor Si-pin diode is used for this purpose. The pin diode generates electron and hole (e-h) pair, when radiation falls on it. To generate one e-h pair, photon energy of ~ 3.65 eV is required and higher energy photons will generate e-h pair in proportional to its energy. Thus, a current is generated in the circuit which is a measure of absolute photon flux [87] of the incident radiation. The AXUV diode has a linear response in wide photon energy range viz. from ~few eV to ~few keV. This covers the complete spectral range of high order harmonics, generated in the present work.

The AXUV diodes have very high quantum efficiency (collection of carrier viz. electrons, by external circuits per incident photon) almost ~ 100%. Due to absence of surface dead region, there is no recombination of carriers generated by the photons in the doped region or at the interface [87]. Also, the AXUV diodes are easy to use, they have good spatial homogeneity, large dynamic ranges and they are ultrahigh vacuum compatible.

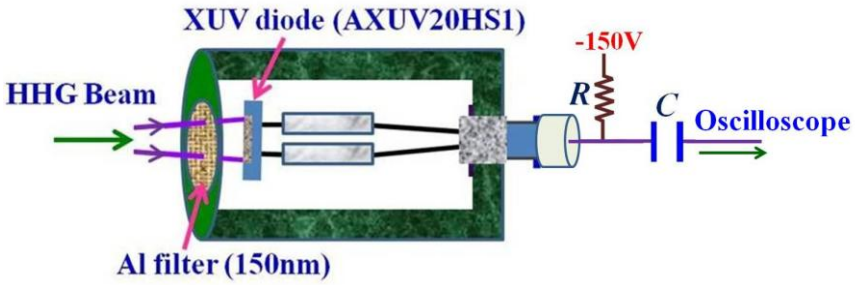

Figure 2.12: *A schematic of AXUV diode assembly (Make: IRD, Model: AXUV20HS1) housing used for photon flux estimation of higher harmonic source.*

In the present work, the AXUV diode (Make: IRD, Model: AXUV20HS1) to estimate the photon flux of higher harmonic source. A schematic of the diode housing assembly is shown in Fig 2.12. In this assembly, the AXUV diode is reverse biased viz. the p junction of the diode is connected to -150V. The capacitor of capacitance "C" is used to block the DC signal (used for the reverse bias) and allow the pulsed current signal generated by incident x-ray photon. This current signal is recorded in an oscilloscope with 50Ω termination.

From the voltage signal recorded on oscilloscope (50 Ω termination), the total charge can be calculated using Eq 2.10. Total number of photons can be estimated using Eq 2.11, where N_{ph} is total number of photons of energy E_{ph}, T_{ph}, is the Al filter transmission at photon energy E_{ph}.

$$Q = \int \frac{V}{R} dt = \frac{T_{ph} N_{ph} E_{ph}}{3.65} \tag{2.10}$$

$$N_{ph} = \frac{3.65}{T_{ph} E_{ph}} \int \frac{V}{R} dt \tag{2.11}$$

As discussed in the previous chapter that the high order harmonic radiation is propagating collinearly with the laser pulse. To accurately measure the absolute photon flux of HHG source using Eq 2.11, the IR laser light is needed to be blocked. An aluminium filter of thickness ~150nm is used in front of diode to block the

incoming IR laser photons. Further, the photon flux can be calculated using Eq 2.11, if the harmonic spectrum has only one harmonic order. However, the harmonic spectrum has multiple harmonic orders, thus spectrally resolved measurement is required. The FFGS (discussed in previous section) can be used for this purpose. From the measured relative intensity of harmonics using FFGS, one can estimate the flux of individual harmonics radiation [96] using the relation

$$N_{ph,q} = \frac{Q}{e}\left(\frac{3.7 \times N_{CCD,q}}{T_q \sum_{q=q_L}^{q_H} N_{CCD}\ E_{ph,q}\,(\mathrm{eV})}\right) \tag{2.9}$$

Where T is transmission of Al filter (thickness ~1500Å), Q is total charge generated by the incident high order harmonic photon in the pin diode, $N_{ph,q}$ is no. of x-ray photons, $N_{CCD,q}$ is intensity and $E_{ph,q}$ is photon energy of q^{th} harmonic order. Eq 2.9 assumes a flat spectral response of the MCP.

2.3.3 Toroidal mirror for x-ray focusing

A grazing incidence toroidal mirror is used for the focusing of higher harmonic radiation, which increases the photon flux in the focal region. Toroidal mirror is developed in-house by bending a cylindrical mirror along its length (Fig. 2.13). The cylindrical mirror has a radius of curvature of 25mm and length 100mm. The technique of making toroidal mirror by bending the cylindrical mirror is that one can change the curvature of the mirror, as per experimental need. The bending of the mirror is implemented by holding the mirror from the front side using studs and applying a torque by pushing the mirror from back at the two ends along its length. It is observed that with slight bending, the required radius of curvature can be obtained in sagittal plane as shown in Fig 2.13(a).

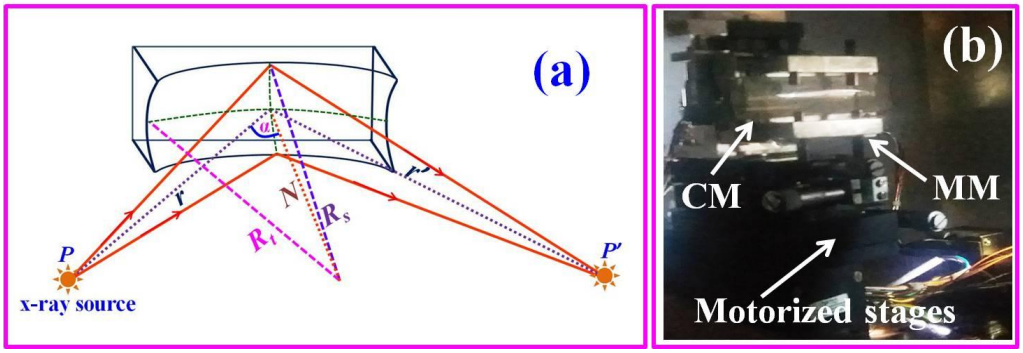

Figure 2.13: *a) Schematic of the toroidal mirror used to image the x-ray source to a point and b) the mounts used to bend the cylindrical mirror to convert it to a toroidal mirror, CM is cylindrical mirror and MM is micrometer.*

In Fig 2.13, R_t and R_s is radius of curvature of meridional/tangential and sagittal plane respectively, *N* is the line drawn normal to the mirror base, r and r' is the distance between the source point (P) and image point (P') from the centre of toroidal mirror respectively, α is the angle between the mirror normal (*N*) and the incident ray to the mirror centre. The mirror equation in both tangential and sagittal plane [99] can be written as

$$\frac{1}{r'}-\frac{1}{r}=\frac{1}{f_s}, \text{ where } f_s=\frac{R_s}{2\cos\alpha} \tag{2.12}$$

$$\frac{1}{r'}-\frac{1}{r}=\frac{1}{f_t}, \text{ where } f_t=\frac{R_t\cos\alpha}{2} \tag{2.13}$$

The reflective optics should be used at grazing incidence to focus x-rays, owing to the higher reflectivity at this angle. To achieve same focal length in the two planes, the radius of curvature of two planes are quite different viz. $R_s >> R_t$ at x-ray wavelength. For a toroidal mirror of 25mm sagittal radius of curvature and at grazing incidence angle of 2 degrees ($\alpha = 88^o$), the sagittal focal length is calculated to be ~ 360mm. The required meridional radius of curvature is calculated to be 20.6 meter. Before focusing of HHG beam, the focusing behaviour of toroidal mirror is tested by focusing the IR laser beam. Figure 2.14a shows the IR laser beam focus using the in-

house developed toroidal mirror. The focal spot is measured at best focus of toroidal mirror as shown by point P' in Fig 2.13a.

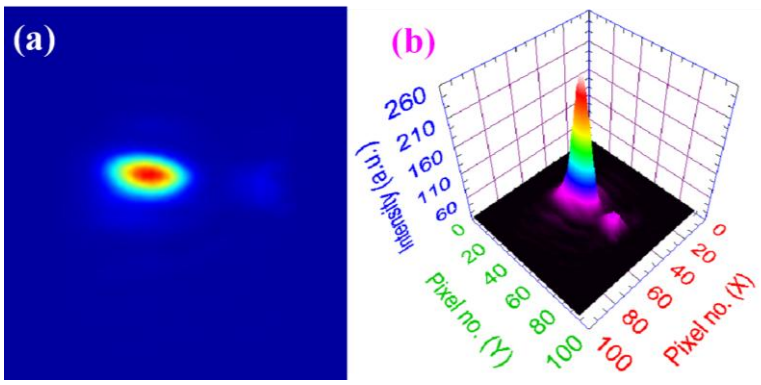

Figure 2.14: *a) The focal spot of IR laser pulse at the image point P' (as shown in Fig 2.13a) b) 3D view of the focal spot shows in a).*

Figure 2.14b shows a 3D focal spot view of Fig 2.14a. The focal spot radius at minor and major axis are measured to be ~ 250μm and ~ 500 μm respectively, which is good size for achieving higher flux at the focus.

Chapter 3:

Higher Harmonic Generation from Plasma Plumes

The higher harmonic radiation can be generated by focusing an ultrashort intense (Intensity ~ $10^{14\text{-}15}$ W/cm^2) laser pulse in a non-linear medium [47]. The characteristics of the generated harmonics depend crucially on the laser and non-linear medium parameters [100]. The use of plasma plume provides a vast scope of research in the field of higher harmonic generation as any solid target plumes can be used for this purpose [101]. Some of the interesting observations have been reported in several plume viz. intensity enhancement by more than two order of magnitude (200×) of 13th harmonic order generated from indium plume[58], the enhancement of 21st harmonic order (20×) from InSb plume [58], 27th harmonic order (6×) from GaAS [58] etc. These enhancements can also be tuned by changing the sign of chirp (positive / negative) in the laser pulse [58, 102]. Different harmonic cutoff orders have also been reported in different material plumes viz. 29th harmonic order in carbon containing plumes [103], 63rd harmonic order from silver plume [55], 101st harmonic order from Magnesium plume [57] etc.

In the earlier investigations carried out in our lab, we had explored different aspects of higher harmonic generation from pre-formed plasma plumes [104-106]. Several target plumes was explored and various laser and plasma plume parameters were optimized. This results in generation of higher harmonics with good intensity and higher cutoff [104-106]. It is also found, that the carbon containing plume is promising for efficient mid-order harmonic generation (9th order to 19th order with a cutoff at 29th order) [103]. Different techniques were also adopted, to improve the harmonic intensity further [56, 104]. This includes the use of two color laser pulses [105], use of extended medium [107,108], use of multiple plasma plumes for quasi

phase matching[109, 110] etc. The spatial and spectral characteristics of plasma plume harmonics have also been investigated and exciting results have been observed viz. the generation of broadband harmonics from nanoparticle containing plumes [111], quantum path signatures in metal plasma plumes [112] etc. However, the coherence property of the higher harmonics from plasma plume remained unexplored.

We present the study of spatial coherence of higher harmonics generated from pre-formed carbon (graphite) plume. The carbon plume has been preferably used for the study, due to its capability to generate intense mid-order harmonics (11^{th} to 29^{th} order) [103]. Although, the spatial coherence property of higher harmonics generated from the inert gases (where only neutral atoms are present prior to focusing of ultrashort laser pulse used for harmonic generation) have been explored by several groups [9, 113] earlier. In case of plasma plumes, the neutral atoms, charges ions, electrons, molecules etc., are present, which makes the study of spatial coherence of higher harmonic generated from plasma plume more interesting and worth investigating.

The spatial coherence of higher harmonics from plasma plumes is studied using a double slit experiment. The parameters were optimized to achieve the best spatial coherence of harmonics. After optimizing the spatial coherence, the study was further extended to explore for the technique which can improve the harmonic intensity further, while maintaining good spatial coherence. We used the spatially shaped laser beam for this purpose, as few studies have shown that the spatial shaping of laser beam may lead to enhancement in the intensity of higher harmonics, generated from gases [114, 115]. The effect of spatial shaping of laser beam on harmonic intensity and spatial coherence remains unexplored in case of plasma plumes. We have investigated the role of spatial shaping of laser beam on intensity and spatial

coherence of higher harmonics from plasma plume [98], which is presented in this chapter in detail.

This chapter has been divided into two sections. In the first section, we discuss about the characterization of spatial coherence property of harmonics and in the second section, we discuss about the effect of spatial shaping of ultrashort laser pulse on yield / conversion efficiency of higher harmonics.

3.1 Study of Spatial coherence of higher harmonics

The study of spatial coherence of higher harmonic source is essential for its application in coherent diffractive imaging / lensless imaging [67], holography [116], high density plasma probing using interferometry [12] etc. The generation of higher harmonics from laser atom interaction, (as explained by three step model [43]) is a coherent process. In this, an intense laser field controls the electron motion throughout the harmonic generation process i.e. ionization, acceleration and recombination [42, 43]. Due to this, the higher harmonic source is expected to be coherent. However, after generation from single atom, the harmonic radiation propagates in plasma plume medium. The medium has inherent ionization and thus significant free electron density is present in the plume. Further, the presence of oscillating laser electric field (used for HHG), makes the free electron density time dependent, which may deteriorate the coherence property of harmonic source. It is therefore not only essential, but also interesting to study the spatial coherence property of higher harmonics in such pre-ionized medium.

The spatial coherence of any source is defined in terms of the electric field correlation at any two distinct points separated in space. It is expressed in terms of the mutual coherence function [117], which can be expressed as

$$\Gamma_{12} = \left\langle E_1(r_1,t) E_2^*(r_2,t+\tau) \right\rangle \tag{3.1}$$

E_1 and E_2 are the complex electric field amplitude at two points S1 and S2 as shown in Fig 3.1.

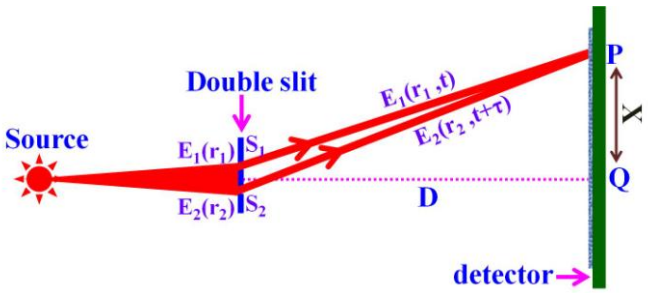

Figure 3.1: *A schematic of spatial coherence measurement of a source.*

The bracket in Eq 3.1, denotes the ensemble average, which can be safely taken to be the time average (for any ergodic process, the ensemble average equals time average [118]) over the laser pulse width. The normalized mutual coherence function (at zero time delay between the two sources S_1 and S_2 at point P) also called as complex coherence factor (CCF) [9, 118], which is define as

$$CCF(\mu_{12}) = \frac{\Gamma_{12}}{\sqrt{\Gamma_{11}\Gamma_{22}}} = \frac{\left\langle E_1 E_2^* \right\rangle}{|E_1||E_2|} \quad \text{, where } 0 \le \mu_{12} \le 1 \tag{3.2}$$

When the field exhibits complete correlation between two spatially separated points, CCF is 1 and source is considered to be fully spatially coherent. When the electric field at two points has no correlation, the CCF is 0 and the source is said to be incoherent. For a partially coherent source the CCF lies between 0 and 1. Experimentally, the spatial coherence of a source is estimated in terms of interference fringe visibility [9, 117] or fringe contrast, which is related to CCF.

$$|\mu_{12}| = \frac{I_1 + I_2}{2\sqrt{I_1 I_2}} V, \text{where } V = \frac{I_{max} - I_{min}}{I_{max} + I_{min}} \tag{3.3}$$

I_1 and I_2 are the source intensities at the position of two slits (S1 and S2), I_{max} and I_{min} is the maximum and minimum intensity of the interference fringe. When the two slits (S1 and S2) are illuminating with equal intensity (I_1=I_2), the CCF is equal to fringe visibility (V). The fringe visibility is a qualitative representation of spatial coherence of a source. The spatial coherence can be expressed quantitatively, in terms of coherence area, which is related to CCF [9] by the relation expressed in Eq 3.4

$$A_c = \iint \left|\mu\left(\Delta x, \Delta y\right)\right| d\Delta x\, d\Delta y = \pi R_c^2 \tag{3.4}$$

In Eq 3.4, Δx and *Δy* is the difference in coordinate between two sampling point (transverse to beam propagation) at the source. Next, for a Gaussian beam, the Gauss-Schell model can be used to estimate the coherence radius of source from the experimentally measured fringe visibility [113, 117].

$$V = \left|\mu(d)\right| = \exp\left(-\frac{(d)^2}{2R_c^2}\right) \tag{3.5}$$

In Eq 3.5, R_c is the coherence radius and d is the slit separation. It is to be noted from Eq 3.5 that the coherence radius can be calculated from the Gaussian fitting of the fringe visibility with slit separation. The slit separation at which, the fringe visibility drops to 61% is taken to be the coherence radius and coherence area of a source can be calculated (A_c=πR_c^2). The harmonic source size (d_s) can be calculated from coherence area (A_c), using Van-Cittert Zernike theorem [9] using Eq 3.6.

$$d_s = \frac{\lambda z}{\sqrt{\pi A_c}} \tag{3.6}$$

In Eq 3.6, d_s represent the source size, z is distance between the source and the double slit, and A_c is the coherence area of radiation source.

3.1.1 Experimental details

The experiment was carried out using a chirped pulse amplification based Ti: sapphire (central wavelength λ_o = 800nm) laser system, capable of operating at 10 Hz repetition rate (the detail of laser system is discussed in section 2.1.1 of this thesis). A schematic diagram of the experimental setup is shown in Fig 3.2a. An uncompressed laser pulse (before the pulse compressor chamber) is splitted into two parts using a beam splitter.

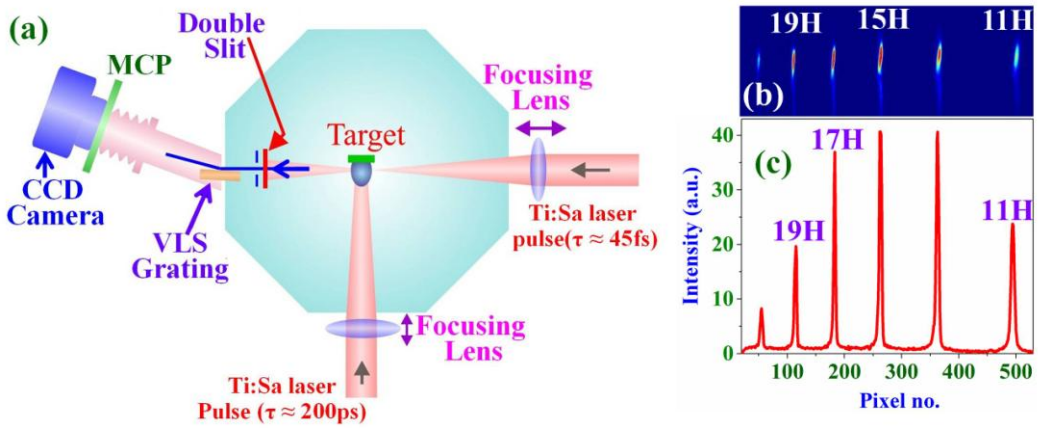

Figure 3.2: *a)* **S***chematic of experimental setup used for higher harmonic generation from carbon plume and study of its spatial coherence b)the image of higher harmonics from carbon plume and c) is the line profile of b)* .

The first part of the laser pulse with energy ~20 mJ and pulse duration ~200 ps (known as prepulse) is focused on solid target surface, using a plano-convex lens of focal length 500mm to intensity ~10^9-10^{10} W/cm^2 [119]. This forms plasma plume on target surface, which is used as a non-linear medium for higher harmonic generation. The plasma plume is allowed to expand for an optimum duration (≈ 50ns) [119]. This serves two purposes, first, due to expansion the plasma plume comes out from the target surface to sufficient distance, so that the ultrashort laser pulse can be focused in

this plume for harmonic generation. Secondly, due to expansion, the plasma is cooled down, so that it predominantly consists of neutral atom / singly charge ions and the electron density is also diluted, which doesn't deteriorate the harmonic intensity by spoiling the phase matching condition. The second part of uncompressed pulsed (called as main pulse) is compressed to 45 fs at ~100mJ energy is focused in the plasma plume to an intensity of ~10^{14}-10^{15} W/cm^2 using a plano-convex lens of 500 mm focal length [119]. The main pulse beam is propagating parallel to the target surface, at an optimum distance (~250 μm). For efficient generation, the laser intensity is optimized by varying the position of laser focus relative to plasma plume. The generated harmonics is dispersed and detected using FFGS (The details discussed in section 2.3.1). The FFGS is adjusted to record the wavelength range of our interest (11^{th} to 21^{st} harmonic from carbon plume) [119]. Figure 3.2b shows a typical image of the harmonic spectrum generated from carbon plume and recorded by FFGS. Figure 3.2c shows the line profile of Fig 3.2b.

For the double slit experiment, high intensity of the harmonics is desirable, so that after passing the radiation through two fine slits, intensity of interference fringes should be good enough to be recorded by FFGS. For this, the laser and plasma plume parameters were optimized viz. optimization of pre-pulse intensity (~ 10^{10} W/cm^2) and main pulse intensity (~ 2×10^{15} W/cm^2), the position of plasma plume relative to laser focus (~3.5mm), distance from the main pulse from target surface (~200μm) etc. After achieving good intensity of higher harmonics, a set of free standing double slits of width ~30μm and different separations (~100μm, ~120μm, ~150μm and ~175μm) were inserted in the harmonic beam path. The double slit was placed at a sufficient distance away from the MCP of FFGS (~ 425 mm); to make sure that the resolution of FFGS (~ 40 μm) is sufficient to resolve the interference fringes. The double slits were

placed at ~175mm away from the harmonic source and just before the slit (width ~1.5mm, length~15mm) of FFGS.

3.1.2 Results and Discussions

For the measurement of interference fringe visibility, the two slits of the double slit setup, should be illuminated equally (I_1=I_2) with harmonic source; else it may introduce measurement error [119]. To ensure this, we have estimated the higher harmonic divergence. Figure 3.3 shows the image and the line profile of experimentally measured harmonic spectrum of 11th to 21st order generated from carbon plume.

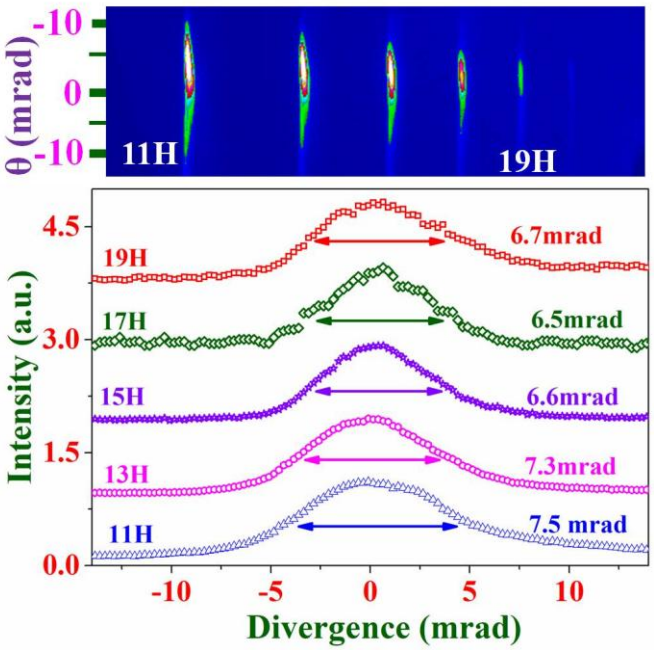

Figure 3.3: *The divergence of higher harmonic radiation source generated from carbon plume and their line profile.*

From Fig 3.3, it can be seen that the divergence of the harmonics (11th to 21st order) are ~6.5-7.5 mrad, as compared to the laser beam divergence of 25mrad. The

harmonic beam profile is also smooth. The harmonic beam size calculated at double slit position ≈1.2mm, whereas the slit separation varied from ≈ 100μm to ≈ 200μm. This ensured that nearly same intensity will fall on both the slits, when they are placed in the beam path.

After inserting double slit in the path of harmonic beam, a raw image showing the unresolved interference pattern is observed on the CCD camera of FFGS. To resolve the interference fringes, the raw image and was magnified (magnification ≈ 2×) and the background noise is also subtracted.

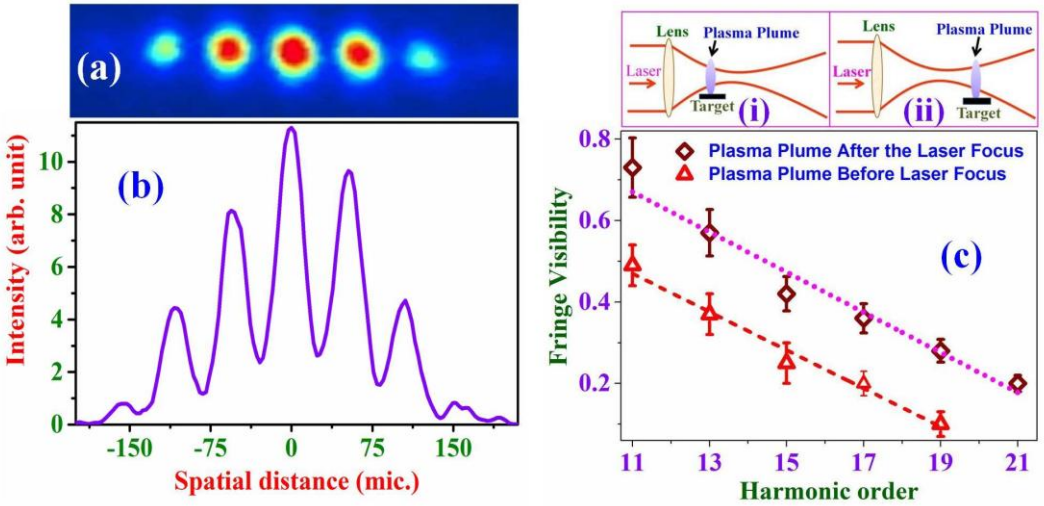

Figure 3.4: *a) interference fringe of 11th harmonic order, b)is line profile of a), and c) shows the variation of fringe visibility with harmonic order with the plasma plume position relative to laser focus. The inset of c) shows the pictorial representation of plasma plume position (i) before and (ii) after the laser focus.*

Fig. 3.4a shows the recorded interference pattern of 11th harmonic order, after background subtraction and Fig. 3.4b shows its line profile. The fringe visibility (V) is calculated using Eq 3.3, where I_{max} is taken to be the intensity of the central fringe, and I_{min} is taken to be the average of the two minimas lying adjacent to the central fringe. Further, the laser and plasma plume parameters were optimized to improve the

fringe visibility. Figure 3.4c shows the variation of fringe visibility at optimum parameter condition for maximum harmonic intensity (~ 6mm) in the two cases, (i) when laser pulse is focused after and (ii) before the plasma plume. Both the conditions are pictorially shown as (i) and (ii) in Fig 3.4c. It can be seen from Fig 3.4c, that the fringe visibility is higher when plasma plume is placed after the laser focus and the fringe visibility decreases with increase in harmonic order in both the cases (i and ii).

The spatial coherence of a source can be quantitatively expressed in terms of coherence radius (as discussed earlier in this section). The Gauss-Shell model is used to calculate the coherence radius using Eq 3.5, from the recorded the fringe visibility at different slit separations [113,117]. The variation of fringe visibility with slit separation is fitted to a Gaussian function (see Fig 3.5a) and the coherence radius is calculated using Eq 3.5 (The coherence radius = slit separation, when the fringe visibility becomes ≈ 0.61).

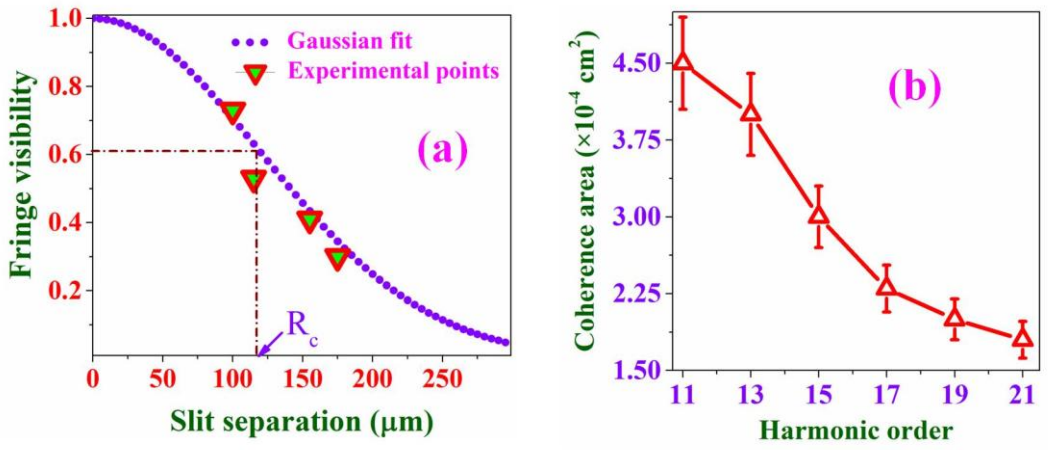

Figure 3.5: *a) the variation of fringe visibility with slit separation and b) shows the variation of coherence area with harmonic order from 11th to 21st*

For 11th harmonic order, the coherence radius is calculated (see Fig 3.5a) to be ≈ 120μm, which gives a coherence area ($A_c = \pi R_c^2$) of ~ 4.5x10^{-4} cm^2. The coherence

areas for harmonic orders 13th to 21st are also calculated in the similar way. Figure 3.5b shows the variation of coherence area with harmonic order. It can be seen from Fig 3.5b that the coherence area decreases significantly from 11th (A_c ~ 4.5×10^{-4} cm^2) to 21st (A_c ~ 1.5×10^{-4} cm^2) harmonic order. The harmonic source size can be estimated from the calculated coherence area using Eq 3.6. Using the source to slit distance ~ 175mm, λ ~ 72.7nm for 11th harmonic order and coherence area (A_c) ~ 4.5×10^{-4}cm^2, the source size is estimated to be ~30μm. For 21st harmonic order, the wavelength (λ) ~38.1nm and the coherence area ~1.5×10^{-4} cm^2, the source size is calculated to be ~35μm. The laser spot size at the optimum plume position (~6mm) is calculated to be ~80μm for a Gaussian beam profile, from the experimentally measured focal spot size ~20μm (at laser focus). This shows that the harmonic source size is smaller, as compared to the laser spot size in the plasma plume.

The spatial coherence of higher harmonics can be theoretically estimated from the integrated time-dependent phase at two spatial points across transverse beam profile of the source [9]. Therefore, the factors, which impart time dependent phase to higher harmonic source, may affect its spatial coherence property. There are several factors that may impart additional phases to higher harmonic radiation, which can be estimated from the wavevector mismatch, for Gaussian laser beam profile [63].

$$\Delta k_q = -n_a\left(r_0\lambda_q f_1 - \frac{\pi\alpha_1}{\lambda_q}\right) + \frac{qe^2 n_e}{c\omega_L\varepsilon_0 m_e} - \frac{2z\, z_R^2\alpha_q I_0}{\left(z^2+z_R^2\right)} + \frac{qz_R}{z^2+z_R^2} \qquad (3.7)$$

In Eq 3.7, the first term is the wave-vector mismatch due to neutral atoms of medium, the second term is due to the free electron present in the non-linear medium, the third term represents the mismatch due to intensity dependent dipole phase and the fourth term is due to Gouy phase, which arises due to focusing a Gaussian laser pulse for higher harmonic generation. Typical laser intensity of ~10$^{14\text{-}15}$ W/cm^2 is usually

used for the generation of higher harmonics. In this intensity range, there will be significant ionization of medium, which increases the free electron density (n_e) and hence the neutral atom density (n_{at}) reduces. Due to this, the first term of Eq 3.7, (contribution of neutral atom) is very small compared to the second term (contribution of free electrons) and can be safely neglected. The phase imparted by third term (contribution of intensity dependent dipole (IDP) phase) in Eq 3.7, is dependent on laser intensity, which is time dependent. Thus, the contribution of IDP phase imparts time dependent phase to the higher harmonic and may affect its spatial coherence. The fourth term (contribution of Gouy Phase) is dependent on Rayleigh range (z_R) and the position of plasma plume (z) relative to laser focus. There is no time dependent part in this term, which can affect the spatial coherence. It is therefore be inferred from the above discussion that the second and the third term of Eq 3.7, will only affect the spatial coherence of higher harmonic source.

We now discuss our observation on the effect of spatial coherence of higher harmonic source on the position of plasma plume relative to the laser focus position. It can be seen from Eq 3.7 that when plasma plume is placed after the laser focus ($z > 0$), the second and third term counteract each other which leads to the lowering of phase mismatch, which improves the spatial coherence. When the plasma plume is placed before the laser focus ($z < 0$), the second and third term of Eq 3.7 add together, which increases the phase mismatch and deteriorates the spatial coherence property. This explains why the spatial coherence of higher harmonics from plasma plume is different at equal distances on both sides of the laser focus.

I shall now discuss the variation of coherence area (or radius) with harmonic order. The fringe visibility is calculated from the time dependent phase, imparted by the second and third term in Eq 3.7. In the second term, variation in electron density,

and in third term, the variation of laser intensity may affect the spatial coherence. Further, to understand the contribution of IDP phase, (the third term in Eq 3.7), consider two points on the harmonic source transverse to its propagation direction. If intensity of laser beams at these two sampling point are same, the IDP phase imparted to the harmonics generated at these two points will also be same. This will nullify the effect of time-dependent phase imparted by IDP on spatial coherence. Hence, the effect of IDP phase can be safely ignored, when the harmonics are generated close to laser axis and the double slit placed symmetrically [9]. This assumption is valid in the present study, as the slit separation is very small (~100μm) and the distance between the source and slit is sufficiently large (~175 mm). Therefore, the other term viz. the second term of Eq 3.7, can be considered to have dominant effect on the spatial coherence of the higher harmonics. For the calculation of fringe visibility, let us consider the two points (P1 and P2), sampled on the harmonic source in the direction transverse to its propagation, with difference in electron density "δne" between them.

$$n_{e1} = n_e \frac{t}{\tau_p} \quad and \quad n_{e2} = \left(n_e + \delta n_e\right)\frac{t}{\tau_p} \tag{3.8}$$

In Eq 3.8, n_e is background electron density, δn_e *is* the difference in time dependent electron density at two sampled points and τ_p is laser pulse duration. As the laser pulse intensity is varying with time, the electron density will also vary with time. The phase difference between the two points can be expressed as [9,119] (from the second term of Eq 3.7)

$$\Delta\phi \approx \left(\Delta k_{P2} - \Delta k_{P1}\right) \times L_m = \frac{qe^2 \delta n_e L_m}{c\omega_L \varepsilon_0 m_e}, \text{ where } \delta n_e = n_{e2} - n_{e1} \tag{3.9}$$

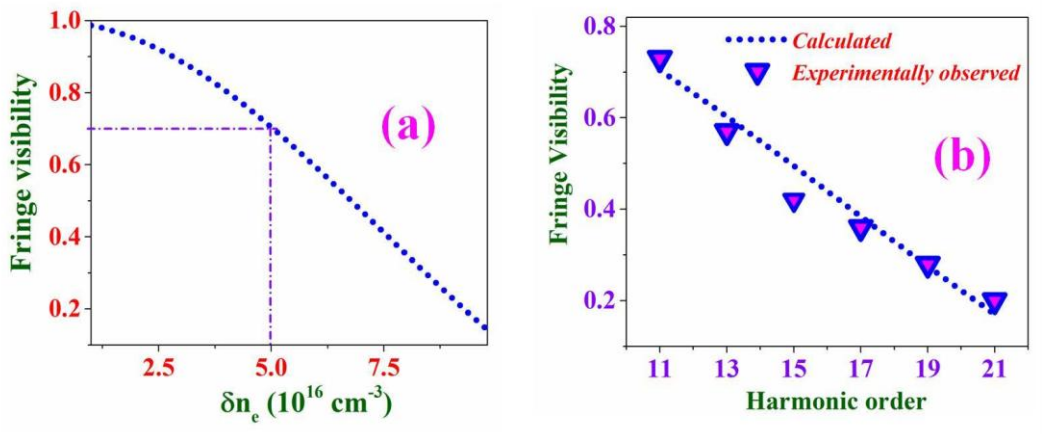

Figure 3.6: *a) the calculated variation of fringe visibility with electron density variation in plume and b) the theoretically calculated variation of fringe visibility of harmonics from 11th 21st order for electron density variation of ≈5×10^{19} cm^{-3}.*

In Eq 3.9, q is the harmonic order, δn_e *is* the difference in time dependent electron density in plasma plume at two sampled points and L_m is the plasma plume length. The complex degree of coherence is calculated using Eq 3.10 [119], which is equal to the experimentally measure fringe visibility.

$$\mu_{12} = \frac{1}{T}\int_{-T/2}^{T/2} \Delta\phi dt = \left| sinc\left[\frac{q e^2 \delta n_e}{2c\omega_L \varepsilon_0 m_e} L_{med} \right] \right| = \text{Finge visibility (V)} \qquad (3.10)$$

The fringe visibility is expressed in terms of the free electron density variation between the two sampled points (δn_e) in Eq 3.10. It can be seen from Eq 3.10, that the background electron density (n_e) is not appearing in the expression for the fringe visibility. The order of magnitude of the free electron density variation (δn_e), which leads to decrease in the fringe visibility to the experimentally observed value, can be estimated using Eq 3.10. The variation is plotted for 11th harmonic order in Fig 3.6a. It can be seen from Fig 3.6a that, at free electron density variation of ~5×10^{16} cm^{-3}, the fringe visibility will reduce to ~0.7 (experimental observed value). The background electron density (n_e) is estimated by a simulation using 1D hydrodynamic code "HELIOS", at pre-pulse intensity ~10^{10} W/cm^2, pulse duration ~ 200 ps, at a delay of

≈ 50 ns, after the plasma plume formation. The electron density (n_e) is estimated to be ~10^{18} cm^{-3} at a distance of ~250 μm away from target surface (optimum condition for the higher harmonic generation) [119]. This shows that even a few percent (≈ 5%) electron density variation, can significantly reduce the fringe visibility (to V ≈ 0.7). Considering this electron density variation, for all harmonic orders from 11^{th} to 21^{st} order, the fringe visibility is calculated using Eq 3.10 and is plotted in Fig 3.6b. It can be seen from Fig 3.6b that the experimentally observed value matches well with the calculated value. Due to absence of the background free electron density (n_e) in theoretically calculated fringe visibility (Eq 3.10), the fringe visibility of the higher harmonics generated from pre-ionized medium viz. plasma plumes should be similar to that of un-ionized medium. On comparison, the spatial coherence of harmonics generated from pre-formed plasma plume and gas jet are found to be similar [9,119].

After optimizing for the spatial coherence of higher harmonic radiation, it is equally important to improve the yield / conversion efficiency of the higher harmonics, maintaining good spatial coherence. This can be achieved by controlling phase mismatch arises due to various factors presented in Eq 3.7. The use of spatial shaping of the driver laser beam used for harmonic generation can be one of the possibilities, which is expected to improve the harmonic yield [114]. The study on the role of spatial beam shaping on conversion efficiency and spatial coherence of the harmonic radiation is discussed in detail in the following section.

3.2 Effect of spatial shaping of laser pulse on higher harmonic generation

In this section, we present our investigation on the effect of laser pulse spatial beam shaping on harmonic yield and spatial coherence of the harmonic radiation generated from carbon plume [103]. We have continued with the carbon plume

harmonics viz. mid order harmonics (11^{th} to 21^{st} order). There are two possible ways to address this issue, the first is to optimize laser and plasma plume parameters viz. optimize the density and length of the plasma nonlinear medium [55,108], use different material plumes (e.g. nanoparticle containing plume etc.) [56, 101], use of multiple plasma jets [120], optimize the plume position relative to laser focus [121], tune laser chirp and spectrum [102] etc. The other possible approach is to shape the laser pulse spatially or temporally and use it for higher harmonic generation [98]. Both the approaches rely on improving the phase matching condition, which will enhance the conversion efficiency of generated harmonics. Theoretical and few experimental studies have shown that the use of spatial shaping (by using axicon-lens combination [122], hard apertures [114] etc.) of laser beam may have significant effect on higher harmonic generation. In the present study, the spatial shaping of the laser beam is performed by placing a variable opening hard aperture in laser beam path. The opening diameter of the aperture is varied and its affect on harmonic intensity is studied.

The reduction in the aperture diameter placed in laser beam path, reduces the laser energy and simultaneously changes the f# of focusing optics (*f/D*, f is focal length and D is diameter of laser beam on focusing optics). Both these factors act together, and affect the focused laser intensity inside the plume. Few experimental studies have been carried out in gas jets where only neutral atoms are present prior to the focusing of ultrashort laser pulse for higher harmonic generation [114, 122]. In case of plasma plume, the scenario is different, as pre-ionization is already present in the medium before HHG. Therefore the plume has free electrons, low charge state ions and neutral atoms, prior to focusing of ultrashort laser pulse for HHG [102]. Therefore, it will be interesting to study, the effect of spatial shaping on higher

harmonic generation from such medium, which is hitherto unexplored. The study also helps to discern the unexplored phase matching processes in plasma plumes, which is crucial to achieve high conversion efficiency with better spatial coherence of higher harmonics [123].

3.2.1 Experimental details

A schematic diagram of the experimental setup is shown in Fig 3.7a. The experiment is carried out using the 10 TW, Ti:Saphhire laser system. A part of uncompressed 200ps laser pulse of energy ~20mJ, is focused on solid graphite surface using 500mm focal length lens, to an intensity $\approx 10^{10}$ W/cm^2. This laser pulse generates plasma plume on solid graphite surface. After an optimized delay of (~50ns), the second part of laser pulse, compressed to ~45fs duration, (energy ~60mJ per pulse, beam diameter ~40mm (1/e^2 diameter)), is focused in the carbon plume using f/6.75 off-axis parabolic mirror (OAPM) to a peak intensity of ~ 10^{15} W/cm^2.

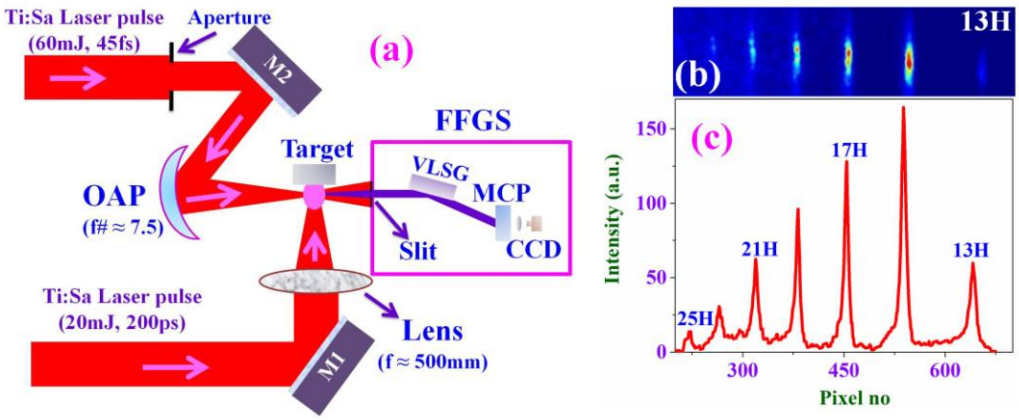

Figure 3.7: a) *A schematic of the experimental used for the study of effect of spatial shaping on higher harmonic generation b) the image showing the recorded harmonic spectrum from 13th to 25th order and c) the line profile of b)*

This ultrashort laser pulse generates higher harmonics from the carbon (graphite) plume. The generated harmonics are analyzed using the FFGS and spatial coherence is measured using double slit. Figure 3.7b shows a typical image of harmonic spectrum from 11th to 21st order generated from carbon plume and Fig 3.7c shows the line profile of Fig 3.7b.

For spatial shaping of laser beam, a variable opening hard aperture (circular aperture) is placed in the path of 45fs laser beam. To ensure a smooth laser beam profile at the OAPM, the aperture is placed at a distance (*d*) large compared to the Fraunhofer distance d_F (where $d_F = 2a^2/\lambda_L$, "λ_L" is the wavelength of the fundamental laser and "*a*" is the aperture size. The laser beam truncation using hard aperture may increase its divergence [124]. The aperturing also reduces the laser beam diameter (*D*), which increases the effective *f-number (f/D)* of *the OAPM*, which will reduce the beam divergence (due to increase in spot size).

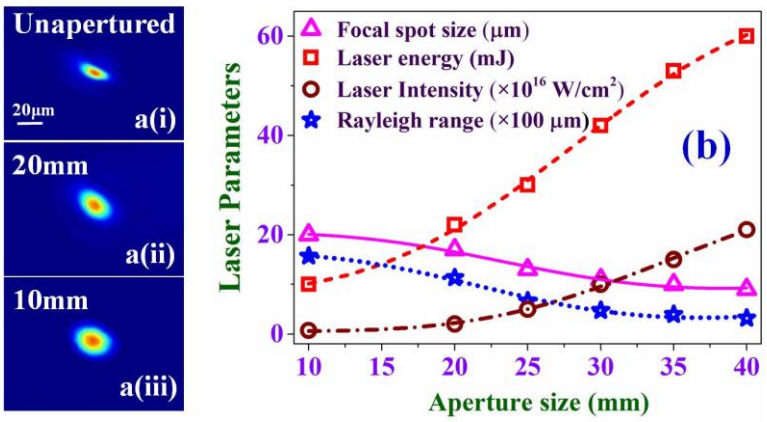

Figure 3.8: *a(i), a(ii) and a(iii)shows the image of focal spot measured at different aperture size and b) the laser energy, Rayleigh range, focal spot size and focused intensity.*

Due to the two counter affects, the estimation of the focal spot is not straight forward. It is therefore essential to experimentally measure the size of focal spot *(ω)*

for different aperture opening diameter. In Fig 3.8a, the image of focal spot at best laser focus ($z=0$) is shown. It can be seen from fig 3.8a (a)(i), (a)(ii) and (a)(iii)), the focal spot size increases with reduction in aperture diameter at the laser focus. Away from the laser focus (~3.5mm), the reverse trend on the variation of focal spot with aperture diameter is observed viz. the focal spot size reduces with increase in aperture diameter. As the hard aperture is placed ~few meters before the focusing optics, the laser beam profile can be taken safely to be Gaussian. With increase in focal spot size (ω_0), the Rayleigh range ($\pi\omega_0^2/\lambda$) increases and simultaneously, the far field divergence ($\theta \sim \lambda/\pi\omega_0$) reduces. This will lead to small laser spot size of the apertured laser beam, as compared to the unapertured laser beam. The variation of laser parameters (laser energy, focal spot size, laser intensity and Rayleigh range) is shown in Fig 3.8b. Due to long distance propagation ($d >> d_F$) of laser beam after hard aperturing, the laser beam profile gets smoothened [125]. Thus, the beam profile of both unapertured and apertured laser beam can be taken to be Gaussian [125]. Taking this assumption, the laser spot size and Rayleigh range of both apertured and unapertured beam is calculated and is shown in Fig 3.8b. It can be seen from Fig 3.8b that, the Rayleigh range (Z_{RA}) increases from 0.32 mm to 1.57 mm, the laser energy decreases from ~60mJ to ~10mJ and the focused intensity at laser focus reduces from ~2×10^{17} W/cm^2 to ~7×10^{15} W/cm^2 by reducing the aperture diameter from ~40 mm to ~10mm. In the present study, the laser energy is reduced by decreasing the flash lamp voltage of the pump lasers of Ti: Saphhire laser system. As the laser system (10TW Ti:Saphhire) is optimized for its operation at 10Hz repetition rate (45 fs pulse duration) at its full energy of ~ 450mJ, which can generate significant heat in the active medium. This shows that, the laser system is already optimized to operate at much higher heat load in the active medium. In the present experiment, ~120mJ laser

energy of the compressed laser pulse (~45fs duration) is used, which lowers the heat load on gain medium (Ti:sapphire crystal). The lowering the flash lamp voltage will further reduces the heat load. Due to this, the laser beam parameter viz. divergence will not be affected significantly and there will no detectable change in spatial coherence of laser as well. Further, the duration of laser pulse at the amplifying stage is ~200ps (stretched pulse), thus the pulse duration will also not change considerably by reduction in the flash lamp voltage.

The photon flux of the higher harmonics is calculated from its spectrum recorded by FFGS, using Eq 2.8. The harmonic yield (HY) is calculated by multiplying the photon flux with photon energy (E_{ph}) and the conversion efficiency (CE) is calculated by dividing the HY by the laser energy (E_L) used for HHG. The CE of the 15^{th} harmonic order is calculated to be ~ 10^{-7} (Eq 2.8), in case of unapertured laser beam [98]. Though the CE derived by above method is not very accurate (error ~ 30 - 40 %); however it is easier to estimate the CE even for the individual harmonic orders using this technique.

3.2.2 The effect on harmonic yield and conversion efficiency

Figure 3.9 shows the variation of CE of 15^{th} harmonic order, at different plasma plume position with respect to the laser focus for 10mm, 20mm, 30mm and 40mm aperture size.

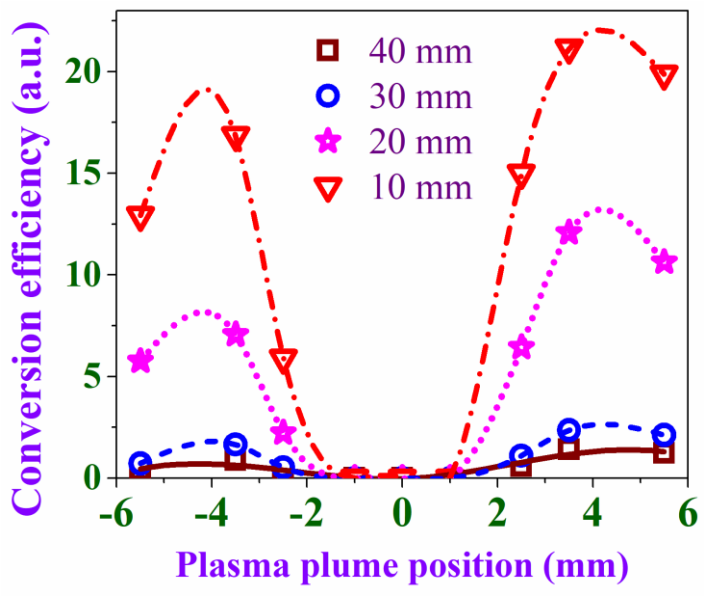

Figure 3.9: *The variation of CE of 15th harmonic order with the plasma plume position relative to the laser focus, for 10mm, 20mm, 30mm and 40mm aperture size.*

It may be noted from Fig 3.9, that the CE peaks at nearly same plasma plume position (~ 3.5mm) for all aperture size and similar behaviour is observed on both side of laser focus.

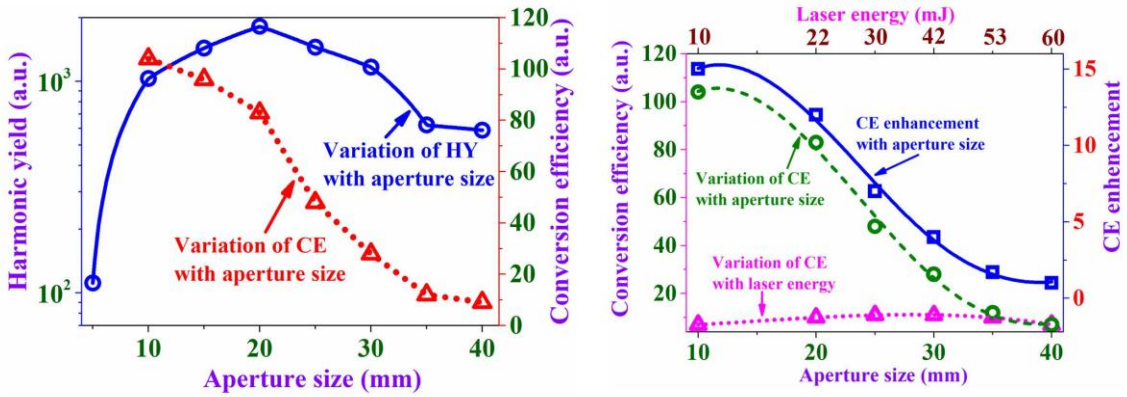

Figure 3.10: *a) The variation of HY (solid blue line) and CE (red dotted curve) with aperture size b) the variation of CE with aperture size (green dash curve), variation of CE with laser energy (magenta dot curve) and the enhancement of CE with aperture size (solid blue curve) for 15th harmonic order.*

The CE and HY of 15th harmonic order at different aperture size are shown in Fig 3.10. With decrease in aperture size, the HY shows a peak at ~20mm aperture size ($1/e^2$ beam diameter of unapertured beam ~ 40mm), whereas the CE increases monotonically. Although, with decrease in aperture size the laser energy decreases, still HY peaks at an optimum aperture size (~20mm), which apparently looks quite interesting. In order to compare the CE on equal footing, the harmonic intensity is compare for both the apertured and unapertured case, at same input laser energy. The variation of CE with aperture diameter and at same input laser energy corresponding to given aperture size and is shown in Fig 3.10b (at z ~ +3.5 mm). The two cases, a) varying aperture size only (the dash green curve) and b) varying the laser energy used for higher harmonics of the unapertured beam (magenta dotted curve) are clearly marked in Fig 3.10b. The enhancement in CE (solid blue curve), due to aperturing (at same energy on the plume), is calculated from the ratio of CE for apertured and unapertured beam (green dashed curve and magenta dotted curve of Fig 3.10b) at same input laser energy used for HHG.

3.2.3 Discussion of the observed results

The experimentally observed variation of CE and HY of harmonic radiation can now be explained, based on the understanding of different factors responsible for it. The theoretical calculation by Ditmire et al [126] has shown the dependence of HY on different laser and nonlinear medium parameters.

$$E_q \;\alpha\; I_L^q \; N_q^2 \; \mathrm{L}_m^2 \;\; \omega_0^2 \,\mathrm{sinc}^2\left(\frac{\Delta k_q L_m}{2}\right) \qquad (3.11)$$

Here E_q is the harmonic yield (HY), q stands for the harmonic order, I_L is the intensity of laser pulse used for higher harmonic generation, L_m is the non-linear medium length

(plasma plume length ~ 600μm in our case), ω_0 is the laser beam radius inside non-linear medium, Δk_q is the wave vector mismatch between the laser and the harmonics, N_q is the density of harmonic emitter and $sinc(x) = sin(x)/x$. The CE (η_q) can be calculated by taking the ratio of harmonic yield and laser energy used for HHG ($\eta_q = E_q / E_L$, where E_L is laser energy used for HHG). It is to be noted from Eq 3.11, that the HY should increase continuously with increase in laser intensity. However, with increase in laser intensity, the ionization of plasma plume medium increases, which leads to depletion of the harmonic generating species (neutral atom/singly charged species) present in the plume and the harmonic intensity starts decreasing. Therefore, it would be detrimental to increase the laser intensity for higher harmonic generation beyond barrier suppression ionization intensity (discussed in chapter 1). The laser intensity is therefore controlled, by moving the plasma plume position away from laser focus. This will increase the laser spot size inside the plume and an optimum intensity for intense harmonic generation can be achieved.

We now try to understand the variation of CE with plasma plume position for different aperture size. It can be seen from Fig 3.8b that changing the aperture diameter, critically affects the spot size, Rayleigh range, and laser intensity. In order to understand the optimum plume position at ~ 3.5mm, we have calculated the laser parameters at this plasma plume position (~3.5mm) using the experimentally measured focal spot size (from Fig 3.8b) and the beam quality parameter [124]. The focal spot size, Rayleigh range, laser intensity at focus (z=0) and z ~ 3.5 mm (plasma plume position for maximum CE) is calculated [98], which is shown in the table-1. It can be noted from table-1, that the intensity of laser pulse at an optimum plasma plume position (z ~ +3.5 mm) is lower compared to the intensity at best focus (z ~ 0) due to increase in the laser spot size. Also, decrease in aperture diameter at optimum

plume position (z ~ +3.5 mm), decreases laser spot size (ω) in the plume. The combined effect of reduction in laser spot size and laser energy with decrease in aperture size, leads to reduction in laser intensity from ~1.5×10^{15} W/cm^2 for unapertured beam to ~7×10^{14} W/cm^2 for 10mm aperture size.

Aperture size (mm)	***Z_R(mm)***	***ω (z=0) (μm)***	***I(W/cm^2) at z=0***	***ω(μm) (z = 3.5mm)***	***I (W/cm^2) at z=3.5mm***
40	0.32	9	25×10^{16}	117	1.5×10^{15}
30	0.48	11	12×10^{16}	103	1.3×10^{15}
20	1.0	16	3×10^{16}	84	1×10^{15}
10	1.57	22	7×10^{15}	70	7×10^{14}

Table-3.1: *Laser parameters with aperture diameter: laser spot size at focus (z~0 and z~3.5mm), Rayleigh range, and laser intensity. The laser spot size is experimentally measured at best focus position (z=0) and the values of other parameters (Z_R, ω and I) are calculated.*

From this one may wrongly infer that lowering the laser intensity prevents the over-ionization in plasma plume, which may lead to enhancement in CE. This possibility may be ruled out, since the CE varies mildly with change in laser energy (hence laser intensity). Also, the laser focal spot size at z ~ 3.5mm decreases with decrease in aperture size, which may lead to decrease in harmonic generation volume (plasma plume length ≈ 600μm is fixed), thus CE should decrease, which is contrary to the experimental observation. The above discussion shows that the last factor "*sinc ($\Delta k\times L_m/2$)"*in Eq 3.11 plays a decisive role in the experimentally observed enhancement in CE and HY. Thus, one needs to have a closer look at the change in phase matching between the laser pulse and the generated harmonics with change in aperture size.

As discussed in chapter one that, the higher harmonics are generated by intense laser field, which induces high order nonlinear polarization in a medium. In this non-linear medium, each atom behaves as a dipole and the total harmonic field is the sum of contribution of all these dipoles along the medium length [5]. Neglecting the absorption in the medium, the harmonic field (in 1D case) can be expressed as

$$E_q\left(l_{med}\right)=\frac{i\omega q}{\varepsilon_0 c}\int_0^{L_m} d_q\left(z\right)e^{i\Delta\phi_q(z)}dz,\ \text{where}\ \Delta\phi_q\left(z\right)=\Delta k_q z \qquad (3.12)$$

In Eq 3.12, the $\Delta\phi_q$ is the phase mismatch between the laser pulse and the q^{th} harmonic order; z is the position of centre of plasma plume from laser focus ($z \sim 0$) and Δk_q is wave vector mismatch between the laser pulse and q^{th} harmonic order. Also, due to small medium length (~600μm), the harmonic generation can be taken to be homogeneous over the plasma plume length.

There are four phase mismatch factors that play crucial role in harmonic generation as discussed in chapter 1. Their combined contribution should be as small as possible (ideally it should be zero) to achieve maximum harmonic yield. The total phase mismatch can be written to be $\Delta\phi_q = \Delta\phi_{at} + \Delta\phi_{el} + \Delta\phi_{IDP} + \Delta\phi_G$. Here, $\Delta\phi_{el}$ and $\Delta\phi_{at}$ is the phase mismatch terms due to free electrons and neutral atoms present in plasma plume, $\Delta\phi_{IDP}$ and $\Delta\phi_G$ is phase mismatch due to IDP phase and Gouy phase respectively. In case of higher harmonics generated from gases, the medium ionization is kept below a critical threshold such that the phase mismatch due to free electron balances the phase mismatch due to neutral atoms, as they are of opposite sign. Further, the optimization of laser geometry is carried out to balance the phase mismatch due to Gouy phase and IDP phase. In pre-formed plasma plumes, due to inherent ionization, significant free electrons are present prior to the focusing of ultrashort laser pulse for HHG. This leads to further depletion of neutral atom density

and therefore, its contribution in phase mismatch can be neglected. Hence, in case of pre-formed plasma plumes, the phase matching should be achieved by optimizing the collective contribution of IDP, free electrons and the Gouy phase. The total phase mismatch along plasma plume length on laser-axis [5] (also known as longitudinal phase mismatch), can be expressed as ($\Delta\phi_{long} = \Delta\phi_{el} + \Delta\phi_{IDP} + \Delta\phi_G$)

$$\Delta\phi_{long} = \frac{qe^2 n_e(z) L_m}{c\omega_L \varepsilon_0 m_e} - \frac{\alpha I_0 z_{RA}^2}{\left(z_{RA}^2 + z^2\right)} + q\tan^{-1}\left(\frac{z}{z_{RA}}\right) \qquad (3.13)$$

In Eq 3.13 L_m is the plasma plume length, n_e is the free electron density, c is the light speed in vacuum, α is the IDP coefficient, m_e is the electron mass, ω_L is the angular laser frequency, ε_0 is permittivity of the free space and z is plasma plume position ($z < 0$ shows the plasma plume position before the laser focus and $z > 0$ shows the plasma plume position after the laser focus).

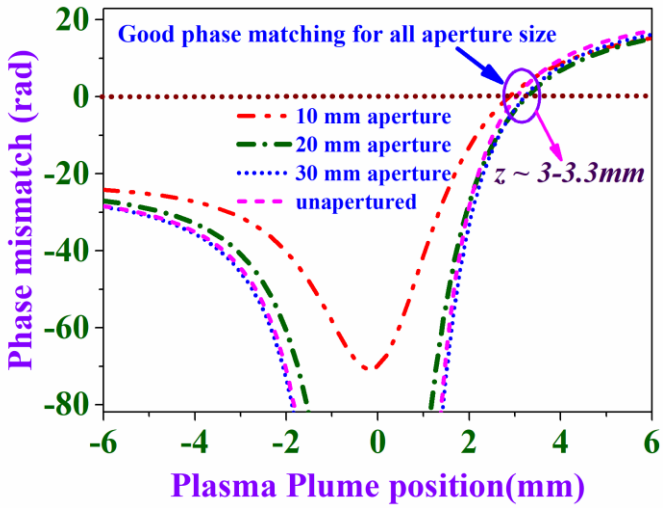

Figure 3.11: *The variation of longitudinal phase mismatch for 15th harmonics order generated from pre-formed carbon plume.*

The longitudinal phase mismatch calculated using Eq 3.13 by using the parameters from table 3 and is plotted for the 15th harmonic order (most intense

harmonics as seen in Fig 3.7c) in Fig 3.11. It may be noted from Fig 3.11, that the phase mismatch is too high close to the laser focus ($z \sim 0$), which results in low CE close to the focus. On moving away from the focus, the phase mismatch reduces, which increases the CE. Also, the phase mismatch is smaller, when plasma plume is placed after laser focus, which leads to asymmetry in CE on both side of focus. This asymmetry in phase mismatch, explains the asymmetric behaviour of CE in Fig 3.9.

It can be further noted from Fig 3.11, that plasma plume position (z) for good phase matching ($\Delta\phi_{long} \sim 0$) doesn't change significantly by changing the aperture diameter (from ~ 40 mm to ~10mm). Therefore the CE should be same at all aperture diameters, which is contrary to the experimental observation (Fig 3.10) viz. it changes significantly with change in aperture size. Thus, further investigation is essential to understand and explain the observed result. In the above calculation, phase matching (Eq 3.13) on laser axis (only 1D) is considered and the phase matching at off-axis points are ignored. As the on-axis phase matching is achieved by optimizing the plasma plume position relative to laser focus, it is essential to explore phase matching at off-axis points. The off-axis phase mismatch is usually small and is often ignored due to its small magnitude. However, in the present scenario, when on-axis phase matching is achieved, the off-axis phase matching may be significant [127] and hence needs a careful analysis. The off-axis phase matching (also known as transverse phase matching) is defined in terms of phase matching between the laser pulse and the higher harmonics at the off-axis points (transverse to the laser propagation direction). It can be expresses as $\Delta\phi_{trans}=\delta\phi\ (\rho, z) - \delta\phi\ (\rho \sim 0, z)$, where ρ is the radial position and z is the longitudinal position of plasma plume. At a given plasma plume position (z), the transverse phase mismatch [5, 127] for a Gaussian laser beam profile, can be expressed as ($\Delta\phi_{trans}= \Delta\phi_{el}+ \Delta\phi_{IDP} +\Delta\phi_{G}$)

$$\Delta\phi_{trans} = -\frac{qe^2 L_m\left(\delta n_e(\rho)\right)}{c\omega_L \varepsilon_0 m_e} + \frac{\alpha I_0 z_{RA}^2}{\left(z_{RA}^2 + z^2\right)} \frac{\rho^2}{\omega^2(z)} + \frac{qk\rho^2}{2R(z)} \qquad (3.14)$$

In Eq 3.14, k is the magnitude of laser wave vector, $R(z)$ is the radius of curvature of laser beam at longitudinal position z and $\delta ne(\rho)$ is the electron density of plasma plume at the radial position ρ. The first term in Eq 3.14 is the phase mismatch due to the radial variation in electron density, the second term represents the radial phase variation of IDP (due to radial laser intensity variation) and the third term is the radial phase variation of the Gaussian beam (like Gouy phase in longitudinal direction). The transverse phase mismatch is calculated using Eq 3.14 at a radial position $\rho \sim 10\mu m$ for different aperture diameters, taking electron density (δn_e) to be ~10% ($\delta n_e \approx 2\times10^{16}$ cm^{-3}). Figure 3.12 shows the off-axis phase mismatch at plasma plume positions (z) ~ +3.5mm and ~ -3.5 mm. It can be seen from Fig 3.12 that, there is monotonic decrease in phase mismatch with decrease in aperture size and it is smaller at z ~ +3.5mm.

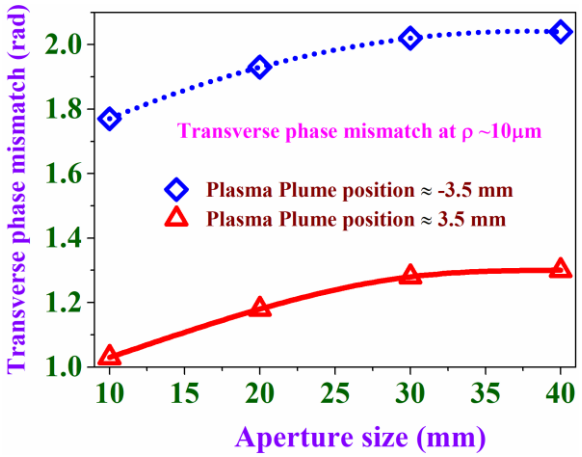

Figure 3.12: *The variation of transverse phase mismatch for 15th harmonics order generated from pre-formed carbon plume at two longitudinal plume positions (z ~ +3.5mm and -3.5mm).*

The improvement in transverse phase matching with aperture diameter can be validated by the measurement of spatial coherence, as any improvement in transverse phase matching should improve spatial coherence. The measurement of spatial coherence will give coherence area (A_c) and on multiplying with the longitudinal coherence length (L_c), gives the coherence volume of harmonic generation viz. $V_c = \pi R_c^2 L_c$, where V_c is coherent volume of harmonic generation and R_c is coherent radius. For a given longitudinal coherence length (by optimizing on-axis phase matching), the coherence volume (V_c) of harmonic generation can be maximized by improving the coherence area (πR_c^2). To study the spatial coherence of higher harmonics, double slit of width 30μm and separation 100μm is used. The double slit interference fringes are recorded for 15th harmonic order for unapertured laser beam and for 15mm aperture size as shown in Fig 3.13.

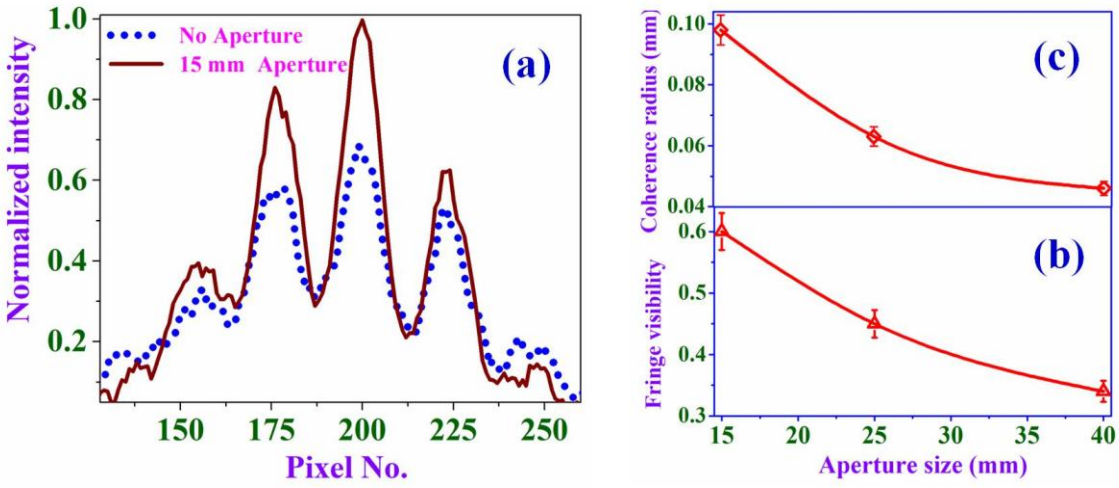

Figure 3.13: *a) The interference recorded for 15th harmonic order using unapertured and using 15mm aperture size laser beam b) the calculated fringe visibility from a) and the coherence radius calculated using Eq 3.6.*

The fringe visibility is calculated from Fig 3.13a using Eq 3.3. The coherence radius is estimated from the experimentally measured fringe visibility using Eq 3.6

i.e. $R_c = d/\sqrt{2\ln(1/V)}$, where R_c is coherence radius, V is fringe visibility and d is slit separation [113, 117]. It is to be noted from Fig 3.13c that, the coherence radius increases by ~ 2.5 times on reducing the aperture diameter from ~ 40mm to ~ 15mm. If the fitted curve in Fig 3.13c is extended to 10mm aperture diameter, the increase in the coherent R_c will be ~ 3, which increases the coherence area ~ 9 ($A_c = \pi R_c^2$). Increase in coherence area ~9 times, will also increase the coherence volume ($V_c = A_c \times L_c$) by ~ 9 times for fixed L_c.

From the above discussion, it can be inferred that at optimum plume position for efficient HHG (z ~ +3.5mm), the coherent harmonic generating volume increases due to improvement in off-axis phase matching. The Eq 3.11 should be modified as it is the coherent volume (V_c), where the emitted harmonic photons from are coherently added and not the whole laser plasma interaction volume [98]. The modified Eq 3.11 (by replacing ω by R_c) can be expressed as

$$E_q \;\alpha\; N_q^2 \;\mathrm{L}_m^2\; I^q \;R_c^2\,\mathrm{sinc}^2\left(\frac{\Delta k L_m}{2}\right) \qquad (3.15)$$

The observed enhancement can now be explained using Eq 3.15. The enhancement in CE [98] can be expressed using Eq 3.15 (considering same input energy for apertured and unapertured laser beam used for harmonic generation and $\Delta\phi \approx \Delta k \times z$) as

$$\varsigma_A \;\approx\; \left(R_{cA}/R_{c0}\right)^2 \;\times\; \left(\mathrm{sinc}\left(\Delta\phi_{long} L_m/2z\right)_A / \mathrm{sinc}\left(\Delta\phi_{long} L_m/2z\right)_0\right)^2 \qquad (3.16)$$

The enhancement in CE at optimum plasma plume position (z ~ +3.5mm, where $\Delta\phi_{long}$ ~ 0), is calculated to be ~9, which is still lower than the experimentally measured value. The difference may be due to considering the variation of phase mismatch homogenously across the plasma plume (in all the above calculations), however slight variation over the medium length can't be ruled out, which adds up additional multiplicative factor in Eq 3.16.

In summary, we have studied the higher harmonic generation from carbon plume, which is an established non-linear medium for efficient mid order harmonic (11^{th} to 21^{st} order) generation, with a cutoff at 29^{th} order. The laser and plasma parameters are optimized to generate intense harmonics and its spatial coherence property is studied. The fringe contrast > 0.7 is observed, which shows high spatial coherence of the harmonic source, generated from plasma plume. A theoretical calculation is used to explain the experimentally observed variation of spatial coherence with harmonic orders. The study was extended to improve the harmonic yield and conversion efficiency by using the spatially shaped laser beam for HHG. The shaping was done by using a hard circular aperture and its effect on yield and conversion efficiency is investigated. The yield maximizes at an optimum aperture size (~20mm), whereas the CE was found to be higher at small aperture size (~10mm). A theoretical formulation based on phase matching between laser and harmonic is developed to explain the experimental observation. The role of off-axis phase matching was found to be crucial, which increases the harmonic generating volume, which is also supported by increase in spatial coherence at small aperture size. The increase in the coherent volume of HHG (V_c), leads to enhancement in conversion efficiency. The study has provided an estimate of optimum parametric conditions, to generate an intense harmonic source with high yield alongwith high spatial coherence.

Chapter 4:
Higher Harmonic Generation from Gas Cell

The generation of intense harmonic radiation from non-linear medium is of paramount interest due to its application in wide area of research viz. In material science [15], in the study of time resolved ultrafast electron dynamics in materials [128] etc. For all these applications, the photon flux is a main concern, which limits its applications further. In the previous chapter, the study on generation and optimization of higher harmonic radiation from pre-formed carbon plume has been presented and the results on maximize of conversion efficiency and yield is discussed [98]. High photon flux is desirable for practical application of this source, in many other research areas [13, 116]. The high conversion efficiency (at smaller laser energy) is also desirable to generate harmonic source at high repetition rate, as the laser energy available with the high repetition rate lasers are very small (~few mJ for kHz laser system to ~few μJ for MHz laser systems) [129]. The issue of low conversion efficiency of HHG from plasma plumes has been addressed by few groups, by adopting several new techniques viz. use of extended plume medium [107, 108], use of quasi phase matching in plasma plume [120] etc., and further enhancements in the conversion efficiency is reported. However, the pre-ionization in the plasma plume medium remains a major concern, which increases phase mismatch and limits maximum achievable photon flux of higher harmonics.

One of the possible approaches to address the issue of low CE is issue to use nonlinear medium, where there is no pre-ionization present viz. inert gases. The study on HHG has also been investigated in inert gas jets, which consists of neutral atom, thereby can provide good harmonic flux [130, 131]. However, the gas jets have few drawbacks, viz. small medium length, small repetition rate operation etc. The gas cell

may be a good alternative to gas jet, as its medium length can be easily varied and it can be used at high repetition rate as well. The gas cell is therefore selected and possibility to generate efficient harmonics at high repetition rate (1 kHz) has been explored. The experimental investigation on HHG from inert gas filled cells is presented in this chapter in detail.

The study is confined to three different inert gases (viz. argon, neon and helium) filled in gas cell of different lengths (5mm, 15mm, 25mm and 35mm). The parametric optimization is carried out to maximize the photon flux in different spectral range viz. photon energy from ~ 25eV to ~150eV. The spectral characteristics of the higher harmonic generated from argon filled cell is also investigated using single colour (λ~800nm) and two colour laser fields (λ~800nm + 400nm). The study is carried out by in the gas pressure range from ~20mbar to ~120mbar. With increase in gas cell pressure, the broadening and splitting is observed in case of single color laser pulses generated harmonics, which is absent in two color case. The splitting in the spectrum may be attributed to the presence of different electron trajectories responsible for harmonic generation [132-135]. Further, the spatial coherence characteristics of higher harmonics for the two cases viz. single color and two colour, is studied using double slit experiment. It was found that the fringe visibility of harmonics is higher, when they are generated using two color laser pulses, as compared to the single color case. Further, the parametric optimization of laser and gas cell is performed to improve the photon flux and the cutoff order of higher harmonics. The photon flux of ~ 250nJ per laser shot is found in argon filled cell for 31^{st} harmonic order, whereas maximum harmonic cutoff exceeding 99^{th} order (λ ~8nm) is recorded in Helium filled gas cell. Although, the grating in FFGs is used in first diffraction order configuration, however on recording small wavelength (~8nm), it

was noticed that the spectrum is flooded with many spectral lined. It is therefore import to calibrate the FFGS precisely, as the VLS grating of FFGS can diffract in higher diffraction also. The FFGS is calibrated using parametric fitting technique using a known spectral line (Al L-Edge @ λ~17.1nm). After calibration, it was found that, in the FFGS spectrum, apart from first diffraction order, higher diffraction orders were also present. The diffraction order is identified and is used to estimate the efficiency of VLS grating of FFGS in higher diffraction orders, in the wavelength range from ~ 8nm to ~ 20nm [96].

4.1 Experimental setup

The experiment is carried out using a kHz Ti: Sapphire laser system operating at a maximum repetition rate of 1 kHz (see section 2.1.2). Figure 4.1 shows a schematic of the experimental setup used in the work, presented in this chapter. High order harmonic radiation was generated by interaction of 45 fs Ti: Saphhire laser pulse with inert gas filled cell of 5mm diameter and different lengths viz. 5mm, 15mm, 25mm and 35mm. The gas cell is vacuum sealed (using 'O' rings) by mounting a 1mm thick aluminium sheets on the both sides the cell. The laser beam is focused at the centre of gas cell using a plano-convex lens of focal length ~750mm (f# 42). The laser pulse itself drill holes on the aluminium covers, placed on both side of gas cells. The peak laser intensity at the centre of gas cell is calculated to be ~2×10^{15} W/cm^2 and can be varied by moving the lens position with respect to gas cell. The harmonic generated from the gas cell, follows the path of the laser beam and comes out of the cell through the laser drilled holes. These harmonics are dispersed and detected using FFGS. As, MCP is used as a xuv detector in FFGS, which required high vacuum (background gas pressure ~10^{-6}mbar) for its safe operation, a differential pumping is provided in the MCP chamber.

The higher harmonic generated from different gases covers large spectral range (UV to soft x-ray). This requires shifting of the spatial position of MCP in spectral dispersion direction, which is done by mounting MCP on a bellow flange. The FFGS is then calibrated for photon flux as well as for wavelength precisely (see section 2.3.1). In order to identify the harmonic orders, a 150nm thick aluminium filter (L-edge at λ≈171 Å) is placed in the path of harmonic radiation. The aluminium filter serves two purposes. First, it blocks the unconverted IR laser light and second, its absorption edge at 17.1nm (L-Edge), which is close to 47^{th} harmonic order is Ti: sapphire laser wavelength (8000 Å / 171 Å ≈ 47), facilitates us to mark the 47^{th} harmonic order in the spectrum viz. all the harmonics above 47^{th} order are blocked and the lower harmonic order ($\leq 47^{th}$ order) are transmitted through the filter.

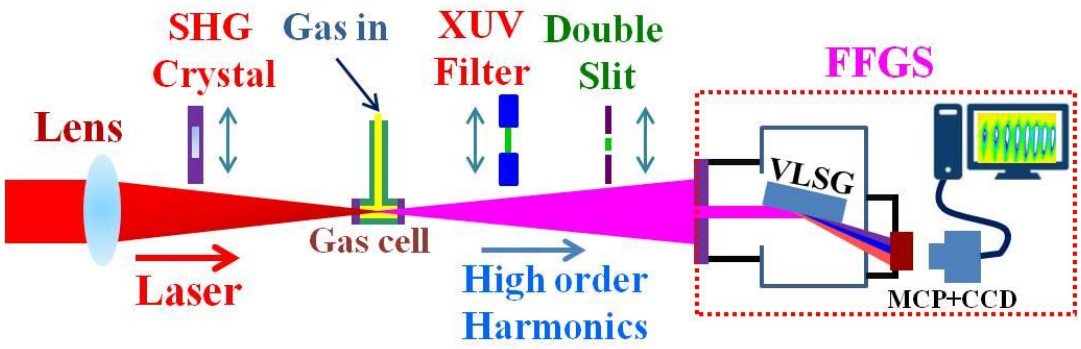

Figure 4.1: *A schematic of experimental setup for higher harmonic generation from gas cell.*

To generate two color laser pulses for the experiment, a SHG crystal (BBO crystal, thickness≈100μm) is inserted in the focused laser beam path. For spatial coherence measurement, a double slit is placed in the path of harmonic beam just before the slit of FFGS. Figure 4.2 shows harmonic spectrum, recorded from argon and neon filled gas cells.

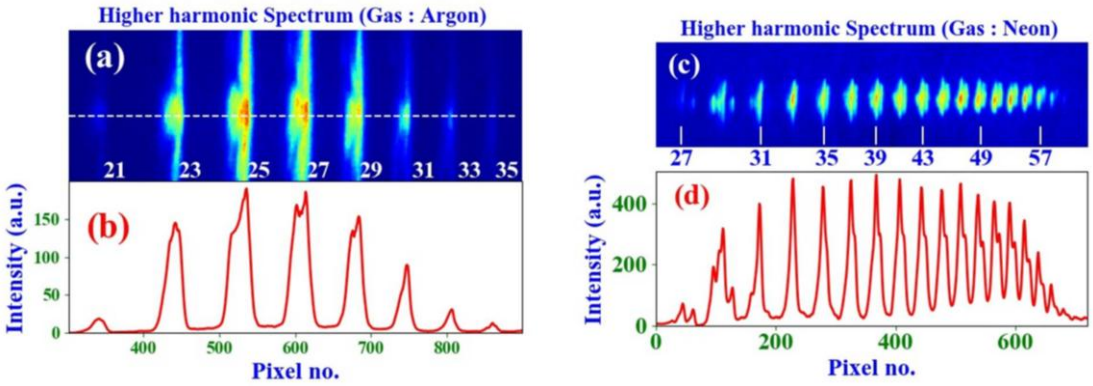

Figure 4.2: *A typical spectrum of higher harmonics from argon and neon filled gas cell.*

Figure 4.2a and Fig 4.2c shows the harmonic spectrum recorded in argon and neon gas respectively. Figure 4.2b and Fig 2d shows the line profile of 4.2a and Fig 4.2c respectively. It can be seen from Fig 4.2 that the in the harmonic spectrum from argon gas, 21^{st} to 35^{th} order is visible, whereas in neon gas 27^{th} to 61^{st} order is visible.

4.2 Parametric optimization and photon flux

The generation of efficient harmonic radiation in wide spectral range, is a major crux of the present research work. Three different inert gases viz. argon, neon and helium are used for HHG. Four different gas cell lengths viz. 5mm, 15mm, 25mm and 35mm, are explored. Variation of intensity of higher harmonic from argon (31^{st} order), with gas pressure and position of gas cell with respect to laser focus, at four different gas cell lengths is shown in Fig 4.3. It can be seen from Fig 4.3 that the peak harmonic intensity is almost similar for the gas cell length 5mm and 15mm and it reduces for the higher gas cell lengths. Also, the optimum parameter condition for maximum harmonic intensity is significantly different for different gas cell length.

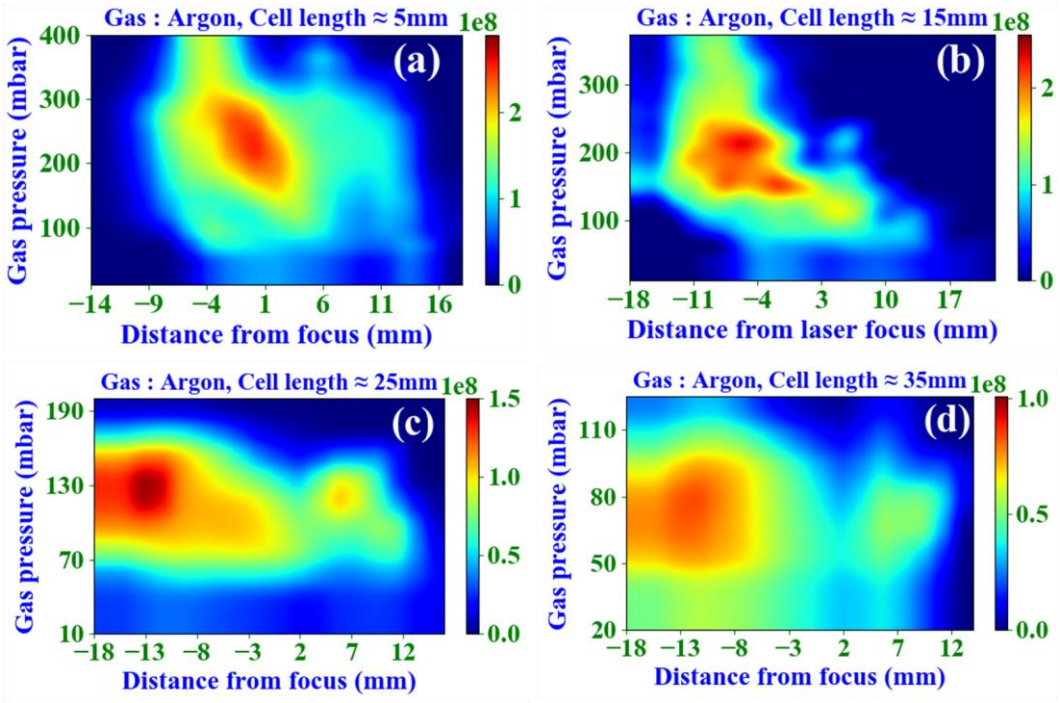

Figure 4.3: *Variation of harmonic intensity with pressure and laser focusing condition for gas cell length a) 5mm, b) 15mm, c) 25mm and d) 35mm.*

Table 4.1 shows the optimum focal position and gas pressure for maximum intensity of harmonics from argon, at the four different length of gas cell. It can be seen from table 4.1 that with increase in gas cell length, the optimum gas pressure decreases and the optimum gas cell position moves away from the laser focus.

Gas cell length	***Optimum gas pressure (mbar)***	***Optimum focal position (mm)***	***Harmonic intensity (a.u.) (error ≈ ±5%)***
5	300	0	265
15	275	-4	260
25	250	-12	150
35	150	-16	90

Table-4.1: *Optimum parameter for maximum harmonic intensity for harmonic generation from argon filled gas cell (for 31st harmonic order).*

Gas cell length	*Optimum gas pressure (mbar)*	*Optimum focal position (mm)*	*Harmonic intensity (a.u.) (error ≈ ±5%)*
5	225	-2	270
15	200	-8	150
25	130	-14	70
35	80	-15	25

Table-4.2: *Optimum parameter for maximum harmonic intensity for harmonic generation from neon filled gas cell (for 41st harmonic order).*

Gas cell length	*Optimum gas pressure (mbar)*	*Optimum focal position (mm)*	*Harmonic intensity (a.u.) (error ≈ ±5%)*
5	450	0	90
15	350	-2	30
25	300	-8	10
35	175	-12	5

Table-4.3: *Optimum parameter for maximum harmonic intensity for harmonic generation from helium filled gas cell (for 49th harmonic order).*

Similar observations have been recorded in case of neon and helium filled gas cells. Table 4.2 and 4.3 shows the harmonic intensity of 41st and 47th harmonic orders generated from neon and helium filled gas cells respectively. It can be seen from table 4.1 to 4.3 that for all gases, the optimum gas pressure decreases with increase in cell length. In case of neon and helium, the optimum gas cell length is 5mm, where overall maximum harmonic intensity is observed.

The observation can be understood from the propagation of higher harmonic beam in nonlinear medium. The number of photons per unit area per unit time can be expressed using Eq 1.22, which takes into account the effect of absorption and phase matching. If absorption in medium is ignored, the Eq 1.22 will reduce to

$$N_{out} \propto \left(\rho L_{med}\right)^2 A_q^2 \left(\frac{\sin\left(\Delta k L_{med}/2\right)}{\left(\Delta k L_{med}/2\right)} \right)^2 \quad (4.1)$$

Where Δk is wavevector mismatch, L_{med} is length of nonlinear medium, ρ is atomic density of medium. The wavector mismatch (Δk) has contribution from four factors. The neutral atom dispersion ($\Delta k_{at} \propto n_a$, where n_a is atomic density of medium) and free electron dispersion ($\Delta k_{at} \propto \eta n_a$, where η is ionization fraction, which can be calculated using Eq 1.12) is dependent to the medium density and on laser intensity used for HHG. The Gouy phase (Eq 1.33) and IDP phase term (Eq 1.35) is dependent on laser intensity and the position of non-linear medium with respect to laser focus. By optimizing the laser focus position, the combined effect of IDP and Gouy phase is minimized, whereas the combination of atomic dispersion and free electron dispersion term is minimized by tuning the medium density and laser intensity.

The above observed result can now be explained (using Eq 4.1 and Eq 1.22). It can be seen from Eq 4.1 that the photon flux of the harmonics, increases quadratically with increase in the atomic density and medium length. However, with increase in atomic density and medium length (beyond absorption length), the absorption of harmonics increases (Eq 1.22 and Eq 1.23). Thus, there is an optimum value of both these parameters, which maximize the photon flux. Further, tuning the laser intensity by moving the gas cell position away from laser focus, leads to optimization of the Gouy and IDP phase terms (Eq 1.33 and Eq 1.35). The optimization of phase matching, viz. reduce the overall wavevector mismatch (Δk), improves the photon flux (from Eq 4.1). In summary, the optimizing the gas cell length, gas cell position and gas pressure leads to enhancement of photon flux. Now question arises, that why the optimum condition should be different for different inert gases. This can be understood using Eq 1.12, which shows that the fractional ionization depends on the

ionization potential of gas atom. For the same laser intensity, the fractional ionization is different for different gas atom, which changes the phase matching condition. Also, the absorption length is different for different species, due to difference in photo-ionization cross section (Eq 1.23) at photon energy of given harmonic order. Hence, the phase matching condition for harmonic generation changes significantly for different gas species.

After optimizing for the harmonic intensity, it is essential to experimentally measure the photon flux/ yield generated from these cells in different inert gases. The photon flux (discussed in chapter 1) is measured using an AXUV diode (Make: IRD, Model: AXUV20HS1). The AXUV diode is covered with an Al filter (thickness ~150nm) and inserted in the harmonic beam path and the harmonic radiation energy is determined (using Eq 2.9). Under same parametric condition, the harmonic spectrum is recorded using FFGS and the relative spectral intensity of the harmonics is measured. From the above two measurements, the FFGS is calibrated in terms of number of photons per digital count (also known as sensitivity of FFGS) to calculate the photon flux of all individual harmonic orders. For the calculation of FFGS sensitivity for individual harmonic order, the grating reflectivity (of FFGS), the fraction of harmonic beam area intercepted by the AXUV diode and photon energy of individual harmonics are taken into account.

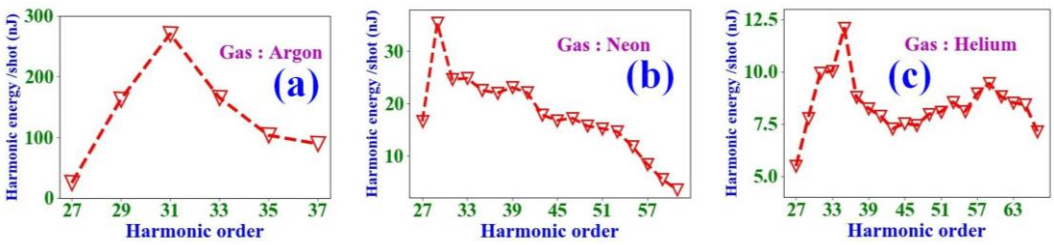

Figure 4.4: *Maximum harmonic yield measured from a) argon (cell length ~15mm) b) neon (cell length ~5mm) and c) helium (cell length ~5mm) filled gas cells respectively.*

Maximum harmonic yield (harmonic energy per laser shot) after optimizing all laser and gas cell parameters, in case of argon, neon and helium is shown in Fig 4.4. It can be seen from Fig 4.4 that the maximum harmonic yield is observed in case of argon filled cell and it is ~250nJ per laser shot for 31st harmonic order. In case of neon and helium, nearly constant harmonic yield of ~20-25nJ for 31st to 43rd harmonic orders and ~8nJ to 10nJ for 35th to 63rd harmonic order respectively is observed. The conversion efficiency for individual harmonics is calculated to be ~10^{-4} for argon, ~ 10^{-5} for neon and ~10^{-6} for helium respectively and for an input laser energy ~4.5mJ in gas cell). The measured yield is similar to the highest reported yield so far, in the literature [136-138].

4.3 Spectral properties and spatial coherence of harmonics from argon gas

The spectral characteristics of the higher harmonic radiation depend on the laser intensity as well as on the gases used for HHG. The time dependent harmonic phase is contributed mainly by two factors [139], which can be expressed as

$$\phi_q(t) = \phi_q^{IR}(t) + \phi_q^{dipole}(t) \tag{4.2}$$

The instantaneous frequency of q^{th} harmonics can be written as

$$\omega_q(t) = \omega_q + \frac{\partial \phi_q(t)}{\partial t} = \omega_q + \Delta\omega_q^{IR}(t) + \Delta\omega_q^{dip}(t) \tag{4.3a}$$

$$\omega_q(t) = \omega_q + \frac{\pi q}{n_c \lambda^{IR}} \int_0^{L_{med}} \frac{\partial n_e(t)}{\partial t} dz + \alpha_q^i \frac{\partial I(t)}{\partial t} \tag{4.3b}$$

Where α_q is dipole phase coefficient for q^{th} harmonic order (α_{short} ~1 to 5×10^{-14} cm^2/W and α_{long} ~ 20 to 25 ×10^{-14} cm^2/W, the superscript i correspond to i^{th} electron trajectory (viz. $i=1$ for short trajectory and $i=2$ for long trajectory), the n_e is free electron density of medium and n_c is critical density at laser wavelength. It can be

noted from Eq 4.3 that the selection of electron trajectory effect the harmonic spectrum and it may be significantly different for the case of short and long trajectories [135,141]. From Eq 4.3b, it may be inferred that the harmonic generated from the short trajectory is spectrally narrow as compared to the long trajectory (as $\alpha_{long} >> \alpha_{short}$). Apart from the change in the spectrum, the generation of harmonics from different trajectory have different divergences [141-143]. The radial phase of the harmonics generated using different trajectory [139] is written as

$$\phi_q(r) \approx -\alpha_q^i I(r) \approx -\alpha_q^i I_0 \exp\left(-\frac{2r^2}{\sigma_0^2}\right) \tag{4.4a}$$

$$\phi_q(r) \approx -\alpha_q^i I_0 + \frac{2\alpha_q^i I_0}{\sigma_0^2} \mathrm{r}^2 \quad (\text{for r} << \sigma_0) \tag{4.4b}$$

Where σ_0 is the radius of the laser beam waist. It can be noted from Eq 4.4a and Eq 4.4b that the radial phase variation is different for the harmonics generated using two different trajectories, which may lead to generation of harmonics with two different divergences [143]. This helps in identifying the contribution of different electron trajectory, from the far field profile of higher harmonics. Several techniques have been proposed and implemented, to identify and control the selection of particular trajectory viz. using shaped laser beam [144], using two color laser fields [133, 145], changing the focal position [146] etc. It is also shown that, by focusing a laser pulse after the non-linear medium, one can get the contribution of both short and long trajectory viz. on-axis phase matching for short trajectory harmonics and off-axis phase matching for the long trajectory [146]. The relative weightage of these electron trajectories in HHG are also estimated [134, 142].

In this section, we present our results on the spectral study of harmonics generated from argon filled gas cell using single color (λ≈800nm) and two color (λ ≈ 800nm+400nm) laser fields. The 45fs laser pulse is focused just after the gas cell to an

intensity of ~2×10^{14} W/cm^2 and the harmonics from both long and short trajectories are observed (see Fig 4.2a). It is important to note from Fig 4.2a, that the harmonic spectrum from argon gas, has different spectral characteristics near centre and in off-centre region. The presence of two groups of harmonics viz. with two different divergences can be noticed from Fig 4.2a. The presence of two groups of harmonics may be attributed to two different electron trajectories, as evident from the above discussions. The low divergence harmonics may be generated by the short trajectory and the large divergence harmonics by the long trajectory. The effect of gas cell (length ~ 15mm) pressure on the harmonic spectrum is studied using single colour as well as using two color laser pulses (see Fig 4.5).

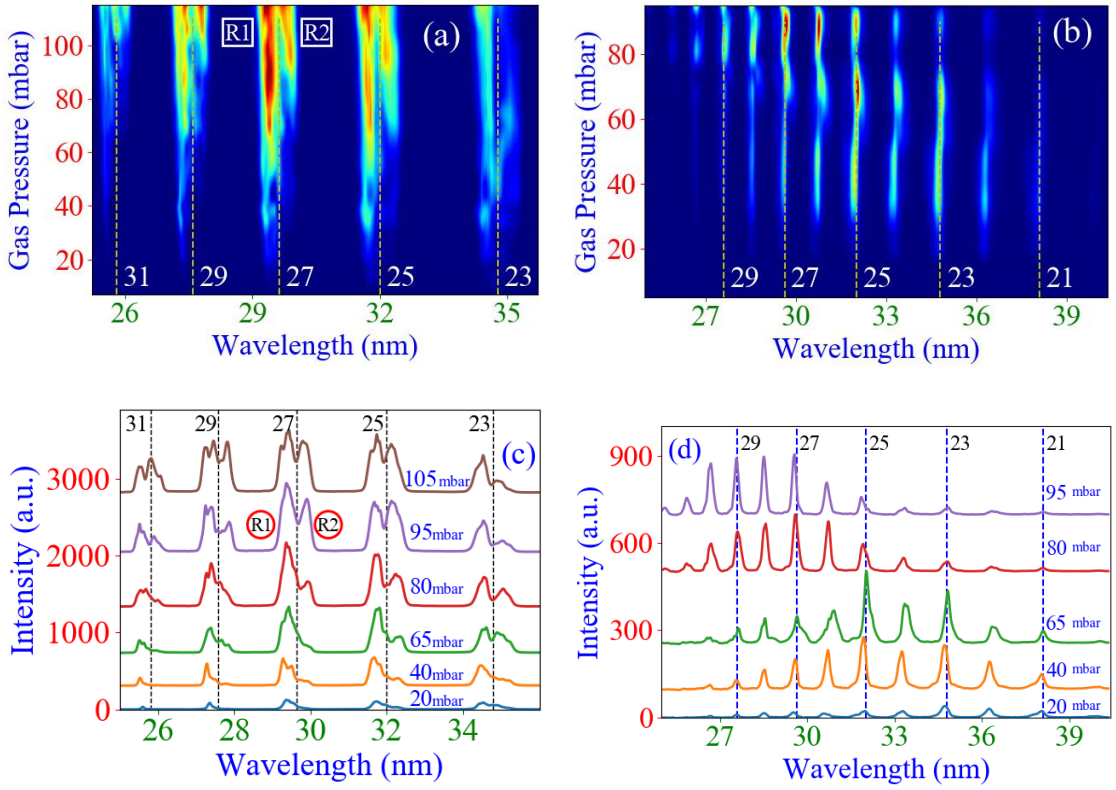

Figure 4.5: *Variation of harmonic spectrum with gas pressure for harmonics generated in argon gas using a) single color laser pulse (λ~800nm) and b) using two color fields (λ~ 800nm + 400nm), c) and d) shows the line profile of a) and b) respectively.*

Figure 4.5 shows the change in the harmonic spectrum with change in gas pressure for 21st to 35th harmonic order. It can be seen from Fig 4.5a that with increase in the gas pressure, the harmonic spectrum starts broadening and beyond 60mbar, it starts splitting. Figure 4.5c shows the lineout of harmonics from Fig 4.5a. It is to be noted from Fig 4.5c that the two splitted harmonics have different spectral widths as well as different spectral shifts with increase in gas pressure viz. the higher divergence harmonics are blue shifted and small divergence harmonics is red shifted. In case of HHG using two colour laser pulses ($\lambda \approx 800nm+400nm$), the splitting is not observed even at higher gas pressures (see Fig 4.5b). The lineout of Fig 4.5b is shown in Fig 4.5d, which shows the absence of splitting and spectral shift with increase in gas pressure.

The spectral shift of the harmonic spectrum can be explained by considering the influence of time dependent IDP phase on harmonic spectrum. The instantaneous generation of harmonic frequency can be expressed using Eq 4.3. The third term (IDP term), depends of the rate of change of laser intensity with time viz. if rate is positive ($dI/dt > 0$), it leads to blue shift, whereas for negative rate ($dI/dt < 0$), there is red shift. Further, the trajectory resolved phase matching simulation has shown that, for the long trajectory phase matching is better on leading edge of laser pulse, whereas for the short trajectory phase matching is better on the trailing edge [143]. Therefore, the harmonic generated using long trajectory is blue-shifted, whereas the harmonic generated using short trajectory is red shifted. Now question arises, that how laser intensity is affected by change in the gas pressure of gas cell. The use of high intensity laser pulse for HHG also ionized the medium and leads to generation of free electrons. The presence of free electron density in the medium leads to various processes viz. generates chirp in the laser beam, ionization induced defocusing (the density for

significant defocusing effect, $n_e \approx \lambda N_c/2z_R$, *for 800nm* wavelength the $n_e \sim 2\times10^{15}$ cm^{-3} [147]) etc, which reduces the laser intensity. As the peak laser intensity is close to BSI (see section 1.3.2), small reduction in laser intensity leads to generation of higher harmonics on both sides (leading and trailing edge) of laser pulse. The temporal change in the laser intensity (due to change in gas pressure), leads to different spectral shift of the two splitted parts (due to change in *dI/dt*). In case of two color laser pulse, the laser intensity used for HHG, is itself low (due to second harmonic conversion as well as generation of B integral distortion [148] in the SHG crystal), which reduces ionization of medium (thus n_e also reduces). Thus, "*dI/dt*" doesn't change significantly with gas pressure and no spectral shift is observed.

At this juncture, it will also be interesting to study the coherence property of these spectrally splitted harmonics. Few studies have shown that the harmonics generated from the short trajectory have higher temporal coherence [10].

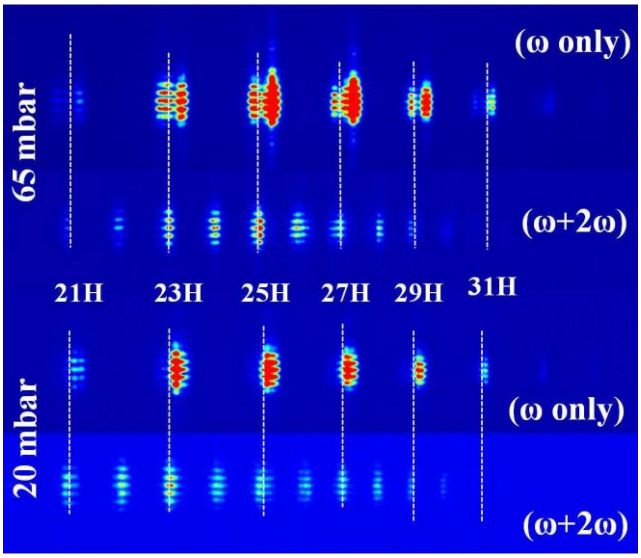

Figure 4.6: *The interference fringes recorded at 20 mbar and 65 mbar gas pressure for harmonic generated using single and two color laser field.*

We have studied the spatial coherence property of the spectrally splitted harmonics, which is hitherto unexplored. Figure 4.6 shows the interference fringe of the harmonics generated using single and two color laser fields at two different gas pressures viz. 20mbar and 65mbar. The interference fringes of the two splitted components are clearly visible at 65mbar, which is absent at 20mbar pressure. The contribution of the two trajectories is identified, based on difference in the divergence and the spectral width of the harmonics. The fringe visibility is calculated using Eq 3.3, and is shown in Fig 4.7. Figure 4.7 shows the experimentally measured fringe visibility for 21st to 31st harmonic orders for gas cell pressures of 20mbar, 40mbar, 65mbar, 80mbar and 95mbar respectively.

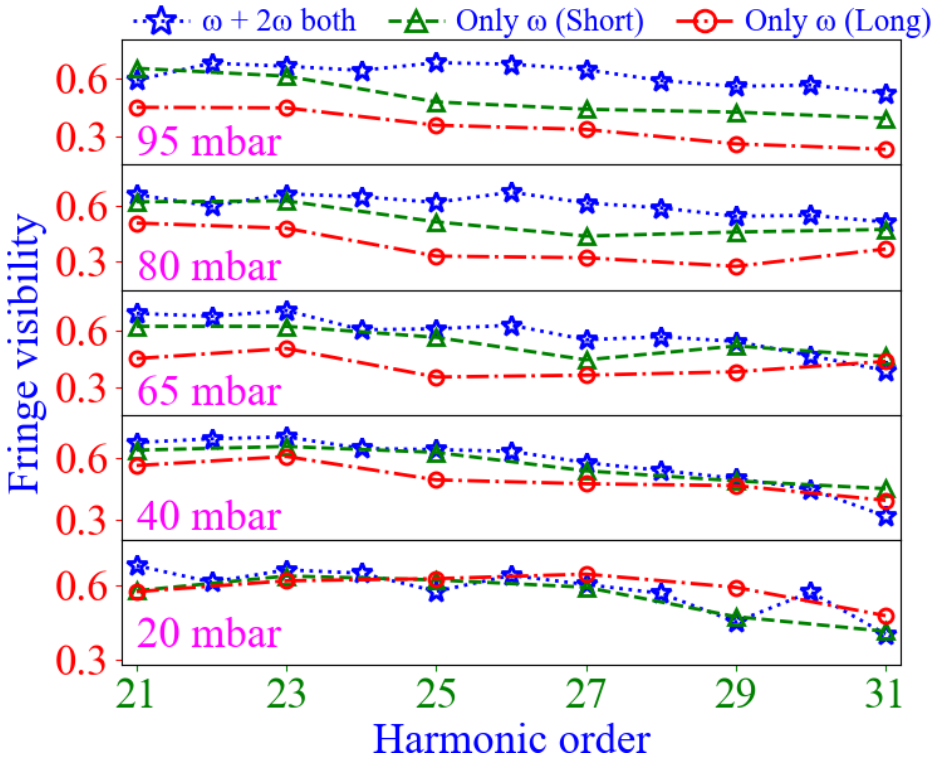

Figure 4.7: *The fringe visibility for the harmonics generated using single colour (two splitted components) and two colour laser pulses for gas pressure from 20mbar to 95mbar. The symbol "star" is fringe visibility of higher harmonics generated using two color, the "up-triangle" symbol for short trajectory harmonics and "circle" for long trajectory harmonics.*

It can be seen from Fig 4.7 that the fringe visibility of harmonic generated using two color laser field is higher than the single color generated harmonics. For single color case, the fringe visibility of the harmonic generated using short electron trajectory is higher as compared to the long trajectory harmonics. It is important to note from Fig 4.7 that the fringe visibility doesn't change significantly by changing in gas pressure for harmonic generated using two color laser pulses; however, it changes significantly for single colour laser in the splitted part for all harmonic orders (from 21^{st} to 31^{st} order). The fringe visibility remains high ≈ 0.7 for two colour laser case, whereas it reduces for the short trajectory harmonics from 0.6 to 0.45 and for the long trajectory, from 0.6 to 0.3 by changing gas pressure from 20mbar to 95mbar.

In order to understand the observed behaviour in the fringe visibility, an analytical theory is developed. The basics theory of spatial coherence is already discussed in section 3.1. The spatial coherence is mainly affected by the factor that impart time dependent phase in transverse direction to harmonic beam propagation. In HHG there are two dominant factors, which may affect its spatial coherence. These are time dependent free electron density in non-linear medium and the IDP phase. In the previous chapter, we theoretically calculated the fringe visibility, by considering the electron density variation, which is a dominant factor in case of plasma plumes. However, in the present scenario, we also need to consider the effect of IDP. The fringe visibility is calculated in similar way as Eq 3.10, by adding the contribution of IDP term (assuming linear intensity variation between the two transverse points similar to Eq 3.18), the fringe visibility is estimated (taking the value of Δk_{IDP} from Eq 3.7) to be

$$\text{Finge visibility (V)} \approx \left| sinc\left[\frac{q e^2 L_{med}}{2c\omega_L \varepsilon_0 m_e} \delta n_e - \frac{2z\, z_R^2 \alpha_q L_{med}}{\left(z^2 + z_R^2\right)} \delta I_0 \right] \right| \qquad (4.5)$$

Where L_{med} is length of gas cell, δne is electron density fluctuation at the two points, ω_L is laser frequency, q is harmonic order, z is position of gas cell relative to laser focus (~-15mm), Z_R is the Rayleigh range of focused laser beam, δI_0 is the laser intensity fluctuation between the two points, α_q is the IDP coefficient for the short and long trajectory for a given harmonic order. At the gas cell position (z = -15mm), Z_R ~ 3 mm, L_{med} ~ 15mm, the fringe visibility calculated in Eq 4.5 can be rewritten as

$$V \approx \left| sinc\left[8.65 \times q \times \delta n_e \left(10^{18} cm^{-3}\right) + 0.02 \times \alpha_q \left(cm^2 / W\right) \times \delta I_0 \left(W / cm^2\right) \right] \right| \qquad (4.6)$$

The fringe visibility can be calculated for harmonic orders from 21st to 31st using Eq 4.6 by taking appropriate parameter values. For this, it is important to estimate the size of higher harmonics beam at the exit of gas cell. It can be seen from Fig 4.2a that the beam size of short trajectory harmonics is much smaller than the long trajectory harmonics viz. the beam size of 23rd harmonics at the exit of gas cell is ~75 μm and ~15μm (assuming the harmonics are generated at the centre of gas cell) for long and short trajectory harmonics respectively. Due to this, the electron density fluctuation experienced by long trajectory harmonics will be higher than short trajectory harmonics. To estimate the density fluctuation, the background free electron density should be estimated and the density fluctuation can be safely taken to be ~ 5% to 10% of the background density [119]. The maximum background electron density, which will lead to generation of efficient harmonics can be calculated using the relation $\Delta k \times L_{med} \sim 2\pi$ [9], which is calculated to be ~ 2 to 3×10^{16} cm^{-3}. The fringe visibility is fitted by taking the density fluctuation to be ~ 10% of the background density viz. for 23rd harmonic order, δne ~2.5×10^{15} cm^{-3} for short trajectory harmonics, δne ~3×10^{15} cm^{-3} for long trajectory harmonics for single color case and δne ~2×10^{15} cm^{-3} for the two color case. The maximum fluctuation in laser intensity

is taken to be ~ 5% of the peak laser intensity (~10^{13} W/cm^2). The fringe visibility is calculated for three different pressures and is shown in Figure 4.8.

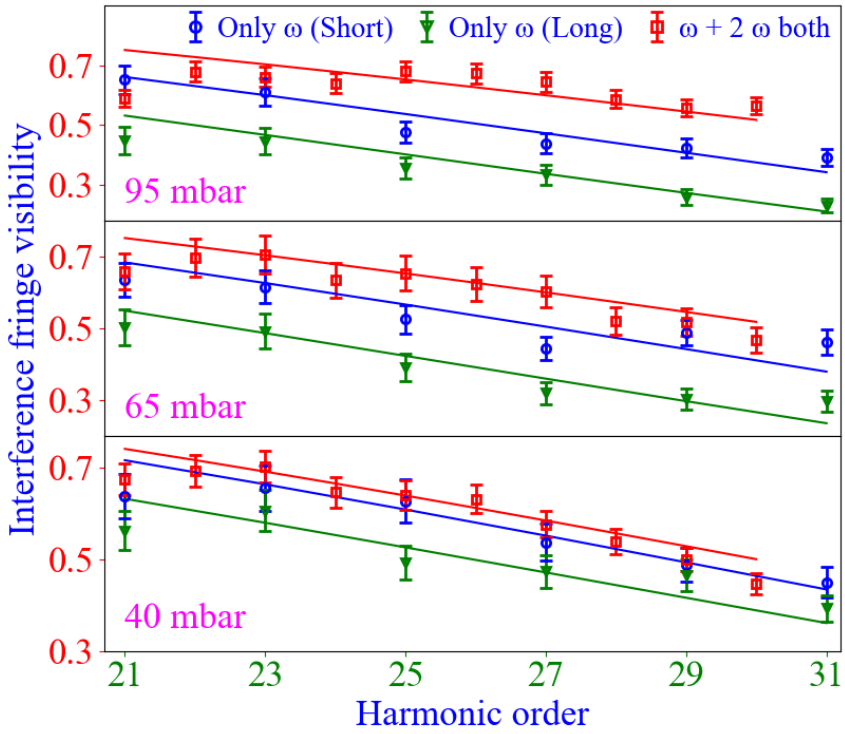

Figure 4.8: *The calculated fringe visibility using Eq 4.6 for 21st to 31st order at gas pressures 40mbar, 65mbar and 95 mbar. The symbol with error bar represents experimental data points and the solid lines represented the theoretically calculated values.*

Figure 4.8 shows the experimentally measured fringe visibility with harmonic (21st to 31st order) order at different gas cell pressure viz. 40mbar, 75 mbar and 95 mbar. It is important to see whether the experimentally observed fringe visibility for different harmonics orders, at different gas pressures, can be fitted using the estimated parameters viz. density fluctuation and the IDP coefficient. The theoretically calculated data matched well with the experimental for all harmonic orders within the experimental error bar. The IDP coefficient used to fit the experimentally measured fringe visibility for 21st to 31st harmonic orders are 25×10^{-14} cm^2/W, 23×10^{-14} cm^2/W, 20×10^{-14} cm^2/W, 18×10^{-14} cm^2/W, 15×10^{-14} cm^2/W, 13×10^{-14} cm^2/W for long

trajectory harmonics, 5×10^{-14} cm^2/W, 7×10^{-14} cm^2/W, 8×10^{-14} cm^2/W, 10×10^{-14} cm^2/W, 12×10^{-14} cm^2/W, 13×10^{-14} cm^2/W for short trajectory harmonics respectively. For two color harmonics the IDP coefficient is taken to be same as the short trajectory harmonics. These estimated values of the IDP coefficient are close to the earlier reported values [149, 150].

4.4 Estimation of higher diffraction order efficiency of VLS grating of FFGS

The aberration corrected, mechanically ruled variable line spaced concave grating is a key element of FFGS (see section 2.3.1), which disperses as well as focuses the spectrum in a flat plane and allows the use of space resolved flat detectors viz. X-ray CCD camera, micro-channel plates etc. In polychromatic source viz. HHG based x-ray source, synchrotron radiation source etc, the wavelength (λ) and its multiples e.g. λ, 2λ, 3λ are simultaneously present in the spectrum. In such cases, the angular position of first diffraction order of wavelength λ and higher diffraction order (2, 3…) of its sub-multiple wavelength ($\lambda/2$, $\lambda/3$…) coincides viz. the position of first diffraction order position of wavelength ($\lambda \sim 200$ Å) coincides with second diffraction order position of the wavelength ($\lambda \sim 100$ Å). This is known as diffraction order contamination and it may lead to ambiguous measurement of the photon flux and spectrum of the source using such spectrographs. It is therefore essential to identify as well as estimate the contribution of higher diffraction orders [96]. Although, photons diffracted in various diffraction orders, depend on the type of grating used viz. mechanically ruled blazed grating (in FFGS), diffracts significant number of photons, whereas the holographic grating diffracts only few percent in higher diffraction orders [151]. However, due to high diffraction efficiency, blazed grating is mostly used in FFGS. FFGS is used in wide spectral x-ray range; however, the width of zero order

diffraction remains a concern, which limits the shortest detected wavelength [95]. The spectral range can be improves by using the FFGS in higher diffraction order mode. This configuration has been successfully exploited to extend the spectral range to water window x-ray regime [152].

The use of FFGS in higher diffraction order mode needs a precise calibration as well as wavelength dependent diffraction efficiency estimation for higher diffraction orders. Previously, the study of higher diffraction orders of variable line spaced grating (VLSG) was studied using nanosecond laser plasma based x-ray source by Schwanda et al [153]. The resonant emission lines of aluminium and boron, was used for the study, in the spectral range $\lambda \sim 50$ to120 Å and a significant deviation between the theoretical and experimentally values were observed [153]. To characterize VLS grating in wide spectral range using resonant emission lines, a large number of target materials are required. The use of higher harmonic source for this purpose, shows significant advantage viz. closely spaced discreet wavelengths are present in wide spectral range, which are odd sub-multiples of laser wavelength. Also, from a single spectrum, one can estimate the higher order diffraction contribution in wide spectral range. This makes the estimation simpler, precise and unambiguous [96]. Precise calibration of FFGS is required to identify the higher diffraction order peak, which is a challenging task, as the spectrum is flooded with multiple peaks. These peaks are of higher harmonic wavelengths, diffracted in first or higher diffraction order by the grating of FFGS. The FFGS is roughly calibrated by using the technique discussed section 4.1, to identify the harmonic orders present in the spectrum.

First, in order to calibrate the diffraction orders in wide spectral range, the harmonic radiation with highest cut-off energy ~150eV (~99^{th} order), generated in

helium gas is used. The laser and gas cell parameters are carefully optimized to achieve reasonably good intensity with highest cutoff order.

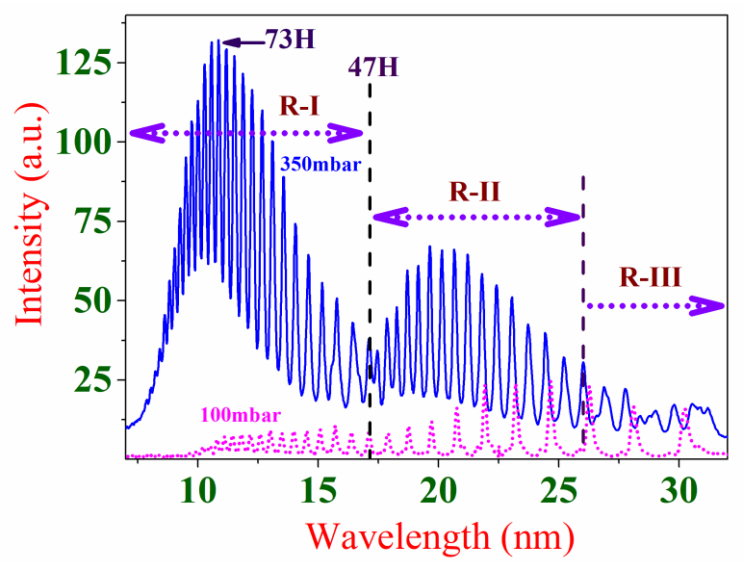

Figure 4.9: *A higher harmonic spectrum exceeding 99th order generated from helium filled gas cell. The three regions marked as RI, RII and RIII, in the figure shows first, second and third diffraction order respectively.*

Figure 4.9 shows the spectrum of higher harmonics generated from helium filled gas cell at ~ 100mbar and ~350 mbar gas pressures. The harmonic spectrum extending from 43rd (λ~186 Å) to 99th orders (λ~80Å) can be seen clearly. It can be noted from Fig 4.9 that the harmonic cutoff is significantly higher (~99th order) at high pressure (~350mbar).

The identification of various diffraction orders is a challenging task, as the wavelength peaks of first and higher diffraction order lie close to each other. In Fig 4.8, it can be seen that the position of harmonic peaks in violet and blue curve matches in wavelength below 17nm; whereas above 17nm wavelength, the harmonic peak in the two curves (blue and magenta) doesn't match. Hence a precise calibration is essential for identification of peaks in various diffraction orders. The most commonly

use technique is based on polynomial fitting by identifying few wavelengths in a given spectral range and then interpolate it to calibrate wide spectral range using the coefficients of the polynomial [154]. However, no fixed polynomial can describe the spectral dispersion (of VLS grating) in whole spectral range; hence marking of first and higher diffraction order wavelengths is extremely difficult [155]. Also, due to propagation effect the harmonic wavelength gets shifted, which adds up further error in the measurement. A ray tracing code is written in python, using the grating parameter (see table 2.3), the groove density variation from Eq 2.3 and grating dispersion from Eq 2.4. A well calibrated spectral line (L-edge of aluminium at λ≈171 Å) is used to mark the position of 45th harmonic order (harmonic order ≈ 8000 Å /171 Å ≈ 47), as the highest harmonics that can pass through the aluminium filter is 45th order. The ray tracing simulation for harmonic orders from 13th (λ~62nm) to 99th (to λ~8nm) is shown in Fig 4.10.

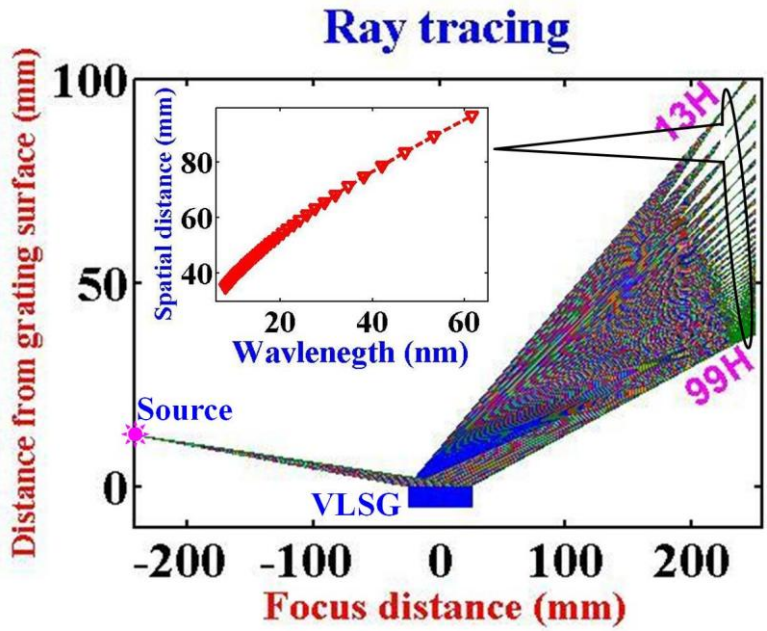

Figure 4.10: *Ray tracing of VLS grating used in FFGS, which shows dispersion from 13th to 99th harmonic order, the inset shows the zoomed image of wavelength dispersion with distance from grating surface (zero position).*

The inset of figure 4.10 shows the wavelength dispersion obtained by connecting the points of focus of VLS grating. It can be seen that the harmonics are focused in a nearly flat plane. For detection of higher harmonics, the MCP is placed at the focus position of VLS grating. The wavelength calibration in whole spectral range is performed and the position of wavelength peaks in first and higher diffraction orders is precisely identified. The marked wavelength region is shown in Fig 4.9 for first, second and third diffraction orders (regions R-I, R-II and R-III). The focal position and spot sizes is also calculated using the ray tracing code in the wavelength range 80Å to 600Å as shown in fig 4.11.

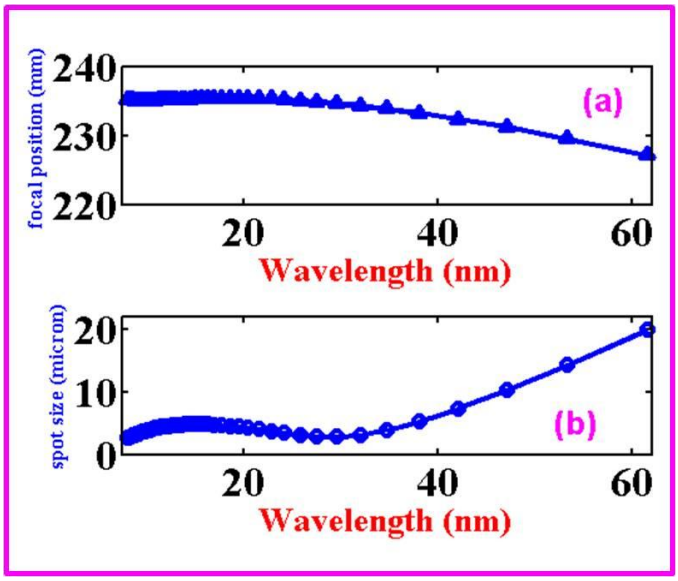

Figure 4.11: *a) focal position of the wavelength dispersed by FFGS from 8nm to 62nm, b) the focal spot size of the focused harmonics by concave VLS grating of FGFGS.*

It can be seen from Fig 4.11 that the focal position at the detector (~ 235mm) is almost flat and the focal spot size is ~5μm, which is much smaller than the MCP channel size (~13 μm) in λ~50Å to λ~300Å. Therefore, the spectral resolution is limited by the spatial resolution of the combination of MCP and imaging CCD camera.

Considering spatial resolution of two pixels of MCP+CCD combination (effective pixel size ~ 20μm), the resolving power is calculated to be ~ 200 at ~ 50Å and ~ 600 at ~ 300Å wavelength. The resolving power is found to be higher in higher diffraction order, viz. the resolving power is ~ 300 at ~100Å wavelength in first diffraction order, ~ 450 in second diffraction orders and ~ 570 in third diffraction orders. Thus for the higher spectral resolution, the spectrograph may be used in higher diffraction order mode. The photon flux is also calculated in various diffraction orders after calibrating FFGS (see section 2.3.2). Figure 4.12 shows the fraction of photon diffracted in second and third order as compared to the first diffraction order.

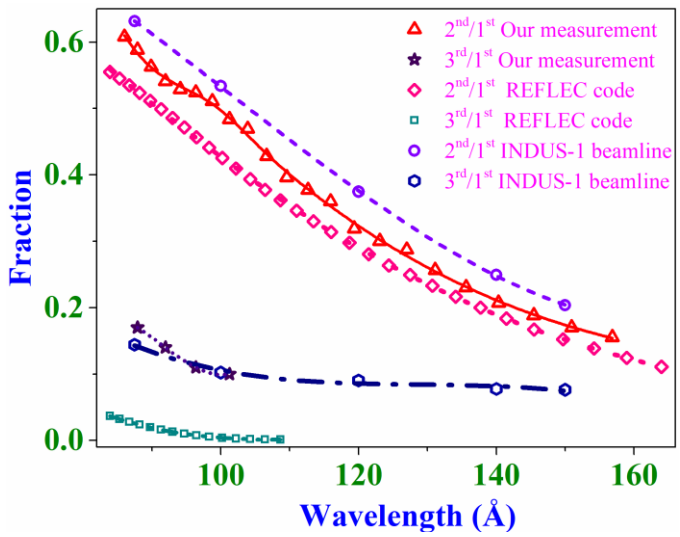

Figure 4.12: *Comparison of the fraction of higher diffraction order contribution for 2nd and 3rd diffraction order measurement using different techniques.*

It can be noted from Fig 4.12 that the fraction at λ ~ 80Å becomes ~ 65% for the 2nd order, which reduces to ~ 20% at 150Å. For third diffraction order, the fraction becomes ~ 15% at λ ~ 100Å. The measured fraction is also compared with the measurement using reflectivity beam line of Indus-1 and using REFLEC code, which shows good matching of the three results.

In summary, the study on HHG from argon, neon and helium filled gas cell is performed. The optimization of various parameters viz. gas cell length, gas pressure and its position relative to laser focus is performed to improve the harmonic efficiency. The maximum harmonic yield in argon gas is achieved to be ~250nJ per laser shot, ~30nJ per laser shot in neon gas and ~15nJ per pulse in helium gas. The study on the spectral and spatial coherence characteristics of higher harmonics generated from argon gas is carried out using single and two color laser pulses. With increase in gas pressure, the harmonic spectrum first broadens and then splits beyond gas pressure of $\geq$ 60mbar for single color case. For the two color case, no broadening and splitting in the harmonic spectrum is observed. The splitting in the spectrum is attributed to the electron trajectories responsible for HHG. The trajectories are identified from the divergence and spectral width of the splitted harmonics. The study on spatial coherence of spectrally resolved harmonics is performed and it is found that the harmonics generated using two color laser pulse is having higher spatial coherence than the single color case. In case of single color laser pulse, the spatial coherence of short trajectory harmonics is higher than the long trajectory harmonics. A dominant role of free electron density fluctuation and time dependent IDP phase is found in deteriorating the spatial coherence of harmonics. The study on parametric optimization is performed in helium gas filled cell, to improve harmonic cutoff. The harmonics up to 99^{th} order is observed in the recorded spectrum. The HHG spectrum in helium is used to characterize the FFGS for first, second and third diffraction orders and it showed that significant fraction of photons, are diffracted in seconds and third diffraction order. The second and third order diffraction efficiencies are measured to be ~60-70% and ~20% respectively compared to first order at 10 nm wavelength.

Chapter 5:
Temporal Characterization of Higher Harmonic Radiation

In the recent past, there has been considerable interest in the temporal characterization of higher harmonic radiation. The generation and optimization of the higher harmonics has pushed up the shortest achievable wavelength to extreme-ultraviolet / soft x-ray region. Also, due to coherent generation process, the higher harmonics should be coherent and should maintain a constant phase relationship between them [156, 157]. Several studies have shown that these coherently generated harmonics are workhorse for the attosecond pulses generation [158-159]. Use of few cycle laser pulses for HHG, results in generation of isolated attosecond pulses (IAP) [160, 161]. The use of multicycle laser pulses has led to the generation of attosecond pulse trains (APT), which are separated from each other by half the laser cycle (~1.33fs for λ~800nm) [11, 157]. Both IAP and APT have opens up new avenues to the experimentalist to explore temporal dynamics of ultrafast phenomena [162,163]. These pulses are promising for the study of many atomic processes like ultrafast electron dynamics in material [164], tunnelling dynamics [165], photo-ionization dynamics [166] etc.

Although, few successful experiments on the study of time resolved electron dynamics using IAP and APT has already been reported, still it is an inception. The use of the attosecond pulses needs precise characterization, which is still a challenging task. The temporal characterization of the attosecond pulses requires measurement of spectral intensity as well as relative phase between these harmonic orders [11, 158]. The characterization of the frequency spectrum (spectral intensity) can directly be carried out using conventional spectrographs (FFGS, discussed in chapter1) [96]. The major challenge is spectral phase measurement, which is a pre-requisite of temporal

characterization of the attosecond pulses. The spectral phase measurement techniques viz. Reconstruction of Attosecond Beating by Interference of Two Photon Transition (RABITT) [167] and Attosecond Streaking [168, 169], mainly rely on the cross correlation of the attosecond pulses with the ultrashort visible/infrared (IR) laser pulses (also known as dressing field). In the present study, a 45fs Ti:Sapphire laser pulse is used for HHG and also as a dressing field needed for characterization of the attosecond pulse trains. The "RABITT" technique has been used to characterize the attosecond pulse trains generated from argon gas filled cell.

5.1 Time structure of higher harmonics

As discussed in previous chapter, that focusing an intense ultrashort laser pulse in nonlinear gaseous medium, results in generation of odd harmonics of the laser frequency, which are phase locked [157]. The theoretical studies have shown that, these phase locked harmonics can lead to generation of a train of attosecond pulses (similar to the mode-locking technique used to generate the femtosecond laser pulse) [11,170]. The width of individual attosecond pulse in pulse train depends on the number of phase locked higher harmonics. Thus, in order to generate shorter attosecond pulse in pulse train, more number of phase locked harmonics is required [11,170]. The reconstruction of the field of the attosecond pulse train, from the phase locking of the odd harmonics order from q_{min} to q_{max} can be expressed as [11, 167]

$$E(t) = \sum_{q=q_{\min}}^{q_{\max}} E_q e^{i\left(q\omega_1 t+\phi_q\right)} \tag{5.1}$$

Where q is the harmonic order, E_q is the field amplitude and ϕ_q is the phase of the q^{th} harmonic order and q_{min} and q_{max} is the lowest and highest harmonic order respectively which are phase-locked. The attosecond pulse train generated by mode-locking of odd

harmonic orders from 17th to 25th orders is reconstructed using Eq 5.1, and shown in Fig 5.1. The electric field is shown in dashed line (magenta curve) and the field intensity in solid line (blue curve). In the reconstruction, we have considered same amplitude and zero relative phases between the harmonic orders. It can be seen from Fig 5.1 that the generated attosecond pulse train has FWHM width of ~ 240 attosecond with pulse to pulse separation of half the laser cycle (~1.33fs).

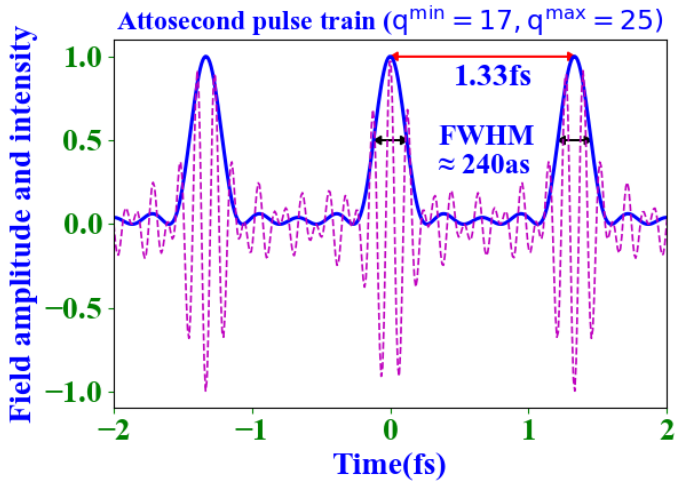

Figure 5.1: *An attosecond pulse train reconstructed from 17th to 25th odd harmonic order using Eq 5.1, for equal amplitude and relative phase*

In the theoretical reconstruction of attosecond pulse train using Eq 5.1, the harmonic frequency is taken to be a delta function. Due to this, the number of attosecond pulses in the pulse train will be infinite. However, practically the individual harmonics has inherent bandwidth. If the highest bandwidth of individual harmonics is $\Delta\omega$, then the attosecond pulses will be confined inside an envelope of duration $\Delta\tau \sim (1/\Delta\omega)$. Consider the maximum bandwidth among the individual harmonics orders is ~ 9e14 Hz ($\Delta\lambda$~0.5nm), which is for the 25th harmonic order (λ~32nm), the width of time envelope ($\Delta\tau$) is calculated to be ~ 1.2fs. Inside the envelope of width 1.2fs, there will be five (1.2fs/240as ≈ 5) attosecond pulses.

In reconstruction of attosecond pulses in Fig 5.1, constant amplitude and zero relative phases between harmonics are considered (ideal case). However, practically the amplitude of harmonics is not same and the relative phase is not zero. There are several factors, which affect the relative phase between harmonics viz. HHG by different electron trajectories [170,171], phase matching in the non-linear medium [172] etc., which leads in elongation of the attosecond pulse duration from transformed limited value. It is therefore essential to experimentally measure the temporal characteristics of the generated attosecond pulse trains from higher harmonic radiation.

5.2 Temporal characterization techniques

Auto-correlation technique used for characterization of femtosecond visible/infrared pulses employ nonlinear medium to generate autocorrelation signal, which is used to measure the pulse duration. The spectrum of higher harmonic extends to XUV/soft x-ray regime, thus the possibility of using nonlinear medium for autocorrelation, can be ruled out. Autocorrelation using xuv/x-ray source mainly rely on single photon ionization of an atom. The autocorrelation technique has been used for the temporal characterization of single harmonic order viz. 9^{th} harmonic order (photon energy ~ 14eV) generated from xenon gas by Kolbayashi et al [173]. The helium atom (ionization potential of Helium ~24.6eV) was singly ionized by absorbing two 9^{th} harmonic photons. For the temporal characterization, the harmonic beam was splitted into two parts and then focused in Helium gas. The delay between the two splitted parts was varied and the flux of singly charge helium ion was measured. Using this technique, the pulse duration of 9^{th} harmonics was measured to be ~27fs. In the similar way, the pulse duration of 27^{th} harmonic order (photon energy

≈ 42eV) was measured by observing double ionization of helium (ionization potential of He^+ ~ 54.4 eV) by Y. Nabekawa et al [174]. The measurement of pulse duration of higher harmonics by autocorrelation (ionization based autocorrelation), is limited to single harmonic orders, whereas there are multiple harmonic orders in their spectrum, which are locked in phase and generates attosecond pulse trains.

For characterization of attosecond pulse trains generated by a group of odd harmonic orders, the cross-correlation technique can be used. In this technique, the higher harmonics and IR laser (dressing field) is simultaneously focused in a low pressure gas sheath. Interaction of harmonic photons with gases generates photoelectrons with energy equal to difference in photon energy and ionization potential of the gas. In the case of odd harmonics these photoelectrons are generated with energy difference equal to twice of laser photon energy. In the presence of dressing field (IR laser pulse) sidebands of these photoelectrons are generated at energies corresponding to even harmonic orders. These sidebands oscillate with the delay between the two pulses [11, 169]. This sideband oscillation is used to measure the relative phase between the harmonic orders using a technique known as "Reconstruction of Attosecond Beating by Interference of Two Photon Transition (RABITT)". This technique works, only when discrete harmonics are present in the spectrum. In the upcoming section, I shall discuss about the RABITT technique [175] and its application for temporal characterization of higher harmonics.

5.3 Reconstruction of Attosecond Beating by Interference of Two Photon Transition (RABITT)

This technique is based on measurement of amplitude and relative phase between the harmonics, using cross-correlation technique and uses them to reconstruct

attosecond pulse train [11, 170]. The spectral phase of higher harmonics is imprinted on the electron wave-packet, which further interacts with the IR photon (known as dressing field). The nature of interaction depends on the time structure of the higher harmonics and the strength of IR field. For characterization of attosecond pulse trains, the intensity of IR laser pulse is kept low, as increasing the IR laser intensity leads to photoelectron streaking, and may create error in phase measurement. However, such streaking is commonly used for the characterization of single attosecond pulses [176,177].

After the first demonstration of temporal characterization of attosecond pulse train (generated from 13^{th} to 19^{th} harmonic order in argon gas) by Paul *et al* [11], few more research groups have reported the attosecond pulse train characterization in different spectral range and under different experimental conditions [176, 177]. However, due to complexity of the processes involved, this field is still an active area of research. The basic principle of RABITT technique is shown in Fig 5.2.

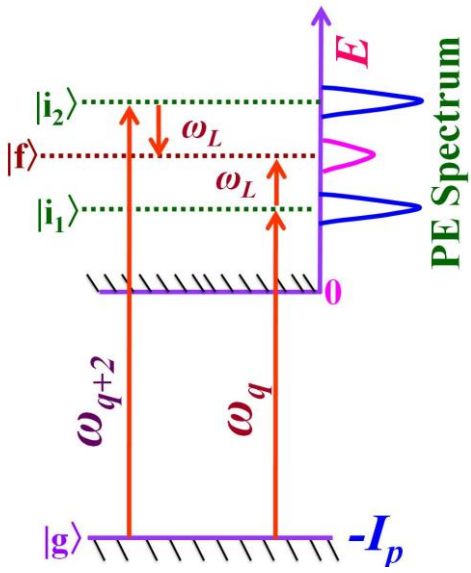

Figure 5.2: *A pictorial representation of RABITT technique, ω_q and ω_{q+2} is frequency of two consecutive odd harmonic order and ω_L is the fundamental laser frequency.*

It can be seen from the Fig 5.2 that the photoelectron peak corresponding to the even harmonic order (ω_{q+1}), is generated either via absorbing one IR photons (with lower odd harmonic photon ω_q) and also via emission of one IR photon (after absorption of next higher odd harmonic order photon ω_{q+2}). The interference of these two pathways of two-photon process (also known as quantum interference) leads to oscillation of the sideband photoelectron peak with the delay between the two pulses [158].

The principle of the RABITT technique can be understood using a perturbation theory approach. When an atom (ionization potential ~ I_p) is exposed to higher harmonic radiation of frequency ω_q ($\hbar\omega_q > I_p$), it will lead to generation of photoelectron of energy $\hbar\omega_q - I_p$. Considering the amplitude of the laser field and higher harmonic field of q^{th} and $(q+2)^{nd}$ order to be

$$E_L(t) = \tilde{E}_0(t)\exp\left(-i\left(\omega_L t + \phi_L\right)\right) + CC \tag{5.2}$$

$$E_q(t) = \tilde{E}_{q0}(t)\exp\left(-i\left(\omega_q t + \phi_q\right)\right) + CC \tag{5.3}$$

$$E_{q+2}(t) = \tilde{E}_{q+2,0}(t)\exp\left(-i\left(\omega_{q+2} t + \phi_{q+2}\right)\right) + CC \tag{5.4}$$

Where E_L, E_q and E_{q+2} is the electric field amplitude of laser and harmonics for q^{th} and $(q+2)^{nd}$ odd orders respectively. The amplitude of higher harmonic field is taken to be small, so that it can be treated as a small perturbation to the atomic system [158, 159]. The probability amplitude for a transition from ground state ($|g\rangle$) to i^{th} state can be expressed using the first order perturbation theory as

$$A_i^{(1)} = \frac{1}{i\hbar}\int dt E_q(t)\langle i|e\hat{r}|g\rangle \exp\left(\frac{i(\mathrm{E}_i - \mathrm{I}_p - \hbar\omega_q)\mathrm{t}}{\hbar} + i\phi_q\right) \tag{5.5}$$

The presence of weak IR laser field can be treated as another perturbation. This leads to two photon transition to the final state ($|f\rangle$) by either absorption or emission

of one infrared laser photon. This two photon transition leads to appearance of sidebands in photoelectron spectrum, whose peak correspond to photon energy of even harmonic order [158, 159]. The sideband signal can be expressed using second order perturbation and is proportional to

$$S(\omega,t) \propto \left| \int_{-\infty}^{\infty} A_f^{(2)} dt \right|^2 , where\ A_f^{(2)} = A_f^{abs} + A_f^{em} \tag{5.6}$$

$$A_f^{abs} = \sum_i \frac{\mu_{fi}\mu_{ig}}{\frac{1}{\hbar}\left(E_i - I_p - \hbar\omega_q\right)} E_q(t) E_L(t-\tau) e^{i\phi^{abs}} \tag{5.7}$$

$$A_f^{em} = \sum_i \frac{\mu_{fi}\mu_{ig}}{\frac{1}{\hbar}\left(E_f - I_p - \hbar\omega_{q+2}\right)} E_{q+2}(t) E_L(t-\tau) e^{i\phi^{em}} \tag{5.8}$$

Where A_f^{abs} and A_f^{em} is the transition amplitude for the sideband generation by absorption and emission of one IR photons respectively, μ_{fi} = <*f\er\i*> and μ_{ig} = <*i\er\g*> are the transition matrix element, the phase ϕ_{abs} and ϕ_{em} can be expressed as [158]

$$\phi^{abs} = \frac{1}{\hbar}\left(E_f - I_p - \hbar\omega_q\right)t + \phi_q - \omega_L(t-\tau) \tag{5.9}$$

$$\phi^{em} = \frac{1}{\hbar}\left(E_f - I_p - \hbar\omega_{q+2}\right)t + \phi_{q+2} + \omega_L(t-\tau) \tag{5.10}$$

Using Eq 5.7 to 5.10, the sideband signal is calculated [158, 167] to be proportional to

$$S(\tau) \propto \cos\left(2\omega_L\tau + \Delta\phi_{q,q+2} + \Delta\phi_f^{at}\right), \text{ where } \Delta\phi_{q,q+2} = \phi_q - \phi_{q+2} \tag{5.11}$$

Where $\Delta\phi_f^{at}$ is the atomic phase of dipole (two-photon transition), that depends on the initial and final states in the continuum, of the target gas atom. It can be seen from Eq 5.11, that there are two unknown terms $\Delta\phi_f^{at}$ *and* $\Delta\phi_{q,q+2}$, and only one measurable quantity viz. the sideband signal. The atomic phase ($\Delta\phi_f^{at}$) is therefore needed to be calculated. The atomic phase was calculated theoretically by few

research groups, from the solution of the time dependent Schrödinger equation (TDSE), and was found to be small compared to the relative phase between harmonics ($\Delta\phi_{q,q+2}$) and can be safely neglected [11,158]. However, for precise characterization, the atomic phase term ($\Delta\phi_f^{at}$) should be taken into account. The expression in Eq 5.11 is applicable to all the sidebands; appear in the recorded photoelectron spectrogram. It can also be noted from Eq 5.11 that, the sideband signal oscillates with twice the laser frequency ($2\omega_L$). The above treatment is valid as long as the harmonic field and the IR laser field intensity are kept low. With increase in the IR laser pulse intensity, other phenomena viz. photoelectron streaking [178], may also takes place.

For the experimental measurement of photoelectron spectrum, a sensitive photoelectron detector with high sensitivity for low energy electrons is required. Further, due to poor generation efficiency of the higher harmonic process, (which result in small photon flux), the spectrograph should have high collection efficiency. A magnetic bottle electron time of flight (MBETOF) can be used for this purpose, due to its high collection efficiency (may extend to 2π rad) [179]. It is therefore essential to develop a MBETOF and characterize it for the measurement of photoelectron spectrum.

5.4 Magnetic Bottle Electron Time of flight (MBETOF) Spectrograph

In the electron time of fight spectrograph, the electrons with different time of flight are detected using a time resolved detector. The electrons with different energy, (velocity) generated at same time are passed through the drift region. These electrons take different time to travel same distance, hence gets dispersed in time. Thus, from the measurement of the arrival time at the detector, one can infer about the electron energy. In the present experiment, the photoelectrons are generated in the interaction

region by photo-ionization of gases by XUV harmonics. The generated photoelectron travel from interaction region to time resolved detector (detection grade MCP) through a drift tube. The time resolution of the detector should be sufficient so that the photoelectrons reaching the detector should be faithfully detected. The electron time of flight spectrographs (ETOF) can be used in different geometries [180–182] viz. field free ETOF, Magnetic bottle ETOF (MBETOF) and VMI based ETOF. The most common type of electron spectrograph used for attosecond pulse characterization is MBETOF and VMI based ETOF. In the present work, I have used MBETOF spectrograph which is discussed here in detail.

In MBETOF spectrograph, magnetic bottle configuration is used, which ensures high collection efficiency (upto 2π radian) [179]. A typical schematic of the MBETOF is shown in Fig 5.3. The MBETOF spectrograph consists of a permanent magnet and a long length solenoid at an optimum separation. The permanent magnet is used to generate strong magnetic field, which collimates the photoelectrons generated from interaction region. The solenoid magnetic field is used for guiding of the photoelectrons to the MCP detector. To increase the magnetic field further in the interaction region, a soft iron cone is placed over permanent magnet, to focus the magnetic field lines from its surface (Fig. 5.3). The spectrograph uses a strong permanent magnet (samarium cobalt, Sm_2Co_{14}) with a soft iron cone (110 deg cone) to focus the magnetic field lines, which increases the magnetic field strength (from ≈ 2.5kG to 5kG) in the interaction region placed at ~1.5mm, away from the cone tip.

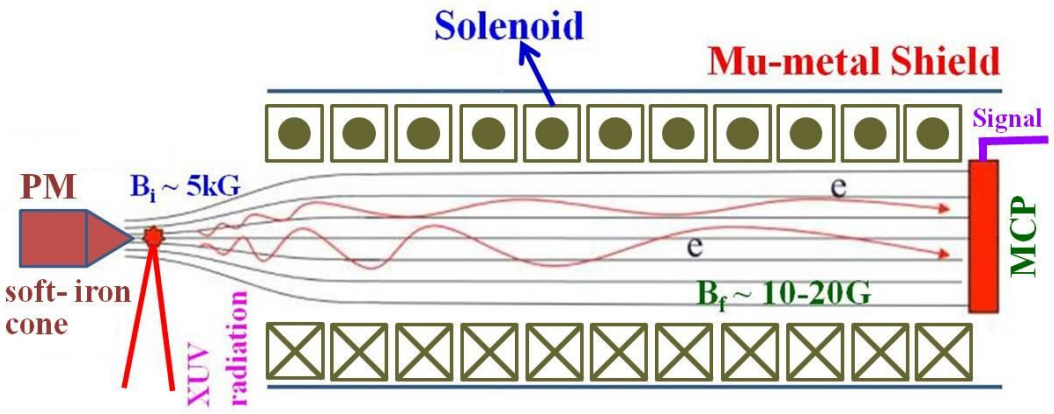

Figure 5.3: *Typical schematic of the magnetic bottle electron time of flight spectrograph.*

In the interaction region, the photoelectrons are generated by XUV harmonics radiation, which follows strong magnetic field ($B_i \approx 5kG$) of the permanent magnet and reaches inside solenoid. A small magnetic field inside the solenoid ($B_f \approx$10G), guide these photoelectrons to MCP detector. The magnetic bottle configuration helps the photoelectron to be guided from interaction region to MCP detector, which is placed at the end of the MBETOF spectrograph. As the photoelectrons are guided in small magnetic field, the spectrograph should be shielded from the earth's magnetic field as well. I have placed 1mm thick μ-metal sheet, to shield the spectrograph from any nearby stray field as well as earth's magnetic field. The guiding of electrons in magnetic field, convert the transverse component of its velocity into longitudinal component, thereby decreasing the temporal spread in the electron energy spectrum arises due to their angular spread and will be discussed later in detail in coming section. After guiding through the solenoid, the electron reaches the MCP detector, where it generates a timing signal. This signal is processed by a data acquisition system (DAS), which consists of several electronic components viz. amplifier, constant fraction discriminator and time to digital convertor as shown in Fig 5.4.

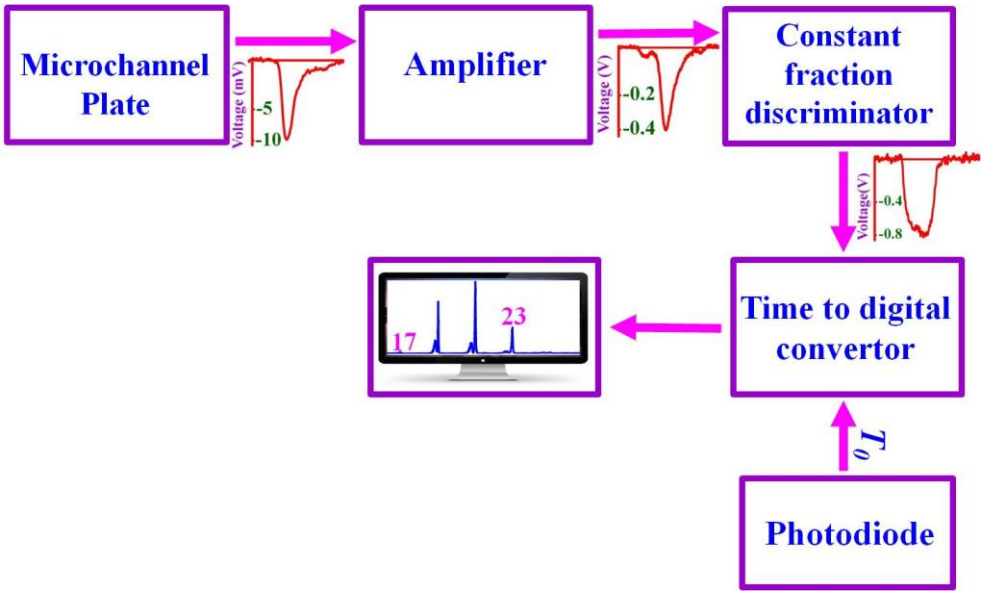

Figure 5.4: *The pictorial representation of data acquisition system. The electron signal is send through amplifier, constant fraction discriminator, time to digital convertor and histogram is recorded on the computer.*

In the MBETOF spectrograph, a detection grade double stage MCP (a gain of ~10^6 at MCP voltage of ≈ 2kV) is used to record the timing signal. The MCP is capable of recording single electron hit. The timing signal is first decoupled from MCP bias voltage by an inbuilt decoupler. The amplitude of the decoupled signal is ~ 10mV with 2ns rise time (Fig 5.5a). This signal is amplified using a low noise RF amplifier (Make: RoentDek Handels GmbH, Germany), which amplify the timing signal from MCP to ~ 100-150V (Fig 5.5b).

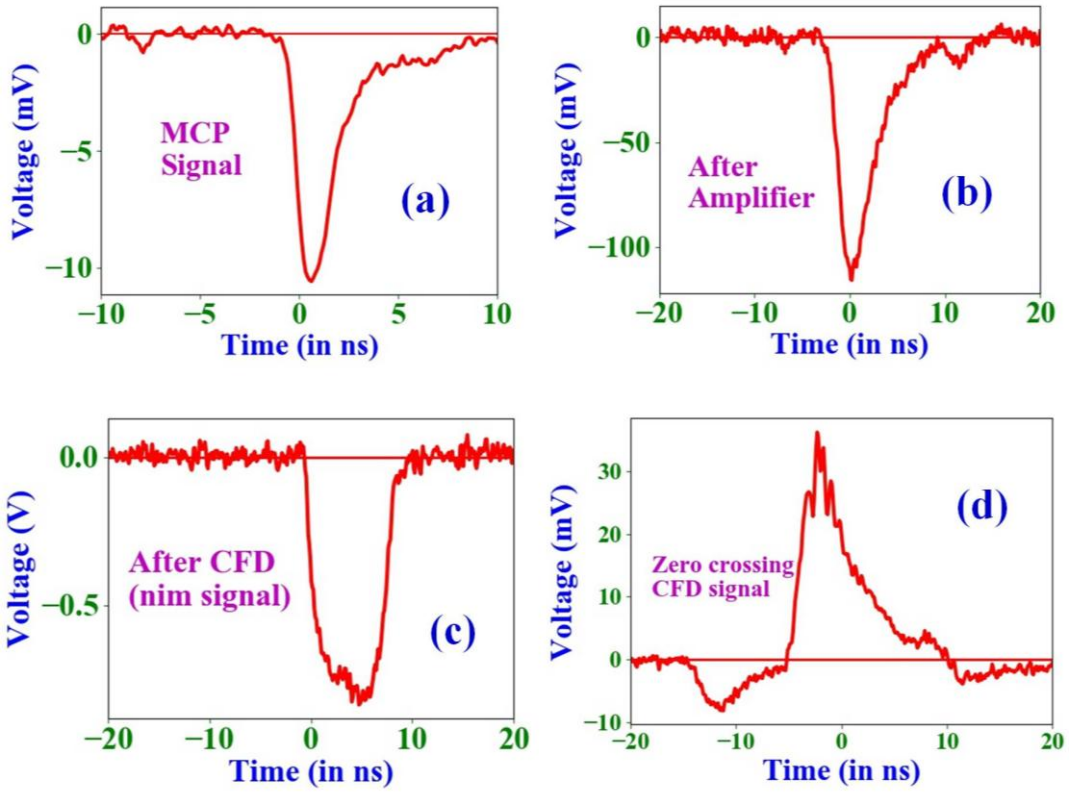

Figure 5.5: *a) the timing signal from MCP b) the amplified signal after the amplifier c) the nim signal from CFD and c) the zero crossing in CFD measured on oscilloscope*

The amplified signal is further send to constant fraction discriminator (CFD, Make: Ametek, Model 935), which reduces the timing jitter, due to any amplitude fluctuation in the MCP signal. The typical timing jitter in CFD is very small (~50ps), which is much smaller than the rise time of the recorded MCP signal (~few ns). In CFD, the applied voltage signal is splitted into two parts (typically in ratio of 80:20). The large fraction is kept as it and smaller part is inverted and then recombined together after a suitable delay between them (delay can be manually adjusted). The recombined signal (Fig 5.5 d) initially becomes slightly negative (due to 20% inverted part) then it become positive (due to 80% positive part) and this lead to a zero crossing signal. The zero crossing signal is observed at an optimum delay (~2ns) between the two pulses. The CFD generates a nim signal (-0.8V) at the time of zero crossing,

shown in Fig 5.5c and the zero crossing at optimum delay ~2ns is shown in Fig 5.5d. The nim signal generated from CFD, is send to the time to digital convertor (TCD, Make: RoentDek Handels GmbH, Germany, and Model: TDC8HP).

The time to digital convertor needs a reference signal (trigger) for zero time marking that initiates the recording of events. The reference signal is taken from the IR laser pulse using a photodiode. After arrival of reference signal in TDC, it starts counting the number of hits of photoelectrons, reaching the MCP detector and a histogram is plotted using software (Cobold-PC, Make: RoentDek Handels GmbH, Germany). The histogram shows the photoelectron count with the arrival time of the photoelectron, which can be used to calculate the photoelectron energy using the relation

$$\text{Photoelectron energy } \left(E_p\right) = \frac{1}{2} m_e \left(\frac{L}{T}\right)^2 \qquad (5.12)$$

Where L is the distance travelled and T is the travel time of electron from interaction region to the MCP detector respectively and m_e is the electron mass.

At this point, it is essential to discuss the important parameters of the MBETOF spectrograph. The energy resolution and the collection efficiency of the photo electrons are key parameters of the spectrograph. The theoretical calculations have shown that the ratio of magnetic field in interaction region (B_i) to the field inside solenoid (B_f) play crucial role in determining the energy resolution of the spectrograph. It is therefore important to measure the magnetic field profile of MBETOF. The magnetic field profile is experimentally measured using an axial hall probe (Make: Bell lab Inc.) and the measured profile is shown in Fig 5.6a.

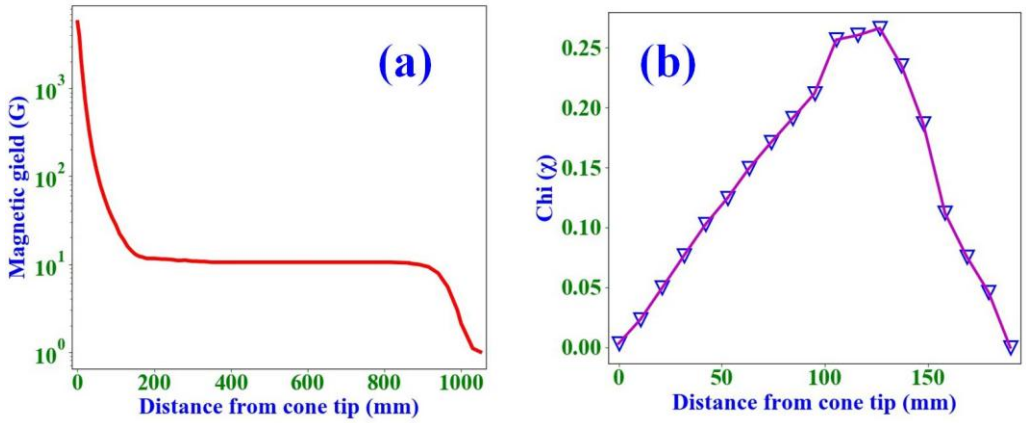

Figure 5.6: *a) typical magnetic field profile of a magnetic bottle type e-TOF spectrograph, b) the adiabeticity parameter in the transition region (upto ≈200mm from permanent magnet).*

In Fig 5.6a, the zero position is the position of soft iron tip of the spectrograph, the solenoid length is ~1meter and separation between the solenoid and the permanent magnet is kept to be ~ 200mm. The energy resolution also depends on the time resolution of the spectrograph. The accuracy in the flight time is also affected by the parallelization of the electrons trajectories before hitting to the MCP, as the photoelectrons emitted at different angle, take different times to reach the MCP detector [5]. Therefore, there is an intrinsic resolution of the MBETOF spectrograph, which can be expressed by

$$\text{Energy resolution}\left(\frac{\Delta E}{E}\right) = 2\frac{\Delta T}{T} = \frac{B_f}{B_i} \approx 2\times 10^{-3} \qquad (5.13)$$

In Eq 5.13, B_i and B_f is the magnetic field in interaction region and inside solenoid respectively. In our case, the intrinsic energy resolution is calculated to be ~ 0.2%.

The other parameter of the spectrograph is the collection efficiency (acceptance angle) of the generated photoelectrons. The flux of photoelectrons is small, due to low generation efficiency of harmonic radiation and low density of gases in interaction region. It is therefore highly desirable to increase the collection

efficiency of the photoelectron signal to the MCP detector. Although the photoelectrons are generated in 4π solid angle, the collection angle of magnetic bottle configuration is close to ~ 2π rad. The absolute collection efficiency of the MBETOF spectrograph [180] is given by relation

$$\text{Collection efficiency } (\eta) = \frac{1}{4\pi}\int_0^{2\pi}\int_0^{\theta_{\max}} \left(1+\beta P_2\left(\cos(\theta)\right)\right)\sin(\theta)\,d\theta\,d\phi \qquad (5.14)$$

Where P_2 is Legendre polynomial, β is asymmetry parameter and θ_{max} is maximum geometrical acceptance angle. For the MBETOF spectrograph, a collection efficiency of 50 % is calculated for neon gas (energy 32.5eV correspond to 23rd harmonic order) from the designed parameters viz. θ_{max} ~ 1.14^{o}, calculated from the MCP size ~25mm and distance between the MCP and interaction region ~1240mm.

The other important parameter is adiabeticity parameter, which ensures that the motion of electron in the magnetic field is adiabetic. The small value of this parameter (<1) ensures good energy resolution and the collection efficiency of MBETOF. The adiabeticity parameter [5] is defined as

$$\text{Adiabeticity parameter } (\chi) \sim \frac{2\pi m_e v}{eB_z^2}\left|\frac{dB_z}{dz}\right| \qquad (5.15)$$

Where v is the electron velocity, B_z is the magnetic field strength. For parallelization of the electron trajectories, the adiabeticity parameter should be less than one [5]. It can be seen from Eq 5.15 that for small χ, the magnetic field in the transition region (B_z) should be large and the magnetic field gradient should be small. It is therefore important to optimize the distance between the permanent magnet and the solenoid. Figure 5.6b shows the adiabeticity parameter variation in the transition region. It can be seen from Fig 5.6b that the adiabeticity parameter is ~0.25 for ~15eV electron energy (for separation between the permanent magnet and solenoid ~200mm), which is within the safe limit.

In order to precisely estimate the photoelectron energy, it is important to calibrate the MBETOF spectrograph, for the path length travelled by electron travel from interaction region to the MCP detector. The reference signal in TDC is received from a photodiode, which send the signal through co-axial cable, whereas the higher harmonics and IR laser beam travels with light speed to the interaction region. This leads to a time offset (T_{off}) in the reference signal. To measure the time offset, the higher harmonic signal is scattered from the gas sheath needle (of MBETOF) and is recorded by the MBETOF spectrograph. The time difference between the reference signal from photodiode and the scattered harmonic signal is taken to be time offset (T_{off} ~ 8ns) and is considered in the calculation of photoelectron energy. Further, the length of the MBETOF spectrograph also needs to be measured accurately, in order to precisely calculate the photoelectron energy.

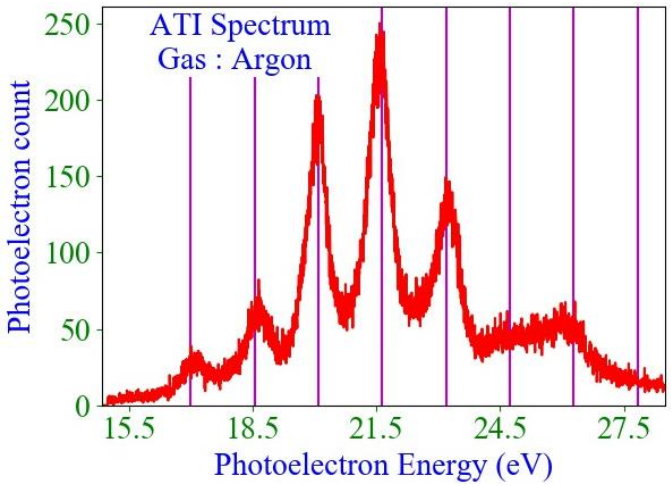

Figure 5.7: *The ATI spectrum generated by focusing IR laser pulse on Argon gas sheath. The magenta vertical line shows the position with energy separated by the IR laser photon energy (~1.55eV).*

The IR laser pulse directly focused in the argon gas sheath to an intensity of $\approx 10^{12}$ W/cm^2 to generate above threshold ionization (ATI) spectrum, shown in Fig 5.7. The energy spacing of ATI peak can be estimated from the measured central

wavelength of the IR laser pulse (λ~800nm) using a visible/IR spectrometer (Make: Avantes Inc.), time offset and energy offset (if any) by modifying the Eq 5.12.

$$\text{Photoelectron energy } (E_p) = \frac{m_e}{2}\left(\frac{L}{T_f + T_{off}}\right)^2 + E_{off} \qquad (5.16)$$

Where E_p is the kinetic energy of the photoelectron, L is TOF spectrograph length, T_{off} is time offset in the reference signal and E_{off} is energy offset, which takes into account any acceleration/deceleration of electron due to any charge accumulation in MBETOF spectrograph. The ATI spectrum in Fig 5.7 is fitted using Eq. 5.16 by taking the length of spectrograph, time and energy offset as fitting parameter. The length of MBETOF is estimated to be ~1240mm, the time offset of ~ 8ns and energy offset of ~0.2eV.

5.5 Experimental Results and Discussions

The experiment is carried out using 1 kHz Ti: sapphire (central wavelength λ~ 800nm) laser system. A schematic diagram of the experimental setup is shown in Fig 5.8. The laser pulse is splitted into two parts using a beam splitter (BS). The transmitted beam carries ~ 4mJ laser energy, whereas the reflected beam carries ~1mJ energy.

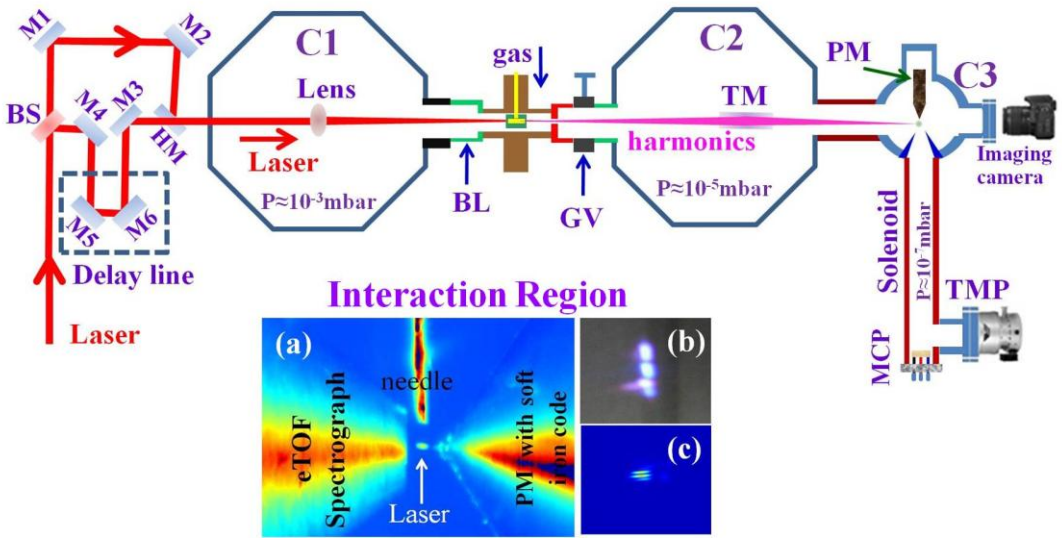

Figure 5.8: *A schematic of experimental setup used for characterization of attosecond pulses. The inset shows a) the image of interaction region alongwith the position of laser pulse focused for photoelectron generation. b) Autocorrelation signal due to two IR beams, and c) shows the interference fringes generated by overlapping of the two beams (harmonic generating beam and the IR beam used for cross-correlation).*

A delay line is installed between the two splitted laser beams, which can be moved with a time step of ~60 attosecond, using piezoelectric stages (10nm resolution). The transmitted laser beam is focused in argon filled gas cell of 15mm length and 5mm diameter using a plano-convex lens of focal length 750mm (f#42) to generate higher harmonics. The generated harmonics (from argon gas filled cell) are focused using a grazing incidence toroidal mirror (R_s~25mm and R_t~10m) on a low pressure gas sheath (~10^{-5}mbar), which leads to generation of photoelectrons through photoelectric effect. These photoelectrons are detected by MBETOF spectrograph. For the cross-correlation measurement, the reflected beam from beamsplitter (BS) is passed through a holed mirror (having hole at the centre, hole diameter ~3mm), where its energy reduces to ~200μJ (after hole). This laser beam moves collinear with the higher harmonic generating laser beam. It also passes through gas cell and is focused using toroidal mirror in the gas sheath. The energy of this beam is tuned by a

combination of polarizer and half wave plate, placed just before the holed mirror (HM).

The cross-correlation of the higher harmonics and dressing laser beam require complete spatial and temporal overlapping. It is essential to ensure the spatio-temporally overlapping of the two beams. This is challenging task, first because both are femtosecond pulses and second the higher harmonic spectrum extends to XUV regime. To ensure the spatio-temporal overlapping, the gas cell is removed from the laser beam path and both IR laser pulses (the higher harmonic generating beam and the dressing laser beam) is spatio-temporally overlapped. The spatial overlapping is achieved by placing a digital camera with an imaging lens to image the focal region and the required vertical and horizontal position of the beam is aligned using mirrors M3 and M6 (Fig 5.8).

The temporal matching of the two beams is achieved in multiple steps. It can be seen from Fig 5.8 that the path of both the beams are same after the holed mirror, therefore it is important to match the path length before the holed mirror. In the first step, the path length of both the beams is roughly matched (using measuring tape) and then a 45deg mirror is placed after toroidal mirror (in vacuum chamber C2) to take both IR beam out of chamber. A fast photodiode (rise time ~ 20ps) is placed in the overlapping region and the temporal matching upto ~200ps is achieved by observing the oscilloscope (bandwidth ~ 4GHz) trace of both the IR laser beams. Although, both the laser beams are aligned collinear, still a small angle remains between the two beams. This small angle between the beams is exploited to achieve the temporal overlapping of the two beams. For this, a second harmonic crystal (BBO, thickness ~ 300μm), is placed in the overlapping region, and a scientific CCD camera (Make: Imaging Source Inc.) with imaging lens, is placed at a far distance (~few meter), to see

the autocorrelation signal. As the two beams may be separated by ~200ps, no autocorrelation signal was observed. We then transiently moved the translation stage of the delay line, which leads to transient second harmonic generation (SHG) and sudden appearance of autocorrelation signal, is observed. The delay stage is adjusted accordingly, to maximize the intensity of autocorrelation signal. The maximized autocorrelation signal can be seen inset "*b"* of Fig 5.8. The maximization of the autocorrelation signal ensures that the two beams are temporally matched within the pulse width. Further, the overlapping region is imaged on CCD camera to observe the interference fringes (Inset "*c*" of Fig 5.8). The interference fringes are observed in the same condition and the delay between the two pulses is scanned to maximize the fringe contrast. The presence of high contrast fringe ensures the complete temporal overlapping of both the pulses (Inset "*c*" of Fig 5.8). After the spatial and temporal matching of the two beams, the gas cell is inserted in the path of laser beam.

To record the photoelectron spectrum, the higher harmonic beam is first focused in low pressure gas sheath using toroidal mirror (TM). The recorded photoelectron spectrum is shown in Fig 5.9. Figure 5.9a shows the recorded photoelectron spectrum, when only the higher harmonics generated from argon gas is focused on neon gas sheath (pressure ~2×10^{-5}mbar). The energy resolution is calculated from the recorded photoelectron spectrum (Fig 5.9a), the energy resolution (ΔE) of ~77meV is measured at ~35eV photoelectron energy (21^{st} harmonic order), whereas energy resolution (ΔE) of ~0.13eV is measured at ~39eV photoelectron energy (25^{th} harmonic order). Thus $E/\Delta E$ is calculated to be ~450 ($\Delta E/E \sim 2.2\times10^{-3}$) and ~330 ($\Delta E/E \sim 3\times10^{-3}$) for photoelectrons correspond to 21^{st} and 25^{th} harmonic order. This resolution is close to the intrinsic resolution calculated for the MBETOF spectrograph using Eq 5.13 ($\Delta E/E \sim 2\times10^{-3}$)

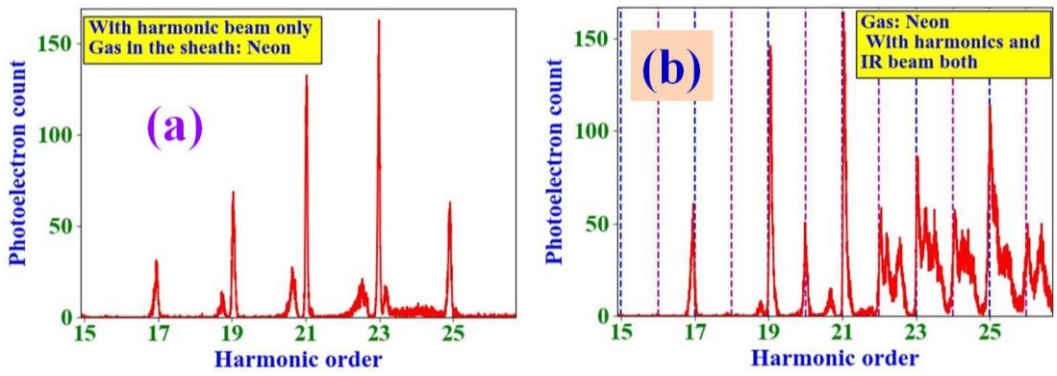

Figure 5.9: *a) The photoelectron spectrum generated from neon gas sheath by focusing higher harmonic beam generated from argon filled gas cell, b) the photoelectron spectrum generated from neon gas sheath by focusing higher harmonic beam and IR beam simultaneously. The magenta vertical lines are photoelectron peak corresponds to even harmonic orders and blue line for odd order.*

After measuring the experimental energy resolution of MBETOF, both the beams (higher harmonics and dressing beam) are simultaneously focused in neon gas sheath. Figure 5.9b shows the photoelectrons generated from neon gas sheath by focusing harmonics and dressing laser beam. The photoelectron spectrum in Fig 5.9b shows peaks at odd harmonic order position (17^{th} to 25^{th} harmonic order) and the sideband signal, correspond to the photoelectron peak at 18^{th} (E_{ph} ~28eV) to 26^{th} (E_{ph} ~ 40eV) harmonic order. For characterization of the attosecond pulse train (generated from Argon gas filled gas cell), the delay scan between the higher harmonics and IR laser pulse (also known as RABITT scan) is performed. Figure 5.10a shows the RABITT scan, which clearly shows the oscillation in photoelectron peaks correspond to odd harmonic order (17^{th} to 25^{th} order) and even harmonic order (from 18^{th} to 26^{th} order). Before measurement of the relative phase between the harmonics orders using Eq 5.11, a fast Fourier transform of the sidebands (photoelectron peaks correspond to even harmonic orders i.e. from 18^{th} to 26^{th} order) is performed, which is shown in Fig 5.10b. It can be seen from Fig 5.10b that the sideband oscillation peak has strong

oscillation frequency close to laser frequency (ω_L) and a very weak oscillation at $2\omega_L$ frequency.

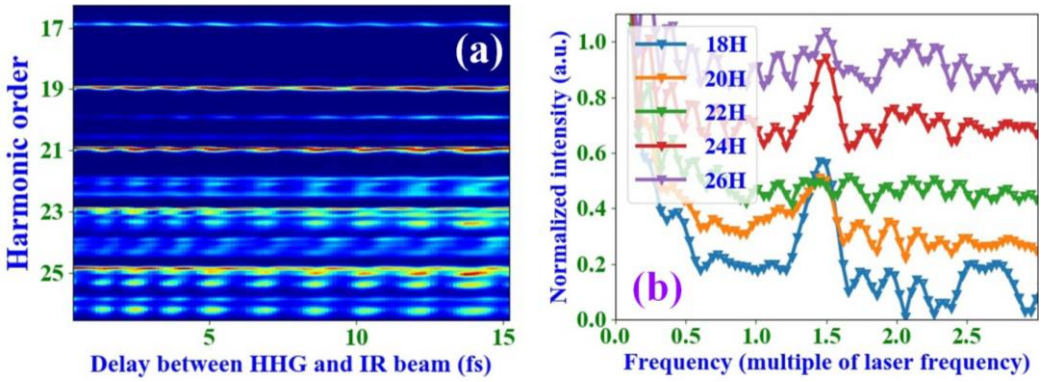

Figure 5.10: *a) The RABITT scan taken when higher harmonics generated from argon gas (from 17th to 25th odd order) and IR pulse is focused in neon gas sheath. The scan is taken with piezo step of 10nm. b) The Fourier transform of the sidebands (correspond to 18th to 26th even order). The oscillation frequency ≈ 2ω (twice the IR laser frequency) can be clearly seen.*

To characterize the attosecond pulse train using photoelectron spectrum with delay (Fig. 5.10(a)) needs a rigorous mathematical analysis to take into account the sideband oscillation at laser frequency and will be taken up in future study. The oscillation at laser frequency may have appeared due to passing both the beams (higher harmonics and dressing beam) collinearly through gas cell, where the harmonic beam itself has modulated.

We explored molecular gases (nitrogen) at low intensity of dressing field (10^{11} W/cm^2), to suppress the sideband oscillation at laser frequency. Being a molecular gas the photoelectron spectrum of N_2 is expected to be complex [183], however due to high resolution of MBETOF, the sideband signal was easily identified. The delay between the higher harmonics and the IR laser pulse is varied and oscillation in photoelectron spectrum generated from nitrogen molecule is observed, as shown in

Fig 5.11a. The sideband oscillation frequency is calculated from the Fourier transform of the sideband photoelectron spectrums (correspond to 18th to 26th even harmonic order). Figure 5.11b shows the fast Fourier transform of the sideband peak, which clearly shows the oscillation frequency at $2\omega_L$ (twice the IR laser frequency) and oscillation at laser frequency (ω_L) is absent.

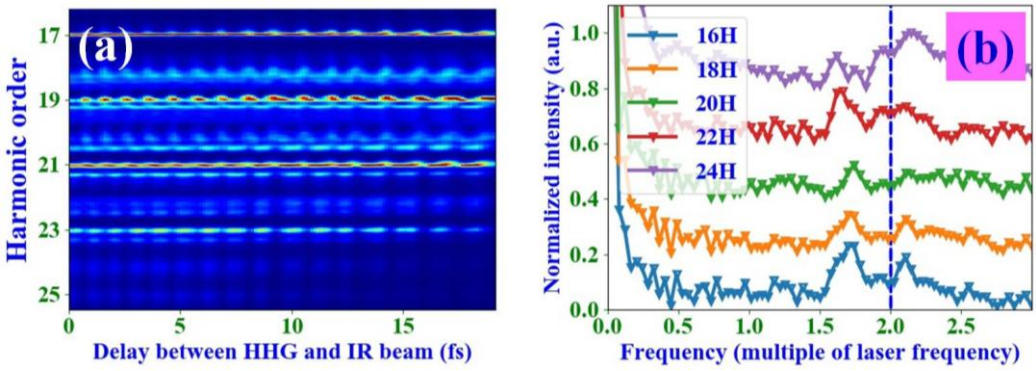

Figure 5.11: *a) The RABITT scan of higher harmonics generated from argon gas (from 17th to 25th odd order) and IR pulse is focused in nitrogen gas sheath. b) The Fourier transform of the sidebands (correspond to 18th to 26th even order) which shows sideband oscillation at $2\omega_L$ frequency.*

The amplitude and relative phase between the harmonics (odd orders) are required to calculate the duration of attosecond pulses in pulse train (using Eq. 5.1). The lineout of the sidebands (correspond to 16th to 24th order) are plotted in Fig 5.12a. The relative phase between the sidebands is calculated with respect to sideband peak correspond to 16th harmonic order (Fig 5.11a). It can be noted from Fig 5.12a that the phase is nearly linear for the sidebands correspond to 16th to 24th order. From the measured relative phase of sideband, the relative phase of odd harmonic orders (from 17th to 25th harmonic) is calculated from Fig 5.12a using Eq 5.11 by arbitrarily assuming the phase of 21st harmonic order to be zero. This will not change the relative

phase between the harmonics and therefore, will not affect the duration of attosecond pulses in pulse train.

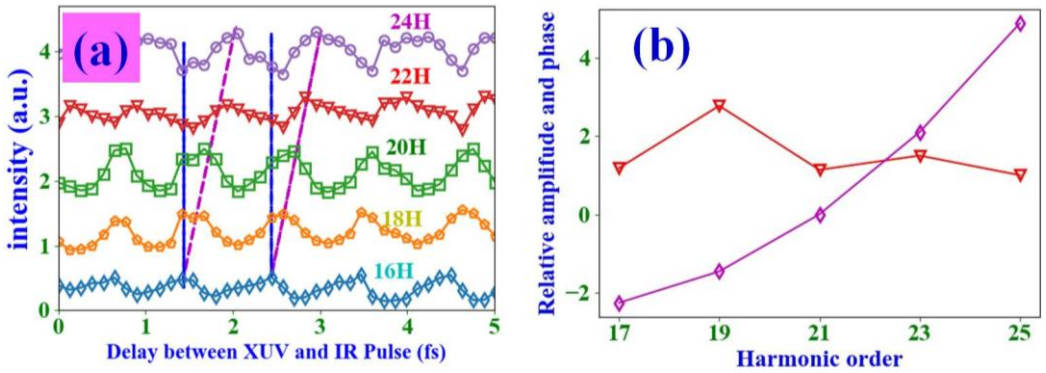

Figure 5.12: *a) The lineout of the RABITT trace from Fig 5.11a for sideband from 16th to 24th orders. The magenta dashed line shows the peak of al sideband order. b) The estimated relative phase (magenta) and amplitude (red) of odd orders from 17th to 25th order.*

The amplitude of the odd harmonic order is measured from the photoelectron count and the photo-ionization cross section at required photon energy. The amplitude is calculated by taking the square root of the ratio of photoelectron count and photo-ionization cross-section. The measured relative amplitude and phase is shown in Fig 5.12b. From the measured phase and amplitude (from Fig 5.12b), the attosecond pulse train is reconstructed using Eq 5.1.

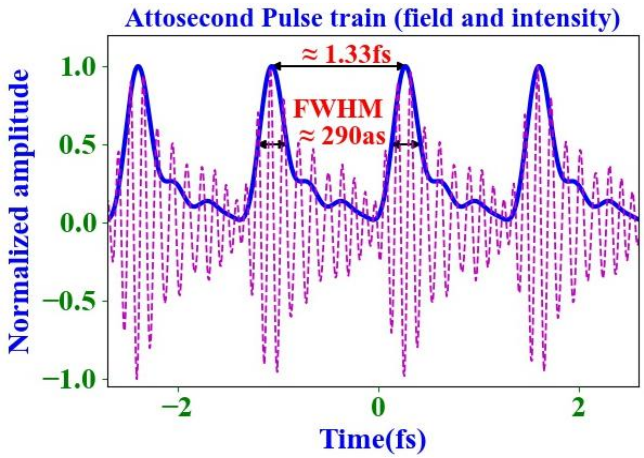

Figure 5.13: *The magenta dash curve shows the field amplitude and the blue solid curve shows the intensity envelope of reconstructed attosecond pulse train. The FWHM width is measured to be ~290as with separation of ~1.33fs between pulses.*

It is to be noted from Fig 5.13, that the duration of attosecond pulse is ~ 290 as (FWHM) and the separation of pulses in pulse train are equal to half the IR laser cycle (~1.33fs). The normalized amplitude of the attosecond pulses in pulse train is shown in Fig 5.13. The magenta curve shows the amplitude and the blue curve shows the intensity of the reconstructed attosecond pulse train (Fig 5.13). It is to be noted from Fig 5.13 that the reconstructed attosecond pulses in the pulse train is asymmetric. In order to understand the asymmetric behaviour of the reconstructed attosecond pulses in pulse train, from the experimentally measured amplitude and relative phase between the higher harmonics, two cases are considered. A) Same amplitude of all odd harmonic orders from 17^{th} to 25^{th} and zeros relative phase and b) take same amplitude of all harmonics and the relative phase from Fig 5.12b.

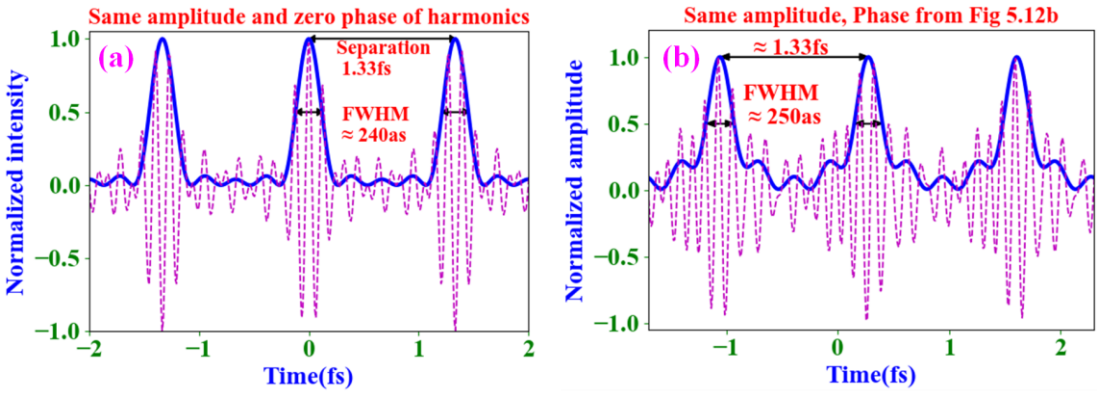

Figure 5.14: *a) Reconstructed pulse train by taking same amplitude and zero phase of 17^{th} to 25^{th} odd harmonic orders b) Reconstructed pulse train by taking same amplitude and the phase of 17^{th} to 25^{th} odd harmonic orders from Fig 5.12b. The magenta dash curve shows the field amplitude and the blue solid curve shows the intensity envelope of reconstructed attosecond pulse train. The FWHM width is measured to be a) ~240as and b) ~250as with separation of half laser period (~1.33fs) between pulses in both cases.*

Figure 5.14 shows the reconstructed attosecond pulse train in two cases. It is to be noted from Fig 5.14a that the width of reconstructed of attosecond pulses for zero

phase and same amplitude is ~240as and the pulse is symmetric. In case b) the pulse duration is ~250as and the pulse is symmetric. This shows that the different relative amplitude of the higher harmonics, is creating the pulse asymmetry and it contributes in increasing the pulse duration of attosecond pulses (~290as) as well.

Although, RABITT is a versatile technique, which uses the photo-ionization technique for estimation of attosecond pulse duration, however this method is only applicable for characterization of attosecond pulses generated from odd harmonics. This technique is not applicable when both odd and even harmonics are present in the spectrum viz. when higher harmonics are generated using two color laser fields. One needs to use other technique viz. iPROOF (improved Phase Retrieval by Omega Oscillation Filtering) [184]. Further, the RABITT technique only estimates the average duration of attosecond pulses in pulse train. For complete characterization of the attosecond pulse train, one has to rely on the other available technique viz. FROG-CRAB, which is based on iterative algorithms [185].

CHAPTER 6:

Multicolour radiography of plasma plumes using higher harmonic source

The carbon containing plasma plume is of great interest due to its application in wide area of research viz. higher harmonic generation [103], charge particle acceleration [186, 187] etc. The characterization of plasma plume is essential to understand the plasma dynamics viz. the ionization and recombination dynamics of the plume [188, 189]. This will help to control the beam charge and energy of the accelerated charge particle [187] and to improve x-ray photon flux generated from such plumes [7,8] etc. The plasma plume may consist of electrons, neutral atoms and highly charged ions [101,191]. Several studies have been reported, which confirms the presence of molecules, small size and large size clusters [192, 193] etc. In laser ablated carbon (graphite) plume, the presence of small molecular cluster viz. carbon dimer molecule (C_2) and large size clusters viz. fullerenes (C_{60}, C_{70} etc.) has been reported [193-195]. The large clusters in the plume are mostly formed from the aggregation of the small carbon fragments, which involve significant time and therefore, are observed at longer delays [193-195] after plasma plume formation. Small clusters are formed due to ion-ion recombination or electron-ion recombination [193-195] and can be present in the plume at shorter delays also. The presence of small carbon clusters (C_2) has recently been observed in carbon plume under similar experimental conditions, which leads to enhancement of higher harmonics, generated from such plumes [196].

Several existing techniques can be used for the characterization of plasma plumes. The available techniques, that can be used for plasma plume characterization are laser interferometry [197-198], optical emission spectroscopy [199,200] and light

scattered from the plume [201] etc. In case of interferometry, the density is calculated from the measured fringe shift. This technique is more useful for the estimation of electron density of the plasma plume rather than atoms or ions. If visible / infrared laser (IR) pulses are used for the interferometry, the dominant contribution in the fringe shift is due the free electrons present in the plume; therefore the electron density can preferably be measured using this technique [202-204]. Also, the critical density of the plasma for visible/infrared laser pulse ($\lambda \sim 800$nm) is $\sim 10^{21}$ cm^{-3}, (~ two orders of magnitude smaller than the solid density) [66]. Using this technique, one can measure the electron density of the plume upto critical density ($\sim 10^{21}$ cm^{-3}) viz. for underdense plasma region only. The x-ray interferometry can alternatively be used for measurement of higher electron density (critical density $\propto \lambda^{-2}$). However, the design of x-ray interferometer is a challenging task, due to unavailability of highly reflecting mirrors and difficulty in analysis of the recorded data [203, 204]. The other technique is optical emission spectroscopy [201], in which the optical emission from plasma species arises from certain electronic transitions, is recording and analysed. The OES can give estimate of only average density information of plasma. In principle, the average density profiles of multiple species viz. neutral atom, ions, molecules etc., can be estimated using OES using optical filters, which can selectively pass a narrow wavelength emission from a particular charged species / neutral atom [14]. The plasma characterization can also be performed from the light scattering from plasma, which can provide the density information [203]. However, like OES the average density of the plasma particle can only be calculated.

In recent years, x-ray radiography is used for determination of density profile of gas atoms ejected from gas jets. Several studies on gas jet characterization using x-ray radiography had been carried out (by only few research groups), using nano-

second x-rays generated by focusing a nano-second infrared (IR) laser pulse on solid target [205–208]. In gas jets, the typical expansion speed of gases from nozzle are ~100m/s, therefore the gases will hardly expand in nanosecond duration (~100 nm) [206]. The nanosecond duration x-ray source is sufficient for the radiography of gas jets, as the blurring in the radiogram image (due to motion of gas particle in the jet, also known as motion blurring / hydrodynamic blurring) will be small and can be safely ignored. Thus, the role of x-ray pulse duration in motion blurring is insignificant, in the measurement of 2D density profile of gases ejected from the gas nozzle.

In plasma plumes formed by focusing a multi-picosecond (≈200ps) laser pulse on solid target, the expansion speed is significantly higher (~ 10^4 to 10^5 m/s) [209]. Therefore, the use of nanosecond x-ray radiography will lead to significant motion blurring (due to high expansion speed ~10-100μm/ns). This can be minimized by using an ultrashort duration x-rays as a backlighter source. One of the most suitable candidates for this purpose is higher harmonic generation based coherent x-ray source, which can deliver extreme ultraviolet pulses of sub femtosecond duration [210].

Apart from this, the gas jet characterization can be performed using monochromatic x-rays, as one need to estimate the density profile of only one species viz. neutral gas atom [207]. The scenario is different in case of plasma plumes, where neutral atoms, the charged ions and molecules can simultaneously be present [192-193]. The simultaneous estimation of these species requires the x-ray radiography of the plasma plume at multiple discrete wavelengths, which is a highly challenging task [211]. This measurement requires a backlighter source, which has multiple discrete wavelengths in the spectrum. A spectrograph is also required, which can disperse these wavelengths, after recording the x-ray radiogram of the plasma plume [211].

In this chapter, we present our study on the first demonstration of multicolor radiography of plasma plumes using higher harmonic radiation as a backlighter source. The presence of multiple discrete wavelengths in harmonic spectrum facilitates to record x-ray radiogram simultaneously at multiple wavelengths and its ultrashort duration will reduce the motion blurring effect. In the present chapter, the characterization of the plasma plume formed by focusing an uncompressed 200ps Ti: Saphhire laser pulse on solid graphite target is discussed. The backlighter higher harmonic source from 11^{th} order (~ 15eV) to 21^{st} order (~ 30eV) with a cutoff extending to 29^{th} harmonic order of Ti: sapphire laser pulse ($\lambda\sim$ 800nm) [103] is generated from the other graphite plume. This technique is used to measure the density profile of multiple species of carbon plume viz. carbon atom, singly charged carbon ion and carbon dimer molecule as well as the calculation of plasma expansion speed [211].

6.1 Experimental Details

The experiment was performed using 10 TW Ti: Sapphire laser system, operating at ~2 TW at 10Hz repetition rate. A schematic of the experimental setup is shown in Fig 6.1. In the experiment, an uncompressed Ti: Sapphire laser pulse of 200ps duration is splitted into two parts using a beam splitter (T ~ 45% and R ~ 55%). The transmitted part of the splitted beam is send to the laser pulse compressor, where it is compressed to ~45fs duration with laser pulse energy of 80mJ. This laser pulse is referred to as main pulse. The reflected uncompressed laser beam (τ ~ 200ps) is further splitted into two parts using beam splitter BS1 (see Fig 6.1). The reflected laser beam (τ ~ 200ps) from the beam splitter BS1 is focused on the carbon (graphite) target using a plano-convex lens of focal length ~ 500mm to an intensity of 10^{10}-10^{11}

W/cm^2. This part of laser beam is referred to as prepulse laser beam. The plasma plume formed by the prepulse laser beam is marked as PP1 in Fig 6.1. For higher harmonic generation, main laser pulse (τ ~ 45fs) is focused in the plasma plume PP1, to an intensity of ~10^{14}-10^{15} W/cm^2 after an optimum delay (~ 50 ns) [103]. The generated harmonics are dispersed and detected using FFGS (see section 2.3.1 for details).

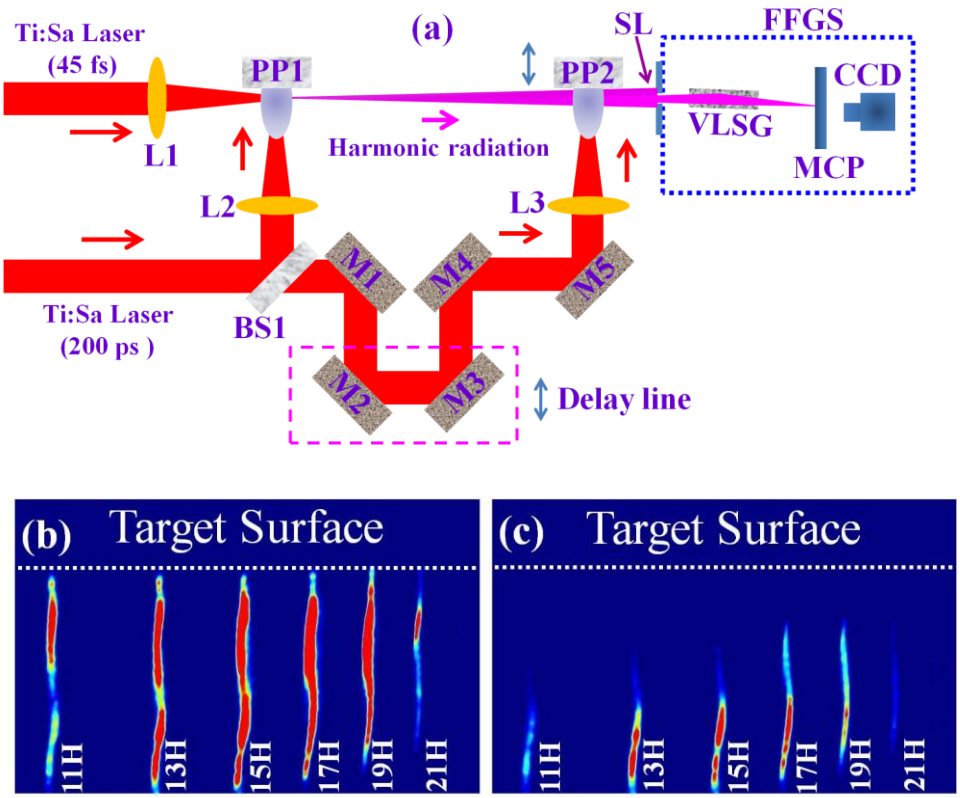

Figure 6.1: *a) A schematic of experimental setup used for the multicolour radiography of plasma plume. The BS stands for beam splitter, M1-M5 are 45deg dielectric mirror, L1-L3 are focusing lenses, PP1 and PP2 are two plasma plumes formed on two solid target surfaces. The higher harmonic spectrum from 11th to 21st harmonic orders b) absence and c) presence of plasma plume PP2.*

Intense harmonics from 11th to 21st order is observed in a single frame recorded using FFGS. The laser and plasma plume parameters viz. prepulse intensity, main pulse intensity, the plasma plume (PP1) position relative to laser

focus etc, are further optimized to achieve high intensity, nearly uniform spatial profile and good shot-to-shot stability (~5% calculated from 10 consecutive laser shots). The uncompressed laser pulse (τ ~ 200ps) transmitted from beam splitted BS1, is focused on second carbon (graphite) target (see Fig 6.1) using ~500 mm focal length plano-convex lens to intensity ~ 10^{11} W/cm^2, to form second plasma plume (marked as PP2 in Fig 6.1). The higher harmonics (from 11th to 21st order) generated from the first carbon plume acts as a backlighter source and passes through the second plume PP2. The target surfaces of plumes PP1 and PP2 are made parallel, so that the harmonic generated from PP1 should pass through plume PP2. A delay line is installed between the plasma plume PP1 and PP2, to study the dynamics of plasma plume PP2 (see Fig 6.1a). After passing through the plume PP2, all harmonics from 11th to 21st order is dispersed and detected using FFGS. Figure 6.1b shows a typical harmonic spectrum generated from carbon plume PP1, without passing through plume PP2. It can be seen from Fig 6.1b that the higher harmonics from 11th to 21st order has nearly smooth spatial profile. It can be seen from Fig 6.1b that the spatial profile of harmonics is slightly wiggling. This may be due to the variation of laser intensity as well as the phase matching condition, which affects the spatial profile of higher harmonic source. The higher intensity of laser pulse leads to higher ionization of medium, which deteriorates the phase matching condition and reduces the harmonic intensity. Further, the high intensity pulse also leads to nonlinear process such as self- phase modulation, which leads to spectral shift of the harmonics spectrum. Thus, the presence of wiggling in the spatial profile is due to combined effect of phase matching as well as the spatial variation of laser intensity across the profile. At the peak of laser pulse, the harmonic intensity is minimal and it increases on both sides.

Figure 6.1c shows change in the intensity profiles of the harmonics, after passing through plume PP2. The reduction in the harmonic intensity (see Fig 6.1c), may have contributions from the neutral atoms, ions and molecules, present in the plasma plume PP2. Owing to the different photo-absorption cross sections and density (of neutral atoms, ions and molecules), the contribution of each species will be different. The simultaneous recording of the harmonic transmissions at different wavelength will enable us to estimate the density of these species [211]. As the transmission is recorded at multiple wavelength (11^{th} harmonic order to 21^{st} harmonic order of 800nm Ti: sapphire laser pulse) simultaneously, the radiography is referred to as multicolour radiography. The plasma plume PP2 is placed at sufficient distance (~ 120mm) away from the plume PP1, so that the harmonic radiation should not be directly generated by the residual laser beam interaction with the second plume PP2. Also, the harmonic beam size at the position of plasma plume PP2 (~1.6mm) is sufficient to record the complete radiogram of plasma plume PP2 in expansion direction [211].

For the analysis of the radiogram, the background emission from plasma plume PP2 is taken into account. Also, the FFGS spectrograph slit is kept parallel to the plasma plume expansion direction, so that the transmission profile (parallel to slit) of all harmonic orders after passing through plasma plume PP2 can be recorded. From the change in harmonic intensity after passing through PP2, the density profile of plasma species (of PP2) in the expansion direction can be calculated. Further, after recording the transmission profile at one transverse position, the plume PP2 is shifted vertically (transversally), so that the density profile at all transverse location can be recorded. The transmission profiles of plasma plume PP2 at different vertical

position are stacked together to generate 2D radiogram of the plasma plume (PP2) [211].

6.2 Results and Discussions

The spatial profile of 13th harmonic order, at optimum condition of all laser and plasma plume parameters is shown in Fig 6.2a. Smooth profile of 13th harmonic order was recorded upto ~ 1mm distance away from the target surface. Figure 6.2b shows the recorded spatial profile of 13th harmonic order, after it passes through the carbon plasma plume PP2.

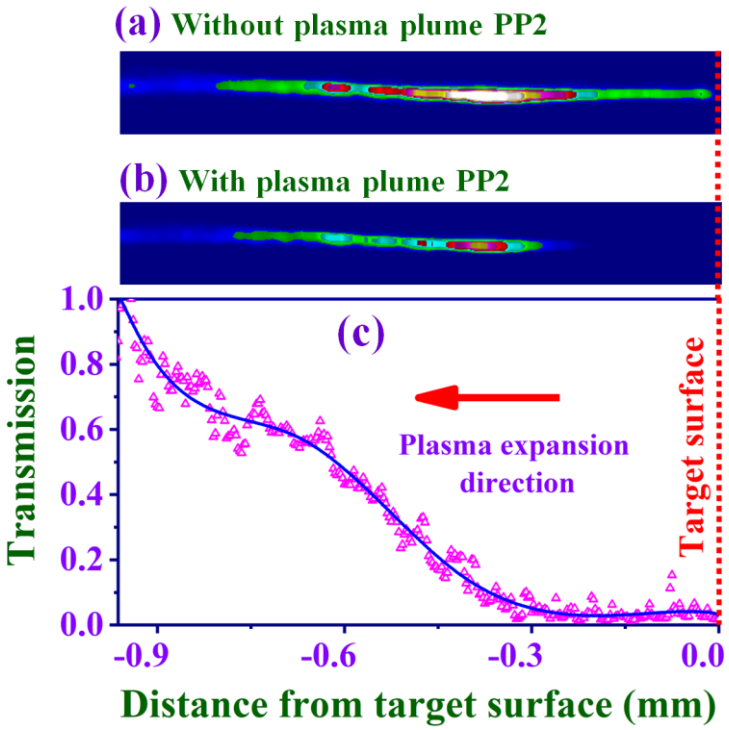

Figure 6.2: *a) The spatial profile of 13th harmonic order without passing through plasma plume PP2 b) the spatial profile after passing through plasma plume PP2 and c) the transmission of 13th harmonic order calculated by ratio of (b) and (a). The upper-triangle symbol shows the calculated transmission from ratio of (b) and (a), and the solid blue line is the best fit.*

The absorption of the harmonics can be clearly seen in Fig 6.2b. Before calculation of transmission, the background is subtracted from Fig 6.2a and Fig 6.2b both. Then, the transmission of 13^{th} harmonic order is calculated by taking the ratio of spatial profiles in Fig 6.2b and Fig 6.2a. The calculated transmission profile is shown in Fig 6.2c. It can be seen that the transmission becomes close to one at ~0.95mm away from the target surface and decreases to very small value close to the target surface. The transmission profile is recorded at different transverse location by shifting the plasma plume PP2 vertically, till the absorption in the spatial profile of harmonics is observed. The plasma plume PP2 is shifted vertical in a step of 50μm on either side of the plume centre to record the 2D radiogram, to a total distance of ~ 1.2mm. The transmission profiles of the harmonics recorded at different vertical position in PP2 are stacked together, to generate the 2D radiogram of the plasma plume PP2. This process is repeated for all harmonics from 11^{th} to 21^{st} order. Further, the 2D radiogram image is smoothened to remove the sharp boundaries between the two transmission profiles in the stack. The smoothened radiogram is shown in Fig 6.3. Figure 6.3a-f shows 2D radiogram of PP2 for a) 11^{th} to f) 21^{st} harmonic orders.

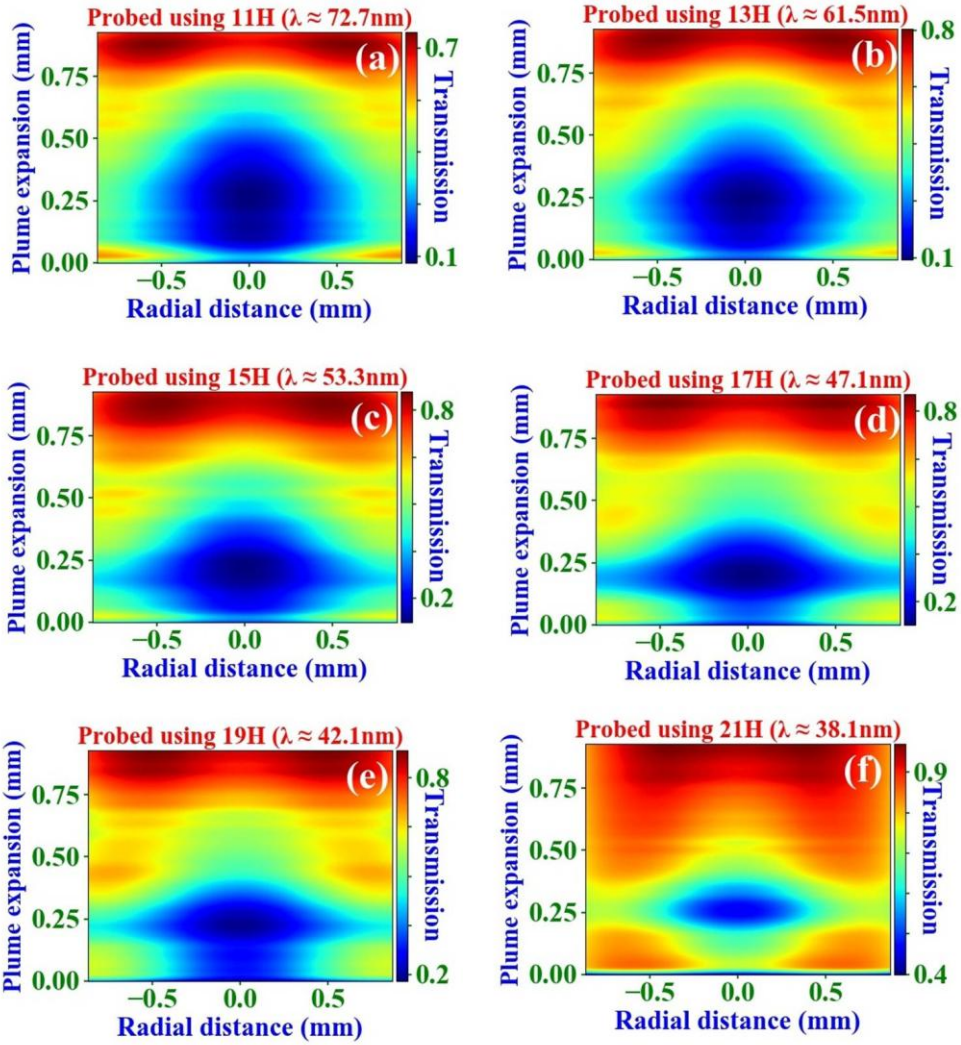

Figure 6.3: *A 2D radiogram generated from the stack of 1D transmission profiles of a) 11th b) 13th c) 15th d) 17th e) 19th and f) 21st orders after passing through the plasma plume PP2.*

It can be seen from Fig 6.3 that, at ~ 200-250μm away from the surface, transmission is minimum for all harmonic orders and with increase in harmonic order, the transmission close to the target surface increases. These transmission profiles (Fig 6.3a-f) can be used for the calculation of the density profile of species, present in plasma plume PP2. For this, it is important to investigate all possible mechanisms as well as the dominant phenomena which are responsible for reduction in the higher harmonic intensity after passing through PP2. There are various possible factors that

may contribute in the reduction of harmonic intensity after it passes through the plume PP2. The first is refraction of harmonic radiation due to the free electrons and ions present in plasma plume. As plasma plume is formed by focusing laser pulse on target surface, it will lead to form a density gradient of electrons with maximum density close to target surface and gradually falling outwards [212]. This electron density gradient will lead to the gradient in refractive index, which refracts the harmonic beam, and may reduce the harmonic intensity. The refraction effects will be smaller, due to smaller wavelength of the harmonic source (for 11^{th} harmonic order λ ~ 72.7 nm and for 21str harmonic order λ~38.1nm), still it may be finite. To further reduce this effect, the study is carried out after a significantly long delay (~ 50ns), so that the electron density will be significantly reduced and the refraction effect can be safely ignored. In the similar way, the refraction effect due to presence of ions in the plume can also be neglected.

The other factors, which may contribute to the reduction in harmonic intensity is a) scattering and b) photo-absorption. Among these two processes, the dominant contribution can be inferred from the cross-section of these two processes. The scattering and photo-absorption cross section are compared in the wavelength range corresponding to 11^{th} harmonic ($\lambda \approx 72.7$nm) to 21^{st} harmonic order ($\lambda \approx 38$nm) [213]. The total scattering cross section (sum of coherent and incoherent cross sections) and photo-absorption cross section at wavelength corresponding to 11^{th} harmonic orders ($\lambda \approx 72.7$nm) is 1.43×10^{-2} cm^2/gm and 3.045×10^{5} cm^2/gm respectively. At wavelength corresponding to 21^{st} harmonic order (λ~38.1nm), the total scattering cross section and photo-absorption cross section is 6.8×10^{-2} cm^2/gm and 1.5×10^{5} cm^2/gm respectively. It is evident from the cross-section values that the total scattering cross section is very small compared to the photo-absorption cross section in the

wavelength range of our study (λ~38.1nm to λ~72.7nm) and can be ignored. The photo-absorption is taken to be a dominant mechanism, which contributes to the reduction of harmonic intensity, after harmonics passing through PP2.

Next, the generated 2D radiogram (Fig 6.3a-f), can be used for measurement of density profiles of different species (atoms, ions, molecules etc.) present in the plume. Let us assume that the target surface is placed in x-z plane, where 200ps Ti: sapphire laser pulse is focused to form plasma plume, *y* is the direction of plasma plume expansion and the backlighter higher harmonic source propagates in the carbon plume in *z* direction. The 2D transmission profile of the plasma plume species (neutral atom, ionic species and molecular species) for a given harmonic order can be expressed using Beer Lamberts law [211]

$$Tr(x,y) = \exp\left\{-\int_z \left(\frac{m_m}{N_a}\rho_m(x,y)\mu_{m,\mathrm{m}} + \frac{m_n}{N_a}\rho_n(x,y)\mu_{m,n} + \frac{m_i}{N_a}\rho_i(x,y)\mu_{m,\mathrm{i}}\right)dz\right\} \quad (6.1)$$

Where $\rho_m(x, y)$, $\rho_n(x, y)$ and $\rho_i(x, y)$, are 2D number density profile of molecules, neutral atoms and ions respectively, $\mu_{m,m}$, $\mu_{m,n}$ and $\mu_{m,i}$, *are* mass attenuation coefficients for molecules, neutral atoms and ions present in the plasma plume, [*Tr(x,y)*] is two dimensional transmission profile of higher harmonics at a given photon energy, *z* is distance travelled by the higher harmonics in plasma plume (PP2), m_m, m_n, m_i is the atomic / molecular weight of molecule, neutral atom and ions and N_a is the Avogadro number. The Eq 6.1 takes into account the contribution of all species present in the carbon plume PP2, which is to be characterized. To measure density profile of one species, only one equation is needed. However, more number of equations is required to calculate the density profile of multiple species.

In the present study, 2D transmission profile is recorded at multiple wavelengths simultaneously, to measure the density profile of multiple species of the

plume. Further, in order to calculate the accurate density profile, the measured density profile from the 2D radiogram using Eq 6.1, is inverse Abel transformed. For Abel inversion, the plasma expansion is taken to be cylindrically symmetric in x-z plane. In the present work, the Abel inversion is carried out using a "PyAbel" module of Python program [214].

The measurement of density profile of different species requires the photo-absorption cross-section at desired photon energy. The photo-absorption cross-section for the neutral atom, in wavelength range from ~38nm (21^{st} harmonic order) to ~72.7 nm (11^{th} harmonic order), is taken from NIST database. For singly charged ions and carbon dimer molecule (C_2), the cross-section database is not available with the NIST, thus it is taken from the literature [215-218]. It can be noted here, that the photo-absorption cross section of singly charged carbon ion, becomes significant at photon energy higher than ~25eV. Therefore, the photo-absorption for singly charged ions is neglected for 11^{th} (photon energy ~17eV) and 13^{th} harmonic order (photon energy ~ 20eV) and it is considered for the higher harmonics above 17^{th} order (photon energy ≈26.3eV). In case of higher charge states (e.g. C^{2+}), the photo-absorption cross section becomes significant only beyond ~40eV [218], which is beyond the wavelength range of the higher harmonics (~17eV to ~32eV) used in the present study. Hence, we can only calculate the density profile of neutral carbon atom (CI), singly charges carbon ion (C^{1+}) and carbon dimer molecule (C_2). The density profile of $C_2(\rho_{C2}(x, y))$ molecule, $CI(\rho_n(x, y))$ and $C^{1+}(\rho_{1+}(x, y))$ can be calculated from the 2D transmission profile of 11^{th}, 13^{th} and 17^{th} harmonic order (as shown in Fig 6.3) using Eq 6.1.

$$-\ln\left[Tr_{13}(x,y)\right]N_a = m_C d\left(\rho_n(x,y)\mu_{13} + 2\rho_{C_2}(x,y)\mu_{C_2,13}\right) \quad (6.2)$$

$$-\ln\left[Tr_{11}(x,y)\right]N_a = m_C d\left(\rho_n(x,y)\mu_{11} + 2\rho_{C_2}(x,y)\mu_{C_2,11}\right) \quad (6.3)$$

$$-\ln\left[Tr_{17}(x,y)\right]N_a = m_C d\left(\rho_n(x,y)\mu_{17} + \rho_{1+}(x,y)\mu_{17,1+} + 2\rho_{C_2}(x,y)\mu_{C_2,17}\right) \quad (6.4)$$

Where $Tr_{11}(x, y)$, $Tr_{13}(x, y)$ and $Tr_{17}(x, y)$ is the 2D transmission profiles of 11^{th} , 13^{th} and 17^{th} harmonic orders shown in Fig 6.3, μ_{11}, μ_{13}, μ_{17} is photo-absorption cross section of neutral carbon atom and $\mu_{C2,11}$, $\mu_{C2,13}$, $\mu_{C2,17}$ is the photo-absorption cross section of C_2 molecule for 11^{th}, 13^{th} and 17^{th} harmonic orders respectively, ρ_n, ρ_{1+}, and ρ_{C2} are the 2D density profiles of neutral carbon atom, single charged carbon ion and carbon dimer molecules, $\mu_{17,1+}$ is the photo-absorption cross section of singly charged carbon ions for 17^{th} harmonic order and d is the distance travelled by the higher harmonic radiation in carbon plume PP2. The Eq 6.2, Eq 6.3 and Eq 6.4 can be analytically solved to calculate the 2D density profile of carbon atom (CI), singly charged carbon ion (CII / C^{1+}) and C_2 molecule. The analytical expression of the density profile of CI ($\rho_n(x, y)$), CII ($\rho_{1+}(x, y)$) and C_2 ($\rho_{C2}(x, y)$) obtained from Eq. 6.2-6.4 can be expressed as

$$\rho_{C_2}(x,y) = \frac{N_a}{2m_C d}\left(\frac{\left(K_{13}\mu_{11} - K_{11}\mu_{13}\right)}{\left(\mu_{11}\mu_{C_2,13} - \mu_{13}\mu_{C_2,11}\right)}\right) \quad (6.5)$$

$$\rho_n(x,y) = \frac{N_a}{m_C d}\left(\frac{\left(K_{13}\mu_{C_2,11} - K_{11}\mu_{C_2,13}\right)}{\left(\mu_{13}\mu_{C_2,11} - \mu_{11}\mu_{C_2,13}\right)}\right) \quad (6.6)$$

$$\rho_{1+}(x,y) = \frac{1}{\mu_{17,1+}}\left(\frac{N_a}{m_C d}K_{17} - \mu_{17}\rho_n(x,y) - 2\mu_{C_2,17}\rho_{C_2}(x,y)\right) \quad (6.7)$$

Where $K_{11} = -\ln\left[Tr_{11}(x,y)\right]$, $K_{13} = -\ln\left[Tr_{13}(x,y)\right]$ *and* $K_{17} = -\ln\left[Tr_{17}(x,y)\right]$

From the 2D radiogram of carbon plume (Fig 6.3), 2D density profiles of CI, C^{1+} and C_2 is calculated using Eq 6.5 to Eq 6.7. For absolute radial density profiles, the 2D density profile is inverse Abel transformed [214]. The density profile of the three species (CI, CII and C_2) after Abel inversion is shown in Fig 6.4a-c.

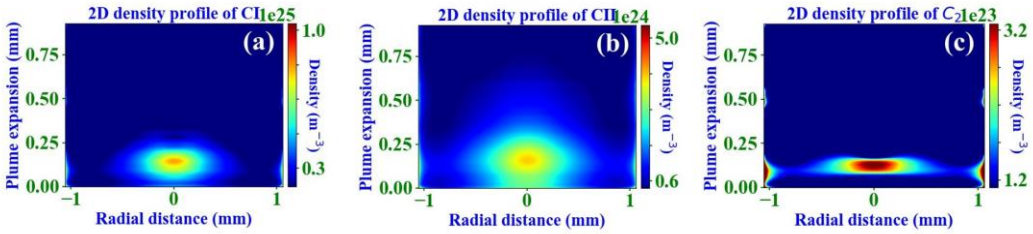

Figure 6.4: *The ABEL inverted 2D density profiles of a) neutral carbon atom (CI) b) singly charged carbon ion (CII) and c) carbon dimer molecule (C_2).*

The two intense regions at ±1mm in Fig 6.4a-c is numerical artefact and it arises due to the inverse Abel transformation of the 2D density profile. The relative density of these species (CI, CII and C_2) is compared by taking a line profile at the radially centre position ($\rho=0$). Figure 6.5 shows the line profile (at $\rho=0$) in the expansion direction of carbon plume. It can be seen from Fig 6.5a-c that all three species shows peaks in their density profile at different spatial positions, away from the target surface.

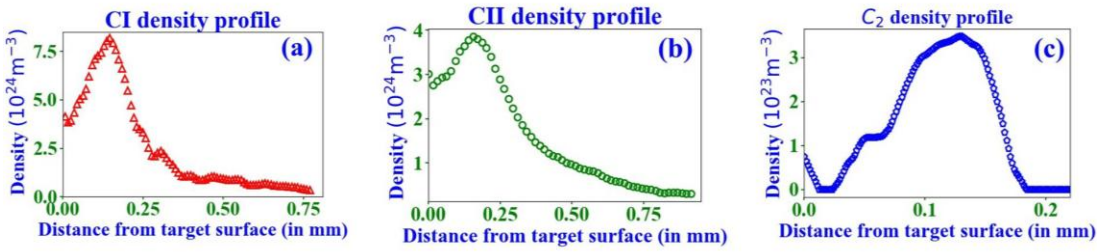

Figure 6.5: *Line profile at radially centre position ($\rho=0$) of the 2D density profile as shown in Fig 6.4 for a) for neutral carbon atom (CI) b) singly charged carbon ion (CII) and c) carbon dimer molecule (C_2).*

The peak density of CI, CII and C_2 is calculated to be ~8×10^{24} m^{-3}, ~4×10^{24} m^{-3} and ~3.5×10^{23} m^{-3}, at spatial position of ~150μm, ~170 μm and ~120μm away from the target surface respectively. The expansion speed of the plasma plume front consist of neutral atom is calculated to be ~10^4 m/s (expansion distance ~ 0.5mm) and for the singly charge carbon ion (*CII*) is calculated to be ~2×10^4 m/s (expansion distance ~ 0.9mm). The similar expansion speed of graphite plume formed by 20ns laser pulse has been reported by Hoffman et al [219], where the expansion velocity is measured to be ~3 $\times10^4$ m/s and ~4.5 $\times10^4$ m/s for CI and CII respectively. The expansion speed reported by Hoffman et al, is on higher side than our measured speed. The difference may be attributed to the high laser fluence ~ 75J/cm^2 as compared to ~ 25J/cm^2 in the present study. In case of molecule (carbon dimer molecule), the expansion speed is calculated to be ~4×10^3 m/s, which is similar to the other reported values, where the expansion speed has been estimated in presence of background gases [194]. Our experimentally observed value matches with the slow moving peak of the C_2 molecule.

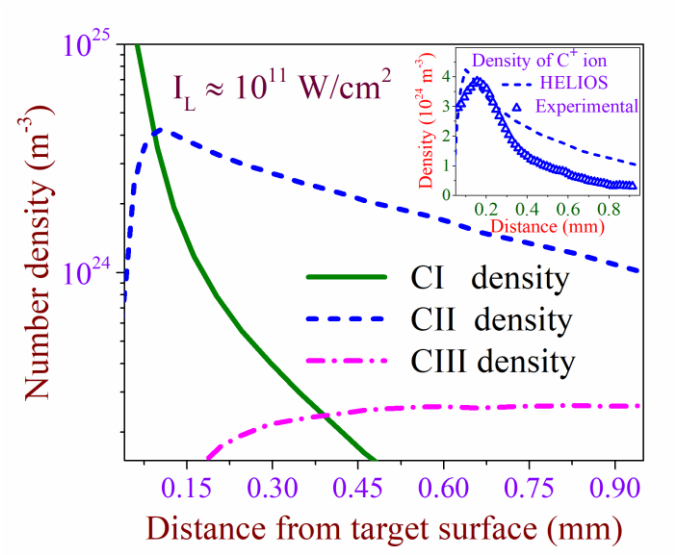

Figure 6.6: *The density profile of CI, CII and CIII calculated using 1D hydrodynamic simulation (HELIOS).The inset shows the comparison of density profile of CII between the calculated and experimentally measured value.*

It is also important to discuss here that, only density profile of neutral carbon atom and singly charged carbon ion is calculated, however, the higher charge states (C^{2+}, C^{3+}…) may be present in the plume. It is necessary to minimize the density of higher charge state, to reduce the possible source of error in our measurement. To ensure this, first low intensity of 200ps laser pulse (~10^{11} W/cm^2) is used and also, it is allowed to expand for sufficient time (≈50ns).

The density profile of neutral carbon atom and charged ions is calculated in our experimental condition, using a 1D hydrodynamic simulation. Figure 6.6 shows the density profile calculated using HELIOS (1D hydrodynamic simulation code) for the neutral carbon atom, singly (blue dashed curve) and doubly (magenta dash-dot curve) charged carbon ion. The density of CI and CII is found to be ~ 8×10^{24} m^{-3} and ~ 4×10^{24} m^{-3} at ~ 100 μm and ~ 170 μm distances away from target surface, which is close to the measured value. The experimentally measured and the calculated value using 1D hydrodynamic simulation is plotted, in inset of Fig 6.6, for singly charged carbon ion. The peak density of the two curves matches well, whereas there is deviation in the density profiles. This deviation may be due to density over estimation by the HELIOS 1D hydrodynamic code. It can also be seen from Fig 6.6 that the density of doubly charged carbon ion (CIII) is negligible, near the target surface. Although, the density is finite at distance greater than 0.3mm, however compared to CI and CII, it is very small (10^{23} m^{-3}). As the hydrodynamic code doesn't take into account the molecule formation, it cannot calculate the molecular density. Also, a dip is observed in the density profile of neutral atom close to targets surface, which may be due to formation of carbon dimer molecule and is not taken into account by the HELIOS code.

There are several sources of error which contribute to estimation of plume density. These include the error in measurement of photo-absorption cross section, shot to shot change in the detected harmonic intensity, error in inverse Abel transform. The error in photo-absorption cross section is taken to be ~ 20% [213] and in Abel inversion is taken to be ~2% [220]. The other source of error is shot to shot fluctuation in harmonic intensity which is estimated to be ~ 5% and it is accounted in transmission (calculated using lamberts' law: "*Transmission (T) = exp (-$\mu_m \rho x$)*". The error in the measured density can be expressed as

$$\frac{\Delta\rho}{\rho} = \frac{1}{\ln(T)}\frac{\Delta T}{T} + \frac{\Delta\mu_m}{\mu_m} + \frac{\Delta x}{x} \qquad (6.8)$$

The error in density measurement is calculated using Eq 6.8. After placing $\Delta T/T$ is ~ 0.05 (taken close to point of maximum density), $\Delta\mu_m/\mu_m$~0.2, $\Delta x/x$ is ~ 0.01. The maximum error in the measurement is calculated to be ~ 35%.

REFERENCES

[1] “Stimulated Optical Radiation in Ruby”, T. H. Maiman, *Nature*, **60**, *187*, 493.

[2] “Generation of Optical Harmonics”, P. A. Franken, A. E. Hill, C. W. Peters, and G. Weinreich, *Phys. Rev. Lett.*, **1961**, *7*, 118–119.

[3] “Optical Third-Harmonic Generation in Gases”, G. H. C. New and J. F. Ward, *Phys. Rev. Lett.*, **1967**, *19*, 556–559.

[4] “Nonlinear Optics”, Boyd, Robert W Boyd, **2008**, Academic Press, USA

[5] “Fundamentals of Attosecond Optics”, Z. Chang, **2016**, CRC Press.

[6] “Studies of multiphoton production of vacuum-ultraviolet radiation in the rare gases”, A. McPherson, G. Gibson, H. Jara, U. Johann, T. S. Luk, I. A. McIntyre, K. Boyer, and C. K. Rhodes, *Journal of the Optical Society of America B*, **1987**, *4*, 595.

[7] “Applications of high-order harmonics”, A. L’Huillier, D. Descamps, A. Johansson, J. Norin, J. Mauritsson, and C.-G. Wahlström, *Eur. Phys. J. D*, **2003**, *26*, 91–98.

[8] “High-flux source of coherent XUV pulses for user applications”, O. Hort, M. Albrecht, V. E. Nefedova, O. Finke, D. D. Mai, S. Reyné, F. Giambruno, F. Frassetto, L. Poletto, J. Andreasson, J. Gautier, S. Sebban, and J. Nejdl, *Opt. Express, OE*, **2019**, *27*, 8871–8883.

[9] “Spatial coherence of short wavelength high-order harmonics”, T. Ditmire, J. W. G. Tisch, E. T. Gumbrell, R. A. Smith, D. D. Meyerhofer, and M. H. R. Hutchinson, *Appl Phys B*, **1997**, *65*, 313–328.

[10] “Temporal Coherence of Ultrashort High-Order Harmonic Pulses”, M. Bellini, C. Lyngå, A. Tozzi, M. B. Gaarde, T. W. Hänsch, A. L’Huillier, and C.-G. Wahlström, *Phys. Rev. Lett.*, **1998**, *81*, 297–300.

[11] “Observation of a Train of Attosecond Pulses from High Harmonic Generation”, P. M. Paul, E. S. Toma, P. Breger, G. Mullot, F. Augé, P. Balcou, H. G. Muller, and P. Agostini, *Science*, **2001**, *292*, 1689–1692.

[12] “Extreme ultraviolet interferometry measurements with high-order harmonics”, D. Descamps, C. Lyngå, J. Norin, A. L’Huillier, C.-G. Wahlström, J.-F. Hergott, H. Merdji, P. Salières, M. Bellini, and T. W. Hänsch, *Opt. Lett., OL*, **2000**, *25*, 135–137.

[13] "Lloyd's mirror interference lithography with EUV radiation from a high-harmonic source", H. Kim, P. Baksh, M. Odstrcil, M. Miszczak, J. G. Frey, L. Juschkin, and W. S. Brocklesby, *Appl. Phys. Express*, **2016**, *9*, 076701.

[14] "Transient absorption spectroscopy using high harmonic generation: a review of ultrafast X-ray dynamics in molecules and solids", G. Romain, M. Hugo J. B., G. Alexander, N. Daniel M., and L. Stephen R., *Phil. Trans. Royal Soc. A: Mathematical, Physical and Engineering Sciences*, **2019**, *377*, 20170463.

[15] "Ultrafast Demagnetization Dynamics at the M Edges of Magnetic Elements Observed Using a Tabletop High-Harmonic Soft X-Ray Source", C. La-O-Vorakiat, M. Siemens, M. M. Murnane, H. C. Kapteyn, S. Mathias, M. Aeschlimann, P. Grychtol, R. Adam, C. M. Schneider, J. M. Shaw, H. Nembach, and T. J. Silva, *Phys. Rev. Lett.*, **2009**, *103*, 257402.

[16] "Investigations of above-threshold ionization using subpicosecond laser pulses", R. R. Freeman and P. H. Bucksbaum, *J. Phys. B: At. Mol. Opt. Phys.*, **1991**, *24*, 325–347.

[17] "Atomic physics with super-high intensity lasers", M. Protopapas, C. H. Keitel, and P. L. Knight, *Rep. Prog. Phys.*, **1997**, *60*, 389–486.

[18] "Mutual Refraction of Electrons and Photons", T. W. B. Kibble, *Phys. Rev.*, **1966**, *150*, 1060–1069.

[19] "Ionization in the Field of a strong Electromagnetic wave", L. V. Keldysh, *Sov. Phys. JETP*, **1964**, 20, 1307.

[20] "Tunneling and barrier-suppression ionization of atoms and ions in a laser radiation field", N. B. Delone and V. P. Krainov, *Physics Uspekhi*, **1998**, *41*, 469.

[21] "Tunnel ionization of complex atoms and of atomic ions in an alternating electromagnetic field", M. V. Ammosov, N. B. Delone and V. P. Krainov, *Sov. Phys. JETP*, **1986**, 64, 1191

[22] "Multiphoton Ionization of Atoms", *Advances in Electronics and Electron Physics*, 36, L. Marton Ed., **1975**, 57–152, *Academic Press*

[23] "Multiphoton ionization of atoms", G. Mainfray and G. Manus, *Rep. Prog. Phys.*, **1991**, *54*, 1333–1372.

[24] "Laser-Induced Breakdown in Optical Materials", W. L. Smith, *Opt. Express*, **1978**, *17*, 175489.

[25] "Elementary processes with two quantum transitions", M. Göppert-Mayer, *Annals Phys*, **1931**, *401*, 273–294.

[26] "Connection Between High-Harmonic Generation and Above-Threshold Ionization", W. Bing-Bing, L. Xiao-Feng, G. Liang-Hui, F. Pan-Ming, G. Dong-Sheng, and R. R. Freeman, *Chinese Phys. Lett.*, **2001**, *18*, 1199–1201.

[27] "Generation of coherent keV x-rays with intense femtosecond laser pulses", J. Seres, P. Wobrauschek, C. Streli, V. S. Yakovlev, E. Seres, F. Krausz, and C. Spielmann, *New J. Phys.*, **2006**, *8*, 251–251.

[28] "Quantum Mechanics of One and Two-Electron Atoms", Hans A Bethe and Edwin E. Saltpeter, **1957,** Springer-Verlag**.**

[29] "Theory of barrier-suppression ionization of atoms", V. P. Krainov, *J. Nonlinear Optic. Phys. Mat.*, **1995**, *04*, 775–798.

[30] "Tunneling ionization of atoms by low-frequency electromagnetic field", A. M. Perelomov, V. S. Popov, and M. V. Terent'ev, *Soviet Phys JETP*,**1966**, 23, 924

[31] "Tunneling ionization of noble gases in a high-intensity laser field", S. Augst, D. Strickland, D. D. Meyerhofer, S. L. Chin, and J. H. Eberly, *Phys. Rev. Lett.*, **1989**, *63*, 2212–2215.

[32] "Near-keV coherent X-ray generation with sub-10-fs lasers", C. Spielmann, C. Kan, N. H. Burnett, T. Brabec, M. Geissler, A. Scrinzi, M. Schnurer, and F. Krausz, *IEEE Journal of Selected Topics in Quantum Electronics*, **1998**, *4*, 249–265.

[33] "Atoms in ultra-intense laser fields", K. Burnett, V. C. Reed, and P. L. Knight, *J. Phys. B: At. Mol. Opt. Phys.*, **1993**, *26*, 561–598.

[34] "Harmonic generation in CO2 laser target interaction", N. H. Burnett, H. A. Baldis, M. C. Richardson, and G. D. Enright, *Applied Physics Letters*, **1977**, *31*, 172–174.

[35] "Observation of harmonics in the visible and ultraviolet created in CO_2 laser-produced plasmas", R. L. Carman, C. K. Rhodes, and R. F. Benjamin, *Phys. Rev. A*, **1981**, *24*, 2649–2663.

[36] "Bright Multi-keV Harmonic Generation from Relativistically Oscillating Plasma Surfaces", B. Dromey, S. Kar, C. Bellei, D. C. Carroll, R. J. Clarke, J. S. Green, S. Kneip, K. Markey, S. R. Nagel, P. T. Simpson, L. Willingale, P. McKenna, D. Neely, Z. Najmudin, K. Krushelnick, P. A. Norreys, and M. Zepf, *Phys. Rev. Lett.*, **2007**, *99*, 085001.

[37] "Short-pulse laser harmonics from oscillating plasma surfaces driven at relativistic intensity", R. Lichters, J. Meyer-ter-Vehn, and A. Pukhov, *Physics of Plasmas*, **1996**, *3*, 3425–3437.

[38] "Coherent Wake Emission of High-Order Harmonics from Overdense Plasmas", F. Quéré, C. Thaury, P. Monot, S. Dobosz, Ph. Martin, J.-P. Geindre, and P. Audebert, *Phys. Rev. Lett.*, **2006**, *96*, 125004.

[39] "Theory of high-order harmonic generation in relativistic laser interaction with overdense plasma", T. Baeva, S. Gordienko, and A. Pukhov, *Phys. Rev. E*, **2006**, *74*, 046404.

[40] "High-order harmonic generation in rare gases with a 1-ps 1053-nm laser", A. L'Huillier and Ph. Balcou, *Phys. Rev. Lett.*, **1993**, *70*, 774–777.

[41] "Bright Coherent Ultrahigh Harmonics in the keV X-ray Regime from Mid-Infrared Femtosecond Lasers", T. Popmintchev, M.-C. Chen, D. Popmintchev, P. Arpin, S. Brown, S. Ališauskas, G. Andriukaitis, T. Balčiunas, O. D. Mücke, A. Pugzlys, A. Baltuška, B. Shim, S. E. Schrauth, A. Gaeta, C. Hernández-García, L. Plaja, A. Becker, A. Jaron-Becker, M. M. Murnane, and H. C. Kapteyn, *Science*, **2012**, *336*, 1287–1291.

[42] "High-order harmonic generation from atoms and ions in the high intensity regime", J. L. Krause, K. J. Schafer, and K. C. Kulander, *Phys. Rev. Lett.*, **1992**, *68*, 3535–3538.

[43] "Plasma perspective on strong field multiphoton ionization", P. B. Corkum, *Phys. Rev. Lett.*, **1993**, *71*, 1994–1997.

[44] "Theory of high-harmonic generation by low-frequency laser fields", M. Lewenstein, Ph. Balcou, M. Yu. Ivanov, A. L'Huillier, and P. B. Corkum, *Phys. Rev. A*, **1994**, *49*, 2117–2132.

[45] "Mechanically ruled aberration-corrected concave gratings for a flat-field grazing-incidence spectrograph", T. Kita, T. Harada, N. Nakano, and H. Kuroda, *Appl. Opt.*, **1983**, *22*, 512–513.

[46] "Quantum efficiencies of imaging detectors with alkali halide photocathodes, 1: Microchannel plates with separate and integral CsI photocathodes", G. R. Carruthers, *Appl. Opt.*, **1987**, *26*, 2925–2930.

[47] "High-order harmonic generation using intense femtosecond pulses", J. J. Macklin, J. D. Kmetec, and C. L. Gordon, *Phys. Rev. Lett.*, **1993**, *70*, 766–769.

[48] "Higher-order harmonic generation in xenon at 1064 nm: The role of phase matching", A. L'Huillier, K. J. Schafer, and K. C. Kulander, *Phys. Rev. Lett.*, **1991**, *66*, 2200–2203.

[49] "High-order harmonic generation at a megahertz-level repetition rate directly driven by an ytterbium-doped-fiber chirped-pulse amplification system", J. Boullet, Y. Zaouter, J. Limpert, S. Petit, Y. Mairesse, B. Fabre, J. Higuet, E. Mével, E. Constant, and E. Cormier, *Opt. Lett.,* **2009**, *34*, 1489–1491.

[50] "Coherent Water Window X Ray by Phase-Matched High-Order Harmonic Generation in Neutral Media", E. J. Takahashi, T. Kanai, K. L. Ishikawa, Y. Nabekawa, and K. Midorikawa, *Phys. Rev. Lett.*, **2008**, *101*, 253901.

[51] "Generation of submicrojoule high harmonics using a long gas jet in a two-color laser field", I. J. Kim, G. H. Lee, S. B. Park, Y. S. Lee, T. K. Kim, C. H. Nam, T. Mocek, and K. Jakubczak, *Appl. Phys. Lett.*, **2008**, *92*, 021125.

[52] "Influence of the medium length on high-order harmonic generation", C. Delfin, C. Altucci, F. D. Filippo, C. de Lisio, M. B. Gaarde, A. L'Huillier, L. Roos, and C.-G. Wahlström, *J. Phys. B: At. Mol. Opt. Phys.*, **1999**, *32*, 5397.

[53] "High-order harmonic generation in laser-produced ions using a near-infrared laser", C.-G. Wahlström, S. Borgström, J. Larsson, and S.-G. Pettersson, *Phys. Rev. A*, **1995**, *51*, 585–591.

[54]"High-order harmonic generation from carbon plasma", R. A. Ganeev, M. Suzuki, M. Baba, and H. Kuroda, *J. Opt. Soc. Am. B,* **2005**, *22*, 1927–1933.

[55] "Optimization of the high-order harmonics generated from silver plasma", R. A. Ganeev, H. Singhal, P. A. Naik, U. Chakravarty, V. Arora, J. A. Chakera, R. A. Khan, M. Raghuramaiah, S. R. Kumbhare, R. P. Kushwaha, and P. D. Gupta, *Appl. Phys. B*, **2007**, *87*, 243–247.

[56] "High-order harmonic generation in laser plasma: Recent achievements", R. A. Ganeev, *Laser Phys.*, **2012**, *22*, 1177–1188.

[57] "Demonstration of the 101st harmonic generated from a laser-produced manganese plasma", R. A. Ganeev, L. B. E. Bom, J.-C. Kieffer, M. Suzuki, H. Kuroda, and T. Ozaki, *Phys. Rev. A*, **2007**, *76*, 023831.

[58] "Harmonic generation from indium-rich plasmas", R. A. Ganeev, H. Singhal, P. A. Naik, V. Arora, U. Chakravarty, J. A. Chakera, R. A. Khan, I. A. Kulagin, P. V. Redkin, M. Raghuramaiah, and P. D. Gupta, *Phys. Rev. A*, **2006**, *74*, 063824.

[59] "Ultrahigh 22 nm resolution coherent diffractive imaging using a desktop 13 nm high harmonic source", M. D. Seaberg, D. E. Adams, E. L. Townsend, D. A. Raymondson, W. F. Schlotter, Y. Liu, C. S. Menoni, L. Rong, C.-C. Chen, J. Miao, H. C. Kapteyn, and M. M. Murnane, *Opt. Express*, **2011**, *19*, 22470–22479.

[60] "Optimizing High Harmonic Generation in Absorbing Gases: Model and Experiment", E. Constant, D. Garzella, P. Breger, E. Mével, Ch. Dorrer, C. Le Blanc, F. Salin, and P. Agostini, *Phys. Rev. Lett.*, **1999**, *82*, 1668–1671.

[61] "Dependence of high-order harmonic intensity on the length of preformed plasma plumes", H. Singhal, V. Arora, B. S. Rao, P. A. Naik, U. Chakravarty, R. A. Khan, and P. D. Gupta, *Phys. Rev. A*, **2009**, *79*, 023807.

[62] "Physical origin of the Gouy phase shift", S. Feng and H. G. Winful, *Opt. Lett.*, **2001**, *26*, 485–487.

[63] "Interplay between absorption, dispersion and refraction in high-order harmonic generation", H. Dachraoui, T. Auguste, A. Helmstedt, P. Bartz, M. Michelswirth, N. Mueller, W. Pfeiffer, P. Salieres, and U. Heinzmann, *J. Phys. B: At. Mol. Opt. Phys.*, **2009**, *42*, 175402.

[64] "Intensity-dependent atomic-phase effects in high-order harmonic generation", J. Peatross and D. D. Meyerhofer, *Phys. Rev. A*, **1995**, *52*, 3976–3987.

[65] "Intensity-dependent phase-matching effects in harmonic generation", J. Peatross, M. V. Fedorov, and K. C. Kulander, *J. Opt. Soc. Am. B*, **1995**, *12*, 863–870.

[66] "Introduction to Plasma Physics and Controlled Fusion", Francis F. Chen, Springer, **2015**,

[67] "Lensless Diffractive Imaging Using Tabletop Coherent High-Harmonic Soft-X-Ray Beams", R. L. Sandberg, A. Paul, D. A. Raymondson, S. Hädrich, D. M. Gaudiosi, J. Holtsnider, R. I. Tobey, O. Cohen, M. M. Murnane, H. C. Kapteyn, C. Song, J. Miao, Y. Liu, and F. Salmassi, *Phys. Rev. Lett.*, **2007**, *99*, 098103.

[68] "Table-top nanoscale coherent imaging with XUV light", J. Rothhardt, G. K. Tadesse, W. Eschen, and J. Limpert, *J. Opt.*, **2018**, *20*, 113001.

[69] "Single attosecond pulse and xuv supercontinuum in the high-order harmonic plateau", Z. Chang, *Phys. Rev. A*, **2004**, *70*, 043802.

[70] "High harmonic generation with long-wavelength few-cycle laser pulses", B. E. Schmidt, A. D. Shiner, M. Giguère, P. Lassonde, C. A. Trallero-Herrero, J.-C. Kieffer, P. B. Corkum, D. M. Villeneuve, and F. Légaré, *J. Phys. B: At. Mol. Opt. Phys.*, **2012**, *45*, 074008.

[71] "Attosecond-chirp compensation with material dispersion to produce near transform-limited attosecond pulses", D. H. Ko, K. T. Kim, and C. H. Nam, *J. Phys. B: At. Mol. Opt. Phys.*, **2012**, *45*, 074015.

[72] "Attosecond chirp compensation in water window by plasma dispersion", Z. Chang, *Opt. Express*, **2018**, *26*, 33238–33244.

[73] "Attosecond physics", F. Krausz and M. Ivanov, *Rev. Mod. Phys.*, **2009**, *81*, 163–234.

[74] "Imaging orbitals with attosecond ", P. Salières, A. Maquet, S. Haessler, J. Caillat, and R. Taïeb, *Rep. Prog. Phys.*, **2012**, *75*, 062401.

[75] "Compression of amplified chirped optical pulses", D. Strickland and G. Mourou, *Opt. Com.*, **1985**, *55*, 447–449.

[76] "60-fsec pulse generation from a self-mode-locked Ti:sapphire laser", D. E. Spence, P. N. Kean, and W. Sibbett, *Opt. Lett.*, **1991**, *16*, 42–44.

[77] "Aberration-free stretcher design for ultrashort-pulse amplification", G. Cheriaux, P. Rousseau, F. Salin, J. P. Chambaret, B. Walker, and L. F. Dimauro, *Opt. Lett.*, **1996**, *21*, 414–416.

[78] "ND : YAG regenerative amplifier", J. E. Murray and W. H. Lowdermilk, *Journal of Applied Physics*, **1980**, *51*, 3548–3556.

[79] "Optical pulse compression with diffraction gratings", E. Treacy, *IEEE Journal of Quantum Electronics*, **1969**, *5*, 454–458.

[80] "Laser Fundamentals", William T. Silfvast, **2004**, Cambridge University Press.

[81] "Short Pulse Laser Interactions with Matter: An Introduction", P. Gibbon, **2005**, Imperial College Press

[82] "Distortion of femtosecond laser pulses in lenses", Z. Bor, *Opt. Lett.*, **1989**, *14*, 119–121.

[83] "*Lasers",* A. E. Siegman, **1986**, University Science Books.

[84] "From nanosecond to femtosecond science," N. Bloembergen, *Rev. Mod. Phys.*, **1999**, *71*, S283–S287.

[85] "A second-order autocorrelator for single-shot measurement of femtosecond laser pulse durations", M. Raghuramaiah, A. K. Sharma, P. A. Naik, P. D. Gupta, and R. A. Ganeev, *Sadhana*, **2001**, *26*, 603–611.

[86] "High-harmonic generation: Ultrafast lasers yield X-rays", I. McKinnie and H. Kapteyn, *Nat Photon*, **2010**, *4*, 149–151.

[87] "Stability and quantum efficiency performance of silicon photodiode detectors in the far ultraviolet", L. R. Canfield, J. Kerner, and R. Korde, *Appl. Opt.*, **1989**, *28*, 3940–3943.

[88] "Charge-coupled device area x-ray detectors", S. M. Gruner, M. W. Tate, and E. F. Eikenberry, *Review of Scientific Instruments*, **2002**, *73*, 2815–2842.

[89] "Microchannel plate detectors", J. Ladislas Wiza, *Nuclear Instruments and Methods*, **1979**, *162*, 587–601.

[90] "Microchannel plate fabrication using glass capillary arrays with Atomic Layer Deposition films for resistance and gain", M. A. Popecki, B. Adams, C. A. Craven, T. Cremer, M. R. Foley, A. Lyashenko, A. O'Mahony, M. J. Minot, M. Aviles, J. L. Bond, M. E. Stochaj, W. Worstell, J. W. Elam, A. U. Mane, O. H. W. Siegmund, C. Ertley, L. M. Kistler, and M. S. Granoff, *Journal of Geophysical Research: Space Physics*, **2016**, *121*, 7449–7460.

[91] "A simple XUV transmission grating spectrograph with sub-\a angström resolution for laser-plasma interaction studies", S. Sailaja, V. Arora, S. R. Kumbhare, P. A. Naik, P. D. Gupta, D. A. Fedin, A. A. Rupasov, and A. S. Shikanov, *Meas. Sci. Technol.*, **1998**, *9*, 1462–1468.

[92] "Aberration-reduced holographic spherical gratings for Rowland circle spectrographs", R. Grange, *Appl. Opt.*, **1992**, *31*, 3744–3749.

[93] "Development of a flat-field XUV spectrograph for laser plasma interaction studies", A. Chowdhury, R. A. Joshi, S. R. Kumbhare, P. A. Naik, and P. D. Gupta, *Sadhana*, **1999**, *24*, 557–566.

[94] "Optimum design of a grazing-incidence flat-field spectrograph with a spherical varied-line-space grating", T. Harada, K. Takahashi, H. Sakuma, and A. Osyczka, *Appl. Opt.*, **1999**, *38*, 2743–2748.

[95] "Grazing-incidence flat-field spectrometer for high-order harmonic diagnostics", L. Poletto, G. Naletto, and G. Tondello, *Opt. Eng*, **2001**, *40*, 178–185.

[96] "Study of Higher Diffraction Order Contribution in a Flat Field Grating Spectrograph Using a High-Order Harmonic Source", M. Kumar, H. Singhal, J. A. Chakera, and P. A. Naik, *Appl Spectrosc*, **2018**, 72(9), 1416-1424.

[97] "Restoration of absolute diffraction efficiency and blaze angle of carbon contaminated gratings by ultraviolet cleaning", M. Kumar, M. H. Modi, H. Singhal, S. Sendhil Raja, J. A. Chakera, R. K. Gupta, P. A. Naik, G. S. Lodha, and P. D. Gupta, *Appl Opt*, **2013**, *52*, 1725–1730.

[98] "Enhancement of conversion efficiency and spatial coherence of high order harmonics generated from pre-formed plasma plumes using an apertured laser beam", M. Kumar, U. Chakravarty, R. Rathore, J. A. Chakera, P. A. Naik, and P. D. Gupta, *J. Phys. B: At. Mol. Opt. Phys.*, **2016**, *49*, 075601.

[99] "Space-resolving flat-field extreme ultraviolet spectrograph system and its aberration analysis with wave-front aberration", I. W. Choi, J. U. Lee, and C. H. Nam, *Appl. Opt.,* **1997**, *36*, 1457–1466.

[100] "High-order harmonic generation in rare gases with an intense short-pulse laser", C.-G. Wahlström, J. Larsson, A. Persson, T. Starczewski, S. Svanberg, P. Salières, Ph. Balcou, and A. L'Huillier, *Phys. Rev. A*, **1993**, *48*, 4709–4720.

[101] "High-order harmonic generation in a laser plasma: a review of recent achievements", R. A. Ganeev, *J. Phys. B: At. Mol. Opt. Phys.*, **2007**, *40*, R213.

[102] "Single-harmonic enhancement by controlling the chirp of the driving laser pulse during high-order harmonic generation from GaAs plasma", R. A. Ganeev, H. Singhal, P. A. Naik, V. Arora, U. Chakravarty, J. A. Chakera, R. A. Khan, P. V. Redkin, M. Raghuramaiah, and P. D. Gupta, *J. Opt. Soc. Am. B,* **2006**, *23*, 2535–2540.

[103] "Use of carbon-containing materials for efficient high-order harmonic generation of laser radiation", R. A. Ganeev, P. A. Naik, H. Singhal, J. A. Chakera, M. Kumar, U. Chakravarty, and P. D. Gupta, *Opt. Comm.*, **2012**, *285*, 2934–2941.

[104] "Strong enhancement and extinction of single harmonic intensity in the mid- and end-plateau regions of the high harmonics generated in weakly excited laser plasmas", R. A. Ganeev, P. A. Naik, H. Singhal, J. A. Chakera, and P. D. Gupta, *Opt. Lett.,* **2007**, *32*, 65–67.

[105] "Enhancement of high-order harmonic generation using a two-color pump in plasma plumes", R. A. Ganeev, H. Singhal, P. A. Naik, I. A. Kulagin, P. V. Redkin, J. A. Chakera, M. Tayyab, R. A. Khan, and P. D. Gupta, *Phys. Rev. A*, **2009**, *80*, 033845.

[106] "Tuning of the high-order harmonics generated from laser plasma plumes and solid surfaces by varying the laser spectrum, chirp, and focal position", R. A. Ganeev, P. A. Naik, H. Singhal, J. A. Chakera, P. D. Gupta, and H. Kuroda, *J. Opt. Soc. Am. B,* **2007**, *24*, 1138–1143.

[107]"Application of laser-produced extended plasma plumes for generation and characterization of the high-order harmonics of 64 fs pulses", R. A. Ganeev, M. Suzuki, and H. Kuroda, *Eur. Phys. J. D*, **2014**, *68*, 1–8.

[108]"Advanced properties of extended plasmas for efficient high-order harmonic generation", R. A. Ganeev, M. Suzuki, and H. Kuroda, *Physics of Plasmas*, **2014**, *21*, 053503.

[109]"Application of mid-infrared pulses for quasi-phase-matching of high-order harmonics in silver plasma", R. A. Ganeev, A. Husakou, M. Suzuki, and H. Kuroda, *Optics Express*, **2016**, *24*, 3414.

[110]"On- and off-axis quasi-phase-matching of the harmonics generated in multi-jet laser-produced plasmas", R. A. Ganeev, *J. Phys. B: At. Mol. Opt. Phys.*, **2016**, *49*, 095402.

[111]"Study of high-order harmonic generation from nanoparticles", H. Singhal, R. A. Ganeev, P. A. Naik, A. K. Srivastava, A. Singh, R. Chari, R. A. Khan, J. A. Chakera, and P. D. Gupta, *J. Phys. B: At. Mol. Opt. Phys.*, **2010**, *43*, 025603.

[112]"Quantum path signatures in harmonic spectra from metal plasma", R. A. Ganeev, C. Hutchison, T. Siegel, A. Zaïr, and J. P. Marangos, *Phys. Rev. A*, **2011**, *83*, 063837.

[113]"Single-shot spatial-coherence measurement of 13 nm high-order harmonic beam by a Young's double-slit measurement", Y. Nagata, K. Furusawa, Y. Nabekawa, and K. Midorikawa, *Opt. Lett.*, **2007**, *32*, 722–724.

[114]"High order harmonic generation optimization with an apertured laser beam", S. Kazamias, F. Weihe, D. Douillet, C. Valentin, T. Planchon, S. Sebban, G. Grillon, F. Augé, D. Hulin, and P. Balcou, *Eur. Phys. J. D*, **2002**, *21*, 353–359.

[115]"Phase-matching for generation of few high order harmonics in a semi-infinite gas cell", L. Van Dao, S. Teichmann, and P. Hannaford, *Physics Letters A*, **2008**, *372*, 5254–5257.

[116]"Single-shot holography using high-order harmonics", J. Schwenke, A. Mai, M. Miranda, X. He, G. Genoud, A. Mikkelsen, S.-G. Pettersson, A. Persson, and A. L'Huillier, *Journal of Modern Optics*, **2008**, *55*, 2723–2730.

[117] "Optical Coherence and Quantum Optics", L. Mandel and E. Wolf, **1995**, Cambridge University Press

[118] "Principles of Optics: Electromagnetic Theory of Propagation, Interference and Diffraction of Light", M. Born, E. Wolf, **2000**, Cambridge university press,

[119]"Study of the spatial coherence of high order harmonic radiation generated from pre-formed plasma plumes", M. Kumar, H. Singhal, J. A. Chakera, P. A. Naik, R. A. Khan, and P. D. Gupta, *Journal of Applied Physics*, **2013**, *114*, 033112.

[120]"Quasi-phase-matching of high-order harmonics in multiple plasma jets", R. A. Ganeev, M. Suzuki, and H. Kuroda, *Phys. Rev. A*, **2014**, *89*, 033821.

[121]"Dependence of high order harmonics intensity on laser focal spot position in preformed plasma plumes", H. Singhal, R. Ganeev, P. A. Naik, V. Arora, U. Chakravarty, and P. D. Gupta, *Journal of Applied Physics*, **2008**, *103*, 013107.

[122]"Generation of extreme ultraviolet radiation with a Bessel–Gaussian beam", L. V. Dao, K. B. Dinh, and P. Hannaford, *Applied Physics Letters*, **2009**, *95*, 131114.

[123]"Controlling high harmonics generation by spatial shaping of high-energy femtosecond beam", A. Dubrouil, Y. Mairesse, B. Fabre, D. Descamps, S. Petit, E. Mével, and E. Constant, *Opt. Lett.,* **2011**, *36*, 2486–2488.

[124]"Analytical expressions of generalized factor of hard-edged diffracted Laguerre–Gaussian beams", Z. Mei, D. Zhao, and C. Zheng, *Optik - International Journal for Light and Electron Optics*, **2005**, *116*, 337–342.

[125]"Thin lens equation for a real laser beam with weak lens aperture truncation", H. Sun, *Opt. Eng*, **1998**, *37*, 2906–2913.

[126]"Calculation and measurement of high-order harmonic energy yields in helium", T. Ditmire, K. Kulander, J. K. Crane, H. Nguyen, and M. D. Perry, *J. Opt. Soc. Am. B*, **1996**, *13*, 406–411.

[127]"Signature of the transversal coherence length in high-order harmonic generation", C. Hernández-García, I. J. Sola, and L. Plaja, *Phys. Rev. A*, **2013**, *88*, 043848.

[128]"Ultrafast electron dynamics in phenylalanine initiated by attosecond pulses", F. Calegari, D. Ayuso, A. Trabattoni, L. Belshaw, S. D. Camillis, S. Anumula, F. Frassetto, L. Poletto, A. Palacios, P. Decleva, J. B. Greenwood, F. Martín, and M. Nisoli, *Science*, **2014**, *346*, 336–339.

[129]"High-flux ultrafast extreme-ultraviolet photoemission spectroscopy at 18.4 MHz pulse repetition rate", T. Saule, S. Heinrich, J. Schötz, N. Lilienfein, M. Högner, O. deVries, M. Plötner, J. Weitenberg, D. Esser, J. Schulte, P. Russbueldt, J. Limpert, M. F. Kling, U. Kleineberg, and I. Pupeza, *Nature Communications*, **2019**, *10*, 458.

[130]"Intensity dependent spectral features in high harmonic generation", K. B. Dinh, P. Hannaford, and L. V. Dao, *Journal of Applied Physics*, **2013**, *113*, 063102.

[131]"Influence of atomic density in high-order harmonic generation", C. Altucci, T. Starczewski, E. Mevel, C.-G. Wahlström, B. Carré, and A. L'Huillier, *J. Opt. Soc. Am. B*, **1996**, *13*, 148–156.

[132]"Quantum path selection in high-harmonic generation by a phase-locked two-color field", N. Ishii, A. Kosuge, T. Hayashi, T. Kanai, J. Itatani, S. Adachi, and S. Watanabe, *Optics Express*, **2008**, *16*, 20876.

[133]"Quantum path contribution to high-order harmonic spectra", E. Brunetti, R. Issac, and D. A. Jaroszynski, *Phys. Rev. A*, **2008**, *77*, 023422.

[134]"Spectral splitting and quantum path study of high-harmonic generation from a semi-infinite gas cell", W. Cao, G. Laurent, C. Jin, H. Li, Z. Wang, C. D. Lin, I. Ben-Itzhak, and C. L. Cocke, *J. Phys. B: At. Mol. Opt. Phys.*, **2012**, *45*, 074013.

[135]"Spatial fingerprint of quantum path interferences in high order harmonic generation", F. Schapper, M. Holler, T. Auguste, A. Zaïr, M. Weger, P. Salières, L. Gallmann, and U. Keller, *Opt. Express*, **2010**, *18*, 2987–2994.

[136]"A high-flux high-order harmonic source", P. Rudawski, C. M. Heyl, F. Brizuela, J. Schwenke, A. Persson, E. Mansten, R. Rakowski, L. Rading, F. Campi, B. Kim, P. Johnsson, and A. L'Huillier, *Review of Scientific Instruments*, **2013**, *84*, 073103.

[137]"Generation of high-energy high-order harmonics by use of a long interaction medium", E. Takahashi, Y. Nabekawa, M. Nurhuda, and K. Midorikawa, *Journal of the Optical Society of America B*, **2003**, *20*, 158.

[138]"High-order harmonic generation using a high-repetition-rate turnkey laser", E. Lorek, E. W. Larsen, C. M. Heyl, S. Carlström, D. Paleček, D. Zigmantas, and J. Mauritsson, *Rev. Sci. Inst.*, **2014**, *85*, 123106.

[139]"Determination of the spectral variation origin in high-order harmonic generation in noble gases", V. E. Nefedova, M. F. Ciappina, O. Finke, M. Albrecht, J. Vábek, M. Kozlová, N. Suárez, E. Pisanty, M. Lewenstein, and J. Nejdl, *Phys. Rev. A*, **2018**, *98*, 033414.

[140]"Quantum path interference in the wavelength-dependent below-threshold harmonic generation", L. He, P. Lan, C. Zhai, Y. Li, Z. Wang, Q. Zhang, and P. Lu, *Phys. Rev. A*, **2015**, *91*, 023428.

[141]"Full Quantum Trajectories Resolved High-Order Harmonic Generation", P. Ye, X. He, H. Teng, M. Zhan, S. Zhong, W. Zhang, L. Wang, and Z. Wei, *Phys. Rev. Lett.*, **2014**, *113*, 073601.

[142]"Attosecond Probing of Nuclear Dynamics with Trajectory-Resolved High-Harmonic Spectroscopy", P. Lan, M. Ruhmann, L. He, C. Zhai, F. Wang, X. Zhu, Q. Zhang, Y. Zhou, M. Li, M. Lein, and P. Lu, *Phys. Rev. Lett.*, **2017**, *119*, 033201.

[143]"Spatially and spectrally resolved quantum-path tracing in high-order harmonic generation", J. Jiang, P. Wei, Z. Zeng, J. Miao, Y. Zheng, X. Ge, C. Li, R. Li, and Z. Xu, *Optics Express*, **2014**, *22*, 15975.

[144]"Macroscopic control of high-order harmonics quantum-path components for the generation of attosecond pulses", H. Merdji, M. Kovačev, W. Boutu, P. Salières, F. Vernay, and B. Carré, *Phys. Rev. A*, **2006**, *74*, 043804.

[145]"Selection of an electron path of high-order harmonic generation in a two-colour femtosecond laser field", C. M. Kim and C. H. Nam, *J. Phys. B: At. Mol. Opt. Phys.*, **2006**, *39*, 3199.

[146]"Theoretical and experimental analysis of quantum path interferences in high-order harmonic generation", T. Auguste, P. Salières, A. S. Wyatt, A. Monmayrant, I. A. Walmsley, E. Cormier, A. Zaïr, M. Holler, A. Guandalini, F. Schapper, J. Biegert, L. Gallmann, and U. Keller, *Phys. Rev. A*, **2009**, *80*, 033817.

[147]"Ionization-induced defocusing of intense laser pulses in high-pressure gases", S. C. Rae, *Optics Communications*, **1993**, *97*, 25–28.

[148]"Wave-front correction of femtosecond terawatt lasers by deformable mirrors", F. Druon, G. Chériaux, J. Faure, J. Nees, M. Nantel, A. Maksimchuk, G. Mourou, J. C. Chanteloup, and G. Vdovin, *Opt. Lett.*, **1998**, *23*, 1043–1045.

[149]"Spatial and spectral properties of the high-order harmonic emission in argon for seeding applications", X. He, M. Miranda, J. Schwenke, O. Guilbaud, T. Ruchon, C. Heyl, E. Georgadiou, R. Rakowski, A. Persson, M. B. Gaarde, and A. L'Huillier, *Phys. Rev. A*, **2009**, *79*, 063829.

[150]"Spectrally resolved spatiotemporal features of quantum paths in high-order harmonic generation", L. He, P. Lan, Q. Zhang, C. Zhai, F. Wang, W. Shi, and P. Lu, *Phys. Rev. A*, ***2015***, 92, 043403

[151]"Comparison of mechanically ruled versus holographically varied line-spacing gratings for a soft-x-ray flat-field spectrograph", T. Yamazaki, E. Gullikson, N.

Miyata, M. Koike, Y. Harada, S. Mrowka, U. Kleineberg, J. H. Underwood, M. M. Yanagihara, and K. Sano, *Appl. Opt.*, **1999**, *38*, 4001–4003.

[152]"Soft-X-Ray Harmonic Comb from Relativistic Electron Spikes", A. S. Pirozhkov *et al.*, *Phys. Rev. Lett.*, **2012**, *108*, 135004.

[153]"Characterization of a flat-field grazing-incidence XUV spectrometer", W. Schwanda, K. Eidmann, and M. C. Richardson, *Journal of X-Ray Science and Technology*, **1993**, *4*, 8–17.

[154]"Different approaches to precise wavelength calibration of a flat-field grating spectrometer for laser-produced plasmas", G. Xiong, J. Zhang, G. Yang, J. Yang, H. Li, Z. Hu, Y. Zhao, M. Wei, and T. Yi, *Phys. Scr.*, **2014**, *89*, 065005.

[155]"Accurate Wavelength Calibration Method for Flat-Field Grating Spectrometers", X. Du, C. Li, Z. Xu, and Q. Wang, *Appl. Spectrosc.*, **2011**, *65*, 1083–1086.

[156]"Attosecond Pulse Trains Using High Order Harmonics", P. Antoine, A. L'Huillier, and M. Lewenstein, *Phys. Rev. Lett.*, **1996**, *77*, 1234–1237.

[157]"XUV attosecond pulses: generation and measurement", G. A. Reider, *J. Phys. D: Appl. Phys.*, **2004**, *37*, R37–R48.

[158]"Experimental studies of attosecond pulse trains", K. Varjú, P. Johnsson, R. López-Martens, T. Remetter, E. Gustafsson, J. Mauritsson, M. B. Gaarde, K. J. Schafer, C. Erny, I. Sola, A. Zaïr, E. Constant, E. Cormier, E. Mével, and A. L'Huillier, *Laser physics*, **2005**, *15*, 888–898.

[159]"Reconstruction of Attosecond Pulse Trains Using an Adiabatic Phase Expansion", K. Varjú, Y. Mairesse, P. Agostini, P. Breger, B. Carré, L. J. Frasinski, E. Gustafsson, P. Johnsson, J. Mauritsson, H. Merdji, P. Monchicourt, A. L'Huillier, and P. Salières , *Phys. Rev. Lett*. **2005**, **95**, 243901.

[160]"Generation of bright isolated attosecond soft X-ray pulses driven by multicycle midinfrared lasers", M.-C. Chen, C. Mancuso, C. Hernández-García, F. Dollar, B. Galloway, D. Popmintchev, P.-C. Huang, B. Walker, L. Plaja, A. A. Jaroń-Becker, A. Becker, M. M. Murnane, H. C. Kapteyn, and T. Popmintchev, *PNAS*, **2014**, *111*, E2361–E2367.

[161]"Generation of isolated sub-40-attosecond pulse with a multicycle chirped laser and a static electric field", M. Mohebbi, *Appl. Phys. B*, **2016**, *122*, 1–10.

[162]"The physics of attosecond light pulses", P. Agostini and L. F. DiMauro, *Rep. Prog. Phys.*, **2004**, *67*, 1563.

[163]"Advances in attosecond science", F. Calegari, G. Sansone, S. Stagira, C. Vozzi, and M. Nisoli, *J. Phys. B: At. Mol. Opt. Phys.*, **2016**, *49*, 062001.

[164]"Ultrafast dynamics in the DNA building blocks thymidine and thymine initiated by ionizing radiation", *E. P. Månsson, S. D. Camillis, M. C. Castrovilli, M. Galli, M. Nisoli, F. Calegari, and J. B. Greenwood, Phys. Chem. Chem. Phys.,* **2017, *19***, *19815*

[165]"Tunneling Dynamics in Multiphoton Ionization and Attoclock Calibration", M. Klaiber, K. Z. Hatsagortsyan, and C. H. Keitel, *Phys. Rev. Lett.*, **2015**, *114*, 083001.

[166]"Atomic photoionization experiment by harmonic-generation spectroscopy", M. V. Frolov, T. S. Sarantseva, N. L. Manakov, K. D. Fulfer, B. P. Wilson, J. Troß, X. Ren, E. D. Poliakoff, A. A. Silaev, N. V. Vvedenskii, A. F. Starace, and C. A. Trallero-Herrero, *Phys. Rev. A*, **2016**, *93*, 031403.

[167]"Reconstruction of attosecond harmonic beating by interference of two-photon transitions", H. G. Muller, *Appl Phys B*, **2002**, *74*, s17.

[168]"Streaking of 43-attosecond soft-X-ray pulses generated by a passively CEP-stable mid-infrared driver", T. Gaumnitz, A. Jain, Y. Pertot, M. Huppert, I. Jordan, F. Ardana-Lamas, and H. J. Wörner, *Opt. Express*, **2017**, *25*, 27506–27518.

[169]"Comparison of attosecond streaking and RABBITT", L. Cattaneo, J. Vos, M. Lucchini, L. Gallmann, C. Cirelli, and U. Keller, *Opt. Express,* **2016**, *24*, 29060–29076.

[170]"Selection of high-order harmonics from a single quantum path for the generation of an attosecond pulse train", D. G. Lee, H. J. Shin, Y. H. Cha, K. H. Hong, J.-H. Kim, and C. H. Nam, *Phys. Rev. A*, **2001**, *63*, 021801.

[171]"Phase control of attosecond pulses in a train", C. Guo, A. Harth, S. Carlström, Y.-C. Cheng, S. Mikaelsson, E. Mårsell, Christoph Heyl, M. Miranda, M. Gisselbrecht, M. B. Gaarde, K. J. Schafer, A. Mikkelsen, Johan Mauritsson, C. L. Arnold, and A. L'Huillier, *J. Phys. B: At. Mol. Opt. Phys.*, **2018**, *51*, 034006.

[172]"Enhanced phase-matching for generation of soft X-ray harmonics and attosecond pulses in atomic gases", V. S. Yakovlev, M. Ivanov, and F. Krausz, *Optics Express*, **2007**, *15*, 15351.

[173]"27-fs extreme ultraviolet pulse generation by high-order harmonics", Y. Kobayashi, T. Sekikawa, Y. Nabekawa, and S. Watanabe, *Opt. Lett.*, **1998**, *23*, 64–66.

[174]"Production of Doubly Charged Helium Ions by Two-Photon Absorption of an Intense Sub-10-fs Soft X-Ray Pulse at 42 eV Photon Energy", Y. Nabekawa, H. Hasegawa, E. J. Takahashi, and K. Midorikawa, *Phys. Rev. Lett.*, **2005**, *94*, 043001.

[175]"Phase dependence of (N+1)-color (N>1) IR-UV photoionization of atoms with higher harmonics", V. Véniard, R. Taïeb, and A. Maquet, *Phys. Rev. A*, **1996**, *54*, 721–728.

[176]"Photonic streaking of attosecond pulse trains", K. T. Kim, C. Zhang, T. Ruchon, J.-F. Hergott, T. Auguste, D. M. Villeneuve, P. B. Corkum, and F. Quéré, *Nature Photon*, **2013**, *7*, 651–656.

[177]"Temporal characterization of individual harmonics of an attosecond pulse train by THz streaking", F. Ardana-Lamas, C. Erny, A. G. Stepanov, I. Gorgisyan, P. Juranić, R. Abela, and C. P. Hauri, *Phys. Rev. A*, **2016**, *93*, 043838.

[178]"Attosecond Streak Camera", J. Itatani, F. Quéré, G. L. Yudin, M. Yu. Ivanov, F. Krausz, and P. B. Corkum, *Phys. Rev. Lett.*, **2002**, *88*, 173903.

[179]"Magnetic field paralleliser for 2π electron-spectrometer and electron-image magnifier", P. Kruit and F. H. Read, *J. Phys. E: Sci. Instrum.*, **1983**, *16*, 313–324.

[180]"Time-of-flight electron spectrometer for a broad range of kinetic energies", A. Kothe, J. Metje, M. Wilke, A. Moguilevski, N. Engel, R. Al-Obaidi, C. Richter, R. Golnak, I. Yu. Kiyan, and E. F. Aziz, *Rev. Sci. Instr.*, **2013**, ***84,*** *023106.*

[181]"Attosecond electron wave packet interferometry", T. Remetter, P. Johnsson, J. Mauritsson, K. Varjú, Y. Ni, F. Lépine, E. Gustafsson, M. Kling, J. Khan, R. López-Martens, K. J. Schafer, M. J. J. Vrakking, and A. L'Huillier, *Nature Physics*, **2006**, *2*, 323.

[182]"Time-of-flight electron spectrometer for a broad range of kinetic energies", A. Kothe, J. Metje, M. Wilke, A. Moguilevski, N. Engel, R. Al-Obaidi, C. Richter, R. Golnak, I. Y. Kiyan, and E. F. Aziz, *Rev. Sci. Instrum.*, **2013**, *84*, 023106.

[183]"Direct observation of an attosecond electron wave packet in a nitrogen molecule", T. Okino, Y. Furukawa, Y. Nabekawa, S. Miyabe, A. A. Eilanlou, E. J. Takahashi, K. Yamanouchi, and K. Midorikawa, *Science Advances*, **2015**, *1*, e1500356.

[184]"Attosecond pulse characterization", G. Laurent, W. Cao, I. Ben-Itzhak, and C. L. Cocke, *Opt. Express*, **2013**, *21*, 16914–16927.

[185]"Frequency-resolved optical gating for complete reconstruction of attosecond bursts", Y. Mairesse and F. Quéré, *Phys. Rev. A*, **2005**, *71*, 011401.

[186]"Self-guided laser wakefield acceleration using ablated plasma targets", T. Matsuoka, C. McGuffey, M. Levin, S. S. Bulanov, V. Chvykov, G. Kalintchenko, S. Reed, P. Rousseau, V. Yanovsky, A Zigler, K. Krushelnick, and A. Maksimchuk, *Plasma Phys. Control. Fusion*, **2009**, *51*, 095003.

[187]"High-quality electron beam from laser wake-field acceleration in laser produced plasma plumes", B. Sanyasi Rao, A. Moorti, R. Rathore, J. Ali Chakera, P. Anant Naik, and P. Dass Gupta, *Appl. Phys. Lett.*, **2013**, *102*, 231108.

[188]"Dynamics of plasma expansion in the pulsed laser material interaction", N. Kumar, S. Dash, A. K. Tyagi, and B. Raj, *Sadhana*, **2010**, *35*, 493–511.

[189]"Influence of surrounding gas, composition and pressure on plasma plume dynamics of nanosecond pulsed laser-induced aluminium plasmas", M. S. Dawood, A. Hamdan, and J. Margot, *AIP Advances*, **2015**, *5*, 107143.

[190]"Strong Field-Induced Frequency Conversion of Laser Radiation in Plasma Plumes: Recent Achievements", R. A. Ganeev, *The Scientific World Journal*, **2013**, 2, 127670

[191]"Carbon molecules for intense high-order harmonics from laser-ablated graphite plume", M. A. Fareed, S. Mondal, Y. Pertot, and T. Ozaki, *J. Phys. B: At. Mol. Opt. Phys.*, **2016**, *49*, 035604.

[192]"Observation of middle-sized metal clusters in femtosecond laser ablation plasmas through nonlinear optics", M. Oujja, J. G. Izquierdo, L. Bañares, R. de Nalda, and M. Castillejo, *Phys. Chem. Chem. Phys.*, **2018**, *20*, 16956–16965.

[193]"Mass spectrometric study of carbon cluster formation in laser ablation of graphite at 355 nm", Y. M. Koo, Y. K. Choi, K. H. Lee, and K. W. Jung, *Bulletin of the Korean Chemical Society*, **2002**, *22*, 309–314.

[194]"Emission characteristics and dynamics of C_2 from laser produced graphite plasma", S. S. Harilal, R. C. Issac, C. V. Bindhu, V. P. N. Nampoori, and C. P. G. Vallabhan, *Journal of Applied Physics*, **1997**, *81*, 3637–3643.

[195]"Late-time particle emission from laser-produced graphite plasma", S. S. Harilal, A. Hassanein, and M. Polek, *Journal of Applied Physics*, **2011**, *110*, 053301.

[196]"Efficient generation of sub-100 eV high-order harmonics from carbon molecules using infrared laser pulses", M. A. Fareed, N. Thiré, S. Mondal, B. E. Schmidt, F. Légaré, and T. Ozaki, *Applied Physics Letters*, **2016**, *108*, 124104.

[197]"High-Frequency Laser Interferometry in Plasma Diagnostics", J. B. Gerardo, J. T. Verdeyen, and M. A. Gusinow, *Journal of Applied Physics*, **1965**, *36*, 2146–2151.

[198]"Two-wavelength interferometry of a laser-produced carbon plasma", C. D. David, *Appl. Phys. Lett.*, **1967**, *11*, 394–396.

[199]"Characterization of laser induced plasmas by optical emission spectroscopy: A review of experiments and methods", C. Aragón and J. A. Aguilera, *Spectr. Acta Part B: Atomic Spectroscopy*, **2008**, *63*, 893–916.

[200]"Optical emission spectroscopy of carbon laser plasma ion source", O. Balki, Md. M. Rahman, and H. E. Elsayed-Ali, *Optics Communications*, **2018**, *412*, 134–140.

[201]"X-ray Thomson scattering in high energy density plasmas", S. H. Glenzer and R. Redmer, *Rev. Mod. Phys.*, **2009**, *81*, 1625–1663.

[202]"Laser-produced annular plasmas", F. Veloso, H. Chuaqui, R. Aliaga-Rossel, M. Favre, I. H. Mitchell, and E. Wyndham, *Review of Scientific Instruments*, **2006**, *77*, 063506.

[203]"Plasma interferometry and how the bound-electron contribution can bend fringes in unexpected ways", J. Nilsen and W. R. Johnson, *Appl. Opt.*, **2005**, *44*, 7295–7301.

[204]"Picosecond-resolution soft-x-ray laser plasma interferometry", J. Filevich, J. J. Rocca, M. C. Marconi, R. F. Smith, J. Dunn, R. Keenan, J. R. Hunter, S. J. Moon, J. Nilsen, A. Ng, and V. N. Shlyaptsev, *Appl. Opt.*, **2004**, *43*, 3938–3946.

[205]"Pulsed X-ray radiography of a gas jet target for laser–matter interaction experiments with the use of a CCD detector", R. Rakowski, A. Bartnik, H. Fiedorowicz, R. Jarocki, J. Kostecki, J. Mikołajczyk, A. Szczurek, M. Szczurek, I. B. Földes, and Zs. Tóth, *Nucl. Inst. Meth. Phys. Res. A:* **2005**, *551*, 139–144.

[206]"Soft X-ray characterization of an elongated gas-puff target dedicated for laser–matter interaction experiments and high harmonic generation", P. W. Wachulak, A. Bartnik, H. Fiedorowicz, R. Jarocki, J. Kostecki, and M. Szczurek, *Nuclear Instruments and Methods in Physics Research Section B: Beam Interactions with Materials and Atoms*, **2012**, *276*, 38–43.

[207]"Contributed Review: The novel gas puff targets for laser-matter interaction experiments", P. W. Wachulak, *Rev. Sci. Inst.*, **2016**, *87*, 091501.

[208]"Characterization of pulsed capillary channel gas puff target using EUV shadowgraphy", P. W. Wachulak, A. Bartnik, Ł. Węgrzyński, T. Fok, J. Kostecki, M. Szczurek, R. Jarocki, and H. Fiedorowicz, *Nucl. Instr.Meth. Phys. Res.B*, **2015**, *345*, 15–21.

[209]"Chirped pulse shadowgraphy for single shot time resolved plasma expansion measurements", Y. B. S. R. Prasad, S. Barnwal, P. A. Naik, J. A. Chakera, R. A. Khan, and P. D. Gupta, *Appl. Phys. Lett.*, **2010**, *96*, 221503.

[210]"Attosecond emission from chromium plasma", L. B. Elouga Bom, S. Haessler, O. Gobert, M. Perdrix, F. Lepetit, J.-F. Hergott, B. Carré, T. Ozaki, and P. Salières, *Opt Express*, **2011**, *19*, 3677–3685.

[211]"High order harmonic radiation source for multicolor extreme ultraviolet radiography of carbon plumes", M. Kumar, H. Singhal, and J. A. Chakera, *Journal of Applied Physics*, **2019**, *125*, 155902.

[212]"Two-wavelength interferometry on excimer laser induced vapour/plasma plumes during the laser pulse", H. Schittenhelm, G. Callies, P. Berger, and H. Hügel, *Applied Surface Science*, **1998**, *127–129*, 922–927.

[213]"Theoretical Form Factor, Attenuation, and Scattering Tabulation for Z=1–92 from E=1–10 eV to E=0.4–1.0 MeV", C. T. Chantler, *Journal of Physical and Chemical Reference Data*, **1995**, *24*, 71–643.

[214]"A direct comparison of high-speed methods for the numerical Abel transform", D. D. Hickstein, S. T. Gibson, R. Yurchak, D. D. Das, and M. Ryazanov, Rev. Sci. Instr. **2019**, 90, 065115

[215]"Photoabsorption cross sections for positive atomic ions with Z equal to or less than 30", R. F. Reilman and S. T. Manson, *The Astrophysical Journal Supplement Series*, **1979**, *40*, 815–880.

[216]"Solar photo rates for planetary atmospheres and atmospheric pollutants", W. F. Huebner, J. J. Keady, and S. P. Lyon, *Astrophys Space Sci*, **1992**, *195*, 1–294.

[217]"Measurement of the Absolute Photoionization Cross Section of C+ near Threshold", H. Kjeldsen, F. Folkmann, J. E. Hansen, H. Knudsen, M. S. Rasmussen, J. B. West, and T. Andersen, *The Astrophysical Journal Letter*, **1999**, *524*, L143.

[218]“Photoionization of C2+ ions”, A. Müller, R. A. Phaneuf, A. Aguilar, M. F. Gharaibeh, A. S. Schlachter, I. Álvarez, C. Cisneros, G. Hinojosa, and B. M. McLaughlin, *Nucl. Instr.Meth. Phys. Res.B*, **2003**, *205*, 301–305.

[219]“Plasma plume induced during laser ablation of graphite”, J. Hoffman, W. Mróz, A. Prokopiuk, and Z. Szymanski, *Appl. Phys. A*, **2008**, *92*, 921–926.

[220] “Reconstruction errors in Abel inversion”, R. K. Paul, J. T. Andrews, K. Bose and P. K. Barhai, *Plasma devices and operations*, **2010**, *13*,281-289.

[221]“Bright circularly polarized soft X-ray high harmonics for X-ray magnetic circular dichroism”, T. Fan, P. Grychtol, R. Knut, C. Hernández-García, D. D. Hickstein, D. Zusin, C. Gentry, F. J. Dollar, C. A. Mancuso, C. W. Hogle, O. Kfir, D. Legut, K. Carva, J. L. Ellis, K. M. Dorney, C. Chen, O. G. Shpyrko, E. E. Fullerton, O. Cohen, P. M. Oppeneer, D. B. Milošević, A. Becker, A. A. Jaroń-Becker, T. Popmintchev, M. M. Murnane, and H. C. Kapteyn, *Proc Natl Acad Sci USA*, **2015**, *112*, 14206–14211.

APPENDIX A:

Al x-ray filter Transmission

In the present research work, the higher harmonics are generated in the range from 17th to 35th in argon. The cutoff order is extended further to 99th order in helium filled gas cell. The x-ray filter (Al) was used to calibrate the FFGS from the Al-Ledge (λ~17.1nm), which is close to 47th harmonic order of 800nm wavelength. To mark the absorption edge, x-ray transmission through 150nm Al filter (used in experiment) is calculated using (https://henke.lbl.gov/optical_constants/filter2.html) and is shown in Fig A1. Usually oxide layer and other contamination layer are deposited over the filter surface, which reduces the x-ray transmission significantly. Therefore, absorption of 150nm Al filter is experimentally measured using INDUS-1 reflectivity beamline, RRCAT, Indore. The maximum absorption is calculated by fitting the Al-filter thickness (150nm) and the Al oxide layer (Al_2O_3) thickness ~ 14nm on each side. The calculated and measured absorption curve matches for oxide layer thickness of ~14nm. The deviation of absorption at higher wavelength is due to presence of contamination deposited over the filter surface over time.

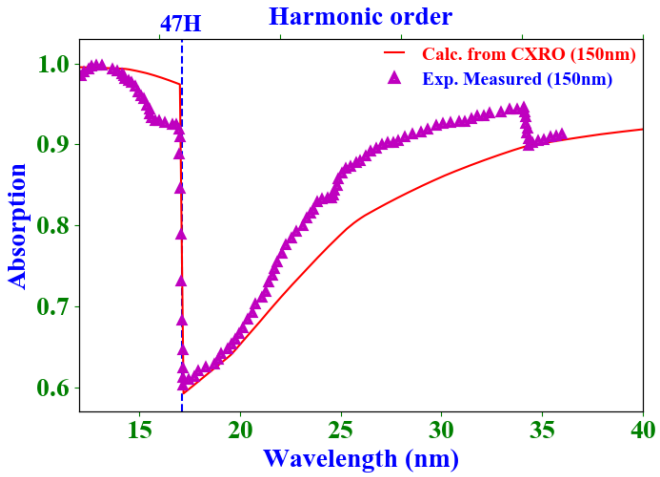

Figure A1: *The variation of x-ray absorption after passing through 150nm thick Al filter. The experimentally measured absorption is measured using INDUS-1, reflectivity beamline, RRCAT, Indore.*

The absorption edge (L-Edge) is close to 47th harmonic order, all harmonic orders below 47th order will be transmitted through the Al filter. After marking 47th harmonic order in the spectrum, the other harmonic orders can be easily identified, as only odd harmonics are present in HHG spectrum for single color case.

Thesis Highlight

Name of the Student: MUKUND KUMAR

Name of the CI/OCC: RRCAT, INDORE **Enrolment No.: PHYS03201404004**

Thesis Title: ***Studies on characterization and application of ultrashort higher harmonic radiation***

Discipline: Physical Sciences **Sub-Area of Discipline: Plasma Physics**

Date of viva voce: 16-06-2020

The present research work is focused on efficient generation, characterization and application of higher harmonic radiation source driven by ultrashort high intensity Ti:sapphire laser pulse at 800 nm. Two different nonlinear media viz. plasma plumes and inert gas filled cells are explored. The phase matching between the driver laser pulse and the generated harmonics generated from nonlinear media plays crucial role in efficient harmonic generation. Various laser and nonlinear medium parameters, which affect the phase matching, are carefully optimized. The use of spatially shaped laser beam is found to improve the harmonic conversion efficiency by one order of magnitude. The harmonic radiation has higher spatial coherence as confirmed from double slit interference, showing fringe contrast > 0.7. In case of gas cell, maximum photon flux of ~ 10^{13} ph/s is achieved at ~ 25nm (31st order), whereas the shortest wavelength down to ~8nm (~ 99th order) is achieved in helium gas. The spectral study of harmonic radiation has revealed the role of different electron trajectories which contributes to the harmonic generation process. These measurements clearly demonstrated the role of trajectories which are responsible for harmonic beam divergence, spectral width and spatial coherence. As higher harmonics are coherent radiation and they are generated from a single driving laser pulse, thus they have definite phase relationship, which may lead to generation of ultrashort (attosecond) pulses. The temporal characterization of these pulses is performed using "RABITT" technique. A high resolution electron time of flight spectrograph viz. MBETOF, is developed in-house for this purpose. It is based on magnetic bottle shape B-field configuration. For temporal pulse shape, cross-correlation signal between the harmonic radiation with its driving laser pulse at IR (800 nm) is recorded. Both odd harmonics (17th to 25th order) generated from argon filed gas cell and IR laser pulse are collinearly focused ions in a low pressure gas sheath (N_2 at ~10^{-5}mbar). This produces photoelectrons of energy corresponding to even harmonic orders (called as sideband energy peaks). The temporal delay scan between the harmonics and IR pulse produces oscillation in signal of sideband electron energy peaks at twice the IR laser frequency. The relative phase between harmonics is measured from sideband photo electron signal oscillation and the signal amplitude. The relative phase and amplitude, is used to reconstruct attosecond pulse train, which is determined to be ~ 300as and repeating at ~ 1.33fs (half laser cycle). The thesis work also presents the application of harmonic radiation in multicolor radiography of the plasma for the first time. Plasma density profile of atoms (CI), ions (CII) and molecules (C_2) are simultaneously recoded for the carbon plume which, is in line with the simulation and other experimental results.

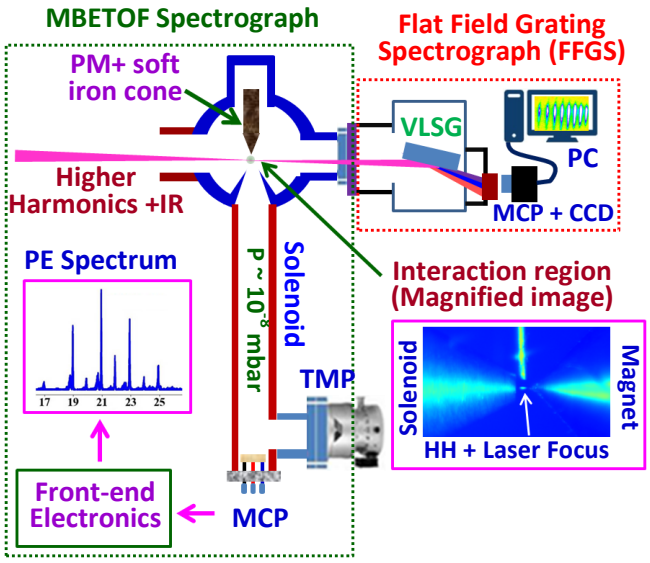

A schematic of an in-house developed magnetic bottle electron time of flight (MBETOF) spectrograph and flat field grating spectrograph (FFGS), HH-Higher harmonics, IR-infrared laser, VLSG-Variable line spaced grating, MCP-microchannel plate, PM-permanent magnet, PE-Photoelectron